

University Library

Author/Filing Title ..OZKAYA, YASAR ALPER

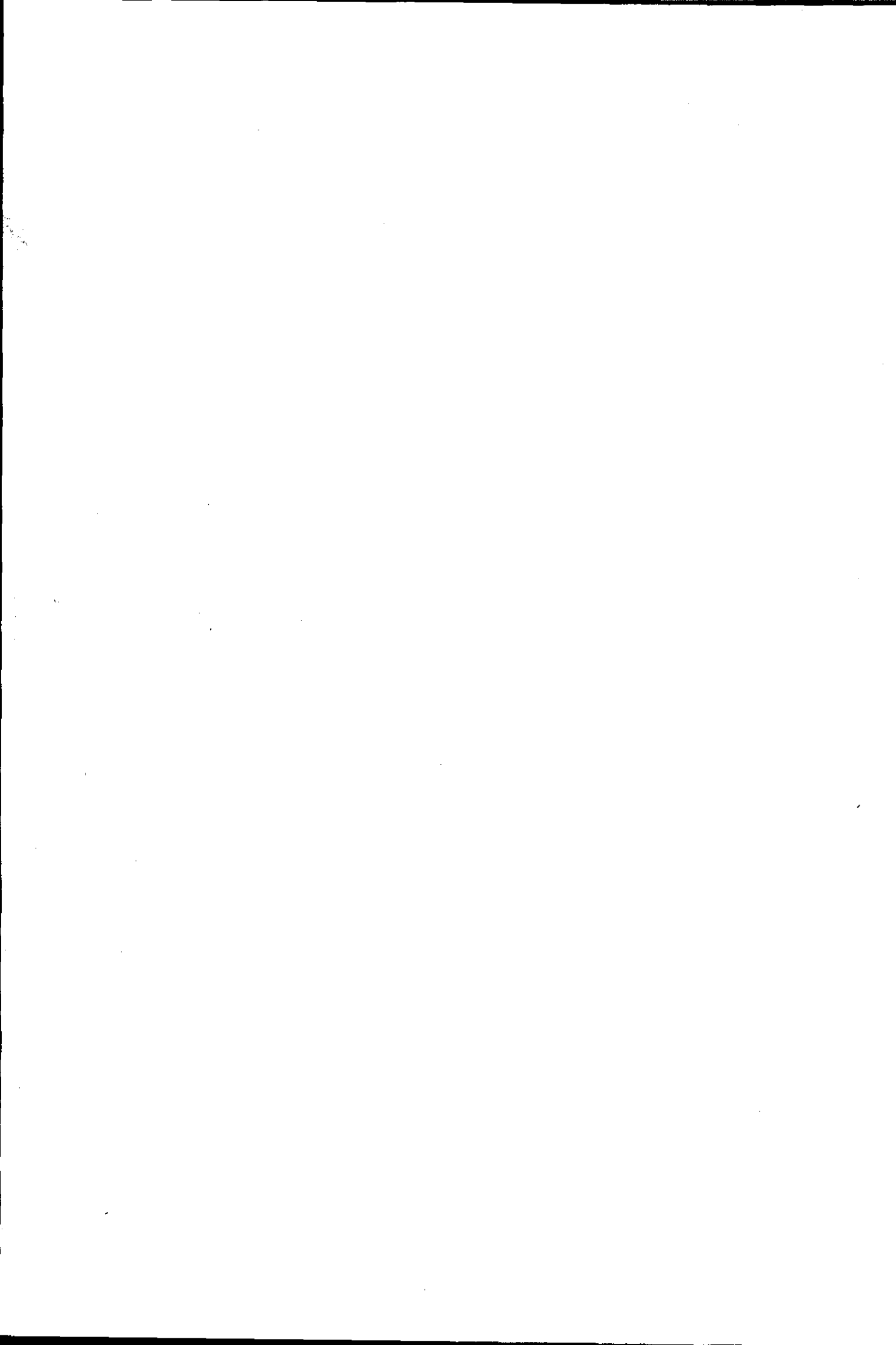
Class Mark T

Please note that fines are charged on ALL
overdue items.

FOR REFERENCE ONLY

0402941535





EVALUATION OF YARN CHARACTERISTICS USING
COMPUTER VISION AND IMAGE PROCESSING

by

Yaşar Alper Özkaya

B.Eng.

A Doctoral Thesis

Submitted in partial fulfilment of the requirements

for the award of

Doctor of Philosophy

of Loughborough University

June 2004

© by Yaşar Alper Özkaya 2004



Loughborough
University
Pilkington Library

Date JUNE 2006

Class THESIS

Acc
No. 0402941535

Abstract

Irregularity, hairiness and twist are among the most important characteristics that define yarn quality. This thesis describes computer vision and image processing techniques developed to evaluate these characteristics.

The optical and electronic aspects such as the illumination, lens parameters and aberrations play crucial role on the quality of yarn images and on the overall performance of image processing. The depth of field limitation being the most important restraint in yarn imaging as well as image distortion in line scan cameras arising from digitisation and yarn movement are modelled mathematically and verified through experiments both for front-lit and back-lit illuminations.

Various light sources and arrangements are tested and relative advantages and disadvantages are discussed based on the image quality. Known problems in defining the hair-core boundaries and determining the total hairiness from yarn images are addressed and image enhancement and processing algorithms developed to overcome these problems are explained. A method to simulate various yarn scanning resolution conditions is described. Using this method, the minimum scanning resolution limits to measure the hairiness and irregularity are investigated.

One of the common methods to measure hairiness is based on using photo-electric sensors to count the number of hairs at certain distances from the core. An image processing technique is developed to simulate these sensors and the results are compared with a commercial tester based on this principle. This method also provided a useful tool for detailed analysis of important limitations of these sensors. A number of indices are developed for determination of total hairiness and the measurements are correlated with a commonly accepted total hairiness index.

The diameter and irregularity measurements obtained from images acquired using different optical arrangements including dark-field and back-lit illuminations as well as a back lighting method that provides imaging of two orthogonal views are correlated with two commercial testers one based on optical and the other on capacitive sensors. Methods implemented to analyse the irregularity including a new visual technique are explained and demonstrated on several yarn samples.

Image processing algorithms based on spatial and frequency domain analysis to measure the yarn twist are described and the measurements are correlated with the actual twist values.

A new yarn simulation algorithm that uses diameter and hairiness data is developed. Yarn board and knitting simulation programs based on this principle are explained. The simulations are compared with actual yarn and fabric images and images from a commercial simulation package both visually in a subjective manner and quantitatively using variance-area curves. The effect of hairiness on yarn and fabric appearance is also discussed.

Keywords: *Computer Vision, Image Processing, Yarn Hairiness, Yarn Irregularity, Yarn Twist, Fabric Simulation*

Declaration

This is to certify that I am responsible for the work submitted in this thesis and that the original work is my own except where due reference to previous work has been noted.

I also certify that neither the thesis nor the original work contained therein has been submitted to this or any other institution for a higher degree.

Yasar Alper Ozkaya

A handwritten signature in black ink, appearing to read 'Yasar Alper Ozkaya', written in a cursive style.

... to my dear parents Aysel & Tahir Özkaya

and my beautiful wife Nazlı

Acknowledgments

I would like to first of all thank to my supervisors Dr. Memis Acar and Dr. Mike Jackson for their valuable guidance, support, patience and trust.

Thanks also go to my colleagues at Mechatronics Research Group. It has been a privilege for me to find out that the help and the knowledge I needed was often next to my desk and always served with a warm chat. I also would like to express my gratitude to Serhat Erpolat, an intriguing character I shared the same house for over three enjoying years.

I would like to thank to my lecturers Prof. Bulent Ozipek, Prof. Emel Onder and all others at Istanbul Technical University Textile Engineering Department for their commitment to me and the fellows at the Textile Testing Lab for providing most of the yarn samples and test facilities. I also would like to express my appreciation to Prof. Benham Pourdeyhimi and Prof. Moon Suh of NCSU School of Textiles for making my visit to their Department possible and very useful.

Finally and above all, my deepest thanks are to my dear parents Aysel and Tahir Ozkaya for all their support, encouragement and prayers, without which I could never have come so far.

Table of Contents

CHAPTER 1- INTRODUCTION TO THESIS	1
1.1 YARNS AND THEIR CHARACTERISTICS	1
1.1.1 GLOBAL YARN PRODUCTION AND THE IMPORTANCE OF YARN QUALITY	3
1.2 COMPUTER VISION FOR YARN CHARACTERISATION	7
1.3 BOUNDARIES OF THE FIELD OF STUDY	9
1.4 OVERVIEW OF THE THESIS	10
CHAPTER 2- LITERATURE SURVEY	13
2.1 INTRODUCTION	13
2.2 MEASUREMENT OF YARN HAIRINESS	13
2.2.1 YARN HAIRINESS AND ITS IMPORTANCE	13
2.3 A REVIEW OF LITERATURE ON EVALUATION OF YARN HAIRINESS	16
2.4 COMMERCIAL HAIRINESS TESTERS	22
2.4.1 THE SHIRLEY YARN HAIRINESS TESTER	22
2.4.2 F-INDEX TESTER	23
2.4.3 MEINERS DEL HAIRINESS METER	24
2.4.4 THE ZWEIGLE G565/G566 HAIRINESS METER	25
2.4.5 THE USTER TESTER 4SX HAIRINESS METER ATTACHMENT	28
2.4.6 KEISOKKI LASERSPOT HAIRINESS TESTER	30
2.4.7 PREMIER IQ QUALICENTER	31
2.4.8 COMPARISON OF COMMERCIAL TESTERS	32
2.5 YARN IRREGULARITY	33
2.5.1 DESCRIPTION AND IMPORTANCE OF YARN IRREGULARITY	33
2.5.2 METHODS OF DESCRIBING IRREGULARITY	34
2.5.2.1 Coefficient of Variation	34
2.5.2.2 Irregularity, U%	34
2.5.2.3 Indices of Irregularity	35
2.5.2.4 Correlation Methods	35
2.5.2.5 Spectral Methods	36
2.5.2.6 Variance-Length Relations	36
2.5.2.7 Data Compression Methods	37
2.5.3 MEASUREMENT OF YARN EVENNESS	38
2.5.4 OPTICAL VS. CAPACITIVE SENSORS	42
2.5.5 COMMERCIAL IRREGULARITY TESTERS	43
2.5.5.1 Zweigle G585	43
2.5.5.2 Uster Tester 4SX CS and OM Modules	45
2.5.5.3 Premier Tester 7000/ Premier iQ QualiCenter	45
2.5.5.4 Lawson Hemphill Yarn Profile Tester	46
2.5.5.5 Keisokki Evenness Tester	46
2.5.5.6 Micro Sensor Inc. On-line Density Tester	47
2.6 USE OF COMPUTER VISION FOR YARN CHARACTERISATION	47
2.6.1 BARELLA-VIAPLANA HAIRINESS METER	47
2.6.2 ITQT HAIRINESS METER	47
2.6.3 YARN IMAGE PROCESSING SYSTEM OF VAS <i>ET. AL.</i>	48
2.6.4 CYBULSKA'S SYSTEM	49
2.6.5 SUH'S YARN SCANNING SYSTEM ATTACHED TO LAWSON HEMPHILL CTT	50
2.6.6 ESTIMATION OF DENSITY USING LASER TRANSMISSION	51
2.6.7 MILLMAN'S LYSS	52
2.6.8 OTHER RELEVANT WORK	56

2.7 CONCLUSIONS	58
<u>CHAPTER 3 - LYSS HARDWARE AND SOFTWARE COMPONENTS</u>	60
3.1 INTRODUCTION	60
3.2 YARN TRANSPORT AND IMAGE ACQUISITION	60
3.3 IMAGE PROCESSING ENVIRONMENT	62
3.4 OTHER AUXILIARY SOFTWARE	63
3.4.1 BACK-LIT ILLUMINATION ANALYSIS PROGRAM	63
3.4.2 DARK-FIELD ILLUMINATION INTENSITY PROFILE ANALYSIS PROGRAM	64
3.4.3 FRONT-LIT ILLUMINATION DEFOCUS PROFILE ANALYSIS PROGRAM	65
<u>CHAPTER 4 - ANALYSIS OF FACTORS AFFECTING YARN IMAGE QUALITY</u>	
66	
4.1 INTRODUCTION	66
4.2 IMAGE FORMATION BASICS AND DEFINITIONS	67
4.3 DIFFRACTION EFFECT OF THE APERTURE	70
4.4 FACTORS AFFECTING YARN IMAGE QUALITY	76
4.5 DEFOCUS ABERRATION	80
4.6 ANALYSIS OF BACKLIT ILLUMINATION	89
4.6.1 FACTORS AFFECTING THE IMAGE BACKGROUND QUALITY IN BACK-LIT ILLUMINATION	90
4.6.2 DIFFRACTION EFFECT OF FIBRES	92
4.6.2.1 Effect of size and distance of the light source on shadow profile	99
4.6.3 OFF-AXIS DISPLACEMENT IN BACK-LIT ILLUMINATION	102
4.7 OTHER OPTICAL ABERRATIONS	103
4.8 IMAGE DIGITISATION	105
4.9 COMPARISON OF BACK-LIT AND FRONT-LIT ILLUMINATIONS	110
4.10 CONCLUSIONS	115
<u>CHAPTER 5 - YARN ILLUMINATION AND IMAGE PROCESSING TECHNIQUES</u>	117
5.1 INTRODUCTION	117
5.2 ILLUMINATION METHODS FOR LOW MAGNIFICATION	118
5.2.1 BACK-LIT ILLUMINATION METHODS	118
5.2.2 IMAGING OF TWO ORTHOGONAL VIEWS	124
5.2.3 DARK FIELD ILLUMINATION	127
5.3 ILLUMINATION METHODS FOR HIGH MAGNIFICATION	129
5.4 YARN IMAGE SEGMENTATION	134
5.4.1 IMAGE ENHANCEMENT AND PREPROCESSING METHODS FOR BACK-LIT YARN IMAGES	134
5.4.1.1 Contrast Enhancement Using Convolution Filters	136
5.4.1.2 Adaptive Two Level Thresholding	138
5.4.1.3 Maxima-Minima Differentiation Method	141
5.4.1.4 Other Adaptive Thresholding Techniques	144
5.4.2 CORE-HAIR SEPARATION METHODS FOR BACK-LIT IMAGES	165
5.4.2.1 Morphological filtering	166
5.4.2.2 Horizontal tracking method	168
5.4.3 PROCESSING OF DARK FIELD YARN IMAGES	171
5.4.4 PROCESSING OF TWO-ORTHOGONAL IMAGES	174
5.4.5 METHODS TO ESTIMATE THE HAIR LENGTH	175
5.4.5.1 Fibre Tracking Algorithm	175
5.4.5.2 Skeltonising and "Bit Quads" Methods	178
5.4.6 COMPARISON OF IMAGE PROCESSING METHODS FOR BACK-LIT YARN IMAGES	181
5.5 DIGITAL MODIFICATION OF SCANNING ASPECT RATIO AND DEFINITION OF ASPECT	

RATIO CLASSES	185
5.6 CONCLUSIONS	186
<u>CHAPTER 6 - EVALUATION OF HAIRINESS</u>	<u>190</u>
6.1 INTRODUCTION	190
6.2 YARN SAMPLES	190
6.3 SIMULATION OF PHOTOELECTRIC SENSORS FOR COUNTING HAIRS USING IMAGE PROCESSING	192
6.4 ESTIMATION OF TOTAL HAIRINESS	202
6.4.1 THW INDEX	202
6.4.2 TH _L INDEX	206
6.4.3 THG INDEX	207
6.5 HAIR DENSITY DISTRIBUTION PROFILES	209
6.6 EFFECT OF SCANNING ASPECT RATIO ON HAIRINESS MEASUREMENTS	212
6.7 CONCLUSIONS	215
<u>CHAPTER 7 - YARN IRREGULARITY</u>	<u>217</u>
7.1 INTRODUCTION	217
7.2 DIAMETER AND IRREGULARITY MEASUREMENTS	217
7.3 EFFECTS OF USING LOWER ASPECT RATIOS ON DIAMETER AND IRREGULARITY MEASUREMENTS	226
7.4 METHODS IMPLEMENTED IN LYSS TO EVALUATE YARN IRREGULARITY	227
7.4.1 CALCULATION OF CV% AND VARIANCE-LENGTH CURVES	227
7.4.2 CALCULATION OF AUTOCORRELATION FUNCTION (CORRELOGRAM)	230
7.4.3 VARIATION PLOTS	233
7.5 CONCLUSIONS	236
<u>CHAPTER 8 - TWIST MEASUREMENT</u>	<u>238</u>
8.1 INTRODUCTION	238
8.2 THE RELATION BETWEEN TWIST AND TWIST ANGLE	239
8.3 CORE EXTRACTION	240
8.4 SPATIAL ANALYSIS METHOD TO EXTRACT THE TWIST ANGLE	242
8.5 FREQUENCY DOMAIN ANALYSIS	244
8.6 A HYBRID METHOD: FREQUENCY DOMAIN FILTERING AND SPATIAL ANALYSIS	252
8.7 RESULTS AND DISCUSSION	255
8.8 CONCLUSIONS	260
<u>CHAPTER 9 - YARN AND FABRIC SIMULATIONS</u>	<u>262</u>
9.1 INTRODUCTION	262
9.2 SIMULATION OF YARNS	263
9.3 YARN BOARD SIMULATION	264
9.4 KNITTING SIMULATION	267
9.4.1 COMPARISON OF FABRIC SIMULATIONS FROM CYROS AND LYSS	271
9.5 VARIANCE-AREA CURVES	274
9.5.1 EFFECT OF HAIRINESS ON B(A) CURVES	277
9.6 SUMMARY AND CONCLUSIONS	280
<u>CHAPTER 10 - SUMMARY OF CONCLUSIONS</u>	<u>281</u>
<u>CHAPTER 11 - SUGGESTIONS FOR FURTHER WORK</u>	<u>287</u>
<u>APPENDIX A - CUSTOM C FUNCTIONS</u>	<u>290</u>
11.1 ABUTALEBTHRESHOLD.C	290
11.2 APPLYHISTOMAP.C	290
11.3 ARRAY2FILE	290
11.4 BACKLIT.C	291
11.5 BACKTHRESHOLD.C	292
11.6 BERNSENTHRESHOLD.C	292

11.7 BITQUADS.C	292
11.8 CARDBOARD.C	293
11.9 CYROS2IMAGE.C	293
11.10DIFFEDGE.C	294
11.11ENHANCEVECTOR.C	294
11.12FINDTHRESHOLDS.C	294
11.13FRESNEL.C	295
11.14HORIZONTALTRACK2.C	295
11.15INTEGRATECOLUMNS.C	296
11.16KAPURTHRESHOLD.C	296
11.17KITLERTHRESHOLD.C	296
11.18KNITSIMHAIRINESS.C	297
11.19LINESCAN.C	297
11.20LOGLINE.C	298
11.21MASKFOURIER.C	298
11.22MERGEIMAGES.C	299
11.23MERGEMAXS.C	299
11.24NIBLACKTHRESHOLD.C	299
11.25OTSUTHRESHOLD.C	300
11.26REMOVE_GHOST.C	300
11.27SAUVOLATHRESHOLD.C	300
11.28PROCESSYARN.C	301
11.29PROCESSYARNDRKFLD.C	302
11.30PROCESSYARNTWOORTHO.C	302
11.31REDUCE2MINS.C	303
11.32SPOKE.C	303
11.33TRACKFIBER.C	304
11.34VACURVE.C	304
11.35YANOWITZTHRESHOLD.C	305
<u>REFERENCES</u>	<u>I</u>

List of Figures

Figure 1-1 Idealized diagrams of basic filament and spun yarn structures (Goswami et.al., 1977, p.77-78)	1
Figure 1-2 Staple yarn production (Mogahzy,1998)	2
Figure 1-3 A fabric fault due to a thick place in the component yarn (S. Schwab Company, Quality Assurance Manual APX 61)	4
Figure 1-4 a) A knitted fabric with diagonal stripes due to periodic variations in the yarn, b) Fabric knitted from a normal yarn (Kirtay, 2003, p. 13)	4
Figure 1-5 Effect of diameter variation on the dyeability (Soll [2000], p.12)	5
Figure 2-1 a) Protruding fibres, b) Loops, c) Wild fibres (Iridag [1994], p. 5)	14
Figure 2-2 Logarithm of number of hairs plotted against the distance of hairs from the yarn axis for different blends (Reproduced from Lappage and Onions [1964], p. T384)	19
Figure 2-3 Working principle of JTRL hairiness instrument.	21
Figure 2-4 The Shirley Yarn Hairiness Meter	22
Figure 2-5 Measuring principle of Shirley Yarn Hairiness Meter (Slack [1970], p. 429)	23
Figure 2-6 F-Index Tester	24
Figure 2-7 Meiners Del Yarn hairiness Meter	24
Figure 2-8 a) Meiners Del Memorandum Portable Yarn Hairiness / Broken Filament Monitor b) The measurement principle	25
Figure 2-9 Zweigle G566 Hairiness Tester (http://www.zweigle.com)	25
Figure 2-10 Measurement principle of Zweigle G565 Hairiness Meter (Iridag, [1994] p. 14)	26
Figure 2-11 Illustration of number of hairs plotted against the distance from the core on a logarithmic scale	27
Figure 2-12 a) Uster Tester 4 SX b) Measuring zone of Hairiness Meter Attachment (OH Module)	28
Figure 2-13 The measuring zone of UT Hairiness Attachment	29
Figure 2-14 The appearance of yarns in the measuring zone of UT Hairiness Attachment	29
Figure 2-15 Left: Picture of a spun yarn filtered with a high pass filter, Right: The same yarn filtered with Keisokki's spatial filter (Keisokki Report [1997])	30
Figure 2-16 Optical setup in Keisokki LASERSPOT	31
Figure 2-17 Premier iQ QualiCenter	31
Figure 2-18 A typical correlogram	36
Figure 2-19 General Shapes of V(L) and B(L).	37
Figure 2-20 Zweigle G585	44
Figure 2-21 Measuring Principle of Zweigle G585	44
Figure 2-22 Measuring principle of UT4 OM Module (Soll [2000], p.4)	45
Figure 2-23 Schematic diagram of ITQT hairiness meter.	48
Figure 2-24 Cybulska's definition of hairiness (Cybulska [1999], p.370)	50
Figure 2-25 Coherent back-lit yarn image Note the fringe patterns on the background arising from the glass plates. (Millman [2000], p. 142)	53
Figure 2-26 Spatially filtered yarn images with stop sizes 0.2mm and 0.6 mm (Millman [2000], p.152)	54
Figure 3-1 LYSS Hardware	61
Figure 3-2 Wit user interface	62
Figure 3-3 Wit definition of "processYarn" operator	63
Figure 3-4 Back-lit Illumination Analysis Program interface	64
Figure 3-5 Dark-Field Illumination Intensity Profile Analysis Program interface	65
Figure 4-1 Image Formation Geometry	69
Figure 4-2 Geometry of Point Spread Function	70
Figure 4-3 Optical and Amplitude Transfer Functions	72
Figure 4-4 Left: The geometric image profile g_g of a 45 μm fibre at 1:1 magnification; Right: The FT of g_g (G_g)	73
Figure 4-5 Normalised spectrum of a 45 μm Fibre and effect of ATF	75
Figure 4-6 Normalised spectrum of a 45 μm fibre and effect of OTF	75
Figure 4-7 Image Profiles of a 45 μm fibre in incoherent and coherent cases	76
Figure 4-8 Normalised frequency spectrum for a 0.3mm yarn core	76

Figure 4-9 Normalised frequency spectra for 14 μ m and 26 μ m fibres (Note that both spectra are normalised using different scales since the powers are different)	77
Figure 4-10 Responsivity of the CCD sensor used in the experiments	78
Figure 4-11 Reflectance Spectra of raw cotton fibre	79
Figure 4-12 Effect of Aperture size on OTF	80
Figure 4-13 Geometry of Defocus Aberration	81
Figure 4-14 Comparison of OTFs calculated from geometrical approximation with those where the diffraction effect is taken into account.	83
Figure 4-15 Defocus profiles of a 45 μ m fibre. F5.6, f=100mm, λ =670nm, m=1, varying δ_o .	84
Figure 4-16 Pictures of a 45 μ m PP fibre at different defocusing distances (first two rows) and corresponding profiles (bottom row). (F5.6, m=1, λ =670nm, f=100mm)	85
Figure 4-17 OTFs for varying F; δ_o =2mm, λ =670nm, f=100mm	86
Figure 4-18 Pictures of a 45 μ m PP fibre with 2mm defocusing and varying f-numbers.	86
Figure 4-19 Effect of out of field degradation at high magnification. The image is taken using a microscope focused to the core edge at m=4.	87
Figure 4-20 Geometry of back-lit illumination	89
Figure 4-21 A back-lit yarn image	90
Figure 4-22 Image of a tungsten filament bulb	91
Figure 4-23 Simulated defocus profiles of a tungsten filament bulb	91
Figure 4-24 Back-lit illumination geometry where the lens and screen is replaced with a single screen placed on the focal plane of the lens.	94
Figure 4-25 Diffraction geometry in 2D	95
Figure 4-26 Comparison of shadow profiles of a 14 μ m fibre, calculations based on Fresnel's diffraction theory and geometrical approximation.	96
Figure 4-27 Picture generated using the intensity profiles of Figure 4-26. Top: Fresnel Diffraction pattern, Bottom: Geometrical approximation.	96
Figure 4-28 The shadow profiles of a 45 μ m PP fibre for different defocusing distances. Pictures on the right show the actual pictures and on the left are the simulations.	98
Figure 4-29 Geometrical explanation of blurring of fibre shadow due to the finite dimension of the light source	99
Figure 4-30 Definition of w_L	100
Figure 4-31 Defocus profiles for varying w_L	101
Figure 4-32 Defocus profiles for varying ρ_0	102
Figure 4-33 Displacement of an off-axis defocused object	103
Figure 4-34 Left: Effect of Spherical Aberration in back-lit illumination; Right: Pictures of a 45 μ fibre at different distances from the optical axis.	104
Figure 4-35 45 μ PP fibre images at 25mm defocus illuminated with a red-LED (a) and white tungsten filament bulb (b) and the corresponding profiles (c). Note the fringe pattern for LED which is more visible.	105
Figure 4-36 CCD sensor array of a line scan camera	106
Figure 4-37 Line scan process	107
Figure 4-38 A spoke target before (a) and after (b) digitisation where m=1, p=14 μ , V_i, t_e =14 μ , AR=1 and n=8 bits. The circles on the pictures correspond to a frequency of 67 lines/mm at this magnification.	108
Figure 4-39 Digitised spoke targets at V_i, t_e =70 μ m (a) and V_i, t_e =14 μ m (b) both sampled at AR=1/5.	109
Figure 4-40	111
Figure 4-41 a) Profiles of a 16 μ m fibre under back-lit illumination at increasing defocus distances, b) (a) After CCD sampling, c) (b) after applying first threshold, d) (b) after second threshold	112
Figure 4-42 a) Defocus Profiles under front-lit illumination, b) (a) after CCD sampling and thresholding at 4% of maximum intensity.	113
Figure 4-43 Comparison of measured diameters	114
Figure 4-44 Comparison of grey level sums relative to the grey level sum of in focus fibres	114
Figure 5-1 Back-lit illumination with a single halogen lamp	119
Figure 5-2 A yarn image acquired using the set-up in Figure 5-1	119
Figure 5-3 Profiles of a 45 μ PP fibre at exact focus plane and at 10mm defocusing using the set-up in Figure 5-1	120
Figure 5-4 Yarn image illuminated with an LED light from behind.	121
Figure 5-5 Field Lens arrangement	121

Figure 5-6 a) Yarn image acquired using the field lens set-up, b) Yarn image after flat field correction	122
Figure 5-7 Profiles of a 45 μ PP fibre at exact focus plane and at 6mm defocusing under field lens illumination	123
Figure 5-8 a) Arrangement where a diffuser is used to increase the effective size of the light source. b) Scattering of light rays after passing through the diffuser.	123
Figure 5-9 a) Image of yarn illuminated using a diffuser, b) (a) after flat field correction	124
Figure 5-10 Arrangement for imaging of two orthogonal views	125
Figure 5-11 Image of a yarn taken using the set-up in Figure 5-10	125
Figure 5-12 Simulated profile of a 0.4mm thick yarn core at 0.7mm defocusing for a 550nm light source with 5mm wide Gaussian profile placed 700mm away compared with the in-focus profile.	126
Figure 5-13 Dark Field Illumination Arrangement	127
Figure 5-14 Yarn images under dark field illumination: a) without and b) with field aperture. (F5,6; m=1)	128
Figure 5-15 Dark field images of two 40/60 wool acrylic Nm 30 yarn samples with a) black and b) red colour (F11; m=1). (c) and (d) show (a) and (b) respectively after image processing (see section 5.4.3).	129
Figure 5-16 Coherent back-lit illumination	130
Figure 5-17 A high magnification 70/30 polyester/cotton image using set-up in Figure 5-16	130
Figure 5-18 A hybrid illumination set-up using coherent back-lit and incoherent front-lit illuminations.	131
Figure 5-19 Yarn image acquired using set-up in Figure 5-18	131
Figure 5-20 Co-axial illumination	132
Figure 5-21 Image of a yarn illuminated with co-axial illumination	132
Figure 5-22 Yarn section in Figure 5-21 under dark field illumination.	133
Figure 5-23 Incoherent back-lit and front-lit illumination hybrid where a ring light is used for front-lit illumination	133
Figure 5-24 Yarn images acquired using ring light for front lit illumination without (Left) and with (right) additional back-lit illumination	134
Figure 5-25 A back-lit yarn image and its histogram	135
Figure 5-26 A horizontal profile showing an isolated background pixel and an out of focus hair.	135
Figure 5-27 Contrast enhancement filters	136
Figure 5-28 Improved Laplacian filter applied to yarn images after Gaussian Filtering	137
Figure 5-29 a) Original image profile, b) (a) after applying 3x3 Gaussian and 3x3 Laplacian filters, c) (a) after applying 3x3 Gaussian and 5x5 differential filter, d) Threshold applied to (c)	137
Figure 5-30 a) Original Image b) After contrast enhancement and thresholding	138
Figure 5-31 Determination of threshold values	139
Figure 5-32 Yarn image after applying a) first threshold b) second threshold	140
Figure 5-33 Yarn image processed using maxima-minima differentiation.	141
Figure 5-34 A defocused hair lying along the scan line intersected with an in-focus hair in the middle. The algorithm only detects the intersecting hair and omits the whole defocused hair	142
Figure 5-35 (a) A yarn image with non-uniform background intensity, (b) (a) after processing with maxima-minima differentiation algorithm	143
Figure 5-36 a) The probability mass function of a yarn image, b) Between class variances for varying threshold values and selection of the optimum threshold.	148
Figure 5-37 The probability mass function (a) and the Gaussian fitting errors for varying thresholds and selection of the optimum threshold (b)	149
Figure 5-38 The probability mass function (a), and the sum of foreground and background entropies for varying thresholds and selection of the optimum threshold (b)	150
Figure 5-39 a) 2D Histogram normalized to 8bits (and inverted for visibility), b) Argument of equation (5.9) for varying (T, \bar{T}) (normalized to 8 bits) and selection of optimum threshold pair.	151
Figure 5-40 Niblack's thresholding method results for 5x5 neighborhood and given k's.	152
Figure 5-41 Results of Sauvola and Pietaksinen's method for varying k and frame sizes (n)	153
Figure 5-42 Bernsen's method applied to a yarn image for varying L and frame size values.	155

Figure 5-43 Cross section through an image, illustrating how "ghost" objects might occur (Trier & Taxt [1995])	156
Figure 5-44 Main steps of Yanowitz and Bruckstein's method	158
Figure 5-45 a) Original yarn image with non-uniform background, (b-k) (a) binarised using the methods of: b) Otsu, c) Kittler & Illingworth, d) Kapur et al., e) Abutaleb, f) Niblack (k=5, n=5x5), g) Sauvola & Pietaksinen (k=0.1, n=9x9, R=128), h) Bernsen (L=0.5, n=5x5), i) Yanowitz & Bruckstein (beta=1.5, iterations=3, Tp=5, Edge detection threshold=12), j) Two level adaptive Thresholding, k) Horizontal Tracking (Slope threshold=20)	161
Figure 5-46 a) Original yarn image with uniform background, (b-k) (a) binarised using the methods of: b) Otsu, c) Kittler & Illingworth, d) Kapur et al., e) Abutaleb, f) Niblack (k=5, n=5x5), g) Sauvola & Pietaksinen (k=0.1, n=9x9, R=128), h) Bernsen (L=0.5, n=5x5), i) Yanowitz & Bruckstein (beta=1.5, iterations=3, Tp=5, Edge detection threshold=12), j) Two level adaptive Thresholding, k) Horizontal Tracking (Slope threshold=20)	162
Figure 5-47 The comparison of the original image profiles with the thresholded profiles obtained using different techniques.	164
Figure 5-48 Integrated columns for the first 25 rows of second thresholded image and location of the core.	165
Figure 5-49 Closing operation. a) Second thresholded image b) (a) after dilation with a 9x9 rectangular structuring element, c) (b) after erosion, d) (c) overlaid on the first thresholded image showing hairs and the core.	167
Figure 5-50 Edge tracking method. a) Second thresholded image, b) Core extracted by tracking c) (b) after correction, d) (c) overlaid on the first thresholded image showing hairs and the core.	169
Figure 5-51 Effect of filtering on neps	170
Figure 5-52 Identification of faults	171
Figure 5-53 (a) A dark field yarn image (b) (a) after applying a threshold @25	171
Figure 5-54 Integration of 70 rows for each column on a dark field image showing the selection of core edges	173
Figure 5-55 (a) Dark field yarn image (b) (a) after hair-core-background separation	173
Figure 5-56 Integrated columns of a two orthogonal yarn image	174
Figure 5-57 A two orthogonal yarn image before and after processing	175
Figure 5-58 Different situations handled in the fibre tracking algorithm	177
Figure 5-59 a) Various hair distribution possibilities. b) (a) after processing, different fibres are marked with different grey tones.	177
Figure 5-60 Binary yarn image before (a) and after (a) skeletonising	178
Figure 5-61 Digital representation of a circle with 1 pixel thickness and 100 pixel diameter	179
Figure 5-62 Bit Quads	180
Figure 5-63 Number of pixels corresponding to yarn (hair+core pixels) found using different segmentation methods (Error bars correspond to +[Standard Deviation])	182
Figure 5-64 Comparison of number of core pixels measured using 3 different processing techniques (Error bars correspond to +[Standard Deviation])	182
Figure 5-65 Comparison of the average hair length calculated from sekeletonising technique with number of pixels without skeletonising	183
Figure 5-66 Comparison of average hair lengths (cm of hair per cm of yarn length) calculated with and without using "Bit Quads" method after skeletonising	184
Figure 5-67 Original image acquired from the camera at 1:1 aspect ratio (a) and the images converted into AR 1:4.9 (b) and AR 1:11.9 (c). The images on the right are after applying the two level thresholding and horizontal tracking algorithms to the images on the left.	186
Figure 6-1 Principle of hair counting method using a photo electric sensor.	192
Figure 6-2 The sub-windows for simulating the photosensors	193
Figure 6-3 (a) Image of a yarn corresponding to 60mm (b-d) Light intensity profiles for photo sensors 1, 2 and 3mm apart from the core	194
Figure 6-4 Change of average N1 values according to the test length	195
Figure 6-5 Comparison of N1, N2, S3 measurements using different sensor dimensions	196
Figure 6-6 Comparison of results using different signal threshold levels	197
Figure 6-7 Comparison of results using different zero length positions	198
Figure 6-8 Comparison of hair numbers from Zweigle G565 and LYSS simulation for four samples with long hairiness	200
Figure 6-9 Comparison of slopes of hair counts <=3mm on logarithmic scale	201
Figure 6-10 Comparison of slopes of hair counts >=1mm on logarithmic scale	201

Figure 6-11 Comparison of USTER H with Zweigle S3	202
Figure 6-12 Comparison of back-lit THw with USTER H index	203
Figure 6-13 Comparison of THw CV% for 1cm sampling length with USTER H CV%	203
Figure 6-14 Comparison of THw with USTER H for grey yarn samples	204
Figure 6-15 Comparison of dark-field THw with USTER H	205
Figure 6-16 Comparison of Dark-Field THw CV% with USTER H CV%	206
Figure 6-17 Comparison of hair skeleton lengths with USTER H	207
Figure 6-18 Comparison of THg with USTER H	208
Figure 6-19 Comparison of THg with USTER H for grey yarn samples	208
Figure 6-20 Comparison of THg CV% for 1cm sampling length with USTER H CV%	209
Figure 6-21 Hair density distribution profile of sample 33	210
Figure 6-22 HDDP compared with Zweigle hair counts on a logarithmic scale	211
Figure 6-23 Comparison of logarithmic slopes of HDDP for distances between 0.75m and 3.25mm with the logarithmic slope of hair counts for distances ≤ 3 mm	211
Figure 6-24 Comparison of THw and THg measurements for smaller aspect ratios	213
Figure 6-25 Comparison of THw CV% measurements for smaller aspect ratios	213
Figure 6-26 Comparison of N1, N2 and S3 values for lower aspect ratios	214
Figure 7-1 Comparison of diameter measurements from CYROS and LYSS	218
Figure 7-2 Comparison of diameter CV% values from CYROS and LYSS	218
Figure 7-3 Comparison of diameter and diameter CV% values from Lawson Hemphill CTT, LYSS and CYROS	219
Figure 7-4 Comparison of yarn counts (Tex) with squares of diameters for 100% cotton samples	220
Figure 7-5 Comparison of diameter measurements from CYROS and dark field images	221
Figure 7-6 Comparison of diameter CV% values from CYROS and dark field images	221
Figure 7-7 Comparison of UT3 mass CV% with diameter CV% from LYSS for 8mm sampling length for 12 100% cotton samples	222
Figure 7-8 Comparison of UT3 mass CV% with elliptical diameter CV% from LYSS for 8mm sampling length for 12 100% cotton samples	223
Figure 7-9 Comparison of UT3 mass CV% with dark field diameter CV% from LYSS for 8mm sampling length for 12 100% cotton samples	223
Figure 7-10 Comparison of UT3 mass CV% with elliptical diameter CV% from LYSS for 2mm sampling length for twelve 100% cotton samples	224
Figure 7-11 Comparison of UT3 mass CV% with CYROS diameter CV% for twelve 100% cotton samples	225
Figure 7-12 Comparison of diameters from single view with elliptical diameter	225
Figure 7-13 Comparison of diameter CV% from one and two views (1mm sampling length)	226
Figure 7-14 Diameter measurements at lower aspect ratios compared with the measurements at AR1:1	226
Figure 7-15 Diameter CV% measurements at lower aspect ratios compared with the measurements at AR1:1	227
Figure 7-16 CV%-Length curves for 18 yarn samples	229
Figure 7-17 Diameter CV%-Length curves for samples 4 and 32	229
Figure 7-18 Diameter CV%-Length curves for samples 29 and 37	230
Figure 7-19 Correlogram for yarn samples 24, 35 and 36	232
Figure 7-20 Variation plots of samples 32 and 33	234
Figure 7-21 Correlograms of samples 32 and 33	234
Figure 7-22 CV-Length curves of samples 32 and 33	235
Figure 7-23 Variation plot of sample 22 showing long duration thin and thick places	235
Figure 7-24 Variance plots given in Figure 7-20 thresholded at 254.	236
Figure 8-1 a)-An ideal yarn diagram showing the relation between twist angle and twist, b)- Calculation of twist from a yarn image	240
Figure 8-2 Twist direction	240
Figure 8-3 A typical yarn image for twist measurement	241
Figure 8-4 Left: The horizontal projection of the image in Figure 8-3 showing the threshold line; Right: Extracted core region	242
Figure 8-5 Steps of the algorithm to determine the twist angle	243
Figure 8-6 a) A vertical sinusoidal grating plotted on a 256x256 image and b) the magnitude component of the FFT of (a)	244

Figure 8-7 a) Sinusoidal grating rotated by 30 degrees, b) the magnitude component of the FFT of (a)	245
Figure 8-8 a) Figure 8-7a after adding random noise, b) the magnitude component of the FFT of (a)	245
Figure 8-9 Transferred spectrum of a 14 μm fibre at 2:1 magnification ($f_{50}/3.5, \lambda=670\text{nm}$)	246
Figure 8-10 Optimum exact focus plane relative to the yarn core for yarn surface imaging	247
Figure 8-11 Transferred spectrum at 0.1mm defocusing	247
Figure 8-12 Transferred spectrum at 0.4mm defocusing	248
Figure 8-13 a) Image of the yarn core, b) Magnitude of FT on logarithmic scale	249
Figure 8-14 Frequency components of S and Z twists.	250
Figure 8-15 Filtered FT (Magnitude); frequencies falling in range $65 < \sqrt{u^2+v^2} < 130$ within zones 1 and 3 are extracted from the original spectrum.	251
Figure 8-16 Mean magnitudes along varying angles	251
Figure 8-17 Determination of twist angle from the frequency having maximum magnitude	252
Figure 8-18 Inverse transform of the filtered spectrum.	253
Figure 8-19 a) Original core image b) Inverse of filtered FT after thresholding at 0	253
Figure 8-20 Output of the hybrid processing algorithm	254
Figure 8-21 Hybrid method applied on a yarn image with poor surface detail	254
Figure 8-22 Application of the hybrid method using 64x64 image portions.	255
Figure 8-23 Seven yarn samples wound on the sample frame for twist measurement	256
Figure 8-24 Comparison of actual twist values with measurements from different algorithms	257
Figure 8-25 Comparison of diameter measurements from back-lit low magnification and front-lit high magnification images	258
Figure 8-26 Comparison of actual twist values with measurements calculated using the mean twist angles from different algorithms and the mean diameters from back-lit images	259
Figure 9-1 Quantisation principle	264
Figure 9-2 a) The actual picture of a yarn bundle; b) The simulated yarn board using the diameter data from LYSS; c) The actual picture of the yarn bundle where the hairs are removed using a 7x7 morphological open operation	265
Figure 9-3 The original HDDP mapped for 50DPI resolution	266
Figure 9-4 Left: The actual picture of the yarn bundle, Right: Corresponding yarn board simulation using hairiness and diameter data.	267
Figure 9-5 Loop geometry. Left: Top view of jersey loops; Right: Construction of sinker and needle loops (Suh [1967], p419)	268
Figure 9-6 Side view of jersey loops (Suh [1967], p419)	269
Figure 9-7 Digitisation of geometrically defined loops	270
Figure 9-8 Knitting simulation (18 courses/inch, 15 wales/inch, 220 needles). Left: With diameter data; Right: With hairiness and diameter data	271
Figure 9-9 First Column: Fabric simulations from LYSS (using yarn data from CTT); Middle column: Actual fabric pictures; Right Column: Simulations from CYROS	273
Figure 9-10 Left: Simulation from LYSS using CYROS data (Sample 2); Right CYROS simulation using the same data	274
Figure 9-11 Comparison of B(A) curves obtained from actual yarn images, LYSS simulations using CTT and CYROS yarn data and CYROS simulations for 5 yarn samples	277
Figure 9-12 The fabric simulations with (a) and without (b) hairiness data for sample 29. (c) and (d) are the simulations for sample 33.	278
Figure 9-13 Comparison of B(A) curves obtained from simulations with and without hairiness data for two yarn samples.	279
Figure 11-1 Conceptual design for yarn surface imaging	288

List of Abbreviations

CCD	: Charge Couple Device
CTF	: Coherent Transfer Function
CV%	: Coefficient of Variation%
CVd%	: Coefficient of Variation% of diameter.
CVh%	: Coefficient of Variation% of hairiness.
CVm%	: Coefficient of Variation% of mass.
CYROS	: Cotton Yarn Rating by On-line Simulation
HDDP	: Hair Density Distribution Profile
LYSS	: Loughborough Yarn Scanning System
N1, N2...	: Number of hair intersections at 1, 2, ... mm from the core.
Ne	: Number of 840 yards strands in one pound of yarn
Nm	: Length in meters of 1 gram of a yarn.
OE	: Open End
OTF	: Optical Transfer Function
PET	: Polyester
PMF	: Probability Mass Function
PP	: Polypropylene
PSF	: Point Spread Function
S3	: Total number of hair intersections at 3 mm and further from the core.
Tex	: Weight in grams of 1000m of a yarn
UT	: Uster Tester
YHM	: Yarn Hairiness Meter

Glossary of Terms

Abrasion: The wearing away of a textile product by rubbing. [100]

Barré: An imperfection, characterized by a ridge or mark running in the crosswise or lengthwise directions of the fabric. Barres can be caused by tension variations in the knitting process, poor quality yarns, problems during the finishing process. [37]

Canvas / Duck: A strong, firm, tightly woven, durable fabric usually of cotton but sometimes of linen, hemp or other fibers. It is usually plain weave but sometimes with a crosswise rib. It is produced in a variety of weights & used in a variety of products such as tents, awnings, sails, upholstery, footwear, jackets, and trousers. [38]

Course, (Knitted fabric) : A row of loops across the width of a fabric. [38]

Crease-resistance: A term used to indicate resistance to, and/or recovery from, creasing of a textile material during use. [38]

Draping : Draping means to hang or to adorn the body form with loose fabric, and to obtain a body fitted garment by using adequate sewing techniques. [38]

Handle : The quality of a fabric or yarn assessed by the reaction obtained from the sense of touch., note: it is concerned with the subjective judgment of roughness, smoothness, harshness, pliability, thickness, etc. [38]

Jersey : Single knit fabric with an intermeshing of stitches in the same direction on the face and a series of semicircular loops on the back. Thus the 2 sides appear different. [38]

Lustre: The display of different intensities of light, reflected both specularly and diffusely from different parts of a surface exposed to the same incident light. High lustre is associated with gross differences of this kind, and empirical measurements of lustre depend on the ratio of the intensities of reflected light for specified angles of incidence and viewing., note: this definition makes these differences in intensity of light the key point, since these form the chief subjective impression on the observer of lustre. Both specular and diffuse light must be present together, for, if diffuse light only is present, the surface is matt, not lustrous, whereas, if specular light only is present, the surface is mirror-like, and again not lustrous. The phrase 'exposed to the same incident light' has been included to rule out shadow effects, which have no part in lustre proper. the general term 'surface' is intended to apply to fibres, yarns, and fabrics, and indeed to other surfaces, e.g., that of a pearl (through there the differently reflecting parts are very close together). In the second sentence of the definition, lustre is regarded as a positive function of the differences, the appropriate adjective of intensification being 'high'. [38]

Nep : A small knot of entangled fibres. (In the case of cotton it usually comprises dead or immature cotton hairs.) [38]

Pill; Pilling: Small accumulations of fibres on the surface of a fabric. Pills can develop during wear, and are held to the fabric by an entanglement with the surface fibres of the material. [38]

Roving : A thin strand of fiber with very little twist. [38]

Sliver : An assembly of fibres in continuous form without twist. [38]

Shrinkage: Widthwise or lengthwise contraction of a fiber, yarn, or fabric, usually after

wetting and redrying or on exposure to elevated temperature. [127]

Stitch Length (knitting) : The length of yarn in a knitted loop. [38]

Wale (knitting) : A column of loops along the length of a fabric. [38]

CHAPTER 1 - Introduction to Thesis

1.1 Yarns and their characteristics

Yarn may be defined as a linear assemblage of fibres or filaments formed into a continuous strand, which can be processed on conventional textile equipment and possesses visual and tactile characteristics (aesthetics) that are usually associated with textile products. The yarns can be categorized into two main groups, namely continuous filament and staple yarns. Basic filament and staple yarn structures are depicted in Figure 1-1.

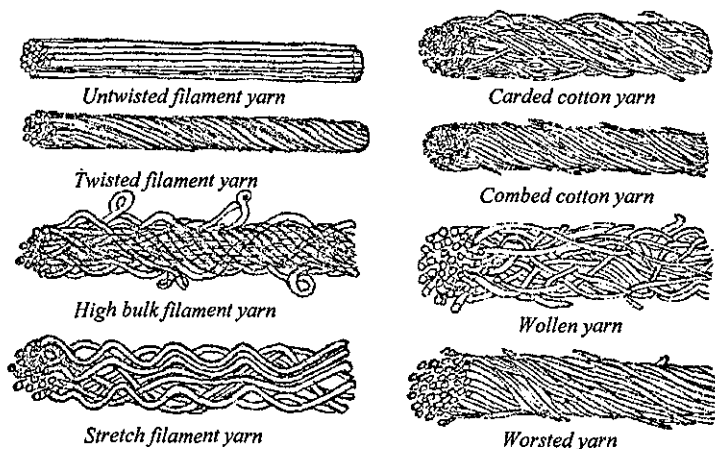


Figure 1-1 Idealized diagrams of basic filament and spun yarn structures (Goswami et.al., 1977, p.77-78)

The filament yarns are produced from synthetic materials such as polyester and polypropylene shaped into fibers by pressing melted raw material through the extremely small openings of so called spinnerets. Depending on the number of holes monofilament or multifilament yarns are produced. Different cross-sectional shapes are obtained in the melt spun man-made fibers using different shapes of the spinneret

holes. The volume and the elasticity of a filament yarn can be improved through a process called texturing. The essential properties of textured yarns and the products made from them are softness, a high degree of elasticity, thermal insulation and moisture-transporting properties. The most important texturing processes are false-twist texturing, stuffer-box texturing and air-jet texturing.

The staple yarns are produced from natural fibres such as wool, cotton and linen and man-made fibres cut into staple fibres from continuous filaments. Most common methods to spin staple yarns are ring spinning, open-end spinning (OE) and jet spinning. The common principle is to assemble the fibres and entangle them to supply cohesion forces between each other to provide a compact structure as illustrated in Figure 1-2.

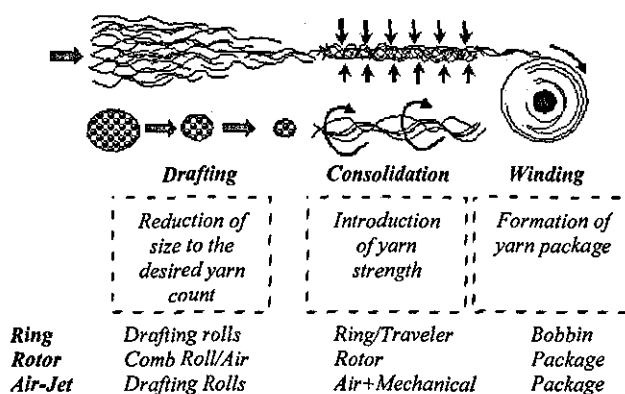


Figure 1-2 Staple yarn production (Mogahzy,1998)

The main characteristics used to qualify a yarn are linear density, structural features, fibre content and uniformity. Linear density is defined as the weight per unit length of a yarn. A common unit to define the linear density is “Tex” which is given as the weight in grams of 1000m of yarn. Similarly, “dtex” and “denier” are given as the weight of 10000 and 9000 metres of yarn respectively. Linear density can also be described indirectly by the length of a certain weight such as metres per gram which is denoted as “Nm” or the number of 840 yards strands in one pound of yarn denoted as “Ne”. The latter index is commonly used for cotton yarns. Structural features of a

yarn include fibre properties, fibre entanglement, packing density, twist, thickness, ellipticity and hairiness. These structural features contribute to the visual and tactile aesthetics of yarns. Fibre content of a yarn is the percentage in weight of each fibre component of which the yarn is formed. Uniformity characteristics of the yarns refer to the variations in linear density, thickness, twist, strength and colour along the yarn, which mainly arise from the variation in number of fibres in cross-section along the length of the yarn.

1.1.1 Global Yarn Production and the Importance of Yarn Quality

The textiles has been an important part of world trade sharing around 3.3% of world exports of manufactures corresponding to some \$147billion in 2001 (Source: WTO). Within the last decade, the yarn production has been in a saturated stage remaining around 170million tonnes/year. However, a report released by International Textile Manufacturers Federation (ITMF) reveals increased investment activity worldwide for textile machinery in 2000 over 1999. Spinning and texturing machinery showed the strongest recovery among the five primary types of machinery covered in the report. This shows an increasing awareness to produce yarns with better quality.

An important aspect of yarn quality is from the perspective of its effect on fabric aesthetics and mechanics. A variation in appearance present in the yarn can easily be seen by human eye in the end product. Figure 1-3 shows a common fabric fault known as “slub” which arises from a thickened place having tapering ends and a diameter several times that of the adjacent normal yarn.

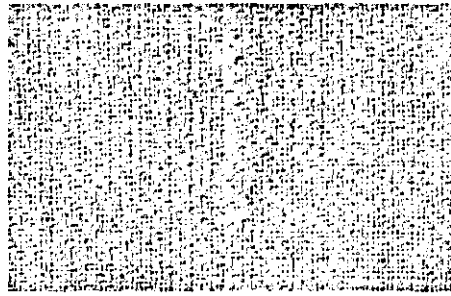


Figure 1-3 A fabric fault due to a thick place in the component yarn (S. Schwab Company, Quality Assurance Manual APX 61)

The problem is particularly serious when a fault (i.e a thick or thin place) appears at precisely regular intervals along the length of the yarn. In such cases, due to the fabric construction geometry, the faults will be located in a pattern that is clearly visible, and defects such as streaks, stripes, barre, or other visual patterns develop in the cloth. Figure 1-4 shows diagonal stripes in a knitted fabric arising from a periodic fault in the yarn.

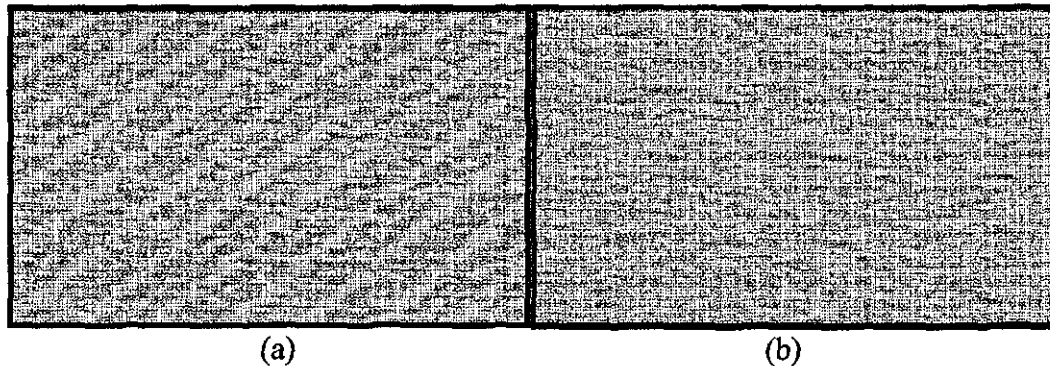


Figure 1-4 a) A knitted fabric with diagonal stripes due to periodic variations in the yarn, b) Fabric knitted from a normal yarn (Kirtay, 2003, p. 13)

Such defects are usually compounded when the fabric is dyed or finished, as a result of the twist variation accompanying them. Twist tends to be higher at thin places in a yarn. Thus, at such locations, the penetration of a dye or finish is likely to be lower than at the thick regions of lower twist. In consequence, the thicker yarn region will tend to be deeper in shade than the thinner ones and, if a visual fault appears in a pattern on the fabric, the pattern will tend to be emphasized by the presence of colour

or by some variation in a visible property, such as crease-resistance controlled by a finish. Figure 1-5 shows the effect of diameter variation on the dyeability.

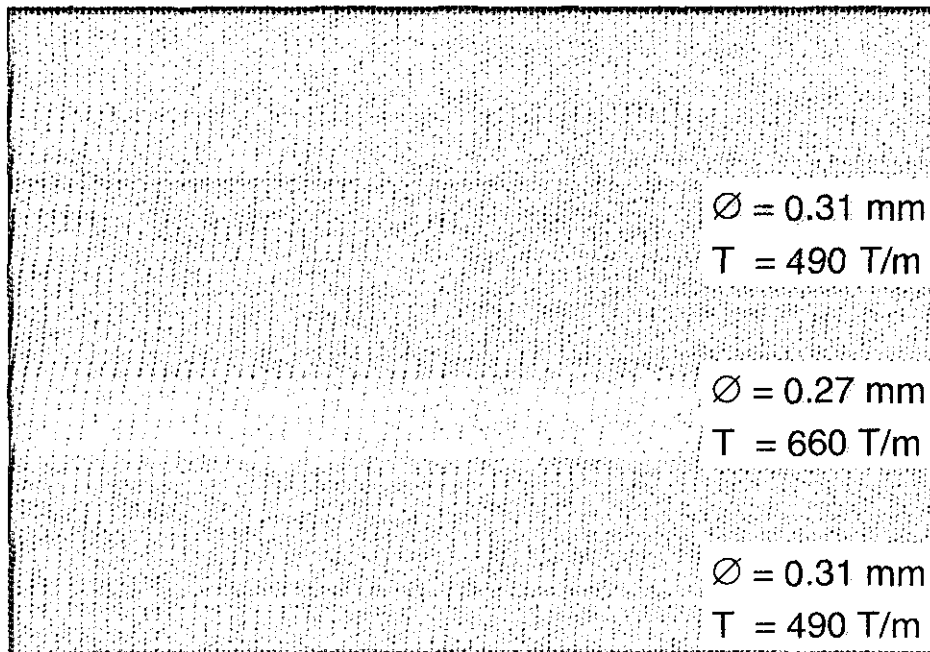


Figure 1-5 Effect of diameter variation on the dyeability (Soll [2000], p.12)

Other fabric properties, such as abrasion or pill-resistance, soil retention, handle, drape, absorbency, reflectance, or lustre, may also be directly influenced by uniformity characteristics and structural characteristics such as twist and hairiness. However, it should be noted here that good yarn quality does not necessarily mean, for example, producing the most regular or strong yarn. For instance, a very irregular yarn can deliberately be aimed for the manufacture of some cotton or linen fabrics or the strength can be sacrificed in some cases in order to improve handle properties or for fabrics that are not meant to be used for long terms. Furthermore, the quality tolerance limits of a yarn depend on the end fabric. For example, appearance faults arising from yarn are less important for fabrics such as canvas compared to woollen garments.

Another important aspect of yarn quality is related with the down-times due to yarn breakages at processes subsequent to spinning. This requires the yarn to be as free as

possible from weak points, which is associated with the irregularity of the yarn. Yarn hairiness is also known to interfere with the knitting and weaving processes. In a yarn with high hairiness, the fibres tend to break off the yarn core and accumulate in the yarn paths that might cause excessive tensions resulting in yarn breakages.

The main objective of yarn quality inspection is to assure the desired yarn characteristics and maximum production efficiency. Yarn characteristics reveal important information on the conditions of the yarn production machinery as well as the quality and suitability of the raw material used. Increasing speeds in yarn production stages mean that a fault that cannot be corrected in time might mean loss or degradation of important amount of raw material which shares around 50%-70% of the total spinning cost (Kirtay, 2003). Nowadays, yarn quality control is performed both on-line and off-line.

On-line control mechanisms aim to minimize the yarn faults at the source. SPIDERweb by Rieter is an example of on-line yarn quality control systems that utilizes a series of control instruments from carding to spinning to improve yarn uniformity. At the yarn spinning stage, instruments such as COROLAB that uses an optical sensor attached to Schlafhorst's Autocorro OE spinning machine or USTER's Quantum Cleaner that incorporates capacitive and optical sensors and can be attached to spinning units are used to detect and clear the irregularities and foreign objects in the yarn as it is being produced. For ring spinning, the yarns go through a process called winding where the weak points are eliminated further by breaking and then re-splicing as they are transferred from small bobbins to big yarn packages. However, on-line clearing of yarn faults during both spinning and winding means a reduction in production speed and the level of this has to be optimised according to the desired quality and down-times that would be recovered in subsequent stages.

Off-line quality control relies on testing limited amount of material which is considered to represent the whole set statistically. It concerns the determination of fibre characteristics at the beginning and throughout the process and the most

important yarn characteristics at the end of the spinning process. Since the off-line testing is carried out under controlled conditions in a laboratory, it provides high accuracy and reproducibility and minimum mill-to-mill variation when measuring yarn characteristics such as evenness, count, hairiness, strength and elongation. Off-line yarn testing is also essential in order to ensure the specified quality characteristics for the stages subsequent to spinning.

1.2 Computer vision for yarn characterisation

Computer vision concerns with extraction of information about a physical object or other observable phenomena from images. Computer vision has a very wide range of applications from medicine to defence, from microscopy to satellite imaging, and from robotics to quality control. Wherever human vision plays an important role in understanding a problem, there is a potential application for computer vision. This has indeed been the case for quality control of textiles since the problems are often from aesthetics point of view. Some major advantages of computer vision for yarn quality inspection can be summarised as follows:

- Conventional sensors for yarn inspection are capable of measuring a single yarn parameter. However, it is possible to measure structural characteristics of the yarns such as thickness, twist, hairiness, ellipticity and colour as well as non-uniformity characteristics simultaneously using computer vision.
- Computer vision is a non-contact and non-destructive measurement method which can be performed continuously at high speeds providing the possibility of adaptation to on-line processes.
- Optical systems are not affected by environmental factors such as moisture and temperature.

- Image of the yarn includes most of the information about the yarn. The acquired images can be stored digitally and used any time for different purposes or analysed with different image processing software.
- For yarn quality assessment, a common trend in recent years is fabric simulations generated using the actual yarn characteristics. Computer vision methods are probably the most suitable for such an application owing to the amount of information provided.
- Yarn scanning resolutions even at micron levels can be achieved using CCD cameras. The optical elements used for image acquisition provide flexibility to change the resolution according to the requirements of different applications.
- Computer vision offers the flexibility to simulate the conventional test instruments and different evaluation techniques. This applies especially to evaluation of hairiness, where numerous measurement techniques are commonly accepted which are, however, not well correlated.

As a summary, computer vision provides very good flexibility, versatility and reproducibility for evaluation of yarn quality. Rapid advances in CCD sensors, data acquisition hardware, computer processing and storage technologies have now enabled computer vision to be applied in some modern testing equipment such as Uster Tester 4 and Lawson Hemphill Yarn Profile Tester. The computer vision technology is already in a stage to be adapted to on-line yarn inspection considering the data acquisition and processing speeds achievable today. It is only a matter of time before the costs of such systems fall to a feasible level and start to being seen on spinning units.

1.3 Boundaries of the Field of Study

The main objective of this research was to develop an off-line yarn testing system based on computer vision and image processing techniques. On the hardware front, optical and digital restraints are analysed and optimum parameters are investigated. On the software front, image processing algorithms to extract the hairiness, diameter and twist characteristics of yarns are developed and the data is correlated with commercial testers. Furthermore, various statistical and visual methods to evaluate yarn quality are implemented.

A test rig is built for yarn transportation with adjustable speed where a spring mechanism is used to apply some tension to the yarn. However, the level of tension is arbitrary and no control mechanism is adapted to keep it constant. For the staple yarns tested during the research the effect of tension variation is assumed to be low considering the fact that the maximum elongation for these yarns would be below 10%. Nevertheless, the transport system would not be very suitable for some textured and especially for elastomeric yarns.

Measurement of diametric irregularity and hairiness of staple yarns has been the primary concern of this work and the image acquisition hardware is selected accordingly. For twist measurement, only the feasibility of using computer vision is investigated using different hardware and illumination methods with no dedicated yarn transport mechanism.

Common statistical data evaluation techniques are implemented and applied to the test data. However, detailed analysis of quality problems and estimation of possible reasons as related to machinery conditions is beyond the boundaries of the study. Furthermore, the underlying theory of the definition of yarn faults such as thin and thick places and neps involves great deal of literature and is not covered within the thesis. Nevertheless it is possible to extract the number of diameter or hairiness occurrences at given fault lengths and beyond certain limits from the test data. It

should also be noted that, the investigation of physical nature of yarn characteristics is not among the objectives of this research.

A fabric simulation principle is introduced that uses both diameter and hairiness data for the first time in the literature. Yarn board and single jersey knitted fabric simulations are implemented in order to demonstrate the principle. However, development of a complicated simulation program that could have a commercial value is beyond the scope of this research. Such a program would require the capability to simulate different types of fabric structures and multi-feeder systems. It would also be ideal to simulate the effects of colour and finishing processes on the fabric, which may be an interesting research topic in the future.

1.4 Overview of the Thesis

The thesis consists of eleven chapters. Chapter 2 explores the literature regarding the important hairiness and irregularity measurement and evaluation methods as well as commercial test instruments. A particular emphasize has been made on the computer vision systems in the literature dedicated to yarn and relevant textiles testing.

Chapter 3 describes the image acquisition hardware and the processing software used for the experiments. Custom program interfaces, macros and function libraries developed during the research are described briefly. Appendix A is a supplementary to this Chapter and describes the inputs, outputs and tasks of some important custom C functions developed during the research.

Chapter 4 is dedicated to the optical aspects of yarn imaging. The depth of field restraint in front-lit and back-lit illumination methods are discussed in a mathematical manner and the established theory is verified through experiments. Other optical aberrations are also discussed as well as image distortion due to digitisation and yarn movement when using line scan cameras.

In Chapter 5, various light sources and arrangements used for low and high magnification imaging are described and relative advantages and disadvantages are discussed based on the image quality. Image enhancement and processing algorithms developed for back-lit and dark field yarn images in order to locate the hair-core boundaries and to measure the total hairiness are explained and the results of different processing algorithms are compared. A method to simulate various yarn scanning resolution conditions is described which is used to investigate the effect of scanning resolution on hairiness and irregularity assessment in subsequent chapters.

Chapter 6 deals with yarn hairiness analysis. The principle of an algorithm developed to simulate photo-electric sensors used to count the number of hairs is explained and restraints of photo-electric methods are discussed based on this model. A number of indices developed for determination of total hairiness are described and the measurements are correlated with a commonly accepted total hairiness index. The effects of scanning resolution on hairiness measurement are investigated.

Chapter 7 deals with the diameter and irregularity measurements. Results obtained from images acquired using different optical arrangements are correlated with commercial testers. The effects of scanning resolution on diameter and irregularity measurements are investigated. Methods implemented to analyse the irregularity including a new visual technique are explained and demonstrated on some yarn samples.

Chapter 8 covers the image processing algorithms developed for yarn twist measurement. The measurements are correlated with the actual values and the results are discussed.

Chapter 9 describes the principles of a new yarn simulation algorithm that uses diameter and hairiness data. Yarn board and knitting simulation programs based on this principle are explained. The simulations are compared with actual yarn and fabric images and images from a commercial simulation package both visually in a

subjective manner and quantitatively using variance-area curves. The effect of hairiness on yarn and fabric appearance is also discussed.

Chapter 10 summarizes the conclusions drawn in the thesis. Finally, Chapter 11 highlights the areas covered in the thesis that need improvement and gives suggestions for further work.

CHAPTER 2 - Literature Survey

2.1 Introduction

This Chapter describes the hairiness and irregularity characteristics of yarns and reviews the recent work in the literature to measure and describe these characteristics. Section 2.2 gives the description of hairiness and explains the importance of it in terms of its influence on yarn and fabric properties. Section 2.3 covers a survey on various instruments and methods developed to evaluate hairiness and in Section 2.4, important commercialised hairiness testers are explained.

In Section 2.5, the definition of “yarn irregularity” is given and its importance is discussed. Various statistical methods to describe yarn irregularity are explained. Various methods to measure irregularity are outlined with particular interest to optical and capacitive methods, which are discussed in more detail. The commercial instruments to measure yarn irregularity are also covered at the end of Section 2.5.

Section 2.6 explores the previous work in the literature that utilise computer vision techniques to assess yarn characteristics. Some relevant image processing techniques other than used for yarn image processing are also addressed in this section.

2.2 Measurement of Yarn Hairiness

2.2.1 Yarn Hairiness and Its Importance

In ring spinning, the hairiness originates within the spinning triangle, where individual or bundles of fibres are twisted and entangled to form a yarn. Ideally, the fibres passing through the zone are grabbed from the leading end at the bottom (tip)

of the triangle, where the yarn is formed, and the trailing end is under control of lateral friction with the fibres around it. In this case, the fibre will fully contribute to the yarn core. However, in some cases fibres are only attached to the core from one or two ends, the remaining part floating around the core. These fibres may have three different forms as shown in Figure 2-1. Fibres having one or both ends outside the core are called *protruding fibres*; those coming out the core and going back in are called *loops* and those having the major part protruding from the core are called *wild fibres*. Wang et.al. (1999b) observed the formation processes of different types of hairiness in worsted ring spinning dynamically by means of a special CCD camera. They showed that protruding fibres are often due to short fibres that cannot be caught from the leading end by the twisting zone or the trailing ends under insufficient control especially at the edges of the spinning triangle. They also suggested that the loops originate mainly from poorly aligned fibres with a U-shape or a large hook or in some cases due to dynamic snap-back of fibres when they are suddenly released from the front roller nip. Wild fibres often occur when a fibre is neither grasped by the twist zone nor under control at the trailing end.

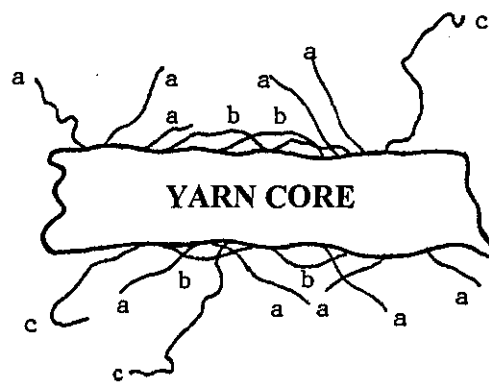


Figure 2-1 a) Protruding fibres, b) Loops, c) Wild fibres (Iridag [1994], p. 5)

In open-end yarns, the hairiness occurs as short hairs protruding from the core and fibres wrapped around the core known as "belt" formed due to the air turbulence in the spinning zone.

One of the problems associated with hairiness is that during the production processes like spinning, weaving, knitting and sewing, the hairs breaking off the yarn may come together and form fibre assemblies which might obscure the paths through which the yarn travels and cause excessive tensions in the yarn, resulting in yarn breakage. The yarn strength is also shown to decrease with increasing hairiness [Yatskovskii, 1961] probably due to the decreasing number of fibres contributing to the strength of the main body.

The hairiness also has an important effect on the end fabric properties. For example, it gives the fabrics a bulky structure and a good handle property (Barella et.al. [1991]). Especially in man-made fibres, a certain degree of hairiness is essential in order to provide a more natural effect. On the other hand, the hairiness is associated with the pilling tendency of fabrics [Hattenschweiler, 1989]. Hairiness variation also has an important influence on the fabric appearance. It is known that high hairiness variation may be one of the causes of "barre effect" on fabrics

With the development of quality management techniques in the last decades it became more important to measure the hairiness parameter of the yarns quantitatively as well as other parameters like evenness and twist to allow an exact quality description of the yarns produced. The need for prediction and an objective comparison of end products requires hairiness to be evaluated quantitatively. Especially the latest software technologies that simulate the production lines and predict the output of the production from the input data, use quantitative data and evaluation techniques. One important example to this is the CAD systems which simulate the yarns and the fabrics according to their components and properties. Furthermore, it is stated that hairiness reveals information on conditions of the production machines. For instance, by observing the yarn hairiness, it is possible to optimise the different components of the spinning machines (such as ring traveller, thread guide, aprons etc.) or to control their current condition (wear and wastage) [Zweigle G566 Literature, 1999].

Since the decade of 1950s there have been many researches on evaluation of yarn hairiness, before then it was regarded as a curious yarn property which interferes with textile processes and produces trouble during weaving and knitting. Various methods to measure the yarn hairiness can be categorised into three groups which are 1) optical and photographic methods, 2) photoelectrical techniques and 3) weighing techniques (Barella, 1970).

2.3 A review of Literature on Evaluation of Yarn Hairiness

Barella [1966, 1970, 1982, 1983, 1993] published comprehensive literature surveys on yarn hairiness. These series covered most of the works in the literature as well as the commercialised instruments developed up to their publication dates. The following survey covers some important work in the literature describing the major approaches to define hairiness as well as test instruments developed to measure it.

The earliest techniques to measure hairiness were based on use of photoelectric sensors (Barella [1953]). The basic principle was to measure the diameter of a yarn using a photoelectric sensor and comparing this value with the actual yarn diameter measured manually using microscopy. Since the photometric diameter would be greater than the actual diameter because of the hairs, the ratio between two different diameter values was used to define the so called "coefficient of hairiness".

The singeing method describes the hairiness as the difference in the yarn weight before and after a singeing process, through which the hairs were eliminated. Boswell and Townsend [1957] investigated the factors affecting the hairiness of worsted yarns using the singeing method. They found this method more suitable than the photometric methods, due to the long hair content of worsted yarns which could not be detected with the photocell because of the very limited field of view. Pillay [1964] also examined the singeing method and the microscopic techniques to define the hairiness and found the former to be more suitable.

One of the main problems of singeing method reported in the literature was that the effect of singeing depended on fibre characteristics. Furthermore, the hairs could not completely be eliminated by any means including singeing, and therefore the loss in weight after singeing could not accurately represent the total hairiness of a yarn (cited in Barella [1966]). This was the most criticised drawback of this method. Another serious problem was the conditioning of the yarn before and after singeing, since if the humidity contents are not the same, the hairiness measurement was severely affected. Singeing method did not appear in the literature after the decade of 1960's.

The measurement of hairiness using optical and photographic means dates back to 1954. Onions and Yates [1954] used microscopic techniques to analyse hairiness. They created 8 reference yarn pictures having different amount of hairiness and compared the microscope observations from a yarn with these pictures to give a hairiness grade between 0 and 7. This method was apparently very slow and lacked objective assessment.

Barella [1955] developed an optical system that projects yarn shadow on a screen allowing manual observation of hairs. He determined the number of protruding ends (N_1), loops (N_2) and wild fibres (N_3) individually as well as the length of protruding ends (L_1) in 1mm yarn sections. These parameters except for N_3 but in addition to a new parameter L_2 defining the length of loops were also used by Jackowski [1961] to measure hairiness. Barella studied the hairiness theory based on these parameters and investigated the effects of yarn production parameters on them. Although being very tedious, this method is probably one of the most interesting ways of measuring hairiness from the computer vision perspective. An important problem with the technique was the entanglement of hairs at the core edges making discrimination between fibres often quite difficult and sometimes even impossible.

Goswami [1969] incorporated a yarn clamping and rotating device in the aforementioned microscopic technique for counting and measuring the length of

protruding fibres in yarns. This device enabled to view the fibres projecting into a plane perpendicular to the screen. The N_1 variations he found were considerably lower than those found by Barella.

An interesting method to measure the hairiness was used in a commercial instrument named CRITER tester in 1962. In this instrument, the hairs are raised by applying an electric field and the yarn is transferred through two tubular electrodes. As the hairs touch the electrode surfaces, the first electrode charges the hairs and the second one discharges them. The current conducted by the yarn to the second electrode is measured and used as a measure of total hairiness. The hairs shorter than 2.5mm could not touch the electrode surface hence did not contribute to the measured hairiness index. Barella [1966] claimed that putting the fibres upright would possibly bring about an increase in hairiness and what is measured on this instrument would be the "potential hairiness" rather than the "actual hairiness".

Lappage & Onions [1964] developed an instrument that counted the number of fibres protruding from a yarn at different distances. A magnified image of the shadow of the yarn was focused on a screen and a small photoconductive cell, mounted at a desired point in the screen detected the passage of the hair shadows. The magnifications parallel and perpendicular to the yarn axis were 13 and 9.3, respectively and the photocell had a sensitive area of 1mm x 0.5mm. The test speed was 21cm/s. They found that the number of hairs decreased exponentially as the distance from the yarn increased. They plotted the logarithm of number of hairs with respect to the distance of the hairs from the yarn axis for different blends of yarns. These graphs showed that the typical worsted, woollen and cotton yarns were clearly different in position and slope, though they were all slightly curved in the same general sense (Figure 2-2). This exponential behaviour of the number of hairs is commonly recognized in the literature. This pioneering work by Lappage and Onions [1964] inspired many hairiness instruments and became one of the standard methods to describe hairiness.

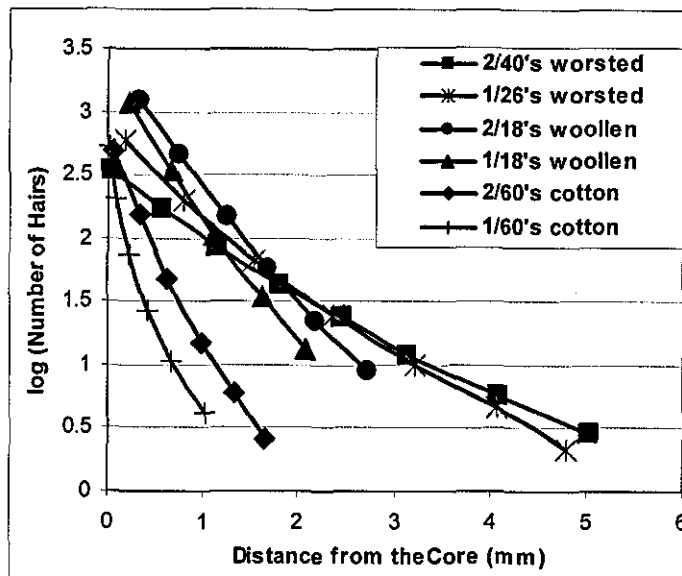


Figure 2-2 Logarithm of number of hairs plotted against the distance of hairs from the yarn axis for different blends (Reproduced from Lappage and Onions [1964], p. T384)

One of the first commercial instruments was developed by Shirley Institute in 1963 that was named Shirley Yarn Hairiness Meter (YHM). The details on this instrument first appeared in the literature in Slack [1970]. The measurement principle was quite similar to that was used by Lappage and Onions [1964], the basic difference being that the shadows of the hairs were not magnified through the lenses but directly projected onto the photocell after passing through a circular aperture with a diameter of 0.5mm. The yarn guide was positioned at an adjustable position relative to the aperture, which allowed counting the number of hairs at any distance from the core. Slack [1970] pointed out that one of the shortcomings of the instrument was the fibres that are separated along the yarn length by less than 0.5mm could not be resolved as separate fibres due to the diameter of the aperture. However, he found that fibres projecting 3mm or more from the yarn rarely occurred as close as less than 0.5mm. The signal threshold level was selected so that a fibre with a diameter of as small as 12 μ m could safely be detected by the photocell. Slack also investigated the effect of raising the hairs by applying an electric field as in CRITER and found that this increased the number of hairs but proportionally to the number of hairs in their natural form. For this reason, he adopted the simpler case of testing the yarn in its

natural state. Another important feature introduced in the YHM is a paralysis time of 1.5ms in order to ensure that a fibre is counted only once, even though the vibration of the fibre may cause multiple signals from the photocell. Some other features of this instrument are covered in Section 2.4.1.

Walton [1968] correlated some spinning conditions with the number of hairs at 3mm from the core obtained from YHM. He found the combed yarns to have more hairiness than the carded yarns. This is mainly due to the reason that the carded yarns possess mostly short hair hairiness with hair lengths less than 3mm.

Barella [1970] developed a new hairiness tester named BV Hairiness Tester which was furnished with a TV camera that scanned the shadow profiles projected onto the objective using back-lit illumination. The instrument was capable of calculating yarn diameter, an index of total hairiness and an index of hair lengths simultaneously. This instrument is an important step forward in the hairiness testing literature due to the introduction of machine vision and signal processing methods for the first time. This early instrument along with the more modern version ITQT developed in 1980 are described in more detail in Section 2.6.1.

Pai & Munshi [1978] used a digital fibrograph for the determination of yarn hairiness. In this method, the yarn was placed between two glass slits and was exposed to a narrow beam of light and a parameter D_1 proportional to the amount of transmitted light through the yarn core and the hairs was measured. Following this, the diameter of the yarn was calculated on a microscope and corresponding light transmission factor D_2 was calculated and subtracted from D_1 giving a measure of total hairiness. They found a good correlation between the hairiness measurements using the fibrograph and the total hair lengths measured using a microscopic method.

In 1983, Zweigle introduced the G656 Hairiness Tester which works on the same principle with Shirley YHM. The major advantage of this instrument was that it could simultaneously count the hairs at various distances from the core between 0

and 12mm with 1mm spacing, where, 0mm corresponds to the edge of the yarn core. The latest version of Zweigle Hairiness Tester is more fully described in Section 2.4.4.

Ghosh *et. al.* [1988] described an electronic instrument called JTRL for measuring the hairiness of jute yarns. This instrument is based on counting the hairs at a fixed distance from the yarn body in a similar fashion with Shirley YHM (Figure 2-3). They confirmed the exponential nature of number of hairs relative to the distance from the core. They reported that since the jute fibres were meshy in character and the filaments had branchings, slubs or slub-like conglomerations of fibres were formed in some zones of yarns, which made the detection of hair counts very difficult at such zones.

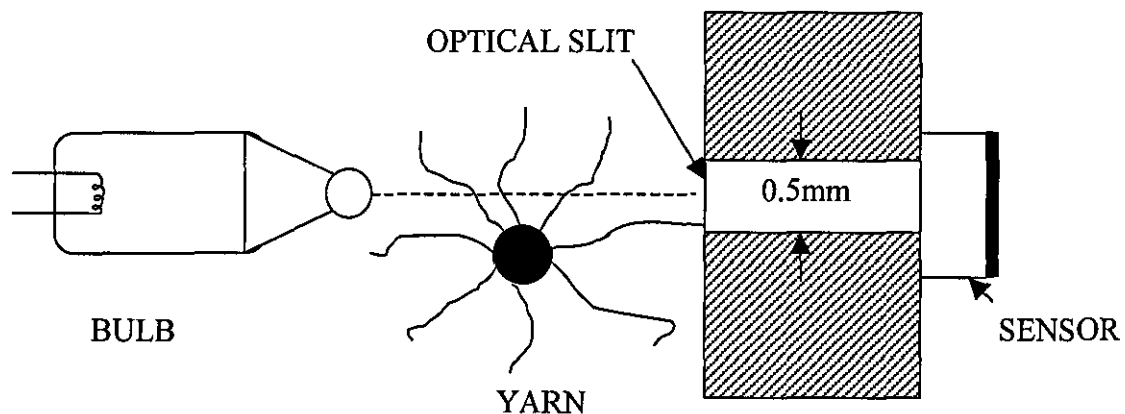


Figure 2-3 Working principle of JTRL hairiness instrument.

A new approach based on optical filtering techniques for measuring the hairiness appeared in the literature in 1980's (Silva *et. al.* [1981], Rodrigues *et. al.* [1983] and Francini & Longobardi [1989]). Silva *et. al.* [1981] and Rodrigues *et. al.* [1983] considered the core as an opaque, metal-like straight wire and blackened the Fourier transformation of the yarn image with a mask having a shape resembling the pattern of helix. The form of the mask was dictated by experience in order to ensure the results were independent of the twist of the yarn. The light that is not blocked by the

mask was collected by a short-focal-length lens and was received by the sensitive area of a phototransistor. The signal from the phototransistor was used as the input for hairiness evaluation.

Francini & Longobardi [1989] used an image divider to obtain two Fourier transforms of the yarn image one passing through a high-pass and the other through a low-pass filter. Filtered images were then integrated by two photodiodes. The exit of the photodiode perceiving low-pass filtered image was used as the information on the core section, leading to irregularity analysis. The amount of light on the other photodiode was considered to be a measure of hairiness.

In 1986, Uster introduced the UT3 Hairiness Attachment, which was based on dark field optics and capable of giving an index of total hairiness. Details of this instrument are given in Section 2.4.5.

2.4 Commercial Hairiness Testers

2.4.1 The Shirley Yarn Hairiness Tester

The Shirley Yarn Hairiness Tester (Figure 2-4) has a single photoelectric sensor, which can be adjusted between 0 and 10 mm from the yarn core.

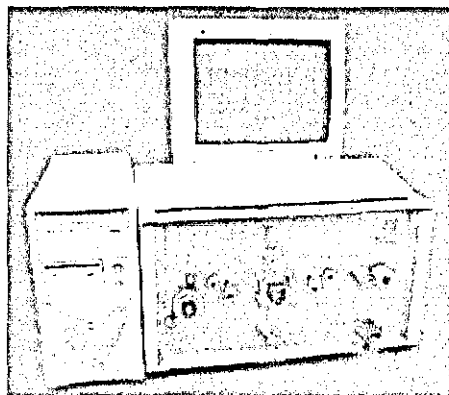


Figure 2-4 The Shirley Yarn Hairiness Meter

The yarn to be tested is passed over a guide, which accurately locates the axis of the yarn relative to a beam of light and a photocell. As the yarn is drawn over the guide, the projecting fibres momentarily interrupt the light beam. Figure 2-5 shows the arrangement of the instrument. The resulting signal from the photocell is amplified, and, if it then exceeds a certain threshold level, it is counted by a Dekatron counter. The inspection zone of the yarn is restricted to 35° each side of a vertical plane and this is assumed to represent the whole yarn surface. The maximum test speed is 100m/min.

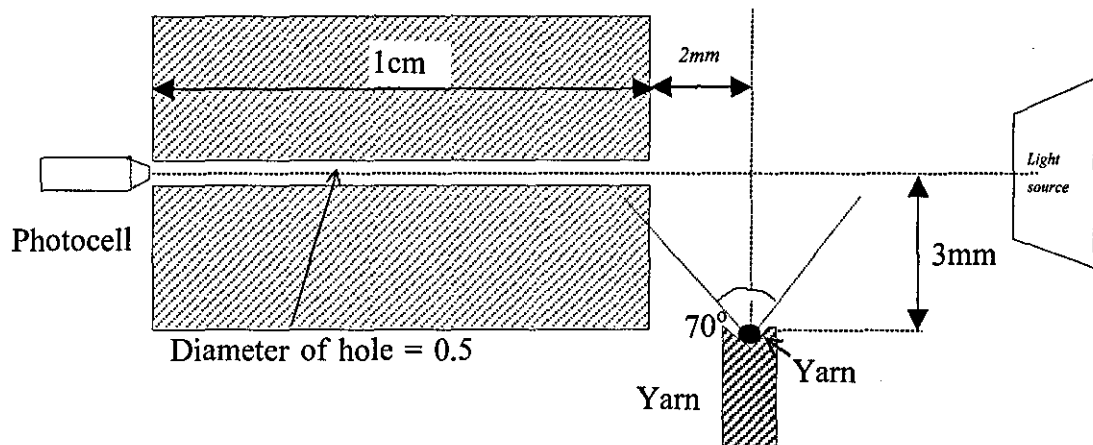


Figure 2-5 Measuring principle of Shirley Yarn Hairiness Meter (Slack [1970], p. 429)

2.4.2 F-Index Tester

This instrument was first introduced in 1974. The basic principle is to project a parallel light beam to the yarn and the number of intersections of the hairs with the imaginary plane formed by the light beam is used to obtain an index of hairiness named "F-index" (Barella & Manich [1982]). The hairs from 0 to 20mm from the core are covered in the measurements. The device has a hair interval resolution of 0.3mm. The F-index is claimed to cover numerical values of average hair length, number of hairs and integrated hairs length. However, to date, no detailed information could be acquired about this tester as to how these values are derived. The maximum test speed is 30m/min and the test length is 1, 10 or 50m.

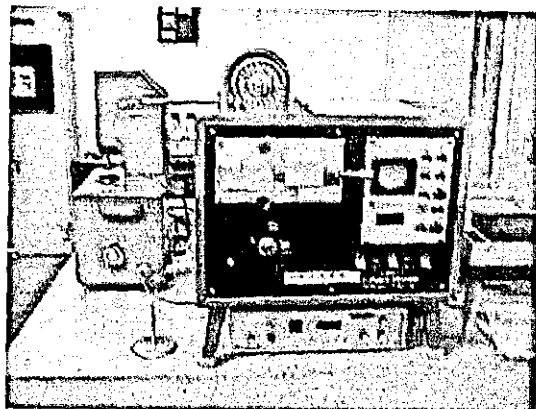


Figure 2-6 F-Index Tester

2.4.3 Meiners Del Hairiness Meter

The Meiners-Del YHM4 Yarn Hairiness Meter MK4 (Figure 2-7), simultaneously measures hair lengths between 0 and 9 mm over a selected test length and at a selected test speed. The yarn transport system uses a skewed roller to produce tension between it and the primary drive roller that determines yarn feeding speed. The drive speed is controlled digitally and is re-checked before every test, to ensure changes in yarn package tension does not affect the speed.

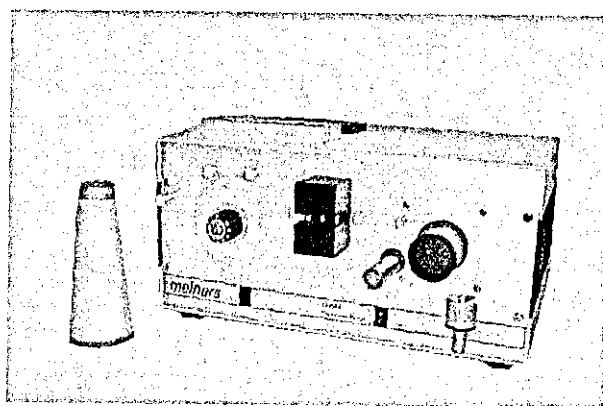


Figure 2-7 Meiners Del Yarn hairiness Meter

Meiners Del also developed a portable battery operated Yarn Hairiness Monitor called Memorandom that is used to check the quality of the yarn whilst being

produced on the machines (Figure 2-8). The principle is to count the number of hairs at a fixed distance as in Shirley YHM. This distance can be modified by changing the measuring head.

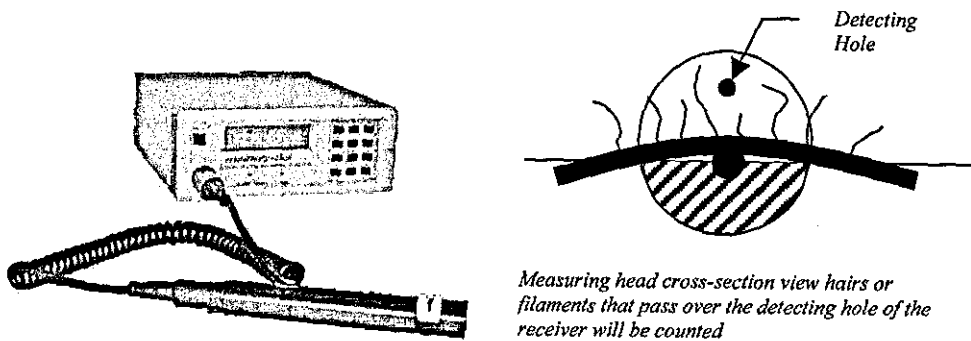


Figure 2-8 a) Meiners Del Memorandum Portable Yarn Hairiness / Broken Filament Monitor b) The measurement principle

2.4.4 The Zweigle G565/G566 Hairiness Meter

Zweigle Hairiness Tester (Figure 2-9) is capable of measuring the number of hairs protruding 1, 2, 3, 4, 6, 8, 10, 12, 15, 18, 21 and 25mm from the yarn core with the aid of photo transistors. The numbers of hairs are displayed on a built-in monitor on logarithmic scale in real time.

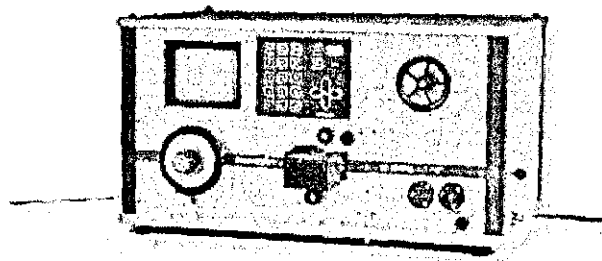


Figure 2-9 Zweigle G566 Hairiness Tester (<http://www.zweigle.com>)

A halogen lamp is used for illumination and the light passes through individual pin holes for every photo transistor (Figure 2-10). The zero reference line is adjusted by

moving the yarn transport pulleys at the measuring zone using a manual screw controlled by the operator. Two photo-electric sensors are employed to assist the operator when adjusting the reference point, which sets off a buzzer when the yarn reaches the reference position. Unfortunately, there is no clear information on the precision of these sensors and the tolerance limits when setting the reference position as related to the maximum difference in position when testing, for example, the same yarn at different times. This information would be quite important in terms of reproducibility of the tests.

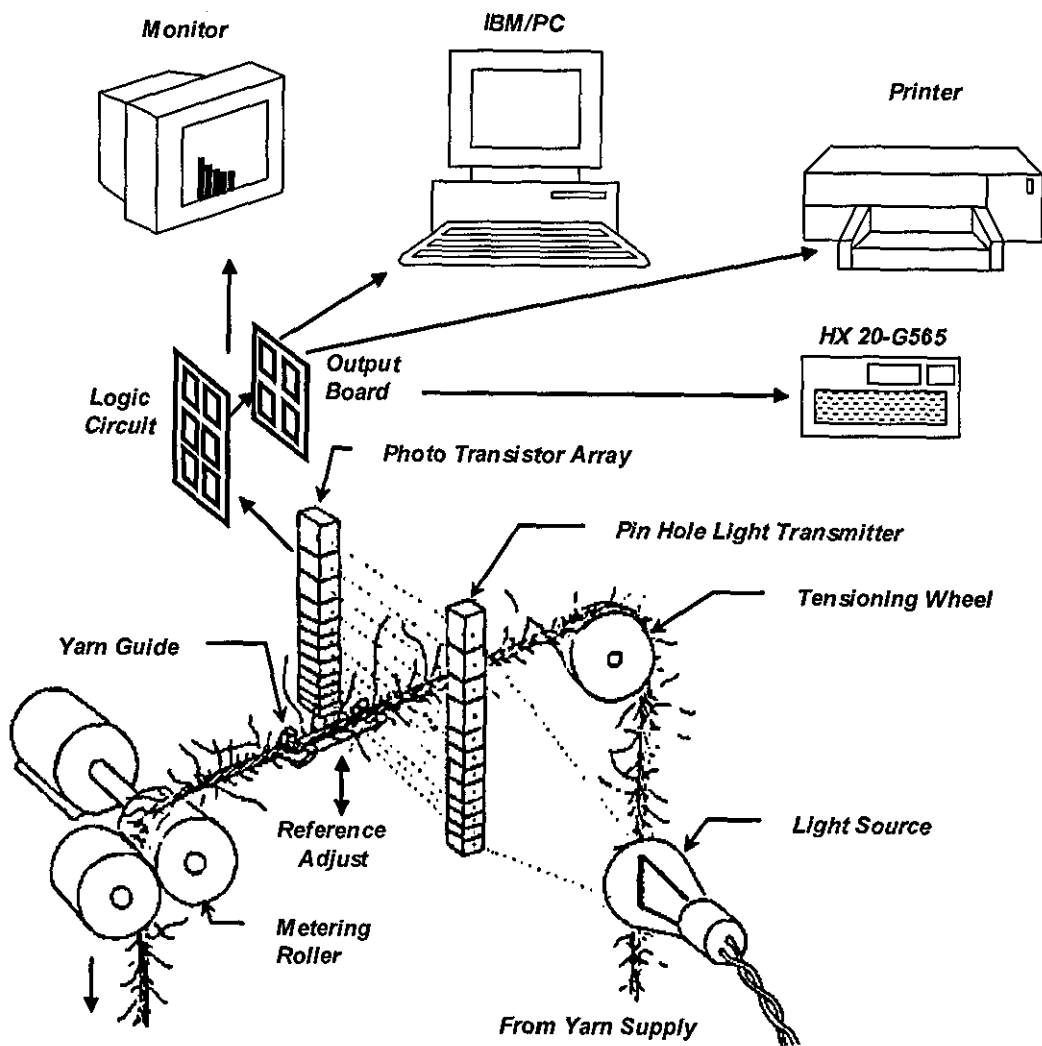


Figure 2-10 Measurement principle of Zweigle G565 Hairiness Meter (Iridag, [1994] p. 14)

It has been previously mentioned that the number of hairs plotted against the distance from the core exhibit a linear trend on the logarithmic scale as illustrated in Figure 2-11. This trend is used in Zweigle G565 for determination of the nature of yarn hairiness. The intersection of the trend line with the x axis (R) gives the length of longest projecting fibre theoretically. Similarly, the point where the trend line crosses the y axis (M) gives the maximum number of projecting fibres.

Although this trend is commonly accepted to be linear, Barella & Manich [1993] found that the distribution obtained from Zweigle G565 could better be described with two trends separated at 3mm from the core.

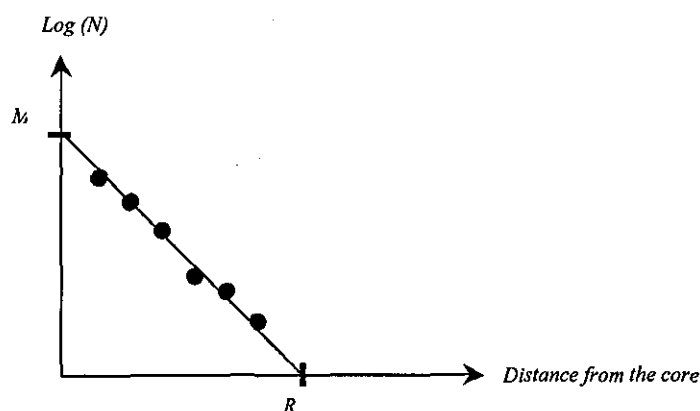


Figure 2-11 Illustration of number of hairs plotted against the distance from the core on a logarithmic scale

Along with the number of hairs at various distances (N_1 , N_2 , etc.), Zweigle G565 calculates three indices from the number of hairs, which are S_3 , T_p and H . S_3 index gives the total number of hairs protruding at 3mm and further from the core while T_p index is calculated from the total number of protruding hairs. H index is based on a method developed by Mangold and Topf [1985] that involves the number of hairs at different lengths.

This device is not capable of measuring hairs less than 1mm. The standard test speed is 50m/min; however, in the latest version of Zweigle Hairiness Tester, G566, it is possible to achieve testing speeds of up to 200m/min with an optional module.

2.4.5 The Uster Tester 4SX Hairiness Meter Attachment

The Uster Tester Hairiness Meter Attachment (Figure 2-12) is conceived originally from a model based on yarn structure. According to this model, the yarn is resultant of a perturbation function that is essentially superficial and a mass function of cohesion that assures yarn compactness and corresponds to the yarn core.

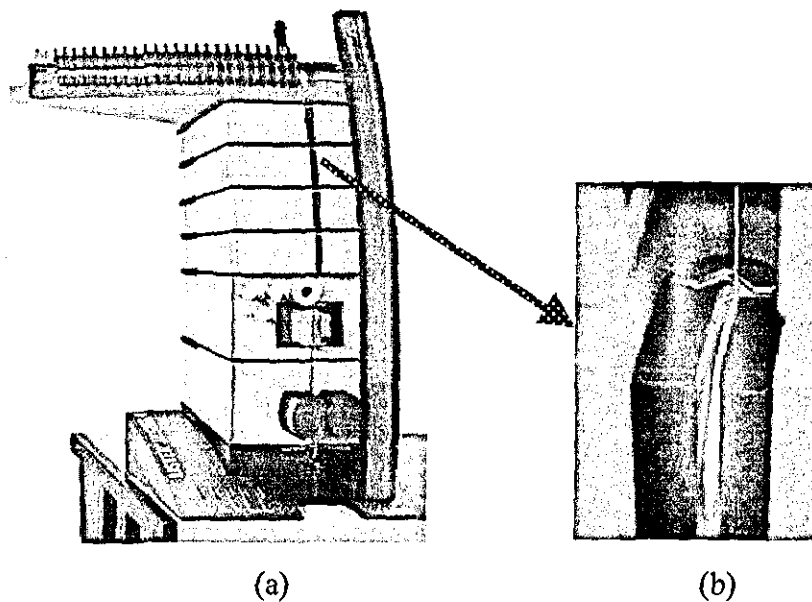


Figure 2-12 a) Uster Tester 4 SX b) Measuring zone of Hairiness Meter Attachment (OH Module)

The measuring field is formed by a homogenous field of parallel light. If a yarn lies in this measuring field, only those rays of scattered light reach the detector which have been scattered by the hairs as illustrated in Figure 2-13. The direct laser light is blocked by an aperture at the detector side. Therefore if no yarn is present then no light falls on the photo-detector. Figure 2-14 shows how yarns appear in the measuring zone of UT3 Hairiness Attachment.

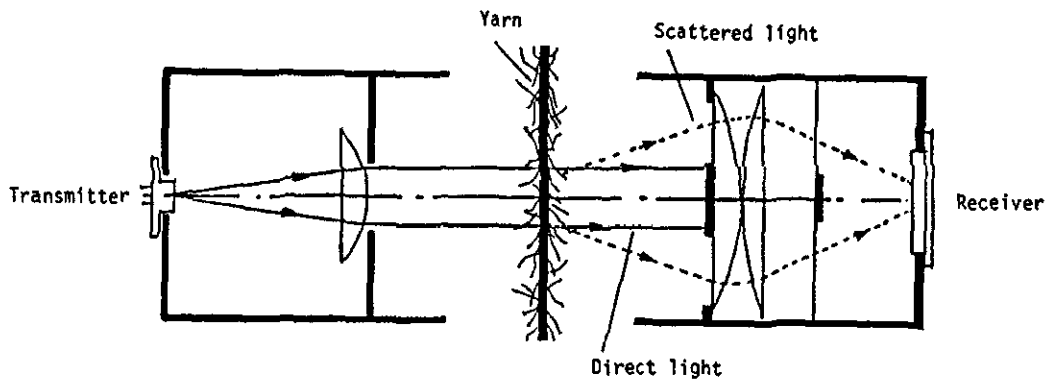


Figure 2-13 The measuring zone of UT Hairiness Attachment

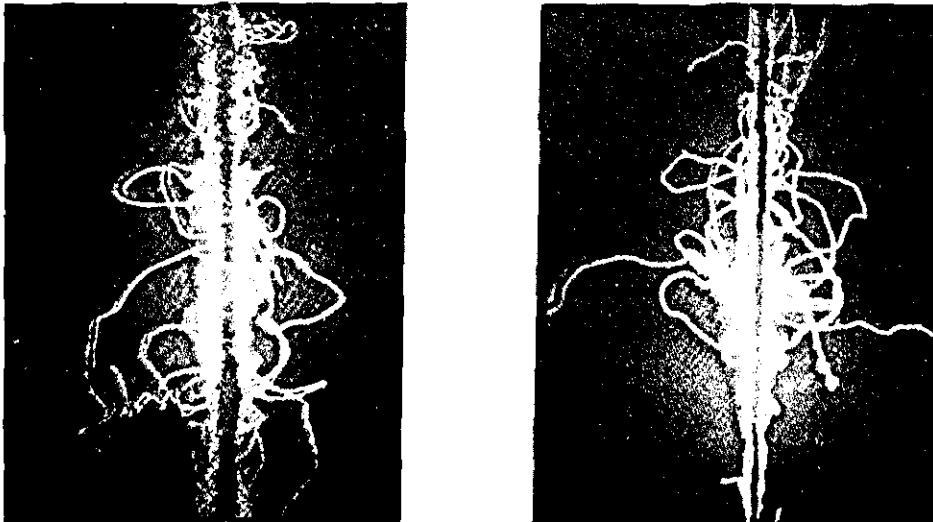


Figure 2-14 The appearance of yarns in the measuring zone of UT Hairiness Attachment

Uster Tester gives an index of Total Hairiness H that corresponds to the total length of hairs in 1cm of yarn segment. According to the company's literature, fibre diameter, transparency and glossiness have only a slight influence on H . However, it is indicated that this is valid for cotton yarns with average fibre fineness with no mention of correction factors, if there is any, for other materials. On the other hand, although it is claimed by Zellweger Uster that the measurement is practically independent of the yarn colour owing to the infrared light, some dyestuffs are reported to absorb infra-red radiation, affecting the hairiness measurement that

results in a lower value being obtained for the dyed yarns (cited in Barella [1993], p.8).

The sampling length for hairiness measurement is 1cm. In earlier literature of UT3 a CVh% value was calculated giving the coefficient of variation for hairiness. However it was later found that a standard deviation value sh would be more appropriate for comparison purposes. CVh% can still be calculated by dividing sh by H . The maximum test speed of Uster Tester 4SX is 400m/min.

2.4.6 Keisokki LASERSPOT Hairiness Tester

LASERSPOT Hairiness Tester developed by Japanese Keisokki Kogyo Company is based on optical filtering techniques. The yarn is assumed to be composed of three parts, which are i) the core, ii) diffusion range (fibres in the proximity of the core such as loops) and iii) hairs. According to the company's literature, a special filter combined with a high pass filter enables a more accurate definition of the core boundaries compared to a single high pass filter, which adds some brightness to the edges of the core possibly effecting the hairiness measurement. This is quite evident from Figure 2-15 showing pictures of a spun yarn spatially filtered with a high pass filter and Keisokki's special filter (Keisokki Report [1997]). Unfortunately, there is no detailed information about the characteristics of this filter.

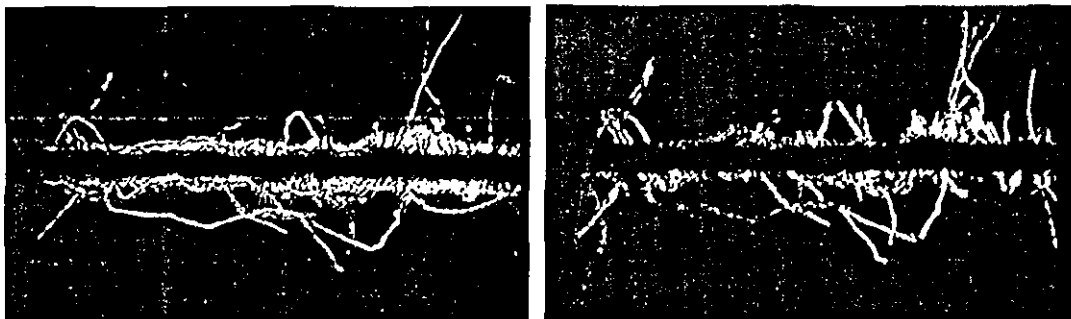


Figure 2-15 Left: Picture of a spun yarn filtered with a high pass filter, Right: The same yarn filtered with Keisokki's spatial filter (Keisokki Report [1997])

Keisokki also introduced another module that incorporates a low pass filter to determine the optical diameter. Figure 2-16 shows the optical set-up used in Keisokki LASERSPOT. The laser source is a 680nm semiconductor laser. It is not clear from the company literature how the dyed yarns are handled using this wavelength. This instrument can achieve a maximum test speed of 400m/min.

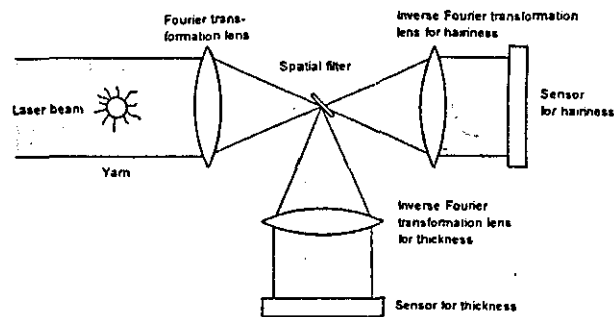


Figure 2-16 Optical setup in Keisokki LASERSPOT

2.4.7 Premier iQ QualiCenter

Premier iQ QualiCenter (Figure 2-17) consists of various modules to measure different characteristics of yarns and slivers. The hairiness attachment employs a laser light source with two sets of detectors for the hairiness index and hair count distribution measurement. The hairiness index is similar to Uster's H Total Hairiness Index. The hair count distribution measurement on the other hand gives the number of hairs longer than 3mm from the core yarn in steps of 1mm up to 12 mm.

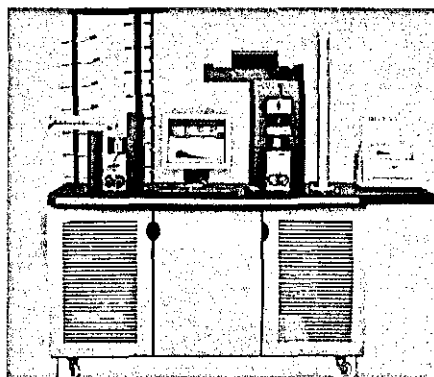


Figure 2-17 Premier iQ QualiCenter

2.4.8 Comparison of Commercial Testers

There are a number of publications in the literature investigating the relations between the indices obtained from different testers. In a communication by Zachert cited in Barella [1993] the F-Index Tester, The Zweigle G565, and the UT3 are compared. They found a very strong correlation between the first two testers with a correlation coefficient of 0.9. However, none of the two agreed so significantly with UT3 exhibiting correlations both with coefficients of less than 0.7. One of the other results found in this work was that the hairiness index of UT3 exhibited a correlation with a coefficient of 0.7 with linear density, which did not exist for the other two devices.

Barella et.al [1992] carried out experiments on open-end and ring spun yarns using Zweigle G565, UT3 and ITQT. They found that for rotor spun yarns, the Zweigle exhibited significantly lower hairiness values due to the apparent reason that these yarns mainly possess short hair hairiness less than 1mm, which cannot be detected by Zweigle G565. Yarns spun with relatively thick fibres also exhibited lower hairiness values on Zweigle G565. Their experiments also revealed that among the T_p , S_3 and L indices of Zweigle G565, T_p exhibited the highest correlation with Uster's H index while the S_3 lowest. They addressed some important drawbacks of the indices used in commercial testers such as Uster Tester giving no information on how the hairs are distributed around the core and Zweigle G565 disregarding the hairs less than 1mm. They concluded that a single measure would not be adequate for hairiness measurement.

A report by Suessen (Spinnovation, 3/2002) indicates that short hairs contribute to a good textile touch in the fabric while fibre ends exceeding 2 mm are generally found to disturb subsequent processing steps causing high additional costs and affecting the performance of the finished textile article. They state that the measuring method according to USTER Hairiness (H) does not by far reflect the actual yarn conditions since no difference is made between long and short hairs. They favour Zweigle's

measuring method with this respect since the hairs are classified according to their length on this instrument. They showed that the hairiness measurements of yarn samples produced on different spinning machines and proven to have different quality characteristics associated with hairiness, were significantly different in terms of Zweigle S3 index while only slightly different in terms of Uster's H index.

According to a private communication with a Keisokki Tester representative at ITMA 2003, the hairiness index of this tester often correlated quite well with Uster's H index, however the correlation tended to drop for more irregular yarns.

2.5 Yarn Irregularity

2.5.1 Description and Importance of Yarn Irregularity

In yarns, there can be a variation in twist, strength, thickness or mass along the length. The term "yarn evenness" or "yarn irregularity" often refers to the variation in mass per unit length or the thickness along the yarn. The variation in mass is more common to describe irregularity due to the information it reveals about the yarn production stages. The variation in thickness is associated with uniformity characteristics from the aesthetics point of view and is more related with the appearance of the end product.

The yarn is always under a stress during winding, weaving and knitting and the level of this stress is generally adjusted according to the mean strength of the yarn. An irregular yarn will obviously have more weak spots and therefore will tend to break more frequently. Yarn breakages cause a serious decrease in the efficiency of the production. For example on a weaving machine breakage of even a single warp yarn among thousands of others, the machine has to stop until the broken yarn is tied back manually. This means not only a down-time but also an appearance fault due to the knot. The irregularity is always aimed to be reduced by on-line control systems during carding, drawing, combing, spinning and winding.

Irregularity also affects the appearance of the finished fabrics, which can be because of both the irregular appearance of the yarns and different dye absorption levels of yarn sections at different thickness and twist values. This is a serious problem that cannot be fixed after the production. Yarn irregularity is also considered as an important factor effecting fabric streakiness (Davis et.al [1996]).

In recent years, various computer aided design systems have been developed for simulating the textile fabrics. Because irregularity of the yarn strongly affects the fabric appearance, some programs use the irregularity data of the yarns that will be used in fabric production in order to create more realistic simulations.

2.5.2 Methods of Describing Irregularity

In this section common statistical analysis methods to describe the irregularity will be discussed. These methods use the mass or diameter values of the successive sections along the yarn.

2.5.2.1 Coefficient of Variation

The coefficient of variation (CV) is commonly used to define variability and to compare the variations of different samples. It is the most widely accepted way of quantifying irregularity. CV is given by:

$$CV\% = \frac{100}{\bar{x}} \sqrt{\frac{1}{T} \int_0^T (x_t - \bar{x})^2 dt} \quad (2.1)$$

where \bar{x} is the mean value of measurements over a time period of T and x_t denotes the measurement at time t .

2.5.2.2 Irregularity, U%

The parameter U is used by the Uster Tester equipment. It is defined by:

$$U\% = \left(\frac{1}{xt} \int_0^t (x_n - \bar{x}) dt \right) \cdot 100 \quad (2.2)$$

where \bar{x} , t and x_n are defined as in equation (2.1)

2.5.2.3 Indices of Irregularity

An index of irregularity expresses the ratio between the measured irregularity and the so-called limiting irregularity of an ideal yarn. The limiting, or minimum, value of irregularity, expressed in terms of CV, is given by:

$$CV_{\text{lim}} = \frac{1}{\sqrt{n}} \text{ or } CV_{\text{lim}} \% = \frac{100}{\sqrt{n}} \quad (2.3)$$

where n is the mean number of fibres in the yarn cross-section.

2.5.2.4 Correlation Methods

The autocorrelation function, or correlogram, is defined as the mathematical function relating the correlation coefficient between two sets of measurements at points separated by a distance L to the value of L . The correlogram is often a damped harmonic curve as illustrated in Figure 2-18. The magnitude of damping is related with the significance of a quasi-period being produced in the diameter or mass variations. Cox & Townsend [1951] tested three different yarn samples one artificially made more irregular than the others. The correlograms of the two samples turned out to be heavily damped, while the correlogram of the irregular yarn revealed a significant quasi-period existing in the yarn. They concluded that correlograms were probably the best method of detecting quasi-periods.

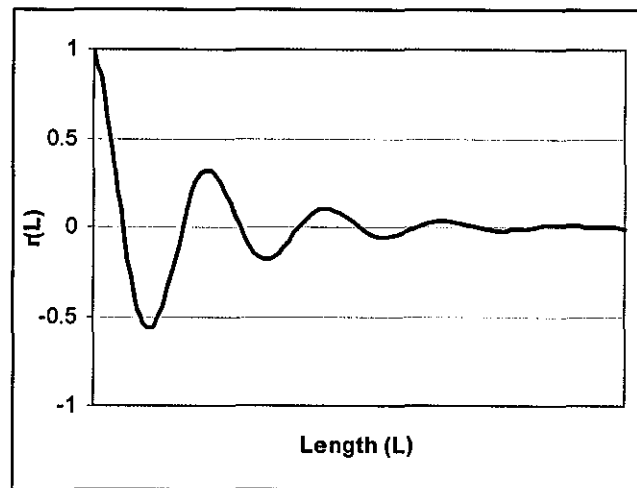


Figure 2-18 A typical correlogram

2.5.2.5 Spectral Methods

In spectral methods, the variation is plotted as a function of wavelength rather than time or length. The major advantage of a spectrogram is its ability to display clearly any periodic mass variations. It is stated that the spectrogram enables an easy detection of the production machine in the whole spinning process chain, which provoked the periodic fault such as that the faults in the short wave length are associated with the machine, upon which the tested material was produced while the peaks or hills with longer wave lengths are associated with a previous process production machine (Zellweger Uster, 1999). However, spectral methods have some disadvantages such as the difficulty of establishing an exact meaning to the height of any particular peak, and the fact that it can yield results only up to a wavelength limit set by the filters, with no possibility of extension in an examination of long-term irregularity [Slater, 1986]. A practical mathematical formulation to calculate the spectrogram is given in Rong & Slater [1995].

2.5.2.6 Variance-Length Relations

The most used contemporary method of expressing the evenness present in a yarn comprehensively is by means of a variance-length curve. Variance-length ($V(L)$) curve is defined as the standardised variance plotted against the length (L) within

which the variance is calculated. A complementary curve $B(L)$ for examination of variance-length relations is also defined as the variance values between the means of lengths L . It is shown by Townsend and Cox [1951] that there is a theoretical relation between $V(L)$ and $B(L)$ curves as follows;

$$V(L) + B(L) = V(\infty) \quad (2.4)$$

where (∞) is the over-all variance. Figure 2-19 shows the general shapes of $V(L)$ and $B(L)$ curves.

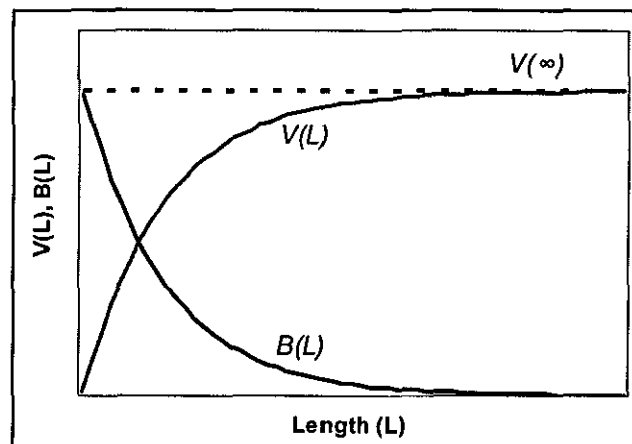


Figure 2-19 General Shapes of $V(L)$ and $B(L)$.

Townsend and Cox [1951] discuss use of numerous characteristics of variance-length curves to describe the nature of irregularities in a yarn. These characteristics are asymptotic value ($V(\infty)$), rapidity of approach to $V(\infty)$, gradient at the origin, scatter of individual variances and count variation. They also derived a statistical relation between the correlogram and the variance-length curve. Tottman & Slater [1981] derived variance-length curves from the data obtained from Uster Evenness Tester.

2.5.2.7 Data Compression Methods

More or less, the methods for measuring the irregularity mentioned above are compressing the data resulting in loss of some information. For example $CV\%$ is

compressing all the data into a single measure, while through a spectrogram all the spatial information is lost. Cox & Townsend [1951] indicated that no single measure is sufficient to assess all features of the irregularity of a yarn. Furthermore, in order to create computer simulations to visualize the appearance of fabrics that will be produced from the yarn under consideration for example, the whole irregularity data would be ideal. However, from the computational point of view this is very expensive in terms of the required storage space for all the irregularity information. For example, to store the diameter data of every mm of 1000m of a yarn would require around 1MB of storage. The data compression methods aim to compress this data while retaining important features.

Suh & Kim. [1996, 1997a, 1997b] used wavelet analysis of yarn profiles for fabric simulation and found that the wavelet could characterise yarn density profiles through the feature analysis by wavelet packet basis. On the other hand, local and transient characteristics such as neps and thin places were well detected by wavelet packet and used as a feature vector data reduction. The fabric simulations they obtained by using the compressed and uncompressed data were found to be very similar. Some problems with on-line data streams including the significance of information loss during data compression are discussed by Lord [1997].

2.5.3 Measurement of Yarn Evenness

Slater [1986] categorised the methods in the literature to measure yarn evenness into 7 groups. Due to their popularity and relevance to this work only capacitive and optical methods are investigated in detail. Other five methods are briefly mentioned below.

- i) **Subjective methods:** The basic principle is winding yarns on a black board and looking for visible faults. There are also some standard pictures corresponding to certain grades and the wound yarn can be categorised into one of these groups according to the most alike standard picture.

- ii) **Mechanical methods:** The common techniques in this category are cutting and weighing method and detecting evenness by devices that respond to changes in yarn diameter.
- iii) **Pneumatic methods:** The yarn to be tested is passed through a narrow tube, into which a stream of air is being forced; and the evenness is defined relative to the air-flow rate.
- iv) **Acoustic methods:** The yarn moves through the sound field between a generator and a pick-up device and the time taken for sound waves to move across the gap is measured and considered as a measure of irregularity.
- v) **Conductometric methods:** Yarn is unwound from a package onto a drum via a bath of electrically conducting fluid and is consequently wetted. A DC voltage is applied to a segment of the yarn and the current, proportional to the conductivity, so to the mass of the yarn, is used as a measure of irregularity.
- vi) **Capacitive methods**

The capacitive methods of determining yarn evenness are the most popular and widely used ones. The measurement relies on conversion from capacitance to voltage. When a non-conducting material (such as fibre assembly) enters the field of the electrode, a capacitance change occurs, and by comparison with the fixed capacitor circuit, a voltage proportional to capacitance change (and hence to the mass of the yarn) can be derived. Mack [1955] investigated the effects of various factors such as yarn density, twist, dielectric constant and geometrical configuration to the change in capacitance.

One of the main limitations of capacitive methods is their cost and the effect of moisture upon the accuracy of measurements. Foster [1957] has found that the effect of moisture is so great that, unless precautions are taken, large errors may arise in the measurement of irregularity. Furthermore, the tests using a capacitive sensor require a time consuming pre-conditioning stage. The arrangement of the plates and the fibre/air ratio in the electrodes are also of great importance and affect the results of the measurements (Slater [1986]). One other disadvantage of the capacitance method is that it cannot give information on the periodicities less than 8 mm, due to the possible minimum length of capacitance plates. Monteiro and Couto [1995] used two capacitive sensors, 1mm different in length to derive a 1mm accuracy measure of the yarn.

vii) **Optical methods.**

The basic principle of optical methods is to direct a light source onto yarn and to obtain a reading that is proportional to the diameter of the yarn. One of the early methods to obtain diametric irregularity was to compare the amount of light measured by a photocell before and after insertion of a yarn; the difference being proportional to the diameter (Onions and Yates [1954]). The photocell readings were calibrated using some wires with known diameters. This technique was however affected by the surface hairs resulting in a significant and inconsistent rise in the diameter measurements. Another common method was direct measurement of yarn diameter manually, using magnified images obtained from a microscope or the projection of the shadow on a screen through some magnifying lenses (Barella [1955]). However, this method was not favoured due to its tedious nature. An interesting approach was adopted by Issum and Chamberlain [1959] where they photographed a running yarn in such a way that a considerable length of the specimen passed before the camera whilst the shutter was open. The resultant picture was a uniform profile with no hairs but with blurry edges. By examining the edge profiles, they calculated minimum and average diameters of the yarn section.

Wulforth [1989] compared the yarn diameters obtained from three different optical methods with microscopic diameters. In the first method, a photodiode and a point-source lamp were used where the yarn diameter was found from the shading off the photocell. The second method was called Laserscan method, where a thin laser beam is recorded by a photosensitive element as the beam moves across the yarn. Scanning was carried out by a rotating mirror onto which the laser beam was directed. The third method utilized a line scan camera, where the length of longest interval of pixels below a certain threshold is considered as the diameter. They found that for monofilament yarns, the first method gave small values due to transmission of light through the monofilament. For filament yarns, the twist was found to have an important effect on both measurements. For the spun yarns with different levels of hairiness, they found the laser method to be seriously effected from the protruding hairs resulting in higher diameters while the line scan method strongly depended on the threshold level for accurate determination of the diameter.

Chu and Tsai [1996a] addressed one of the main restrictions in optical methods as the light source emitting inhomogeneous intensity. They introduced an area compensation method to overcome this problem. Zweigle also addressed the issue and in Zweigle G580, they employed two sensors first one measuring the light intensity partly blocked by yarn and the other a reference unblocked intensity value.

One of the other major concerns in diameter measurement is the cross-sectional profiles of yarns seldom being circular. Slate [1986] indicates that the asymmetrical yarn sections would tend to be presented to the light source in preferential direction of alignment, rather than in a random manner, because of the guide rollers etc., of the transport mechanism. However, this is arguable unless the measurement is taken at a section touching such a surface. Since, otherwise, the yarns rotate during the transfer due to the twist migration caused by the tension and this allows the yarn to be viewed from random angles. Boguslavskii [1971] derived some equations regarding the possible errors in calculating the diameter from a single view. A common method to overcome the asymmetry problem is to measure the diameter from two orthogonal

views of the yarn section. Söll [1999] states that two-dimensional arrangement of the optoelectronic sensors provides a more accurate description of the yarn. Tsai and Chu [1996b] used a sensor device with two incident beams of light perpendicular to each other. They found that the CV% values calculated from elliptical diameters were smaller than those obtained from single view diameters. Their CVd% values were only slightly higher than the Uster's CVm% values. An objection was raised by Barella [1998] to Tsai and Chu's results arguing that the CVd% values should theoretically be twice as CVm% values.

2.5.4 Optical vs. Capacitive Sensors

It is difficult to make a comparison between optical and capacitive sensors since they measure different characteristics. Riddle et.al.[1997] compared the data obtained from a UT3 capacitive sensor and Zweigle G580 optical sensor for several samples. The crosscorrelation between the data from different testers showed very small correlation (less than 0.02).

A basic distinction between capacitive and optical sensors is commonly accepted such as that the former is related with number of fibres in cross section while the latter with appearance, since it is the diameter variation that the human eye sees. Rousseau and Maron [1963] showed that the irregularity values from Zellweger's capacitive sensor did not correlate well with the appearance of fabrics evaluated in a subjective manner.

From the testing point of view, the optical methods make their appeal with high resolutions that can be achieved as high as at μm levels. Furthermore, the measurements are not affected by humidity or the fibre properties such as conductivity and therefore the tests do not require any conditioning and can be carried out straightaway at any stage. This also provides optical sensors with suitability to be adapted for on-line yarn monitoring. Their low cost and more importantly that the yarn can be monitored from a distance not requiring it to pass between some plates also contribute to this advantage.

Söll [2000] suggested that the capacitive sensors are the only way for measuring the irregularities of slivers and rovings. He also gave a comparison of capacitive and optical sensors in terms of their ability to identify different yarn faults and pointed out that periodic faults caused by damaged roller surfaces, belts or gear wheels could best be detected by capacitive sensors. Price et.al [2002] found that the numbers of thick and thin places obtained from corolab (optical) were higher than those found from Uster Tester 3 (capacitive); however, the measurements from two testers exhibited a reasonable correlation with each other. He also found a very good agreement between two testers in terms of CV% values.

Some systems have been developed that use two different sensors to obtain simultaneous diameter and mass readings leading to a more complete definition of yarn quality as well as prediction of yarn density. Jasper et.al. [2000] developed a multi-sensor simultaneous yarn measurement system by combining optical and capacitive sensors. Uster Tester 4SX can also provide simultaneous diameter and mass measurements with the employment of an optional OM module that measures the diameter.

2.5.5 Commercial Irregularity Testers

2.5.5.1 Zweigle G585

Zweigle G585 (Figure 2-20) instrument is based on so called "absolute optical measurement" using infrared light. It operates with a precision of 0.01 mm over a measuring field length of 2 mm and at a sampling interval also of 2 mm. The speed of measurement may be selected on a graduated scale between 100 and 400 m/min.

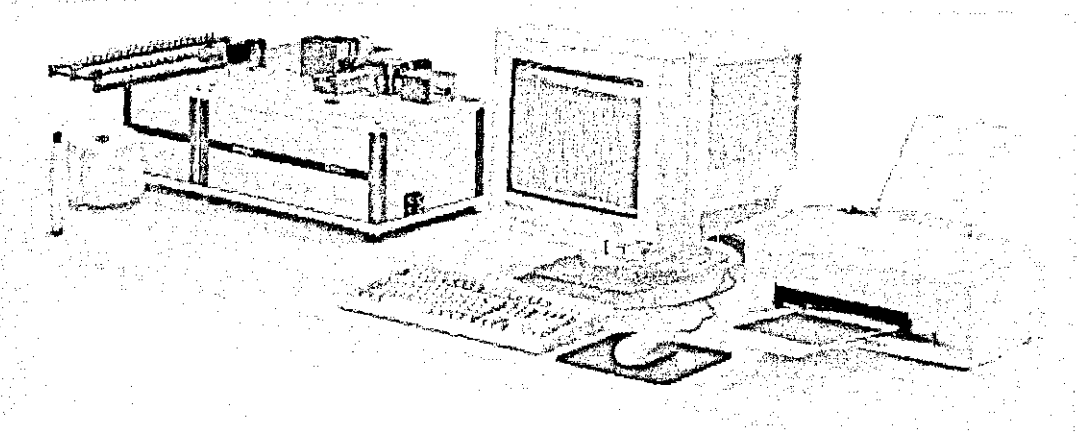


Figure 2-20 Zweigle G585

The measuring system compares the yarn diameter with the constant reference mean and records variations in length and diameter (Figure 2-21). The measurement with respect to a reference intensity avoids the readings from being affected by ageing of the light source. The irregularity data from G585 can be used on a software package named OASYS to generate fabric simulations.

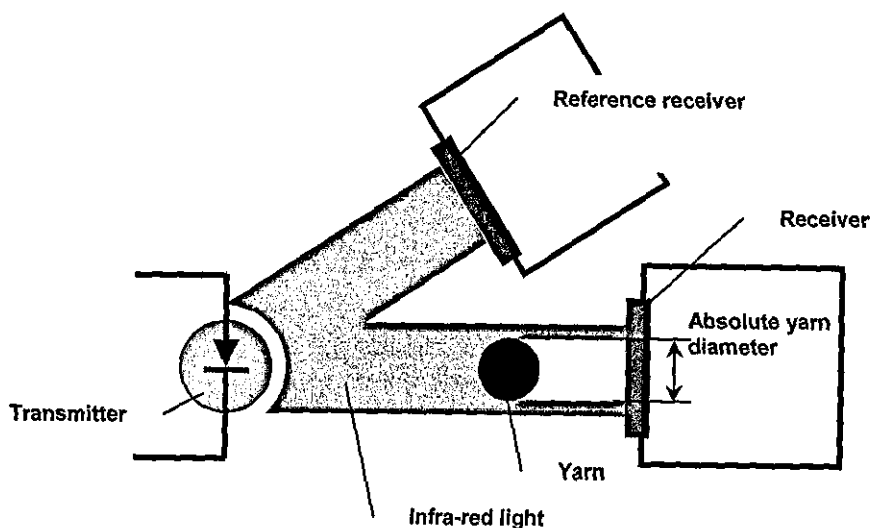


Figure 2-21 Measuring Principle of Zweigle G585

2.5.5.2 Uster Tester 4SX CS and OM Modules

The UT 4 CS Module measures the mass variation of yarns, rovings and slivers at 8mm resolution and it can determine the imperfections in yarns such as thick places, thin places and neps. However it is questionable how such yarn faults can be detected accurately with a sampling length of 8mm since some faults occur within a shorter segment.

The OM Module is furnished with two line scan CCD cameras positioned at right angles that enable imaging of two orthogonal views using coherent back-lit illumination as illustrated in Figure 2-22. The yarn diameters from two views are extracted using image processing algorithms and a mean diameter is then calculated. The sampling rate is 0.3mm. Along with the diameter and statistical diametric irregularity characteristics, OM module also gives a roundness measure for the yarns being tested. The maximum test speed on UT4 SX is 400m/min.

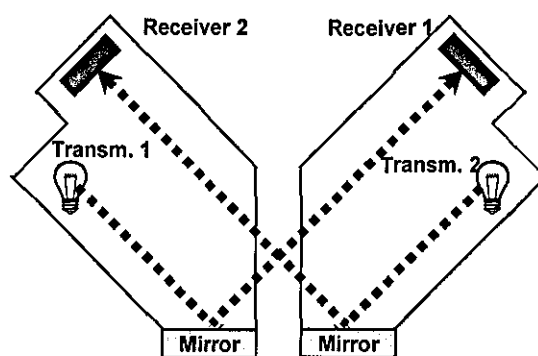


Figure 2-22 Measuring principle of UT4 OM Module (Soll [2000], p.4)

2.5.5.3 Premier Tester 7000/ Premier iQ QualiCenter

This equipment uses the same principle as Zweigle G585 to measure diametric irregularity. The main difference is that the sampling length is 1mm. The data from Premier Tester 7000 can directly be used in a dedicated fabric simulation program called CYROS.

The latest yarn testing instrument iQ QualiCenter from Premier features a nep classification module that employs an Optical light source with RGB detectors for the detection of fibre neps and trash neps. It is suggested in the company literature that the fibre neps, which are detrimental to the fabric quality, need more attention than the trash neps, which is predominantly the seed coat type since the seed coat neps eventually fall off during subsequent processes or dissolved in chemical processing.

Along with the optical determination of diameter as in Premier 7000, Premier iQ QualiCenter has another optional module that measures the mass variation of yarns and slivers using a capacitive sensor.

2.5.5.4 Lawson Hemphill Yarn Profile Tester

Lawson Hemphill developed a new yarn transport system, CTT, that is furnished with a close circuit tension control system to provide constant tension at various yarn transfer speeds. The yarn profile tester (YPT) is an optional module that can be attached to this apparatus. YPT uses a line scan CCD camera to inspect the yarn at a resolution of 2 scans/mm at 100m/min and is capable of measuring the hairiness and diameter simultaneously. The resolution can be increased to a maximum of 10 scans/mm by reducing the test speed to 20m/min. However, it is questionable how accurate the hairiness measurement would be at such a low resolution (see Section 6.6). Lawson Hemphill also introduced a so called Electronic Inspection Board program that can generate yarn board simulations using the irregularity data.

2.5.5.5 Keisokki Evenness Tester

Keisokki Evenness Tester uses a similar technology with UT4 CS Module that assesses the mass variation in a yarn.

2.5.5.6 Micro Sensor Inc. On-line Density Tester

This is a hand-held tester equipped with a capacitive sensor allowing a spot check in the production process. This instrument is reported to be incapable of detecting high frequency faults (Aminuddin and Riddle, 1999).

2.6 Use of Computer Vision for Yarn Characterisation

2.6.1 Barella-Viaplana Hairiness Meter

This instrument was developed by Barella & Viaplana [1970] to measure hairiness. In this method, the yarn is scanned perpendicular to the core axis using a TV camera. Along each scan profile, the longer-duration pulse was considered to represent the yarn core. They calculated two hairiness indices V and L as well as the yarn diameter D. The V index was found by counting the number of pulses caused by the hairs, which was claimed to represent the total hairiness. L index is the sum of the distances of these pulsing points to the core representing the index of total hair length. They also described another parameter L/V which is found to be a better measure for discriminating the nature of hairiness, that if this ratio is small the short hairs will predominate and vice versa.

Barella and Vigo [1972] found that for worsted yarns, the V index was strongly correlated with the total hairiness calculated manually by integrating the lengths of loops and protruding fibres. This correlation was slightly lower for cotton yarns (Barella and Vigo [1973]).

2.6.2 ITQT Hairiness Meter

ITQT Hairiness Meter (Barella *et. al.* [1980]) is a further developed version of B-V Hairiness Meter furnished with a 1728-pixel line scan camera. The illumination was basically a dark field set-up using incandescent lamps of tubular type as shown in Figure 2-23. To separate the hairs from the core, the system calculates two threshold values relative to the peak of the video signal obtained by comparing the original

video signal with the dark zone in the image and crest of this video signal. One interesting feature of this system is that the brightness of lamps is also adjusted according to the lowest and the highest intensities in the CCD array, to allow a video signal of constant amplitude to be obtained from any part of the yarn.

Barella [1992] found after a series of experiments carried out on ITQT, Uster and Zweigle that the V/L index from ITQT and Uster's H Index were both sensitive to short hair hairiness which could not be detected by Zweigle. No information could be found on the accuracy of the diameter measurement of ITQT tester.

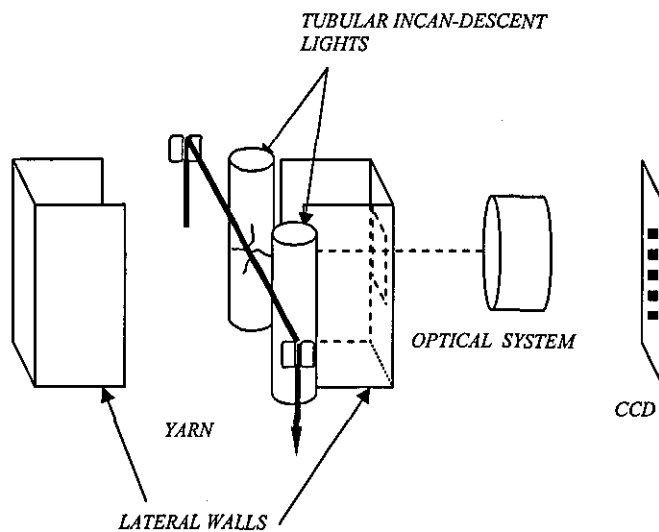


Figure 2-23 Schematic diagram of ITQT hairiness meter.

2.6.3 Yarn Image Processing System of Vas *et. al.*

Vas *et. al.* [1994] developed an image processing system to measure the twist and the diameter of yarns. The hardware was composed of a projection microscope and a 760x576 CCD camera. The optical arrangement was designed so that the yarn could

be analysed in a micro mode for measuring the local diameter of fibres, or a macro mode for yarn diameter and twist. They used back lighting for yarn diameter measurement and a hybrid of front and back lightings for twist measurement.

The image processing stage utilised a number of filters such as sobel and Laplacian for feature enhancement. To determine the core-hair boundaries they used three approaches. The first one was to take the mid way points through the slopes at the edges of the core as the core boundaries. The second method was to set a fixed threshold relative to the maximum intensity, and the third was to select the distance between two manually movable crosshairs, which could not be performed in the case of automatic inspection. For measuring the twist angles, they first applied a Laplacian filter to the image and then determined local gradients within 3x3 sub windows which were then averaged. They performed tensile tests on some yarn samples and investigated the twist and diameter changes at breakage points.

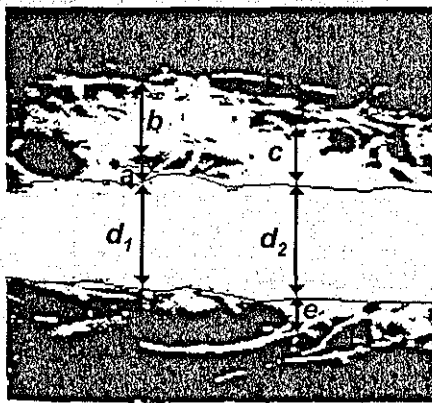
2.6.4 Cybulska's System

Cybulska [1999] described some image analysis methods to assess thickness, hairiness and twist of yarns. She used 512x512, 8 bit images of front-lit illuminated yarns representing 2.1 mm of yarn section. She introduced a new two step approach for locating the edge of the core. The first step is the same as the other methods found in the literature which is based on determination of core edges from the longest set of connected pixels for every line perpendicular to the core axis. For the second step, points generating the edge of the yarn core are assumed to be randomly distributed along some curves $f_1(x)$ and $f_2(x)$ and the edges found from the first step are corrected according to these curves. This method appears to be very interesting in that it addresses one of the problems of yarn image processing which is the definition of core-hair boundaries. Unfortunately, no detail is given on how the correction functions $f_1(x)$ and $f_2(x)$ are determined.

Cybulska defined the hairiness as the ratio between the number of yarn pixels and the number of core pixels along each line perpendicular to the core as shown in Figure

2-24. This definition of hairiness is quite similar to the “coefficient of hairiness” calculated using photoelectric methods such as in Barella [1955]. Obviously, this method only gives information on short hair hairiness due to the small field of view.

Cybulska also implemented a filtering and segmentation algorithm to calculate the twist. One of the most important features of the method is the evaluation of linear density from twist and thickness parameters. Unfortunately, no detail is given on how this is achieved.



$$w(x_1) = \frac{(a+b)}{d_1} * 100 \text{ [%]}$$

$$w(x_2) = \frac{(c+e)}{d_2} * 100 \text{ [%]}$$

Figure 2-24 Cybulska's definition of hairiness (Cybulska [1999], p.370)

2.6.5 Suh's Yarn Scanning System Attached to Lawson Hemphill CTT

Suh *et. al.* [2000] described an experimental step for measuring yarn mass (every 8mm) with a capacitive sensor and yarn diameter (every 1mm) with an optical sensor (1024-pixel, 12-bit line scan camera) simultaneously. To define the diameter, the maximum, minimum and average $((\text{max.} + \text{min.})/2)$ values of 1024-pixel line-scan CCD array are calculated and starting from the 0th pixel, the pixel falling between the value of average ± 130 ($\%3$ of $4096=12\text{bit}$) is considered as the bottom of the yarn. By continuing to scan the array, the next pixel in the same range is considered as the top of the yarn and the difference between top and the bottom is considered as yarn diameter.

They studied a wavelet data compression algorithm, which could compress the data down to 4%. They also created knitted fabric simulations using the mass and diameter data and showed that the appearances of fabrics based on one of the mass, diameter, density or inverse density information were different from each other. However they did not propose a suitable irregularity measure to be used for design purposes. One of the advantages of this system could be that the mass and diameter information together could lead to estimation of the twist.

2.6.6 Estimation of Density Using Laser Transmission

A paper of particular interest by Riddle & Davis [2000] focuses on obtaining laser transmission values to measure densities and density variations of cotton yarns. They used a 2048-pixel colour line scan camera. The magnification was 14.9 leading to a yarn section of 1.7mm. The source of light used to form a yarn density profile was a 20mW, 633nm laser. By subtracting the image from the reference image obtained with no yarn present in the scene, the yarn region was obtained. They assumed that the natural logarithm of the ratio of beam intensities (the ratio of the intensity of the beam with no yarn present [I_0] to the intensity of the beam with yarn present [I]) divided by the thickness of the material provided a function proportional to the transverse density across a thin cross section of the fibre-yarn. They provided the ratio between the linear density and the square of the diameter as a measure of the stability of the packing fraction, as they are proportional to each other. The density profiles they obtained were in agreement with the ones Langenhove found in a series of papers (Langenhove [1997a, 1997b, 1997c]) to simulate the mechanical properties of a yarn based on the properties and arrangement of its fibres. This data was used as a source of irregularity measure for a fabric simulation program.

The laser transmission is also used by Militky et.al. [1999] for characterisation of fabric porosity. They acquired fabric images under a microscope using a 752x524 CCD camera. They defined a relative porosity parameter PL as the area of white objects in the thresholded and inverted fabric images divided by the whole area of

the image. The results gave good correlation (84%) between the PL parameter and the air permeability of the fabrics.

Some possible problems in using the light transmission for textiles are examined by Taylor [1999]. He developed a fibre optic sensor to measure the mass of optically thin cotton samples by integrating light transmission and reflectance signals. He used near infrared light due to the strong absorption band of cellulose (the basic compound in cotton). He studied the effect of air gaps within the fibre bundle on light transmission and found that changes in light transmission, due to an air gap, were more severe for thick fibre bundles. For example: a 10% air gap gave a 6.55% reduction in the observed absorbance for a specimen transmitting 40% while the same gap in a specimen transmitting at 60% gave a 3.31% absorbance error. He also investigated the effect of bulk thickness on light transmissivity. He found a change in transmissivity with increased tension on the yarn. He explained the result that there was a change in light transmissivity relative to the increased tension although there was no change in the mass, with the changes in the secondary scattered light, which is re-scattering of the scattered light back to the detector.

2.6.7 Millman's LYSS

Millman [2000] developed a computer vision system for yarn quality inspection named LYSS, which employed a dedicated yarn transport mechanism and a 1024-pixel line scan camera. In his work, he addressed the major optical and electronic limitations in yarn imaging with particular emphasis on misfocus aberration. He came up with the idea of using glass guide plates to force the hairs within a tolerable depth to minimize the effects of defocusing.

Millman tested and compared various illumination techniques including coherent and incoherent back-lit, front-lit, dark field and coherent spatial filtering methods for yarn imaging using an area scan camera. He found coherent back-lit illumination to be superior in contrast but on the contrary, quite sensitive to fringe formation which degraded the images. Furthermore, this type of illumination did not cooperate well

with the glass guide plates creating significant fringes in the background (Figure 2-25). For incoherent back lighting, he used a field lens focusing a tungsten filament light source onto the aperture of the camera lens. Owing to its practicality and adequate image quality, he employed this set-up as the major illumination arrangement on LYSS.

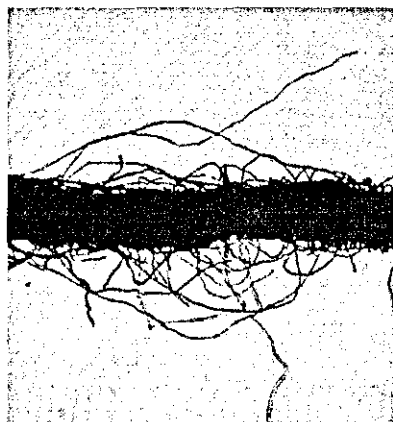


Figure 2-25 Coherent back-lit yarn image Note the fringe patterns on the background arising from the glass plates. (Millman [2000], p. 142)

Millman designed a series of spatial filter masks for real-time spatial filtering using coherent light. One of the major problems he encountered when using this technique was the varying thickness or refractive index across the glass plates causing phase distortions hence producing distortions in the image. Some of the images from his work obtained by using different spot sizes are shown in Figure 2-26. He commented that the distinction of surface fibres and the core using this method was very good which could be used for measuring the overall hairiness as in Uster Tester 3. However, the effect of high pass filtering on the core edges causing an artificial increase in the brightness, which is also addressed in Keisokki's sales literature [1997] is inherent in these images. Furthermore, there would probably be a need for using different masks for different fibre and yarn characteristics.

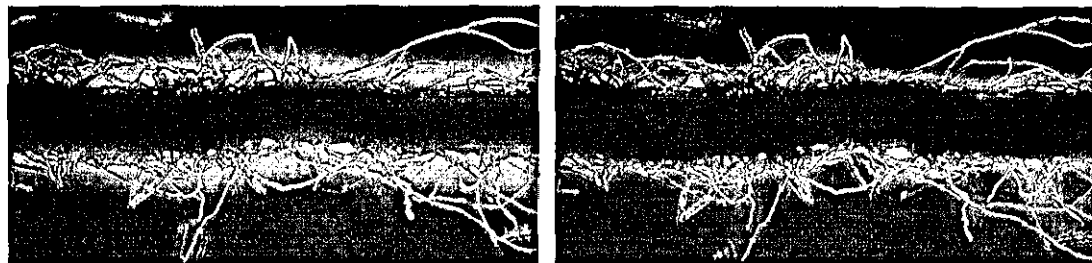


Figure 2-26 Spatially filtered yarn images with stop sizes 0.2mm and 0.6 mm
(Millman [2000], p.152)

Millman utilised a number of image enhancement techniques for back-lit yarn images, such as flat field correction and Laplacian high pass filters. He defined an automatic threshold level at one third between the maximum and minimum intensities in the images. The core-hair separation was carried out simply by identifying the longest connected yarn pixels at each scan line as the core.

For hairiness measurement, he developed a new index, called "M index" which represents the integrated shadows from hair profiles and is given in units of grey levels per line. He stated that the peripheral fibres far from the core had shallower shadow depressions in the line light profile, due to yarn motion and fibre vibration and by thresholding, the hair was converted into pixels disregarding the fibre diameter and the fact that fibre may not have completely occupied the line it is detected on, but the grey levels reflected this information. He also simulated the V and L indices developed by Barella [1970]. He found a reasonable correlation between the UT3 and the V index (0.855). However, there was an offset whereby the UT3 appeared to have a hairiness value when there was no V index. The correlation between the M index and the UT3 H index was not as quite good as for the V index (0.6826), however with much less offset compared with V index. He also found that hairiness measurement through one or two sides of the yarn gave strongly related results, but double sided index having smaller CV%. Millman also gave an NL index to simulate the Zweigle G565 instrument (L index) which is calculated by multiplying the quantities from differential count (the number of hairs intersecting a particular boundary subtracted from those of the boundary adjacent to it nearer the

core) by their respective distances. The correlation between NL measured on LYSS and the V index was fairly strong (0.9309), which is related to the reason that they both measured overall hairiness and were obtained from the same yarn samples. Although he did not correlate his N and L values with Zweigle G565 or a similar tester, his N values could be expected to be much higher than the Zweigle G565 would exhibit. This is because Millman did not take the sensor resolutions of these testers into account and simply calculated the number of hair intersections along columns in the images at certain distances from the core. This point is more fully discussed in Chapter 6.

Millman also compared the results of diameter and irregularity measurements with the Uster Tester 3 evenness tester and the Zweigle G580. He found a very good correlation between yarn counts and his diameter measurements (with 0.9754 power regression coefficient). The diameter measurements from LYSS and Zweigle G580 also agreed almost perfectly ($R^2=0.9981$ linear regression) however, G580 exhibited around 20% smaller values. Furthermore the LYSS CV%*s* did not correlate well neither with Zweigle G580 nor with UT3 exhibiting values lower than each. He stated that the reason for LYSS having lower CV%*s* than the Zweigle G580 could be due to the presence of dense surface fibres being identified as part of the core on G580 increasing the diameter variation. However, this statement appears to be in contradiction with LYSS diameters being higher than the Zweigle G580. Furthermore, Millman calculated the CV%*s* for a 1mm sampling length whereas the G580 uses 2mm, which means that the CV% values from LYSS would be even smaller if a 2mm sampling length were used.

Millman also demonstrated a frequency domain analysis method for yarn twist measurement. He obtained the fourier transform of high magnification front-lit yarn images and applied an annulus mask in order to remove high and low frequencies. The outer radius of the mask was taken to the edge of the transform, while the inner radius was a couple of pixels wide. However, Millman pointed out the need for optimising these diameters more systematically. He then integrated the values in the

transform over thin sectors 0.01 radians in angular width. The sector having the highest integration was associated with the twist angle. The algorithm was not verified against the actual twist values of yarns, rather, the twists of a number of samples attached on a rotating linear slide were calculated at different stages as some known amount of twist was released from the samples by untwisting. The decrease in twist was clearly seen but not in good agreement with the amount of twists released. It would probably be more convenient to verify the algorithm against the actual number of twists in yarn since in his method as the yarn is untwisted the twist propagation cannot be expected to be uniform resulting in proportional decrease in twist at different sections of yarn.

2.6.8 Other Relevant Work

Alagha et.al. [1994] used image analysis techniques to assess the structural parameters of friction spun yarns. They adopted a tracer fibre technique to quantify features such as yarn and helix diameter, fibre migration, fibre angle and twist distribution within the yarn.

King and Allen [1994] described high speed photographic techniques to investigate texturing process for synthetic yarns and formation process for staple yarns. They addressed the limitations in object speed arising from the allowable minimum exposure times of cameras and photographic films. They investigated various illumination sources and found pulsed copper-vapour laser illumination to be very effective for high speed imaging.

Neckar and Voborova [2003] developed an elegant method to describe hairiness using image analysis techniques. In this method, they obtained a frequency profile of black pixels (that belong to core and hairs) perpendicular to the core axis by integrating the columns of around 800 images from different sections of a yarn. Based on this profile, they calculated some statistical parameters describing total hairiness, internal structure of hairiness region as well as the yarn diameter. They also defined two different total hairiness functions one related with comfort

properties and the other with the tendency of hairs to break off the main body during production stages. They found a very good correlation with their total hairiness index and Uster Tester's H index. A similar method is also developed during this research to obtain so called "hair density distribution profiles" as described in Chapter 5.

Pourdeyhimi et. al. described a number of image processing methods to measure the fiber orientation distribution in nonwovens which are considered to be relevant with yarn twist measurement here. They first developed a simulation program [Pourdeyhimi et.al., 1996] that can generate nonwoven images with fibres of certain diameter distributed at a given mean orientation angle and a standard deviation. One of the techniques they implemented to measure the fibre orientation was a direct tracking algorithm [Pourdeyhimi & Dent, 1996] which was composed of thresholding, thinning and a rule based tracking steps. A similar algorithm is also implemented during this research for twist measurement as described in Chapter 8. Another method was to analyse the images in frequency domain [Pourdeyhimi et.al., 1997]. This involved measurement of orientations by scanning the Fourier Transform of the images radially within an annulus at the centre of the image with a certain width and with a certain radius. They pointed that the dimensions of the annulus mask effected the measurements, and the method could be influenced from varying fibre widths. They also applied windowing functions to the original images to rid of the zero frequencies. Pourdeyhimi and Dent [1997] also tested flow field analysis methods on nonwoven images. This was based on using a gradient edge operator within small windows to determine the orientations of local textures. Among all the methods they found tracking method to be the most accurate both on simulated and real images [Pourdeyhimi et.al., 1999]. In a recent publication Pourdeyhimi & Kim [2002] compared a method based on Hough Transformation with the Fourier Transformation method and found the latter to be more reliable.

Huang and Xu [2002] presented image analysis techniques to evaluate dimensional properties of cotton fibre. They applied an adaptive thresholding method based on the histogram, which they claimed prevented the unfocused fibres to appear wider in

the thresholded image. This was because under a defocusing condition the background appeared darker leading a higher threshold value which favoured the background pixels upon thresholding. However, it is not quite clear why the background was darker under defocusing. They implemented numerous techniques such as edge tracing and transverse scanning in order to determine the width and length of the fibres. The techniques are interesting because they simply work on thresholded images not requiring a thinning procedure for example.

Ikiz [2000] used image analysis techniques to measure the lengths of fibres. He found back-lit illumination advantageous compared to front lit illumination. He implemented various thinning algorithms and addressed the problems in determining the contour lengths arising from digitisation.

2.7 Conclusions

For assessment of hairiness and irregularity, many methods have been developed within the last 50 years. However, only a few of them survived to date. In 1990's an ongoing trend can be seen in the application of computer vision techniques for yarn characterisation, which resulted in usage of CCD cameras in two well known commercial testers (Uster Tester 4 and Lawson Hemphill).

Nowadays, only two conventional methods are commonly accepted to evaluate hairiness, which are the Total Hairiness Index as in Uster Tester and the measurement of number of hairs at certain distances from the core as in Zweigle G566 and Shirley YHM. However, these methods describe different characteristics and do not correlate well with each other. Computer vision makes its appeal especially from this point of view providing possibilities not only to simulate these testers but also to develop new indices for describing hairiness in other possible ways.

Optical and capacitive methods to measure irregularity have different applications and one cannot be considered completely advantageous over another. It is quite clear

that computer vision techniques can only provide irregularity measurement based on the variation of diameter. However, there is a possibility of estimating the mass variation using twist and diameter information that can both be measured optically. It would be worth studying these relations to estimate linear density by measuring twist and diameter using computer vision. The measurement of yarn density using laser transmission suggested by Riddle and Davis is also quite interesting in this respect. If a density measure can be obtained along with the diameter, the twist could possibly be estimated from these two.

Numerous researchers working on computer vision techniques for diameter and hairiness measurement use one dimensional data rather than two dimensional images. However, the latter case would probably allow a better definition of core hair boundaries. There is also a lack of research on the effect of image aspect ratio on the measurements. Such an investigation would serve to establish a theory on speed limitations when using computer vision for yarn characterisation.

The boundary between the core and the hairs is still ambiguous. Many researchers defined the core as the longest connected set of pixels along the lines perpendicular to the core axis. This approach would bring about an increase in diameter due to the surface fibres. Consequently, the diametric variation would also be altered. Therefore, an improved method for determination of core hair boundaries needs to be developed.

CHAPTER 3 - LYSS Hardware and Software Components

3.1 Introduction

Following the tradition on the yarn scanning research at Loughborough University, the vision system studied during this research is called as Loughborough Yarn Scanning System (LYSS). This Chapter describes the hardware and software components of LYSS. Section 3.2 gives technical details about the mechanical and electronic parts of yarn transportation and image acquisition set-up. The image processing algorithms are implemented using a commercial software package called "Wit", which is briefly explained in Section 3.3 along with the Wit Definition Language that allows creation of custom C function libraries that work within Wit environment. Section 3.4 describes a number of applications programmed using Visual Basic 6 (VB6) and VB for Office Applications to carry out various optical design and analysis work.

3.2 Yarn Transport and Image Acquisition

In LYSS, a servo motor attached to a gear box with a gear ratio of 50:1 is employed for yarn transport. The yarn is unwound from the package and transferred through ceramic pins, a tensioning mechanism and two rubber-coated rollers with 60mm diameter as illustrated in Figure 3-1. The tensioning mechanism is similar to those used in sewing machines and the level of tension is adjusted manually. This level is selected so that the yarn vibration is avoided during the transport and no slippage occurs at the transfer rollers.

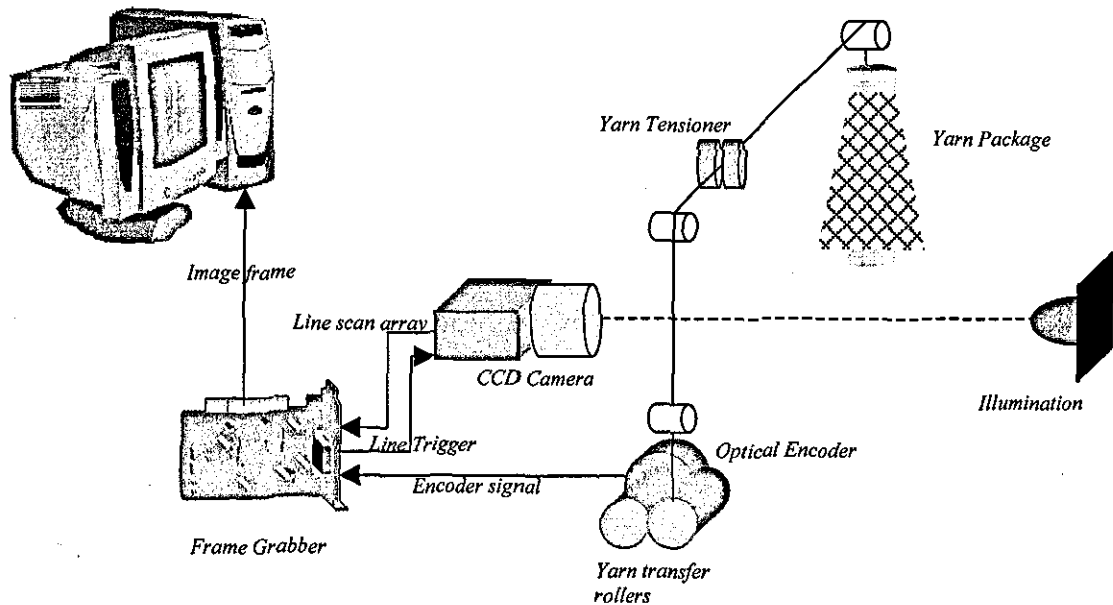


Figure 3-1 LYSS Hardware

A three channel optical incremental encoder module is used to give speed feedback and to control image trigger. The number of holes on the code wheel is 1024 which provides a resolution of 2μ at the surface of the transfer rollers. The CCD line scan camera is a Dalsa Spyder SP-14-02K40 that has a 2048×1 -pixel CCD array and gives an 8-bit output at a maximum line rate of 18.7 KHz. The pixel pitch is $14\mu \times 14\mu$ and the fill factor is 100%. The camera is accompanied with an F-mount 100mm Cosina close up lens that can provide a variable zoom of up to 1:1 magnification with the close up attachment.

Image acquisition is performed through a Viper Digital frame grabber. The line scanning rate can either be set at a constant frequency or synchronised with a 5V differential signal from the encoder. The exposure time of the camera can be set manually or automatically using a number of options based on the durations between falling and rising edges of the differential encoder signal.

3.3 Image Processing Environment

Wit image processing software provides a graphical user interface that incorporates various image processing and basic logical and arithmetic functions. These functions can be called at the user level using graphical Wit operators, which, just like functions, have certain types of inputs and outputs. Various operators are interconnected with each other to build up an algorithm called an “igraph” in Wit terminology. Figure 3-2 shows the Wit design interface and an igraph developed to acquire and process yarn images in real time.

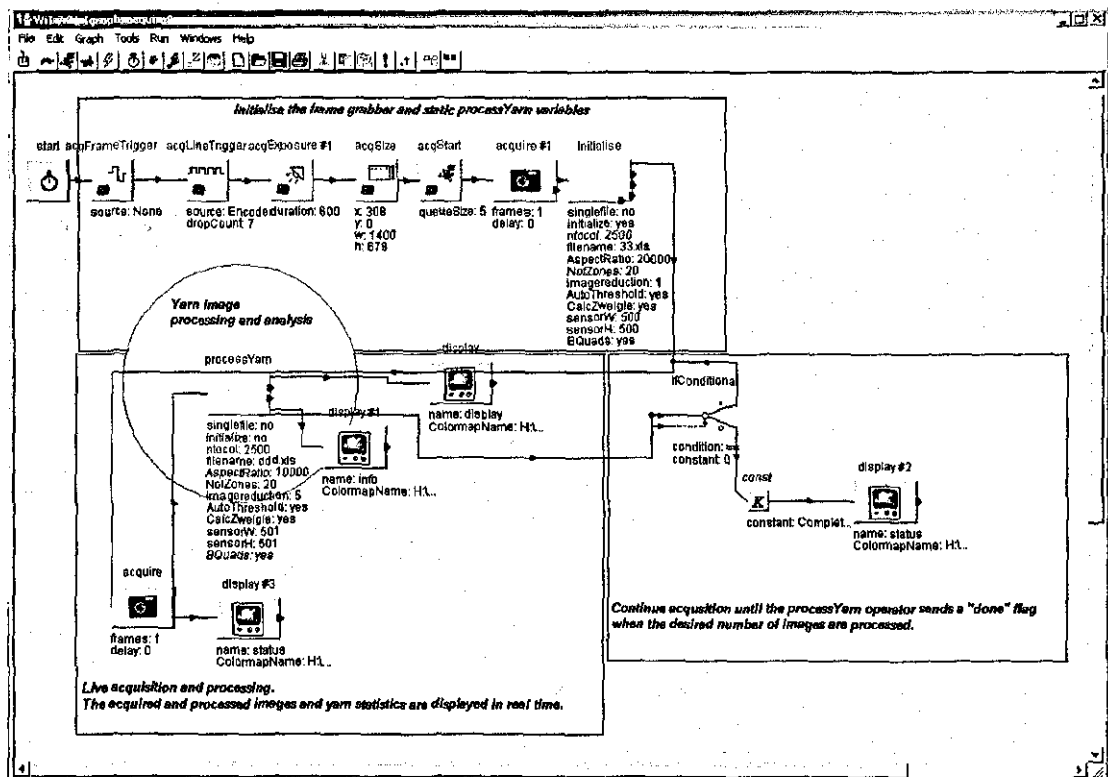


Figure 3-2 Wit user interface

Custom function libraries can be designed using C language and incorporated into Wit environment. To do this, the inputs and outputs of custom functions are first defined using Wit definition language and then the body of the function is written in C and compiled as a Dynamic Link Library (DLL). These functions can then be accessed from Wit just like standard operators. The “processYarn” operator in Figure

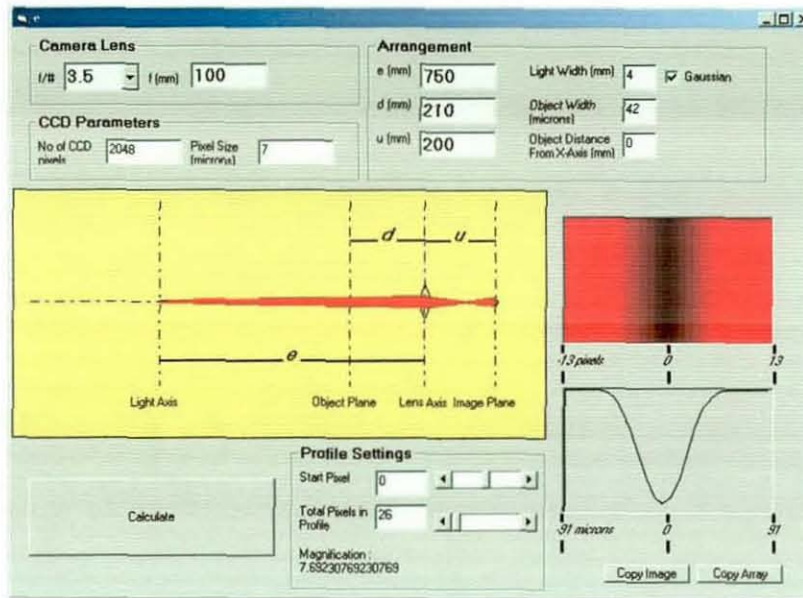


Figure 3-4 Back-lit Illumination Analysis Program interface

3.4.2 Dark-Field Illumination Intensity Profile Analysis Program

This program has extensively been used when designing the dark field arrangement discussed in Section 5.2.3. The sizes of the LED array and the field aperture as well as the relative arrangements of the light source, field aperture, yarn and the camera are optimised to ensure that minimum amount of light reaches to the camera to avoid glare and there is a uniform intensity distribution at the yarn plane within the field of view. The LED light sources are assumed to emit a light beam with a Gaussian profile and 10^0 divergence and again the ray tracing approach is adopted. The program interface is shown in Figure 3-5.

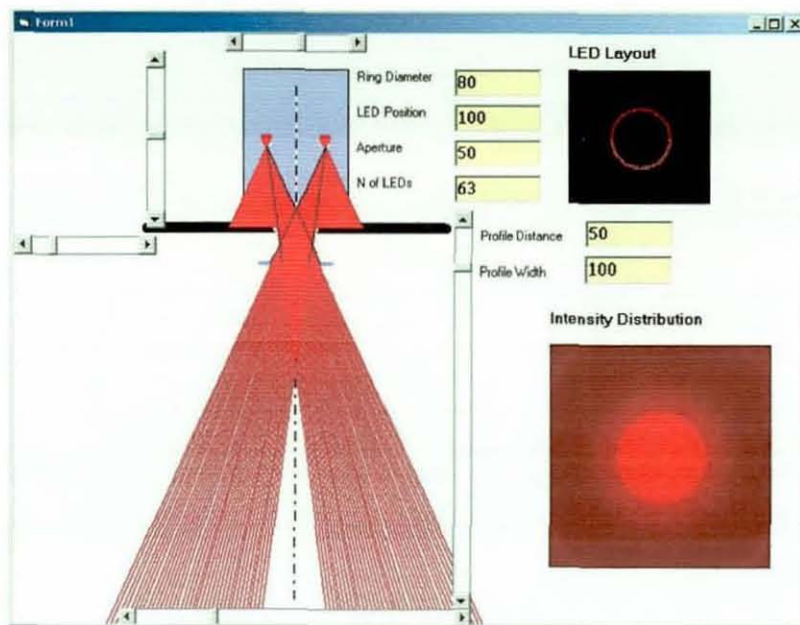


Figure 3-5 Dark-Field Illumination Intensity Profile Analysis Program interface

3.4.3 Front-lit Illumination Defocus Profile Analysis Program

This program is composed of a number of macros that run under Microsoft Excel. It generates the ideal profile and the spectrum of a fibre and calculates the Optical Transfer Functions (OTF) under given conditions using Hopkins' formula (Hopkins, 1955). The OTFs based on the geometrical optics are also calculated for comparison. The program can apply OTFs to the object spectrum and generate the defocus profile of a fibre with a given width and at a given defocusing distance. The built-in Excel functions are used to calculate the Bessel Functions and the Analysis Toolpack is used to perform Fourier Transformations. This program has served as the main tool in front-lit illumination analysis discussed in Chapter 4.

CHAPTER 4 - Analysis of Factors Affecting Yarn Image Quality

4.1 Introduction

Image formation involves the projection of points in 3D world to points in a 2D image plane. In this process, either the object is illuminated by a source of radiant energy or the object is itself a source of radiant energy. The radiant energy reflected, transmitted, or emitted by the object propagates through space. An image formation system intercepts the propagating radiant energy and transforms it in such a manner that an image is formed in the image plane. It is evident that the shape of the object and natures of both the radiant energy from the object and the image formation system will both play role on the characteristics of the image formed.

For the computer vision application in this research, the object of interest is a yarn that is made up of a main body composed of low spatial frequencies and hairs protruding from this body that possess relatively higher frequencies. The illumination is within the range from ultraviolet to infrared of the electromagnetic spectrum and is emitted from a light source. The image formation system is composed of a CCD sensor sensitive within this spectrum and an optical system that is capable of mapping the radiant flux from the object onto the sensor.

Ideally, if the yarn is described by a function $G(x,y,z)$ the corresponding image should be $m.G(x,y)$, where m is a constant scaling factor. However, due to aberrations arising from the image formation system, the image departs from ideal often blurring and being distorted. In this Chapter, the image formation process is studied

theoretically and factors playing a role in this process are investigated addressing various aberrations and their effects on image quality.

In the first section to follow (4.2), basic definitions are given regarding the optical image formation process to provide a background for the discussions throughout the chapter. Section 4.3 deals with the diffraction phenomena that is associated with the wave nature of the light. The factors affecting the image quality under front-lit illumination including the wavelength of the light source and the aperture are discussed in Section 4.4. The defocus aberration, probably being the most significant problem in front-lit illumination, is investigated in Section 4.5. All the analyses in Sections 4.3 through 4.5 are performed using a custom Visual Basic program and Excel Data Analysis Pack.

It is evident that there is a major difference between front-lit and back-lit illuminations, since the object is the yarn in the former case while it is the light source in the latter case. For this reason back-lit illumination is studied separately in Section 4.6. The effects of the characteristics and arrangement of the light source are investigated based on a mathematical model of diffraction of the light due to obscuring fibres.

Other possible aberrations arising from the lens and the alteration of the image due to the digitisation process are covered in Sections 4.7 and 4.8. The final section (4.9) gives a comparison of front-lit and back-lit illuminations in terms of the maximum resolutions that can be achieved and the defocus tolerances based on the theoretical models. The analysis in Sections 4.6 through 4.8 are carried out using custom C functions.

4.2 Image Formation Basics and Definitions

Lens systems used with cameras include many elements such as field, glare and cold stops, baffles and generally a combination of lenses. However, it is a common

practise to consider a lens system as a single lens and an aperture stop combination as shown in Figure 4-1. Following this, an imaging system is often described with a single focal length f , and a value known as the f-number (F or $F\#$), which is related to the aperture size D as follows;

$$F = \frac{f}{D} \quad (4.1)$$

Numerical Aperture NA that is related to the cone of light passing through the lens is given by;

$$NA = \sin U = \frac{D}{2f} = \frac{1}{2F} \quad (4.2)$$

An extended object is often regarded as an array of point sources and the location and size of the image formed by a given optical system can be determined by locating respective images of the sources making up the object (Smith [2000], p.21). The position of the image of an object formed by a "perfect lens" can be found using the lens formula as follows:

$$\frac{1}{f} = \frac{1}{s_o} + \frac{1}{s_i} \quad (4.3)$$

or using Newton's image equation given as;

$$x_i = \frac{f^2}{x_o} \quad (4.4)$$

The lateral (or inverse) magnification m of an optical system is given by the ratio of image size to object size, i.e.;

$$m = \frac{h_i}{h_o} = \frac{s_i}{s_o} \quad (4.5)$$

Effective f-number and Numerical Aperture that account for magnification are defined as follows;

$$F_{eff} = \frac{s_i}{D}, \quad N_{eff} = \sin U_i = \frac{D}{2s_i} = \frac{1}{2F_{eff}} \quad (4.6)$$

Since the image of an object is not always formed on plane of the screen, following two variables will also be used throughout the chapter for a more general definition;

s_s : The distance of the screen from the lens

s_e : The distance between lens and the plane where the object is in focus

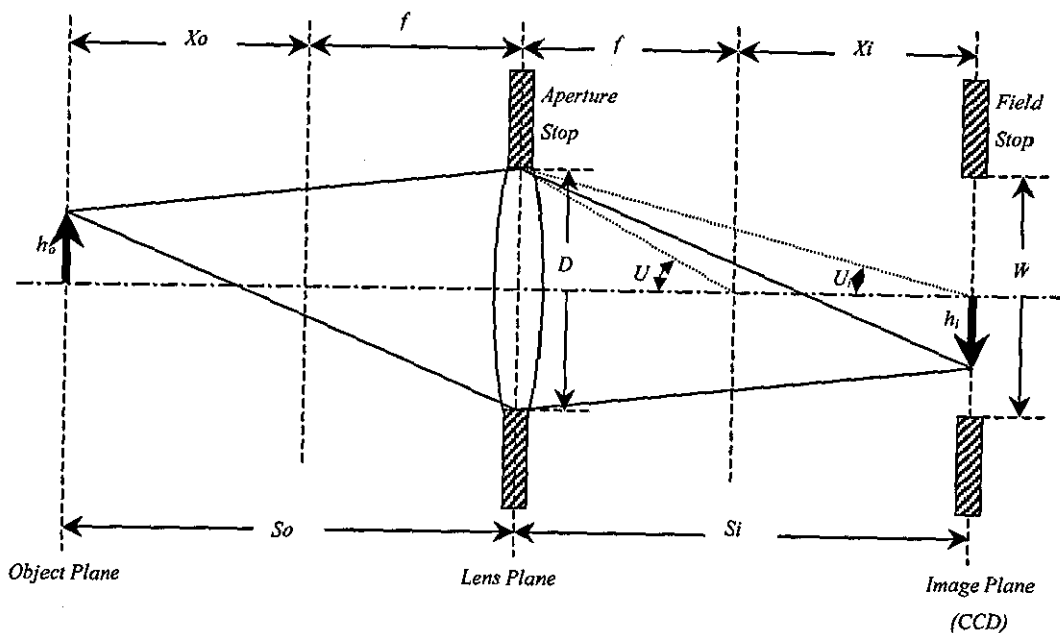


Figure 4-1 Image Formation Geometry

4.3 Diffraction Effect of the Aperture

Since the light travels in wave motion rather than in straight lines, no lens can form a true point image. This is due to the fact that waves “bend” around corners of the aperture to a small but finite degree, which is described with a phenomenon known as “diffraction”. Due to diffraction and other possible aberrations, the image of a point on the object plane located at (x,y) will turn out to be a blur spot over a finite area centred at (X,Y) as depicted in Figure 4-2. This spot is generally described by a function $h(X,Y; x,y)$ known as the **point spread function** and the intensity distribution on the image plane $g_2(X,Y)$ can be found by adding up the contributions from all points on the object, i.e.;

$$g_2(X,Y) = \iint_{-\infty}^{\infty} g_1(x,y)h(X,Y; x,y)dx dy \quad (4.7)$$

Where $g_1(x,y)$ is the intensity distribution on the object plane.

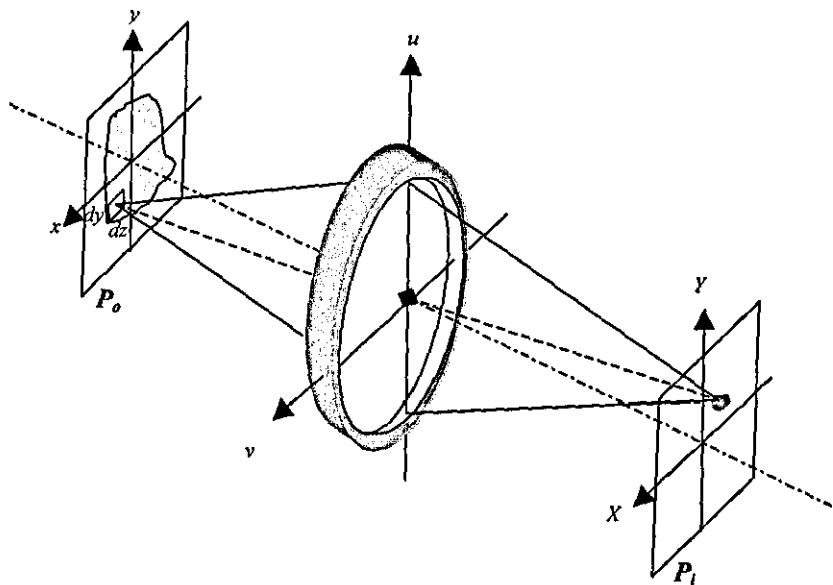


Figure 4-2 Geometry of Point Spread Function

Using *reduced coordinates* x', y' in the object space (Goodman [1996, p130]) and the geometrical optics prediction image g_g , which are defined by;

$$\begin{aligned} x' &= mx, & y' &= my \\ g_g &= \frac{1}{|m|} g_o \left(\frac{x}{m}, \frac{y}{m} \right) \end{aligned} \quad (4.8)$$

And assuming that the point spread function remains the same for all points on the object (space invariance), equation 4.7 can be written as a convolution integral as follows;

$$\begin{aligned} g_2(X, Y) &= \int_{-\infty}^{\infty} \int_{-\infty}^{\infty} g_g(x', y') h(X-x, Y-y) dx' dy \\ \text{or} & \\ g_2 &= h * g_g \end{aligned} \quad (4.9)$$

Which means that the image in a diffraction limited system can be found by convolving the geometrically estimated image with the point spread function.

In the case of coherent light, since the phase is not changed through the system, one has to deal with a spread function that corresponds to the field amplitude of the object, which is called the **amplitude spread function** (Hecht, [2002], p. 532).

Using convolution theorem, which tells that the convolution of two functions equals the inverse Fourier Transform (FT) of the multiplication of the FTs of two functions, eq. (4.9) can be rewritten as

$$G_2 = G_g . H \quad (4.10)$$

Where G_g , G_2 and H are the Fourier Transforms of g_g , g_2 and h respectively. H is referred to as the frequency response of the optical system and known as **Optical**

Transfer Function or **OTF** for short. For coherent light, the frequency response of the system is described by **Amplitude Transfer Function (ATF)**. In optical analysis the form of equation (4.10) is used rather than equation (4.9), hence the frequency content G_g is generally of interest rather than g_g .

The ATF of a diffraction limited system is the pupil function $P(u, v)$ scaled by λs_i and the autocorrelation of ATF for incoherent illumination (Goodmans, p134-137) as depicted in Figure 4-3, where f_0 corresponds to the cut-off frequency given as

$$f_0 = \frac{D}{2\lambda s_i} = \frac{1}{2F_{eff}} \quad (4.11)$$

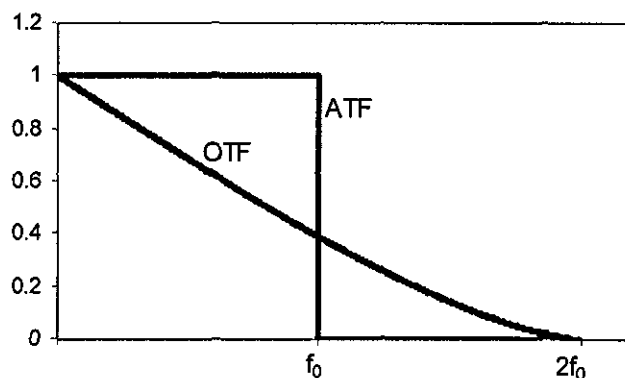


Figure 4-3 Optical and Amplitude Transfer Functions

In calculations, the object (g_o) and the geometric image (g_g) functions of a fibre having a diameter of w_f will be defined using a rectangle function as follows;

$$g_o = \text{rect}\left(\frac{x}{w_f}\right) \quad \text{and} \quad g_g = \text{rect}\left(\frac{X}{m.w_f}\right) \quad (4.12)$$

where

$$\text{rect}\left(\frac{x}{b}\right) = \begin{cases} 1 & |x/b| < \frac{1}{2} \\ \frac{1}{2} & |x/b| = \frac{1}{2} \\ 0 & \text{otherwise} \end{cases} \quad (4.13)$$

The frequency spectrum then becomes;

$$G_g(f_x) = \text{sinc}\left(\frac{f_x}{m.w_f}\right) \quad \text{where} \quad \text{sinc}(x) = \frac{\sin 2\pi x}{2\pi x} \quad (4.14)$$

The geometrical image profile of a 45 μ fibre and its frequency spectrum are depicted in Figure 4-4.

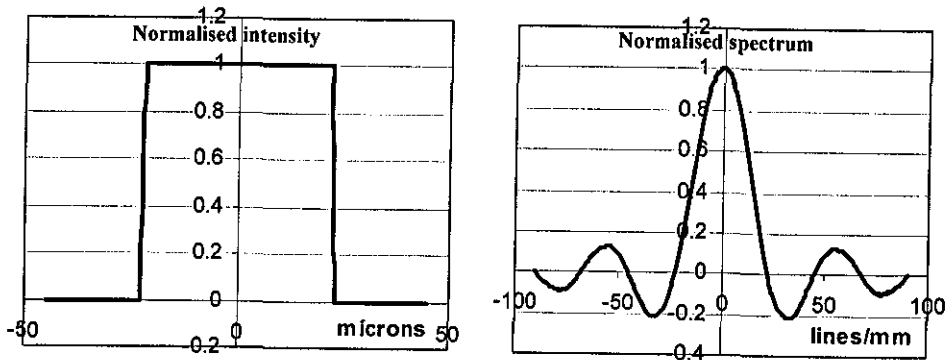


Figure 4-4 Left: The geometric image profile g_g of a 45 μ m fibre at 1:1 magnification; Right: The FT of g_g (G_g)

The pupil function $P(u,v)$ for a circular aperture is defined using circular coordinates with a circ function as follows;

$$P(r) = \text{circ}\left(\frac{2r}{D}\right) \quad (4.15)$$

where $r = \sqrt{(u^2 + v^2)}$

If the illumination is coherent then the transfer function is defined as;

$$H(\rho) = \text{circ}\left(\frac{2\lambda s_i \rho}{D}\right) \quad (4.16)$$

where $\rho = \sqrt{f_u^2 + f_v^2}$.

And under incoherent illumination, the transfer function will be the autocorrelation of (4.16), which is;

$$H(\rho) = \left\{ \begin{array}{l} \frac{2}{\pi} \left[\arccos\left(\frac{\rho}{2\rho_0}\right) - \frac{\rho}{2\rho_0} \sqrt{1 - \left(\frac{\rho}{2\rho_0}\right)^2} \right] \quad \rho \leq \rho_0 \\ 0 \quad \text{otherwise} \end{array} \right\} \quad (4.17)$$

The image profile g_2 can be obtained by taking the inverse FT of G_2 which is simply found by multiplying G_g and H . Figure 4-5 and Figure 4-6 show the image spectra for coherent and incoherent illuminations respectively, calculated for a 45μ fibre imaged with an f100/8 lens at unit magnification. The image profiles for coherent and incoherent illuminations are shown in Figure 4-7. It can be seen that the edges appear sharper in coherent case, which suggest that coherent imaging gives a better contrast. However, the location of the edge is easier to determine in incoherent case, simply by taking the half point between the maximum and the minimum on the slope that corresponds to the edge. In order to make a judgement between the coherent and incoherent illuminations, the required frequency and the contrast should both be taken into account. It can be said that incoherent illumination passes higher

frequencies, but with reducing amplitudes for increasing frequencies. A more detailed comparison of two illuminations can be found in Goodman [1996, p.154].

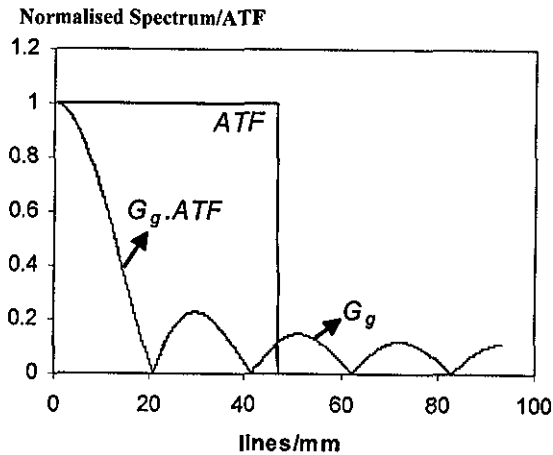


Figure 4-5 Normalised spectrum of a 45 µm Fibre and effect of ATF

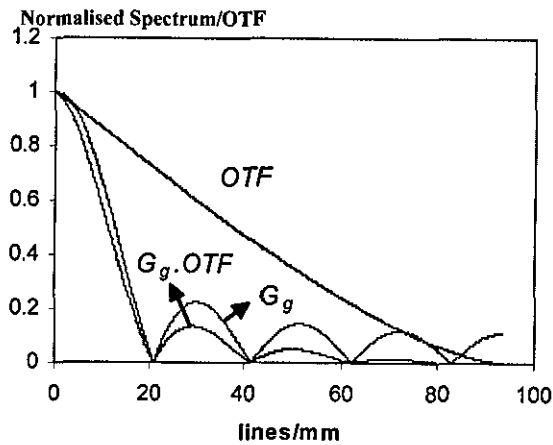


Figure 4-6 Normalised spectrum of a 45 µm fibre and effect of OTF

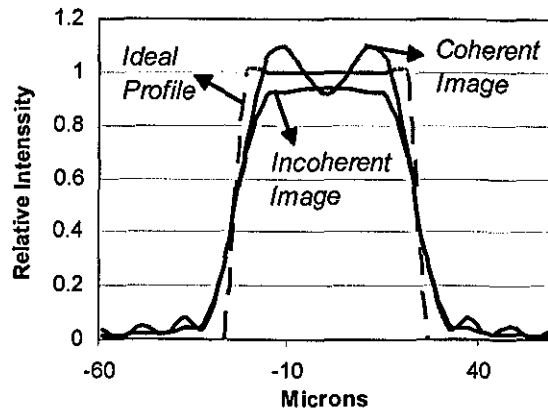


Figure 4-7 Image Profiles of a 45 μ m fibre in incoherent and coherent cases

4.4 Factors affecting yarn image quality

A typical yarn consists of a core and relatively much thinner hairs protruding from it. The diameters of textile fibres vary from 5 μ m for synthetic fibres to 80 μ m for wool fibres. Figure 4-8 shows the frequency spectrum for a 0.3mm yarn core. In Figure 4-9 the spectra of 14 and 26 μ m fibres are shown. It can be seen that the core region of the yarn mainly consists of low frequencies, and for decreasing diameters higher frequencies tend to dominate an important region of the spectrum. Therefore, the frequency response of the optical system has an important effect on the image quality especially that of the hairs, since as the object gets thinner, the transfer function attenuates the object spectrum more severely resulting in blurring of the image.

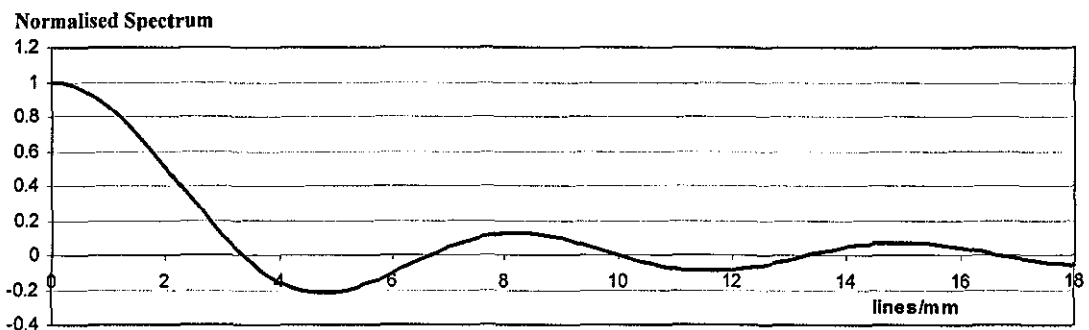


Figure 4-8 Normalised frequency spectrum for a 0.3mm yarn core

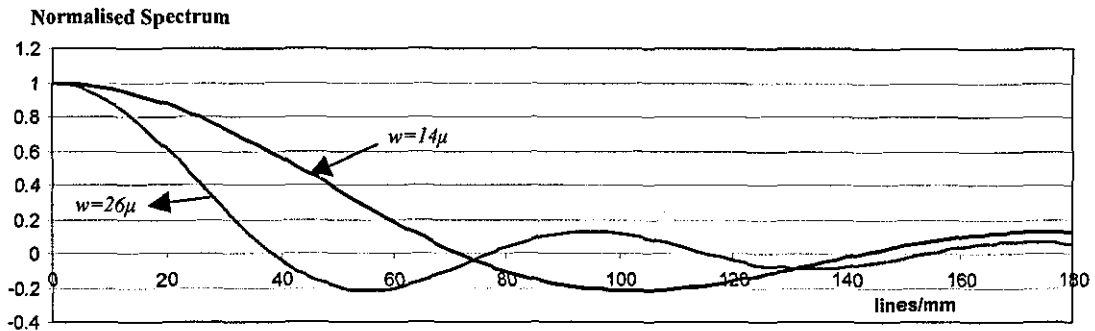


Figure 4-9 Normalised frequency spectra for 14µm and 26µm fibres (Note that both spectra are normalised using different scales since the powers are different)

The resolution requirements for a yarn imaging system depend on the purpose of the application. For yarn surface inspection for example, in order to resolve the surface fibres and the rims, high frequencies gain importance and even a moderate low pass filter effect can be undesirable. For diameter measurement however, the problem is less important. For hairiness measurement, the aim is often to be able to detect the hairs and the diffraction effect of the aperture is generally not important in this sense, however diffraction noticeably affects the capability to resolve the gaps between separate hairs and those between hairs and the core. The latter is especially important for accurate definition of hair core boundaries.

From eq. (4.11), it can be seen that the cut-off frequency is inversely proportional with the wavelength of the light source. Therefore, in order to improve the frequency response, this wavelength should be kept as low as possible. However there is a limit to how small the wavelength can be since the CCD sensors only work for a specific bandwidth of light. The responsivity of the CCD sensor used in this research reaches its maximum between 690 and 700nm as can be seen from Figure 4-10 (Dalsa Spyder Manual) and it drops to less than half the maximum for 400nm. Nevertheless, it is possible to purchase CCD cameras sensitive in the near UV region of the visible spectrum.

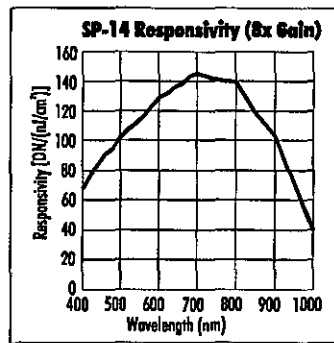


Figure 4-10 Responsivity of the CCD sensor used in the experiments

The reflectance properties of textile fibres also play an important role in determining the suitable wavelength for illumination. Figure 4-11 shows typical reflectance spectra within the visible spectrum for raw cotton fibres. It can be seen that cotton exhibits a strong absorption for wavelengths below 500nm. This means that low wavelengths are not quite suitable for front-lit or dark field illuminations since the scattering of light from the fibres would be very little. For back-lit illumination on the other hand, the fibres will depart from being opaque and the shadows of the fibres will get brighter for low wavelengths since there will be significant transmission. For these reasons a wavelength of 670nm in the near IR region of the spectrum where cotton exhibits almost 93% reflectance, is assumed in the discussions throughout the chapter. A detailed study on reflectance properties of cotton fibres in visible and near infrared spectra can be found in Montalvo et. al. [1993].

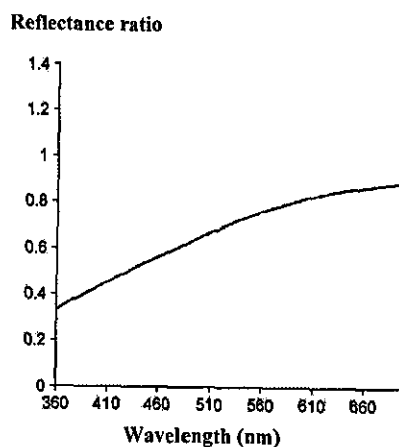


Figure 4-11 Reflectance Spectra of raw cotton fibre

It has to be noted at this point that in actuality, no light source can emit a single wavelength, but a band of different wavelengths. However, for some light sources, this band is very narrow and the light source can be considered as monochromatic. On the other hand, a white halogen lamp for example, radiates a wide band of wavelengths and in order to perform optical analysis for such a light source, all wavelengths have to be considered and a weighed average has to be found according to the radiation of each wavelength from the source and the responsivity of the camera.

The aperture size also plays a major role in the low pass filtering effect of the optical system. Figure 4-12 shows the OTFs for a circular aperture for varying f-numbers. It is clear that as the aperture size decreases, the cut-off frequency drops. Consequently, the resulting image will be more blurred. However, as will be discussed in next section, the depth of field is inversely affected with the aperture size.

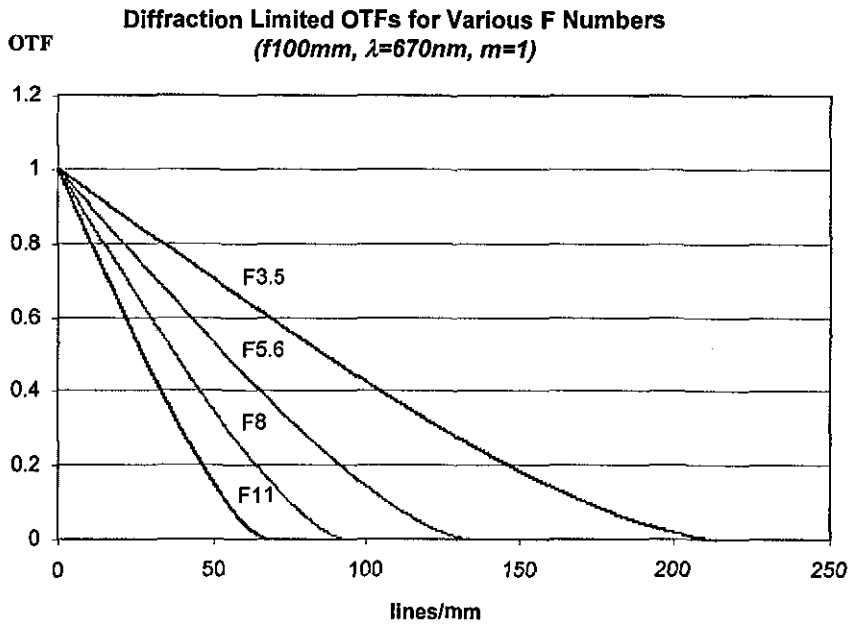


Figure 4-12 Effect of Aperture size on OTF

4.5 Defocus Aberration

In Figure 4-13, the exact focus plane for the object and the image plane (screen or CCD) in an optical system are shown. When the object is moved a distance δ_o from the exact focus plane, the image of it will be displaced a distance δ_i from the screen creating a blur spot of width B on the screen. From the figure, following relations can be found using geometry.

$$\delta_i = \frac{\delta_o f^2 m}{f - \delta_o m} \quad (4.18)$$

$$B = \frac{f \delta_i / F}{f + f m + \delta_i} \quad (4.19)$$

The spherical wave front (solid line) emerging from exit pupil centred at F corresponds to the wave front from the object when it is in focus and the reference

wave front (dashed line) centred at R to when there is an aberration (out of field aberration in this case). The distance between these two wave fronts is used as a measure of defining aberrations and is called Optical Path Difference (OPD), which is in some references given the notation w_{20} .

For modest amounts of OPD, the following approximation can be made [Smith, 2000]:

$$OPD = \frac{\delta_i \sin^2 \alpha}{2} = \frac{\delta_i (NA_{eff})^2}{2} = \frac{\delta_i}{8F_{eff}^2} \tag{4.20}$$

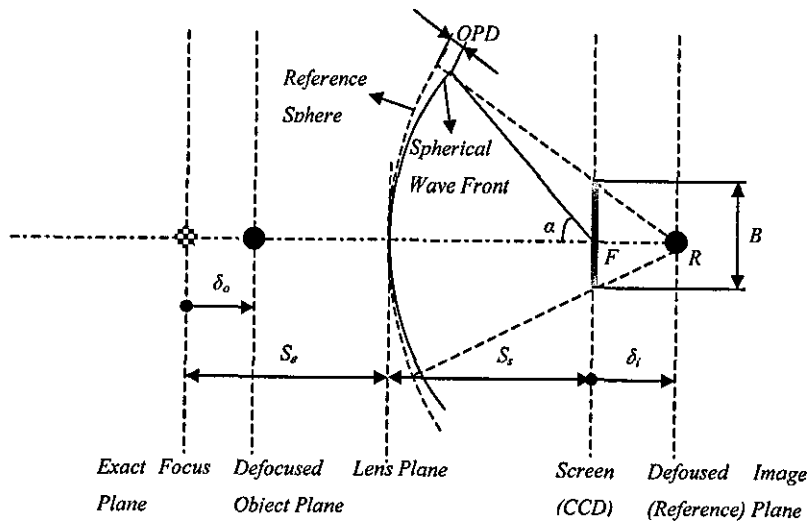


Figure 4-13 Geometry of Defocus Aberration

According to the geometrical optics, the blur spot B in Figure 4-13 has a uniform intensity distribution. By taking this spot as the point spread function, the OTF can be found by applying the Fourier Transform. Consequently, the OTF based on geometrical optics for a circular aperture is simply the FT of the circular blur spot with a diameter of B which is;

$$OTF_{geom}(s) = F \left(circ \left(\frac{B}{2} \right) \right) = \frac{2J_1(\pi Bs)}{\pi Bs} \tag{4.21}$$

However, this geometrical approximation does not take the diffraction effect of the aperture into account. Hopkins (1955) derived the following formula to calculate the frequency response (OTF) of a defocused optical system with a circular aperture under incoherent illumination:

$$D(s) = \frac{4}{\pi a} \cos \frac{a|s|}{2} \left\{ \beta J_1(a) + \frac{1}{2} \sin 2\beta [J_1(a) - J_3(a)] - \frac{1}{4} \sin 4\beta [J_3(a) - J_5(a)] + \dots \right\} \\ - \frac{4}{\pi a} \sin \frac{a|s|}{2} \left\{ \sin \beta [J_0(a) - J_2(a)] - \frac{1}{3} \sin 3\beta [J_2(a) - J_4(a)] + \frac{1}{5} \sin 5\beta [J_4(a) - J_6(a)] - \dots \right\} \quad (4.22)$$

Where

$$a = \frac{4\pi}{\lambda} OPD |s| \quad \text{and} \quad \beta = \cos^{-1} \frac{|s|}{2}$$

and J_n denotes the n th order Bessel Function.

Figure 4-14 shows the OTFs calculated for varying OPDs on the basis of geometrical optics along with those calculated from eq. (4.22). It can be seen that diffraction effects become negligible for OPDs greater than 2λ . This fact is also noted by Goodman (p151) where it is stated that, when severe aberrations are present, the PSF is determined primarily by geometrical optics effects, and diffraction plays a negligible role in determining its shape. Similar conclusions are also drawn in Hopkins [1955] and Smith [2000]. This is of particular importance to the next section where the background formation in backlit illumination is analysed using geometrical approach.

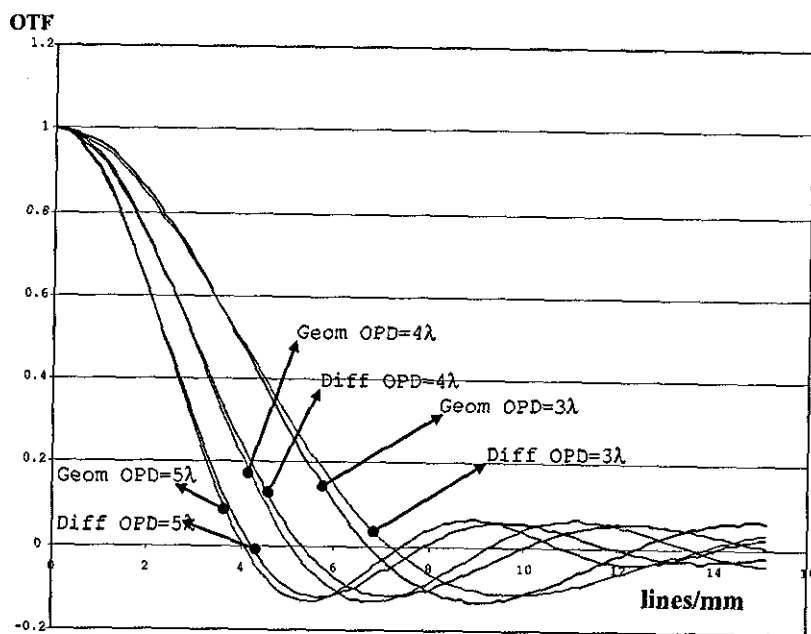
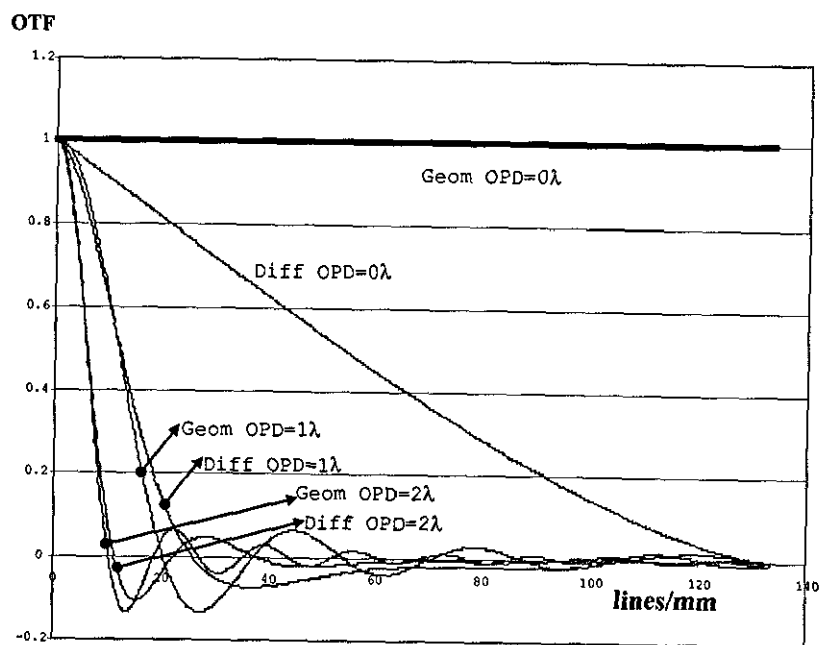


Figure 4-14 Comparison of OTFs calculated from geometrical approximation with those where the diffraction effect is taken into account.

Figure 4-15 shows defocus profiles of a 45 μm fibre for varying δ_0 calculated using eq. (4.22). It can be seen that when there is 5mm defocusing, the image widens

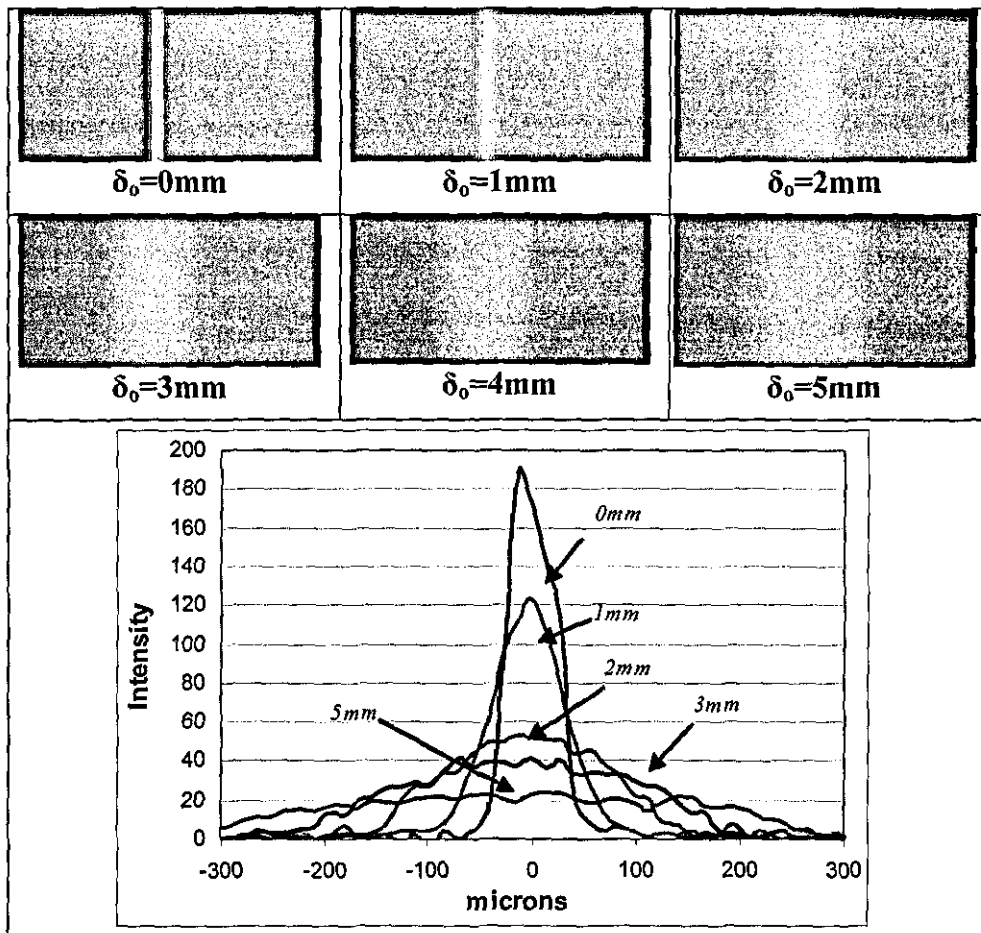


Figure 4-16 Pictures of a 45µm PP fibre at different defocusing distances (first two rows) and corresponding profiles (bottom row). ($F5.6$, $m=1$, $\lambda=670\text{nm}$, $f=100\text{mm}$)

One way to increase the depth of field is to decrease the aperture. It can be seen from eq. (4.20) that the OPD is inversely proportional with the aperture size, meaning that for the same amount of δ_o , OPD will be less for smaller apertures. Figure 4-17 shows the OTFs for varying f-numbers, where δ_o is held constant at 2mm. It is clear that when there is defocusing, decreasing the aperture size improves the image quality by passing higher frequencies. However, on the contrary, as the aperture size decreases, smaller amount of light energy is allowed through the optical system, therefore the light source has to be more powerful in order to achieve the same brightness in the image. Figure 4-18 shows pictures of the 45µm PP fibre for different aperture sizes when there is 2mm defocusing. The improvement in the image profile can be seen as

the aperture is decreased; however, the brightness on the other hand noticeably drops.

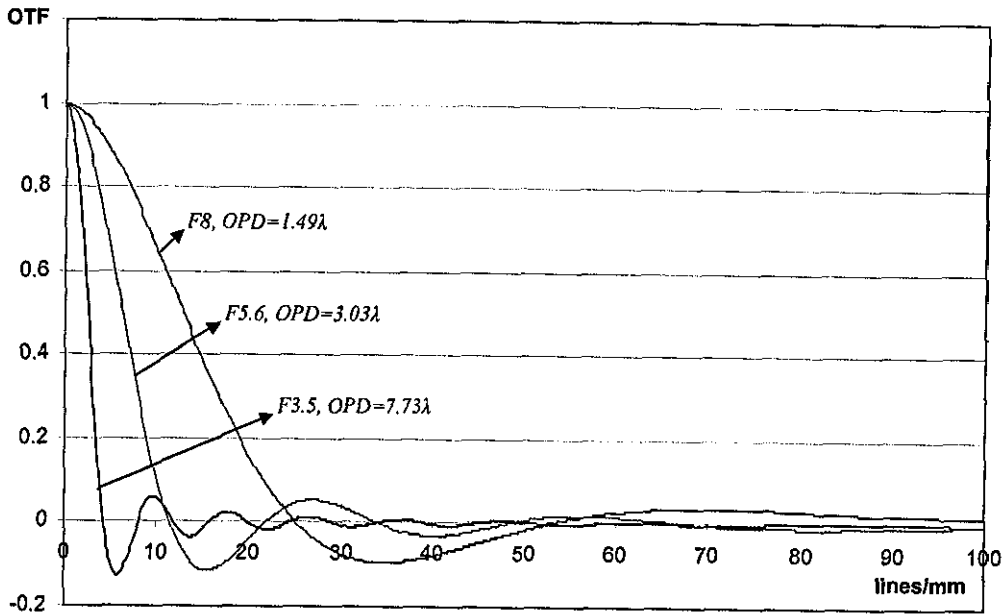


Figure 4-17 OTFs for varying F; $\delta_o=2\text{mm}$, $\lambda=670\text{nm}$, $f=100\text{mm}$

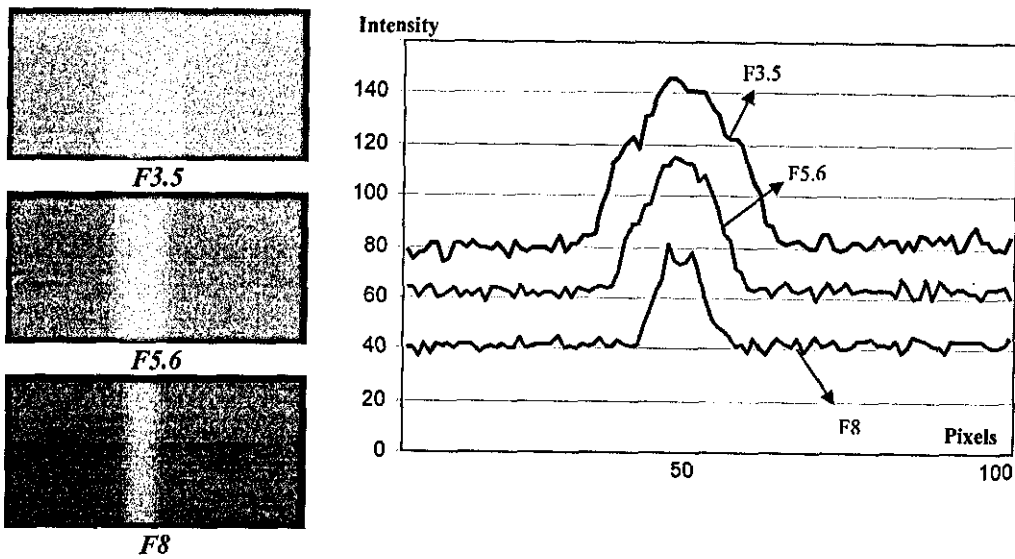


Figure 4-18 Pictures of a 45μm PP fibre with 2mm defocusing and varying f-numbers.

According to Raleigh's resolution criteria, the OPD should not exceed $\lambda/4$ in order to be able to resolve the PSFs accurately. The resolving power of the optical system is especially important for high magnification yarn inspection where the surface details are of interest. Figure 4-19 shows a yarn image taken using a microscope focused to the edges of the yarn core, where defocusing is quite significant due to the small focal length of the microscope lens. For a yarn core with a diameter of 0.6mm, if the camera is focused between the core edge and the surface, the required depth of field will be 0.15mm. In order to meet Raleigh's resolution criteria within this depth using a lens with 100mm focal length and a magnification of 4, the aperture has to be set to a minimum of F4.25 according to eq. (4.20).

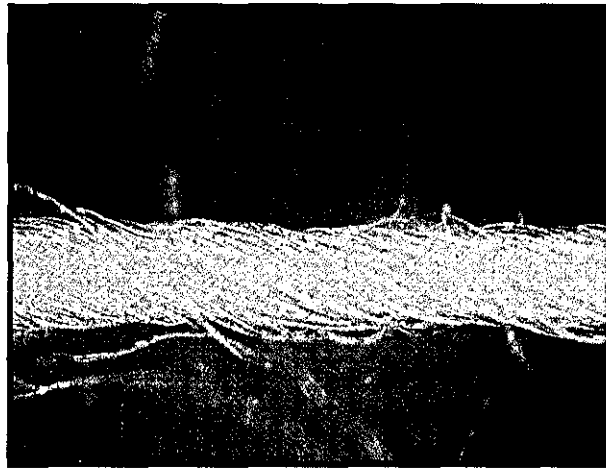


Figure 4-19 Effect of out of field degradation at high magnification. The image is taken using a microscope focused to the core edge at $m=4$.

For a magnification of 1 that is used for detecting hairs, Raleigh's resolution criteria can only be met within 1.3mm depth even when the aperture is set to F11. Considering fibres as long as 25mm and the possibility that a hair can travel parallel to the optical axis, this depth is not sufficient for accurate definition of hairs.

Millman [2000] suggested use of guide plates to force the protruding fibres into a region, where the effect of misfocus would be in desirable limits. He showed that using a 0.5mm guide gap, it was possible to resolve $40\mu\text{m}$ separations at the wall

extremities. Millman [2000] also investigated applicability of real pupil misfocus correction and wavefront encoding methods to improve the misfocus tolerance in yarn imaging. However, he found the former method to be realistic only for low values of maximum misfocus at around $OPD=2\lambda$, which is only suitable for high magnification imaging. He also recorded that the wave front encoding method was unacceptable due to the non-circular shape of 2D OTF, which badly attenuated the non-vertical and horizontal frequencies. He concluded that for low magnification inspection, yarn guiding was the only way for misfocus correction. However, a major problem he encountered was the fringe patterns in yarn images when using back-lit coherent illumination, which was corrected using flat field correction. Another problem would possibly be the dust and short fibres accumulating in the guide plates, which can seriously affect the images. However, Millman suggested a conceptual design for yarn transfer which incorporated a different design of guide plates with an automatic cleaning mechanism.

It is shown in section 4.9 that hairs as thin as $16\mu\text{m}$ can theoretically be detected up to a defocusing of 7mm when using an F8 aperture using a threshold at 5% of the maximum intensity. However, the minimum separation that can be resolved is more than $400\mu\text{m}$ in this case. Nevertheless, since the surface fibres are generally in focus, the required separation can be as low as $30\mu\text{m}$ in order to separate surface fibres from the core. For front-lit illumination, unless a means of mechanical guidance of the fibres is used, the hairiness measurement can be misleading. A method aiming to force the fibres into a finite plane was implemented in CRITER tester using static electricity. However, Barella [1966] opposed the idea of forcing the fibres into a plane arguing that the hairiness should ideally be measured in fibres' actual form.

It has to be noted at this point that, the main illumination type that Millman [2000] used was back-lit illumination. However, he carried out all his calculations for front lit objects and assumed that the same rules would apply for the back-lit case. This would only be true if the back light source were planar and on the same plane with

the object. A distinction has been made in this thesis between front-lit and back-lit illuminations and it has been shown that the back-lit illumination can provide enormous misfocus tolerance compared to front-lit illumination. Therefore, when using back-lit illumination no need for guide plates is seen.

4.6 Analysis of Backlit Illumination

The basic principle of backlit illumination is to place the object between the lens and a light source to allow the shadow of the object to be imaged by the system as shown in Figure 4-20., where each point on the light source emits a diverging wave front which will first be obstructed by the object and then the aperture before reaching the lens. The wave front is then focused to a point and diverging from there falls on the screen creating an intensity distribution pattern. This pattern will be governed especially by the nature of the light source and the diffraction effects from both the object and the aperture. A typical back-lit image consists of a bright background and a dark shadow of the yarn as shown in Figure 4-21. In the first section to follow, the formation of image background will be analysed which is followed by the investigation of the factors playing role on the shadows of the fibres.

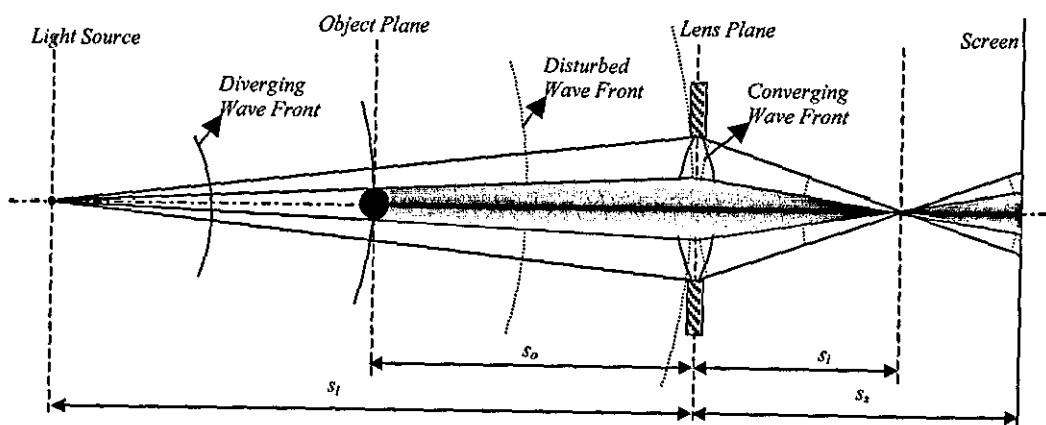


Figure 4-20 Geometry of back-lit illumination

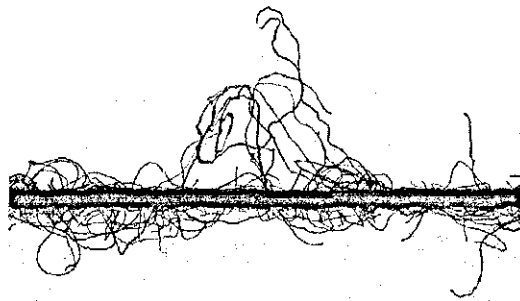


Figure 4-21 A back-lit yarn image

4.6.1 Factors Affecting the Image Background Quality in Back-lit Illumination

When there is no object present in Figure 4-20 the resulting image will be a blurred picture of the light source, which is essentially the background in a back-lit image. If the light source were at the exact focus plane, i.e. $s_L = s_e$ the image of the light source itself would form on the screen. Figure 4-22 shows an image obtained by placing a tungsten filament bulb on the plane of exact focus using unit magnification. As the light source is moved further from s_e , this image will blur as was previously mentioned in the previous section. Figure 4-23 shows the image profiles for increasing defocusing distances of the light source. These profiles are obtained by convolving the profile in the exact focus plane case with the point spread functions for different defocus distances. Since there is severe defocus in all cases, the PSFs were simply calculated using geometrical optics. It can be seen that as the light source is moved further, the profile gets wider and flattens providing a broad and uniform background in the image formed; but on the other hand, the maximum intensity decreases dramatically, which requires the intensity of light source or the exposure time to be increased. For example, when the light is moved from s_e to $s_e + 100\text{mm}$, the profile widens from 2mm to 11mm, while the maximum intensity drops by 99.2%.

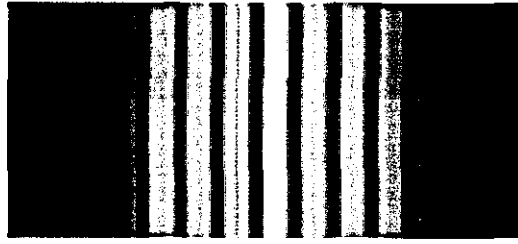


Figure 4-22 Image of a tungsten filament bulb

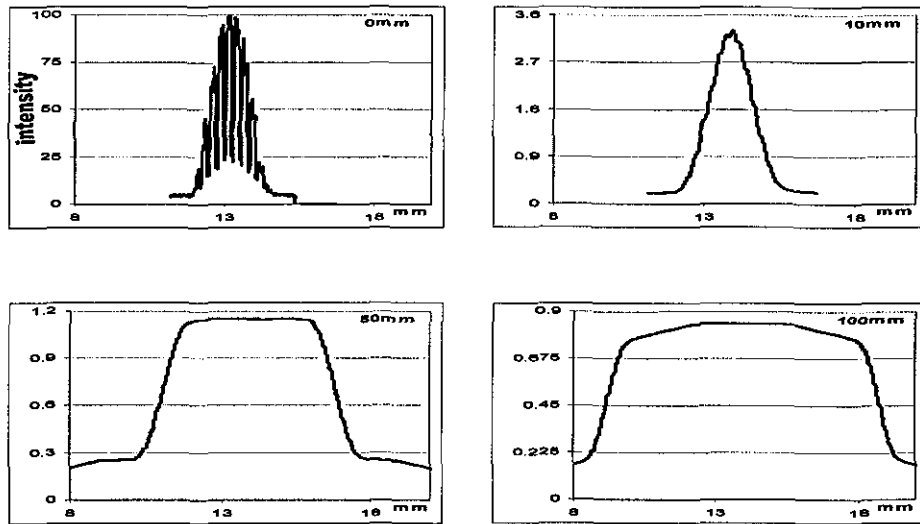


Figure 4-23 Simulated defocus profiles of a tungsten filament bulb

There is, however, a limit to the width of the profile as the light source is moved further, which is related with the aperture size and the magnification as follows:

$$w_b = \frac{fm}{F} \quad (4.23)$$

This equation can be obtained by taking $s_L = \infty$ in Figure 4-20. To give an example, if a lens with a focal length of 100mm and an aperture of F3.5 is used and assuming unit magnification, the maximum blur size will be 28mm. If the length of CCD array is more than this value, some pixels at the edges will not receive any light. The size of illuminated region on the screen can be increased using a field lens or a broader

light source, for example by putting a diffuser between the light source and the object. These techniques are both tested and discussed in section 5.2.1.

4.6.2 Diffraction Effect of Fibres

As was briefly mentioned at the beginning of Section 4.6, when the yarn is inserted in front of the light source, the light waves diffract around the edges of fibres and the core. Diffraction phenomena are generally classified into two types which are Fraunhofer (or far field) and Fresnel (or near field) diffraction. Fraunhofer diffraction occurs in cases where the light source and the screen are effectively at infinite distances from the object whereas Fresnel diffraction theory treats cases where the incident wave is spherical and the screen is at a finite distance from the object. The boundaries between two types of diffractions can be found in Hecht [2002] and Gaskill [1993]. An excellent brief discussion on the subject can also be found in Lytle [1999a and 1999b]. There is also an interesting theory of diffraction in the literature first introduced by Keller [1961], which treats the problem using geometrical optics.

The diffraction phenomena for back-lit imaging set-up of Figure 4-20 falls into the Fresnel region. Fraunhofer diffraction could only be obtained if the light source were at infinity, for example by using a laser, and the screen were placed at the focal plane of the lens which is essentially equivalent to moving it to the infinity when there is no lens. In textile literature, Fraunhofer diffraction theory has been used by a number of researchers for measuring fibre diameters. Earliest communication on the subject appeared in 1921 by Duerden, where he reported experiments with a laboratory diffraction apparatus and compared the results with microscopic techniques. Later publications appeared in Curtis [1928], Burns [1930] and Mathews [1932] (all four references cited in Sommerville [2003]). Onions [1959] explained the theory of how fibres interact with an incident monochromatic light, where he assumed a bundle of parallel fibres to be a group of equivalent slits. A similar assumption is also made in this thesis. Edmonds [1988] recorded photographic images of diffraction patterns and

later analysed to measure fibre diameter. However there is not much research addressing the Fresnel diffraction caused by fibres. Lynch and Thomas [1971] examined the diffraction patterns produced by single wool and other fibres using a He-Ne laser beam. He found that the surface imperfections of fibres created complicated diffraction patterns. Glasbey et.al. [1994] used a microscopic imaging technique for measuring the fibre diameters under back-lit illumination. He observed fringes at the edges of the fibres which created a significant rise in the intensity especially at the vicinity of the edge. The diffraction was regarded as being one of the factors affecting the image but a mathematical treatment is not given in the paper. He then explained the fibres acting as lenses, hence the fringes at the edges. During this research, similar fringes are also observed in the experiments and it is found that they can accurately be explained using Fresnel diffraction theory.

The Fresnel calculations in this section are based on a rather numeric method following Hecht [2002, Chapter 10], however analytical treatments of the subject using Fourier Transformations can be found in Goodman [1996, p. 66], Born and Wolf [1964, p. 428] and Gaskill [1993, p. 365].

To perform the analysis, the optical arrangement in Figure 4-20 is simplified as in Figure 4-24 by replacing the lens and screen combination with a single screen that is placed on the exact focus plane of the lens, where every point on the light source emits a spherical wave front which is first partly obscured by the fibre and then falls on the screen.

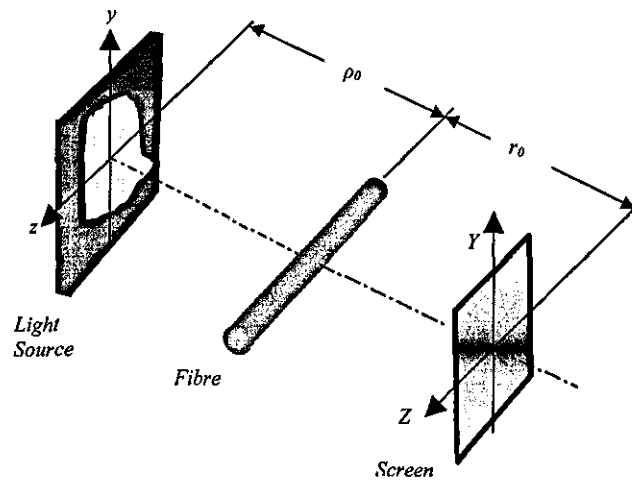


Figure 4-24 Back-lit illumination geometry where the lens and screen is replaced with a single screen placed on the focal plane of the lens.

The diffraction occurs at the edges of the fibre and the intensity distribution on the screen diverges from what would be expected from geometrical optics. The solution to the problem in three dimensions is quite complicated; therefore the analysis will be carried out in two dimensions as shown in Figure 4-25. This reduces the problem to the complementary case of a single slit problem, where the fibre is considered as an opaque obstacle having a width w_f and negligible thickness. The basic difference is that in single slit problem, there is a single contributing region that extends from top of the slit to the bottom, whereas in this complementary case there are two regions one extending from top of the fibre to ∞ and the other from the bottom to $-\infty$. So, the solution to the single slit problem (Hecht [2002], p. 503) is modified and following formula is obtained that gives the intensity at a point P on the screen arising from a point S on the light source (see Figure 4-25);

$$I_p = \frac{I_0}{2} \left\{ [F_1(\infty) - F_1(v_2)]^2 + [F_2(\infty) - F_2(v_2)]^2 + [F_1(-\infty) - F_1(v_1)]^2 + [F_2(-\infty) - F_2(v_1)]^2 \right\} \quad (4.24)$$

Where I_0 is the irradiance arriving at P when there is no obstruction and $F_1()$ and $F_2()$ are the Fresnel integrals defined by;

$$F_1(w) = \int_0^w \cos\left(\frac{\pi w'^2}{2}\right) dw' \quad (4.25)$$

$$F_2(w) = \int_0^w \sin\left(\frac{\pi w'^2}{2}\right) dw'$$

And v_n is a dimensionless variable given as

$$v_n \equiv y_n \left[\frac{2(\rho + r)}{\lambda \rho r} \right]^{1/2} \quad (4.26)$$

Which when $\rho \rightarrow \infty$ (plane wave) reduces to

$$v_n \equiv y_n \left[\frac{2r}{\lambda r} \right]^{1/2} \quad (4.27)$$

It is worth noting that when there is no fibre, i.e. $w_f=0$ hence $y_1, y_2 \rightarrow \infty$, the intensity at P, I_p , will simply equal to I_0 , the unobstructed irradiance (note that $F_{1,2}(\infty) = -F_{1,2}(-\infty) = 0.5$).

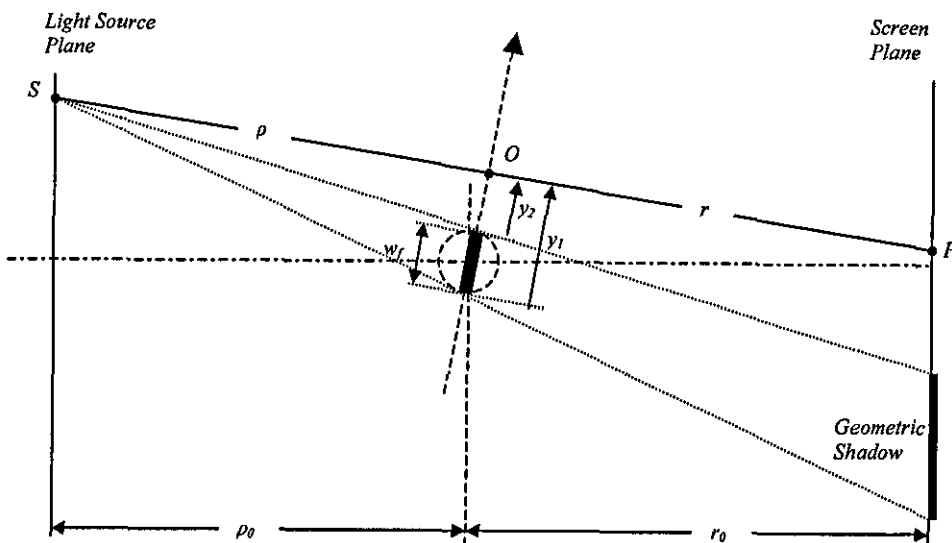


Figure 4-25 Diffraction geometry in 2D

A C program is written to calculate the intensities for every point P on the screen for any given values of ρ_0 , r_0 and w_s , by adding up the contributions from every point S on the light source. Figure 4-26 shows a simulated intensity profile on a screen placed at 5 mm distance from a 14 μm fibre that is illuminated from 100mm behind with a 670nm light source having 1mm wide Gaussian profile (for definition of the width of the light source see Figure 4-30). The simulation program can also calculate the geometrical shadow for comparison in order to envision the effects of diffraction as shown in Figure 4-27. It can be seen that due to diffraction, the shadow is wider than that would be expected from geometry. Most interesting effect of diffraction is that the intensity rises above the actual background intensity at the edges of the shadow and as departing from the edge, it keeps oscillating above and below the actual background intensity with decreasing amplitude.

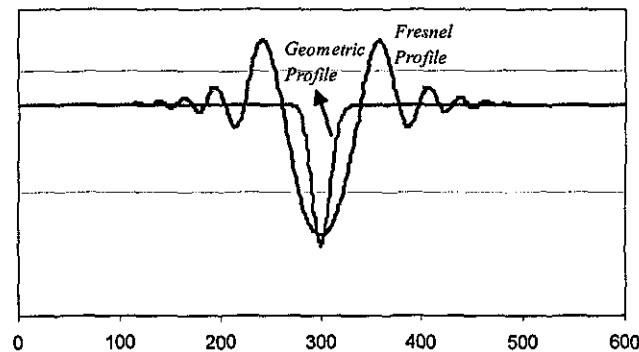


Figure 4-26 Comparison of shadow profiles of a 14 μm fibre, calculations based on Fresnel's diffraction theory and geometrical approximation.

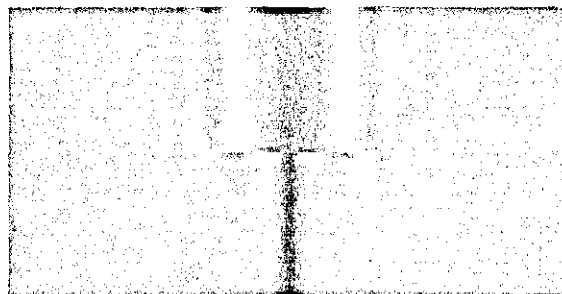


Figure 4-27 Picture generated using the intensity profiles of Figure 4-26. Top: Fresnel Diffraction pattern, Bottom: Geometrical approximation.

Figure 4-28 shows pictures of a 45 μm fibre at different distances from the exact focus plane illuminated with a single red LED light source 550mm away. The pictures on the left are the simulated pictures based on diffraction and on the right are the actual pictures. The intensity distribution on the light plane used in the simulations is calculated by taking a picture of the light source. Despite the approximations made in the simulations such as monochromatic assumption of the light source and investigation of diffraction in 2D geometry, very good agreement is observed with the actual pictures, hence the diffraction model has been found quite adequate in analysing the back-lit illumination.

One of the points to note about the effects of diffraction is that the oscillation in intensity tends to become more localized as the distance from exact focus plane (r) approaches zero and the intensity oscillations at the vicinity of the edges are quite significant for all values of r , which has an important effect on the image processing as discussed in the next chapter. It can also be seen from the pictures that the fibre can still easily be detected even when it is moved 45mm from the exact focus plane. This is a very important superiority of back lighting compared to front-lit illumination, where the same fibre dramatically blurs at 5mm defocusing (see Figure 4-16).

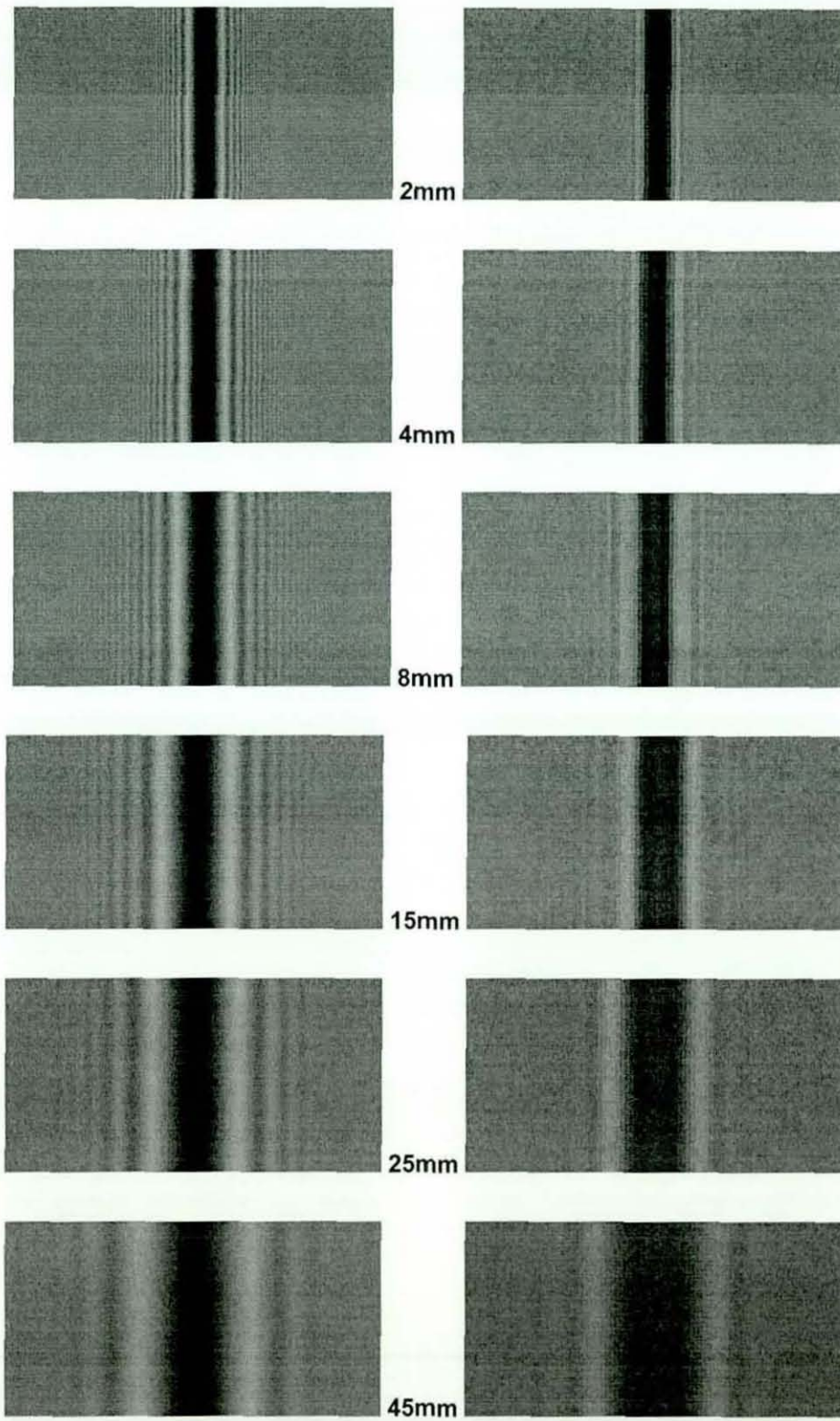


Figure 4-28 The shadow profiles of a 45 μm PP fibre for different defocusing distances. Pictures on the right show the actual pictures and on the left are the simulations.

4.6.2.1 Effect of size and distance of the light source on shadow profile

A point S on the light source, as shown in Figure 4-29, creates a shadow centred at a point C_g on the screen. If the light is a point source, there will be a single shadow on the screen, however if the light source has a finite width, all points on the light source will create shadows each centred at different locations on the screen. Since one shadow from one point may partly overlap with one from another point they blend into each other and the resultant shadow will blur and widen.

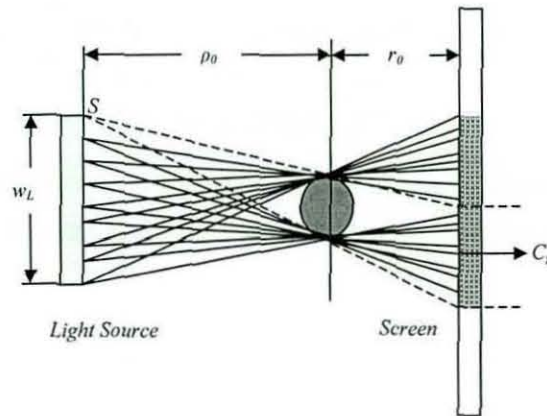


Figure 4-29 Geometrical explanation of blurring of fibre shadow due to the finite dimension of the light source

The amount of blurring in the shadow will depend on the size of the light source (w_L), as can be predicted from Figure 4-29. On the other hand, the width of the shadow on the screen depends on both w_L and the distance of the light source from the fibre (ρ_0) as well as the distance between the fibre and the screen (r_0). As ρ_0 gets larger, the rays from the light source will make smaller angles with the edges of the fibre creating a narrower shadow on the screen. Geometrically, if $\rho_0 \rightarrow \infty$, then it can be expected to achieve an infinite depth of field, i.e. no matter how far the fibre is taken away from the screen, its shadow remains unaltered. However, this is not the case in practise; therefore a more detailed analysis is necessary that takes diffraction into account.

In the analysis to follow a light source is defined with a Gaussian profile as shown in Figure 4-30, where the width of the light source w_L is associated with the distance between the points of the Gaussian profile where its value drops to 0,01.

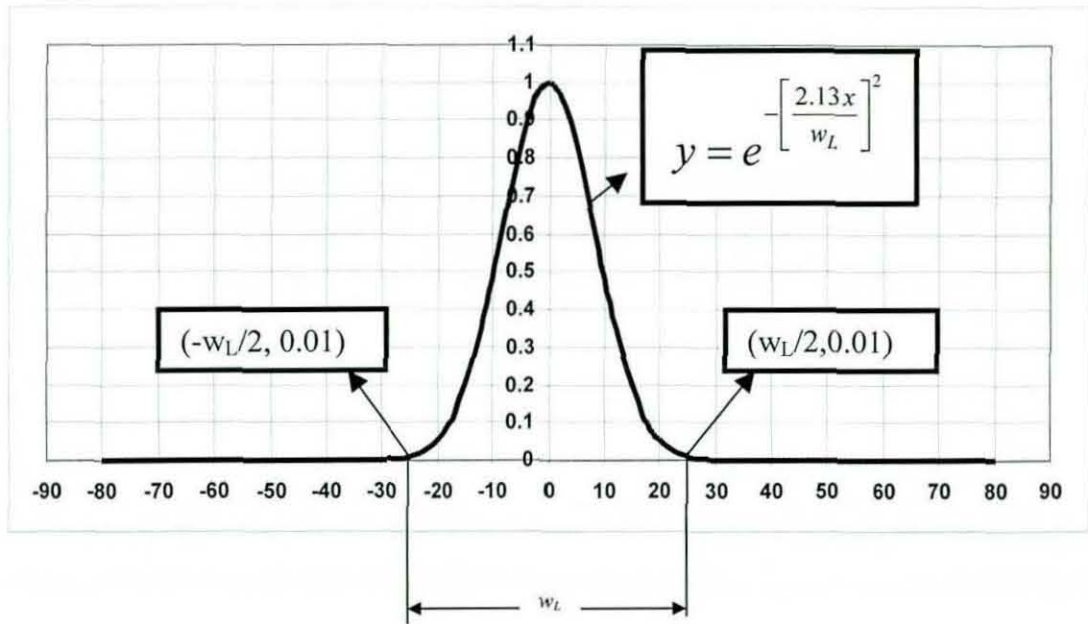


Figure 4-30 Definition of w_L

Figure 4-31 shows Fresnel profiles of a 10mm defocused 45 μ m fibre, illuminated with a light source with varying w_L from 250mm behind. As it was predicted from geometry in Figure 4-29, the profiles tend to fade dramatically as the size of the light source is increased. It can be seen that when w_L is 5mm, the fibre is clearly visible, however, when w_L is increased to 15mm, the contrast appears to drop to an undesirable level.

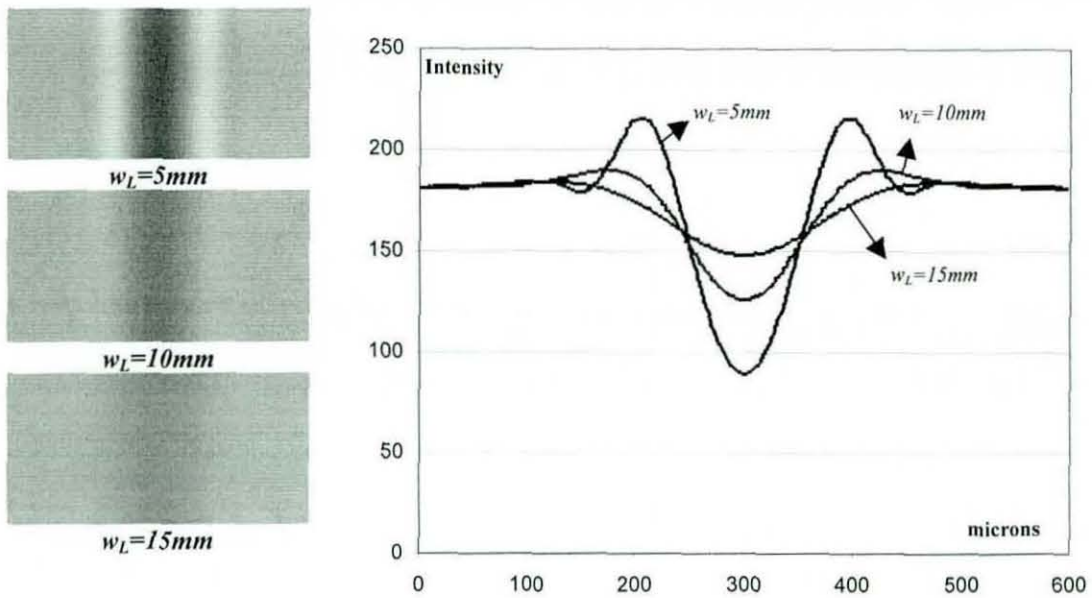


Figure 4-31 Defocus profiles for varying w_L

Figure 4-32 shows the simulated profiles for a $45\mu\text{m}$ fibre that is defocused 10mm and illuminated with a light source of width 5mm at different distances. Since for large values of ρ_0 the spherical waves incident on the fibre takes the shape of plane waves, the width of the profile is altered only very slightly as the light is moved from 500mm to infinity as can be seen from the figure. However as $\rho_0 \rightarrow \text{inf}$ (eg by using a laser or a lens), the fringe patterns around the main peak of the shadow become more evident. This reveals the reason for the fringes encountered when using a laser source for backlit illumination. These patterns create important problems in the image processing stage.

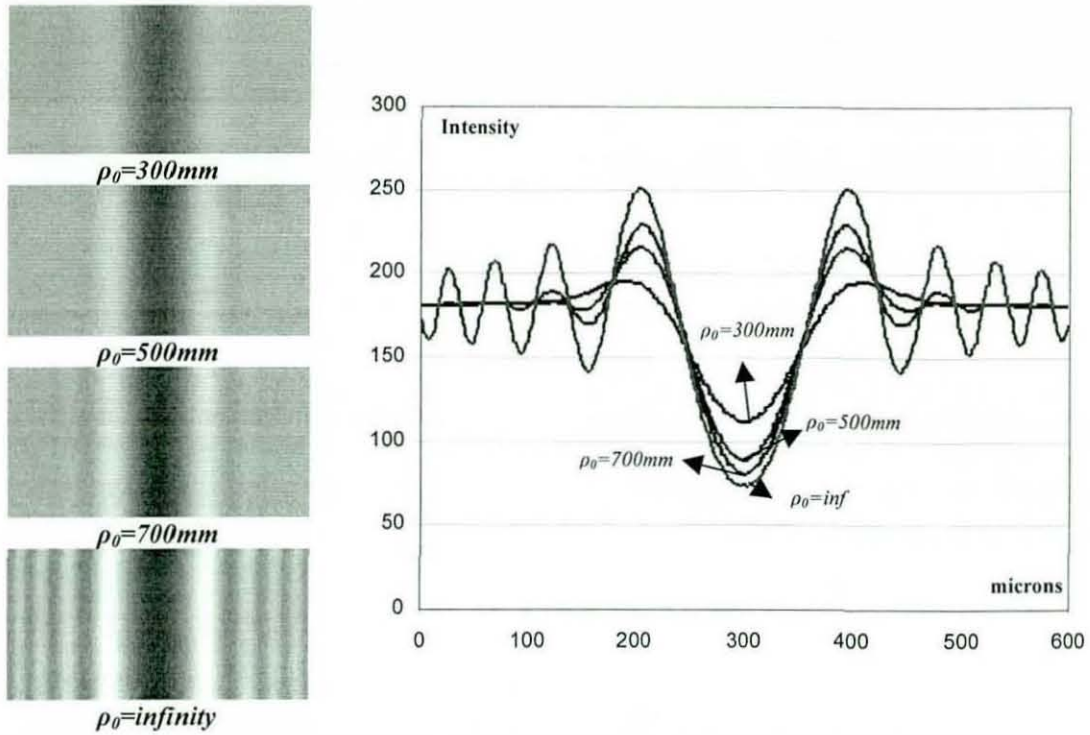


Figure 4-32 Defocus profiles for varying ρ_0

4.6.3 Off-Axis Displacement in Back-Lit Illumination

One of the problems in back-lit illumination occurs while imaging an off-axis object that is out of focus. If the fibre is placed a distance h_o further from the optical axis as shown in Figure 4-33, the corresponding centre in the image will appear a distance h_{ic} from the optical axis creating a position error Δh_{io} given as;

$$\Delta h_{io} = h_o \cdot \frac{r_0}{\rho_0} \quad (4.28)$$

This will result in a miscalculation of object's position which is especially important when the distances of the fibres from the core are of interest. To reduce the error, the light source has to be placed as far as possible from the object. For sufficient distances of the light source and reasonable amounts of h_o , the position error can be neglected. For example, if $\rho_0=500\text{mm}$ and the fibre is 12mm off the optical axis and

when there is 20mm defocusing (which requires the fibre to be at least 23.3mm), then the position error will be 0.5 mm, i.e. the fibre will appear to be 12.5mm off the optical axis.

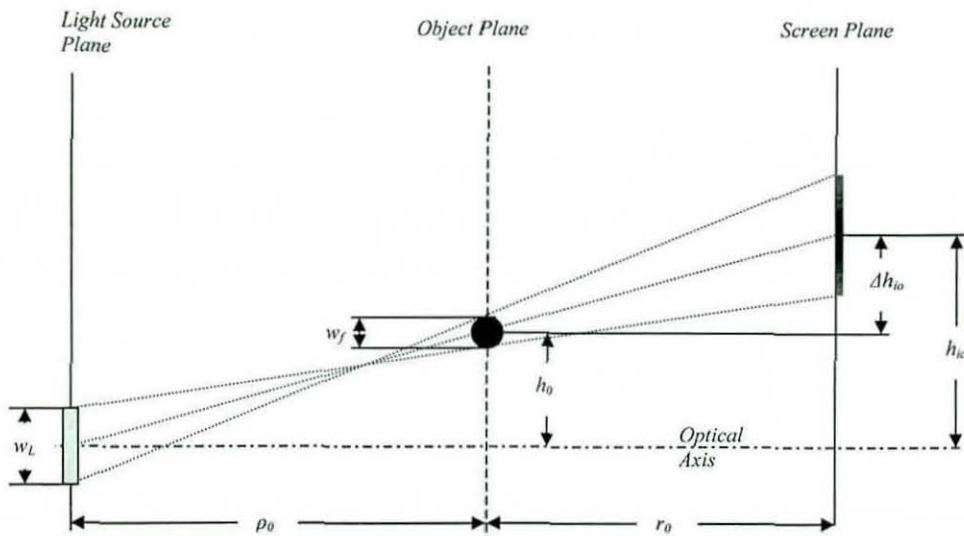


Figure 4-33 Displacement of an off-axis defocused object

4.7 Other Optical Aberrations

It was stated in Section 4.2 that the position and size of the image of an object formed by a “perfect lens” can be determined using the lens formula. The “perfect lens” notion was then replaced with “diffraction limited lens” taking the diffraction effect of the aperture into account and in this case the image of an object departed slightly from the geometrical prediction, but the position of any image point could still be predicted using lens formula. If the image departs from what would be expected from diffraction limited assumption then the lens is said to be aberrated, however well corrected lenses that can be considered as “diffraction limited” are commercially available. In this section different types of aberrations will briefly be discussed for a more complete treatment of the optical image formation.

If the focus of a lens varies with the aperture, then there is said to be **spherical aberration**. If this sort of aberration is present in the lens, then especially for backlit illumination, as the fibres on the exact focus plane depart from the optical axis, some blurring occurs as illustrated in Figure 4-34a. However as can be seen in Figure 4-34b this is not observed on the actual images; if the spherical aberration were severe the fibre 8mm off axis would appear blurred.

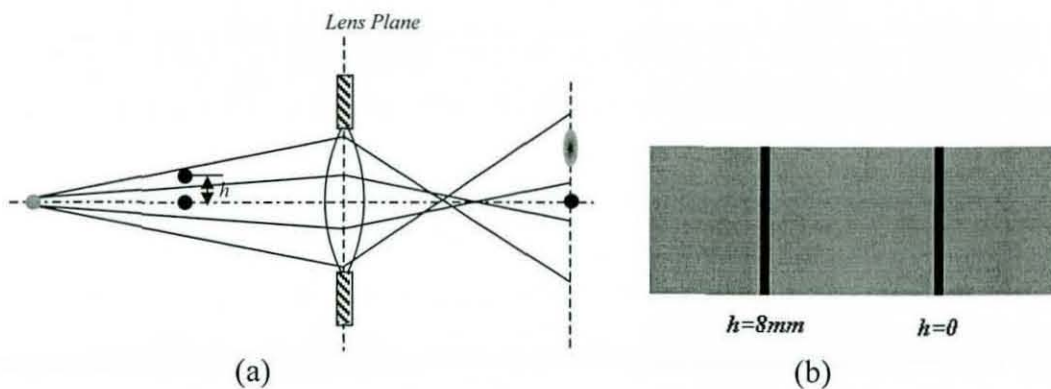


Figure 4-34 Left: Effect of Spherical Aberration in back-lit illumination; Right: Pictures of a 45μ fibre at different distances from the optical axis.

One of the important aberrations is the chromatic aberration. If the light source emits a wide band of wavelengths since the refraction index of the lens material depends on the wavelength of the light, as the wavelength gets smaller the focus will get closer to the lens. As the light source approaches monochromatic, the image can be expected to get sharper. Furthermore, as was discussed in section 3 the diffraction effect of the fibre depends on the wavelength as well. Actually, using non-chromatic light has been found superior in this sense that the fringe patterns around the edges of the fibres arising from diffraction get dimmer for non-chromatic light as can be seen in Figure 4-35.

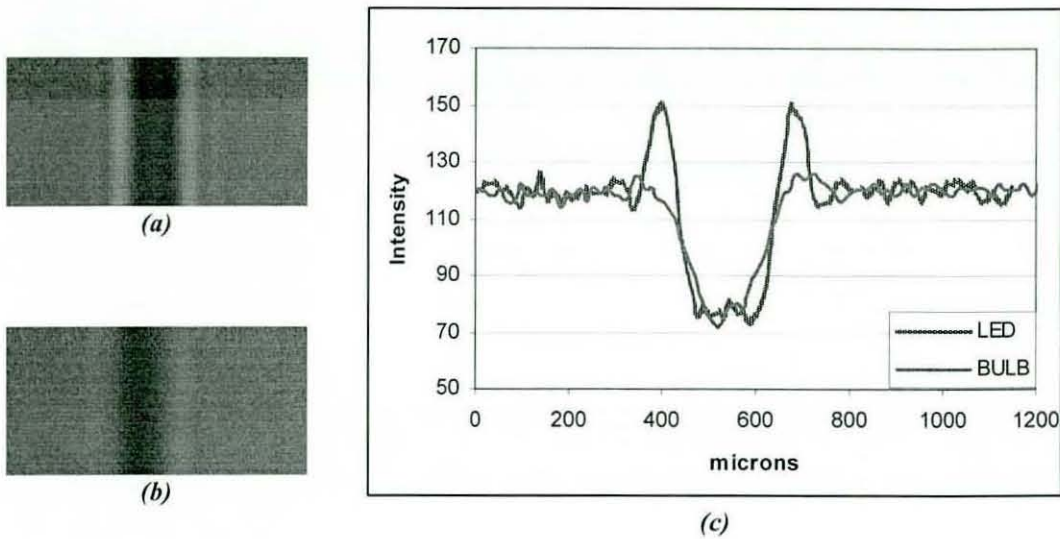


Figure 4-35 45 μ m PP fibre images at 25mm defocus illuminated with a red-LED (a) and white tungsten filament bulb (b) and the corresponding profiles (c). Note the fringe pattern for LED which is more visible.

Other aberrations that may be present in an optical system are coma, astigmatism and distortion. All these aberrations are magnified departing from the optical axis and mostly act as low pass filters. For low magnifications, the degradation of the image due to digitisation and added noise has been found to surpass their effects. For high magnifications on the other hand, diffraction effect of the aperture and especially the out of field aberration are the most significant degradations and other aberrations can be neglected for a good quality lens and small apertures.

4.8 Image Digitisation

A line scan camera uses an array of N rectangular photosensitive elements arranged in a single line as depicted in Figure 4-36. In general, each element has a square shape and the fill factor defined by the ratio p/c_x effectively approaches 100% with the aid of some tiny lenses placed on the sensors [Greer, 1999]. The fill factor of the camera used during this research is also 100% with square shape sensor elements according to its manual. Therefore it will be assumed that $c_x=c_y=p$ during the analysis.

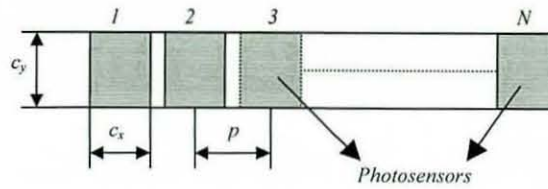


Figure 4-36 CCD sensor array of a line scan camera

As the object moves at a speed of V_o relative to the camera, the optical image moves on the sensor array at a speed of V_i that equals $V_o.m$ and the line scan camera takes repetitive scans of the optical image building up a 2D picture. At each scan, an analogue signal is generated proportional to the light energy received by the sensor, which is controlled by the exposure time t_e . The signal equals zero if the light energy is below the minimum responsivity of the sensor and has a maximum if the energy is above the maximum responsivity. The analogue signal is then sampled according to the number of CCD elements and quantized into 2^n levels producing a digital grey scale image $g_d(X,Y)$, where n is the bit rate of the camera. The time between the start of two successive exposures is denoted by t_s . If there is a constant exposure control, t_s can be less than t_e , otherwise t_s equals t_e . Vertical Image Aspect Ratio is defined as;

$$AR = \frac{p}{t_s V_i} \quad (4.29)$$

Sampling time is the reciprocal of the line rate, which is related with the data rate of the camera as follows;

$$\frac{1}{t_s} = \text{Line Rate (line scans / sec)} = \frac{\text{Data Rate(Hz)}}{N.n} \quad (4.30)$$

Figure 4-37 depicts the image acquisition and digitisation process. Following this figure, the digital image g_d can mathematically be modelled based on the optical image g_2 as follows;

$$\left\{ \left[g_2(X, Y) * \text{rect} \left(\frac{X}{Np} \right) \right] \otimes \left[\text{rect} \left(\frac{X}{c_x}, \frac{Y}{c_y} \right) \otimes \text{rect} \left(\frac{X}{c_x}, \frac{Y}{t_e * V_i} \right) \right] \right\} * \text{comb} \left(\frac{X}{p}, \frac{Y}{t_s V_i} \right) \quad (4.31)$$

Or in frequency domain,

$$\left\{ \left[G_2(f_x, f_y) \otimes \text{sinc} \left(\frac{f_x}{Np} \right) \right] * \left[\text{sinc} \left(\frac{f_x}{c_x}, \frac{f_y}{c_y} \right) * \text{sinc} \left(\frac{f_x}{c_x}, \frac{f_y}{t_e * V_i} \right) \right] \right\} \otimes \text{comb} \left(\frac{X}{p}, \frac{Y}{t_s V_i} \right) \quad (4.32)$$

where $\text{rect}(X, Y)$ refers to the 2D equivalent of the 1D rect function described in eq 4.13.

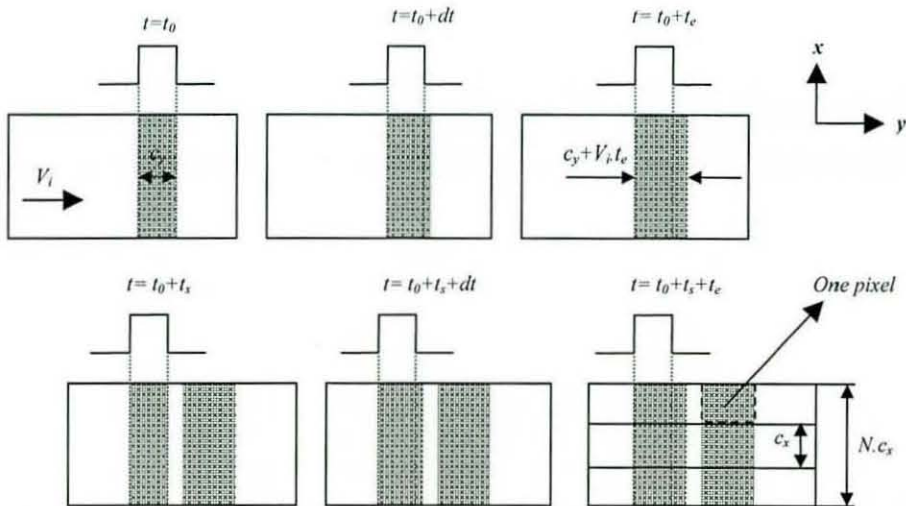


Figure 4-37 Line scan process

In eq. (4.31), the optical image is firstly cropped on x axis using the first rectangle function, since the parts of the optical image outside the CCD array are not detected by the sensors. The next two rectangle functions those are first being convolved with each other and then with the image provide a weighed average of the portion of the optical image scanned by each sensor during one exposure. Finally, the comb function at the tail of the equation handles the sampling.

A program is written that can generate high resolution spoke target pictures and then simulate the effects of pixelisation as well as the exposure and sampling times using equation (4.31). Figure 4-38 shows a spoke target picture after digitising using the parameters given below the figure. The pixel effects can clearly be seen in the picture. It can also be seen that for high frequencies (towards the centre) the contrast seriously drops. If the magnification were higher, each circle on the same spoke target image would correspond to higher frequencies; however the speed V_i would also increase parallel to the magnification, hence the alteration of the frequencies arising from $rect\left(\frac{X}{p}, \frac{Y}{t_e * V_i}\right)$ component of eq. (4.31) remains the same in the vertical direction giving an improvement only in the horizontal direction in the digital image.

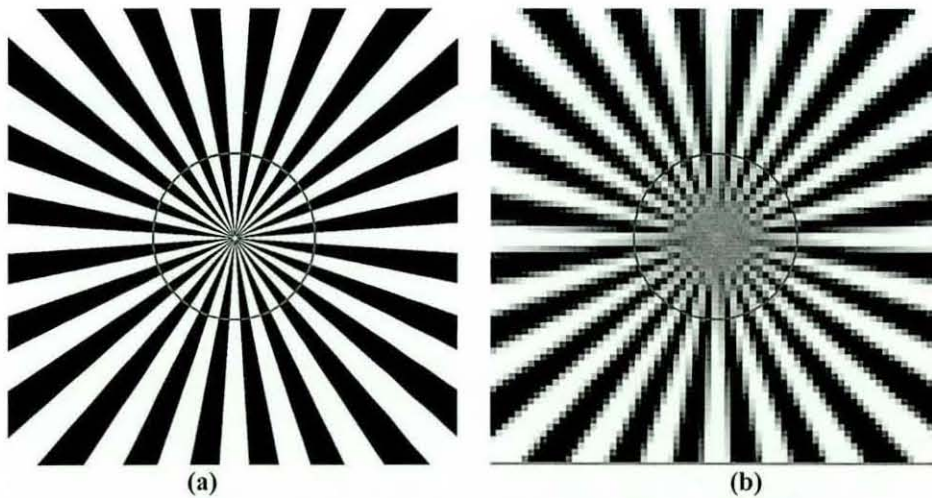


Figure 4-38 A spoke target before (a) and after (b) digitisation where $m=1$, $p=14\mu$, $V_i \cdot t_e=14\mu$, $AR=1$ and $n=8$ bits. The circles on the pictures correspond to a frequency of 67 lines/mm at this magnification.

Figure 4-39 shows the spoke target image after being digitised using a lower aspect ratio. The picture on the left corresponds to an exposure time that is equal to the sampling time, and for the second picture, the exposure time is set to one fifth of the sampling time. As the aspect ratio is decreased, the vertical frequencies are seriously attenuated. Furthermore, aliasing occurs if the sampling frequency is lower than the object Nyquist frequency, this can be seen on the midway between the centre and the

vertical edges of the pictures. It can also be seen that the contrast is better if the exposure time is lower.

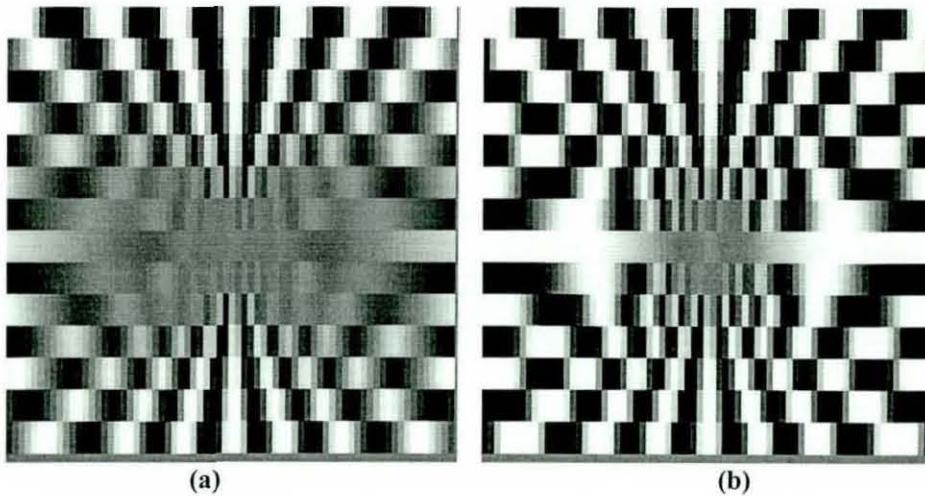


Figure 4-39 Digitised spoke targets at $V_i, t_e=70\mu\text{m}$ (a) and $V_i, t_e=14\mu\text{m}$ (b) both sampled at $AR=1/5$.

It was shown in equation (4.30) that the sampling time is inversely proportional to the data rate of the camera, so the minimum sampling time, i.e. the maximum aspect ratio that can be achieved at a certain object speed, is primarily determined by the maximum data rate of the camera. The minimum exposure time also has the same limit as the sampling time, so at the maximum line rate, the contrast cannot be improved by using an exposure time less than the sampling time as in Figure 4-39b. The effect of using lower aspect ratios is investigated for both hairiness and irregularity measurements in the relevant chapters in order to determine the minimum aspect ratio that can reliably be used in yarn testing. This limit determines the maximum testing speed as follows.

$$(V_0)_{\max} = \frac{(\text{Line Rate})_{\max} \cdot c_y}{(AR)_{\min} m} \quad (4.33)$$

For example, for the camera used in this research, the maximum line rate is 18.8 kHz and $c_y=14\mu\text{m}$. If aspect ratios down to 1/5 can reliably be used at a magnification of

1, then the maximum yarn speed will be 79m/min. Currently there are line scan cameras in the market that can achieve 5 times the data rate of this camera (e.g. Dalsa CT-F3-2048) and if such a camera were used, the maximum speed would be nearly 400m/min. However the prices for such cameras are currently quite high (The price of Dalsa CT-F3-2048 is \$17688 as of May 2004), but it can be expected in the near future that they drop down to a reasonable level for a yarn testing equipment.

4.9 Comparison of back-lit and front-lit illuminations

It has been shown in previous sections that the fibre profiles turn out to be different under front-lit and back-lit illuminations at the same defocus distances. In this section two different illumination types are compared in terms of their ability to detect out of focus fibres and minimum allowable separation between fibres in order to be able to resolve the gap between them. Also analysed is the effect of thresholding on fibre diameters under various misfocus conditions.

Figure 4-40 shows ideal profiles of two 16 μm fibres separated by 160 μm . When the fibres are defocused by 2mm under front-lit illumination, the fibre profiles get wider and shorter and upon digitisation they blur further as shown in the same figure. If a threshold is applied to the profile, the fibre widths will turn out to be wider than they actually are. Furthermore, if the threshold level is below the minimum intensity in the middle of separation distance of the fibres, the fibres will not be identified as separate. It is appropriate at this point to make a couple of definitions to be used throughout the section. The minimum separation distance in order for two fibres to be identified as separate for a specific threshold level and misfocus will be referred to as **minimum resolvability**. The fibre width measured upon thresholding is called **measured diameter** and **grey level sums**, which will be used in hairiness evaluation in Chapter 6, is defined as the sum of intensities above the threshold level beneath the profile. Finally, **maximum allowable misfocus** is the defocusing distance where the fibre cannot be detected at all, i.e. the peak intensity falls below the threshold.

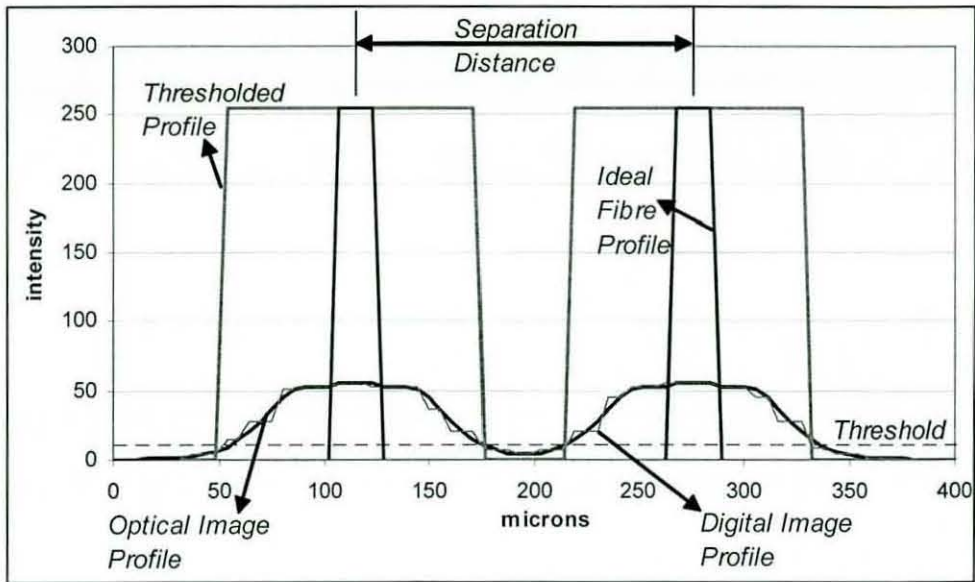


Figure 4-40

The two arrangements that will be compared are a front-lit illumination with F8 aperture and a back-lit illumination where the light source has a 5mm Gaussian profile and placed at 700mm from the camera objective. The magnification is taken as 1 and the lens with a focal length of 100mm. Analysed fibre width is 16μ . The pitch of the camera is taken as 14μ with a fill factor of 100% and the vertical aspect ratio as 1. Finally, the wavelength is assumed to be 670nm.

Figure 4-41 shows defocus profiles under back-lit illumination along with the digitised and thresholded versions. Two different threshold levels are analysed for back-lit images, the first taken as 50% and the second 70% of the background intensity. These values are selected arbitrarily to provide a comparison between different threshold levels in back-lit images. It can be seen that the first threshold cannot detect fibres defocused more than 8.5mm, while the second can pass all defocus profiles. On the contrary, the first threshold appears more advantageous than the second in that, measured diameters are the same for all defocusing distances.

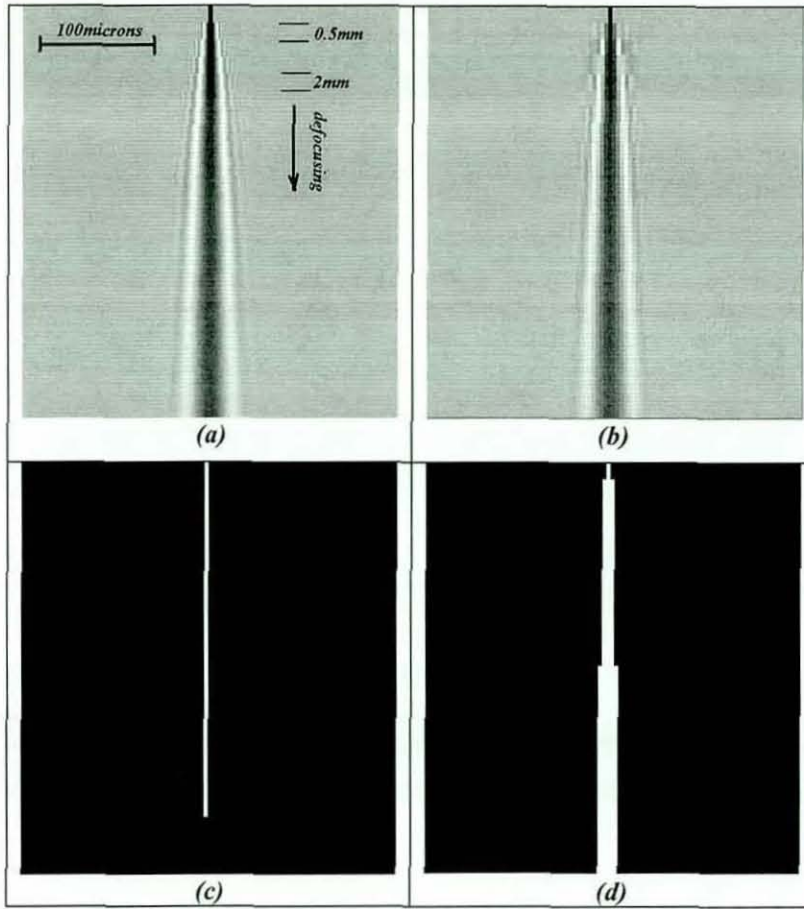


Figure 4-41 a) Profiles of a $16\mu\text{m}$ fibre under back-lit illumination at increasing defocus distances, b) (a) After CCD sampling, c) (b) after applying first threshold, d) (b) after second threshold

Figure 4-42a shows defocus profiles for front-lit illumination. The threshold level applied in this case is taken as 4% of the maximum intensity. This corresponds to a grey level value of 10 in an 8bit image. The experiments with dark field and front-lit illuminations showed that this threshold level is the minimum that can be applied due to the background noise. A rapid increase is seen in the measured diameter with increasing defocus distances in Figure 4-42b. The maximum allowable misfocus on the other hand turns out to be 7.5mm. However in actuality this distance will be less due to other possible degradations in the acquisition system.

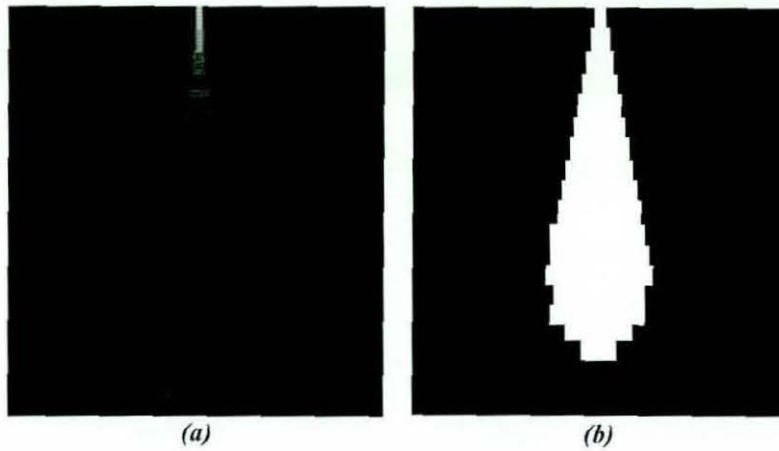


Figure 4-42 a) Defocus Profiles under front-lit illumination, b) (a) after CCD sampling and thresholding at 4% of maximum intensity.

Figure 4-43 shows comparison of measured diameters for thresholded images mentioned above. The change in diameter is quite significant for front-lit images where the measured diameter rises from 42 to 378 μm when the fibre is defocused by 7mm, while for the second thresholded back-lit image it changes only from 28 to 56 μm . First thresholded back-lit image on the other hand exhibits the most consistent measurements for varying defocus distances, however at 8.5mm defocus the fibre cannot be detected at all. Depending on the widening of the fibre profiles, minimum resolvability for front lit illumination varies from 45 μm for in-focus fibres to 445 μm for a defocusing of 7mm. The back-lit illumination requires a minimum fibre separation of 32 μm for in-focus fibres and up to 70 μm for defocused fibres as far as 11mm.

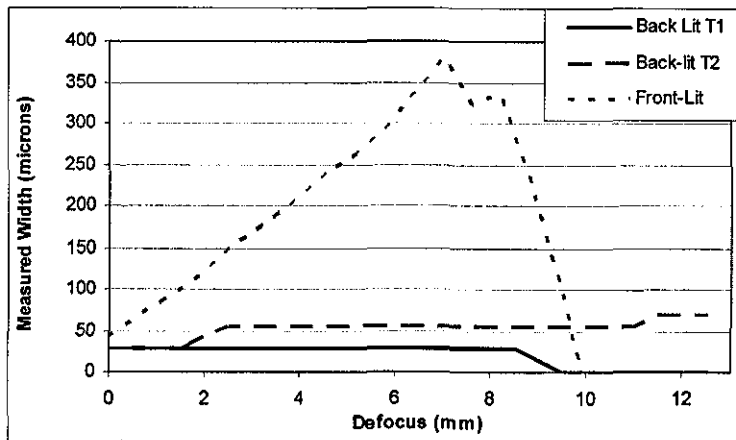


Figure 4-43 Comparison of measured diameters

In Figure 4-44 relative grey level sums within the thresholded profiles is shown. The front-lit image exhibits very good consistency up to a defocus distance of 7mm. Second thresholded back-lit image also appears to exhibit a small variation that is only within a range of $\pm 20\%$ for defocusing up to 11.5mm, while for the first thresholded image, the intensity sum drops by 25% at 8mm defocusing. It can be said that for both illumination techniques the grey level sums are not seriously affected by defocusing.

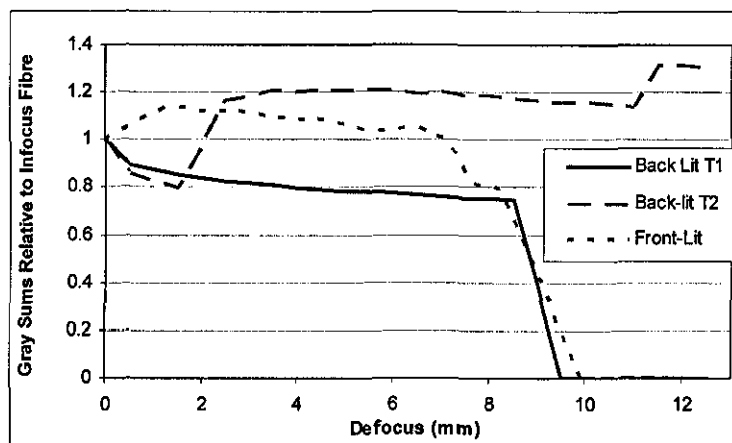


Figure 4-44 Comparison of grey level sums relative to the grey level sum of in focus fibres

4.10 Conclusions

Front-lit illumination is theoretically modelled and investigated in detail. It is seen that under front-lit illumination, the defocus aberration creates a very significant problem widening the observed diameter and decreasing the contrast. Possible improvements on depth of field are discussed regarding the light and lens characteristics, however no method is found to achieve the required depth of field to detect the hairs. The mechanical guiding technique suggested by Millman appears to be the best solution to this problem.

A mathematical equation is derived using the Fresnel diffraction theory in order to model the back-lit illumination. The effects of illumination parameters such as the size of the light source and its distance from the yarn are investigated. It is seen that moving the light away from the yarn increased the defocusing characteristics, however this improvement was only negligible after around 500mm and the fringe patterns started to become more significant further from that distance. It is also observed that a chromatic light source could be advantageous over a monochromatic one in terms of the decreasing amplitude of fringes appearing in the images. The size of the light source is found to be very important and it is seen that the contrast of a defocused fibre in the image can rapidly decrease as the size of the light source is increased.

Other aberrations such as off-axis displacement in back-lit illumination, spherical aberration and chromatic aberration are briefly mentioned but their effects are found negligible for the imaging system used in this research.

Digitisation of the yarn images regarding the line rate of the camera, the exposure times, the dimensions of CCD array and the yarn transfer speed is also modelled and the effects of these parameters on yarn image quality are discussed.

Based on the theoretical models, front and back-lit illuminations are compared under various defocus distances. Back-lit illumination is shown to be superior to front-lit illumination in terms of its capability to detect out-of-focus fibres. Integration of grey levels of both front-lit and back-lit images is found to give better information on fibre widths compared to counting the pixels considering the widening in widths under out-of-focus conditions.

CHAPTER 5 - Yarn Illumination and Image Processing Techniques

5.1 Introduction

In Chapter 3, the image formation process has been analysed and the factors affecting the yarn image quality have been investigated. This chapter covers experimental results using different light sources and arrangements as well as processing algorithms developed to process images acquired using different set-ups.

It is evident that the light and the illumination arrangement together play an important part in the acquisition and overall pre-processing of yarn images. The illumination methods in the literature used for yarn imaging can be categorised in three main groups, which are back-lit (e.g. Zweigle G565), front-lit (e.g. Cybulska [1999]) and dark field (Uster Tester Hairiness Attachment) illuminations. Both methods are implemented using various set-ups during this research with particular interest to back-lit illumination due to many advantages that it provides such as superior misfocus tolerance and contrast.

The first section (5.2) describes different back-lit illumination arrangements and a dark field illumination set-up both used for low magnification yarn inspection, which aims measurement of hairiness and diametric irregularity. This is followed by investigation of a number of illumination methods used for high magnification yarn imaging (Section 5.3).

In Section 5.4, the problem of yarn image segmentation is addressed and various image processing algorithms for low magnification images are introduced to perform

this task. Image processing algorithms for high magnification images to measure the yarn twist are covered in Chapter 7.

5.2 Illumination methods for low magnification

5.2.1 Back-lit illumination methods

Factors affecting the background quality and blurring of defocused fibres in backlit illumination were investigated in section 3.5. This section briefly discusses some practical results obtained using different back lighting set-ups. The comparison will be based on three different criteria namely the uniformity and width of the background in the images, the allowable minimum exposure times which depends on the maximum intensity of the light source and the shadow quality in terms of blurring and contrast. The back-lit yarn images in this section are acquired at a yarn transfer speed of 6m/min.

The simplest case for backlit illumination is placing the yarn between a light source and the camera as shown in Figure 5-1. The background formation in this arrangement is due to the blurring of the light source as discussed in section 3.5. Also discussed were the limitations on field of view depending on the distance of light source from the yarn (r_0), the aperture size and magnification. Figure 5-2 shows an image acquired using a 20W tungsten filament bulb placed 550mm from the yarn. It can be seen from the image that all pixels can not effectively be used on the CCD array. In the image shown in Figure 5-2, only 1500 pixels out of 2048 can be used which corresponds to a 21mm wide section on the object plane while 28.8mm were possible. An obvious solution to this is to increase the aperture. Although the maximum aperture for the lens used in the experiments is 3.5, lenses with smaller f-numbers are commercially available. For the arrangement given in Figure 5-1, an f-number of 2.6 would suffice to efficiently use the whole range of CCD array.

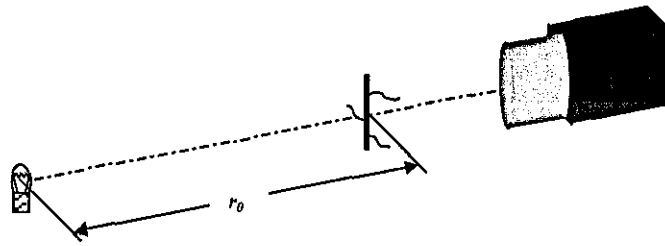


Figure 5-1 Back-lit illumination with a single halogen lamp

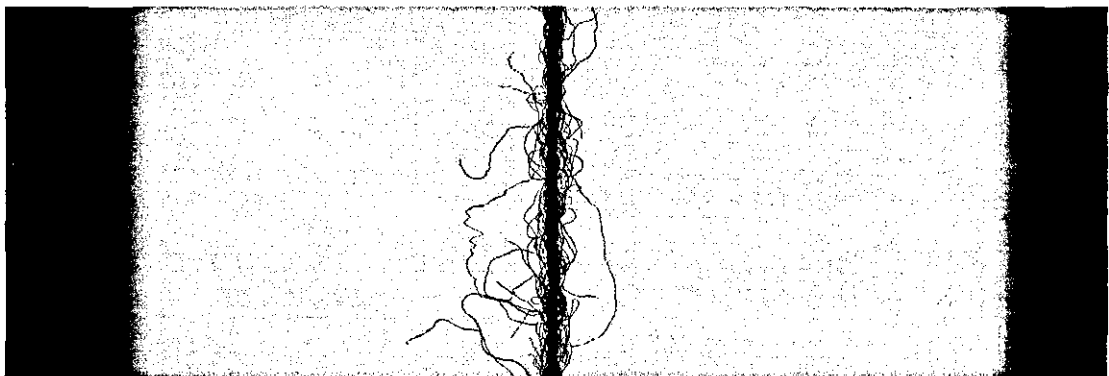


Figure 5-2 A yarn image acquired using the set-up in Figure 5-1

The image quality on the other hand is quite satisfactory and almost none of the out of focus fibres significantly blur in the images. Figure 5-3 shows profiles of a $45\mu\text{m}$ Polypropylene (PP) fibre at 0 and 10mm from the exact focus plane, where it can be seen that the fibre profile is only slightly attenuated even at 10mm defocusing. The minimum allowable exposure time is around 500ns with the halogen tungsten bulb used in the experiment. However, similar bulbs with as much as 22.5 times more power are commercially available, which can reduce the required exposure times down to much less than 50ns enabling the use of maximum line rate of the camera.

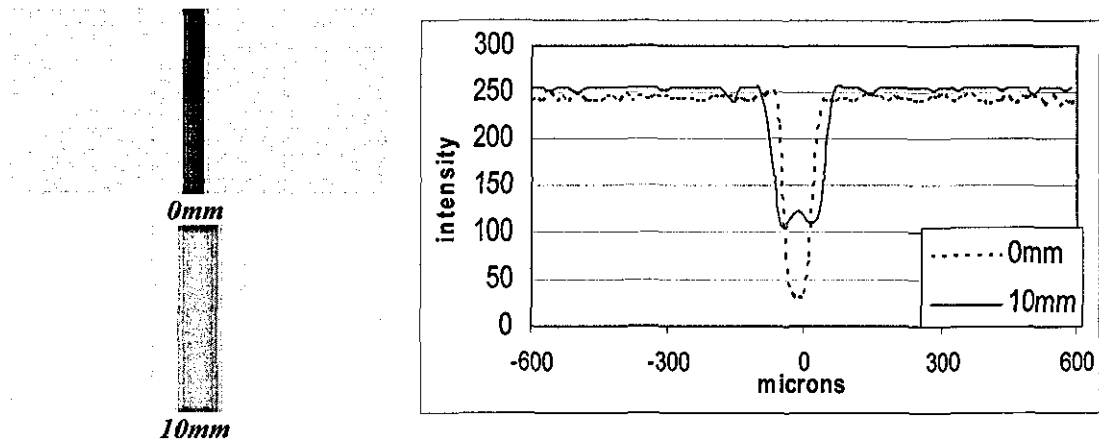


Figure 5-3 Profiles of a 45 μ PP fibre at exact focus plane and at 10mm defocusing using the set-up in Figure 5-1

An LED light source with 1800mcd luminance and 670nm wavelength is also tested with the same arrangement. Figure 5-4 shows an image acquired using this LED light. The image characteristics are almost the same as when a halogen lamp is used. The diffraction fringes however are slightly clearer with the LED light. The reason for this has been explained in section 4.7. The required exposure time for a single line acquisition was around 20 μ s which means that a similar LED light had to be 268cd to enable the maximum line rate. However a single LED with this luminance is not commercially available. A set of LED lights can be used together in order to achieve the required illumination intensity but this will degrade the yarn image quality as the effective width of the light source is increased (see section 2.3). For this reason, halogen lamp is found superior to the LED light sources for back-lit illumination.

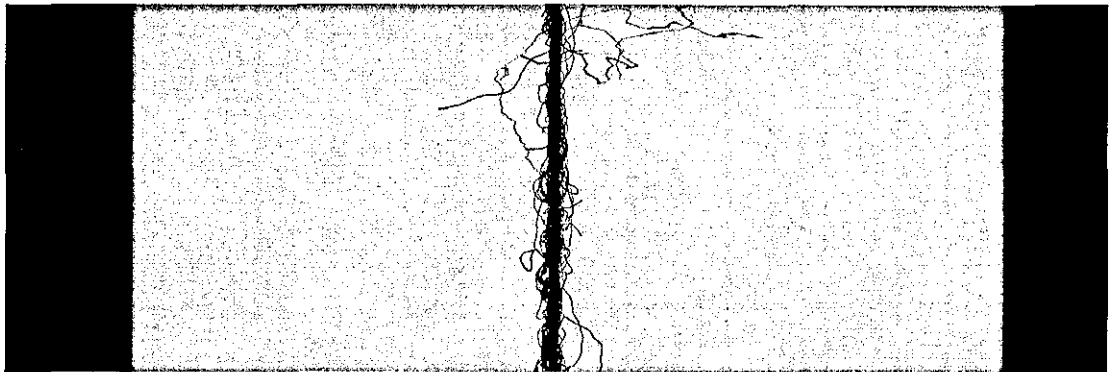


Figure 5-4 Yarn image illuminated with an LED light from behind.

In order to increase the effective field of view, a field lens can be used as shown in Figure 5-5. The basic principle in this arrangement is to focus the light source to the aperture of the camera lens.

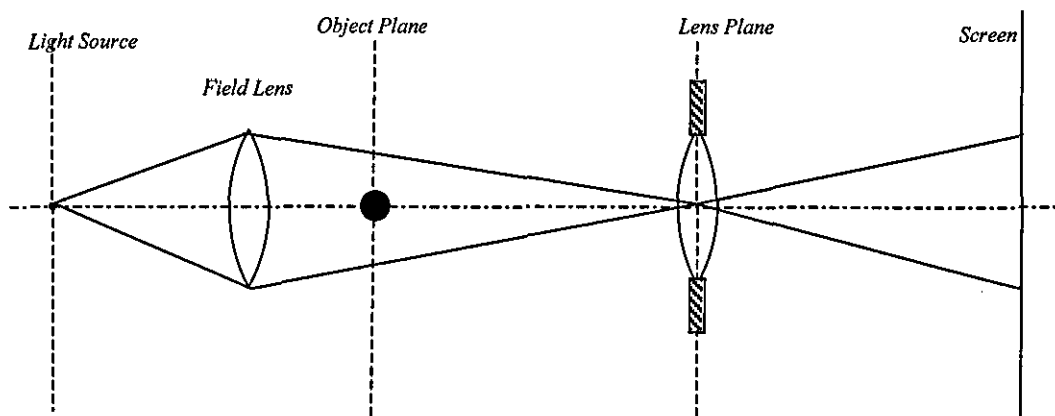


Figure 5-5 Field Lens arrangement

Figure 5-6a shows an image captured using a halogen lamp and a 30mm field lens. It can be seen that the whole range of CCD array contribute in the image. Another important superiority compared to other techniques is that the exposure time can be set to 50ns for each line scan even at one fifth of the maximum intensity of the filament bulb. At this exposure setting, it is easily possible to achieve the maximum line rate of the camera (18.8 kHz). The background however is not quite uniform in the image because of the non-uniformity of the light source. The background can be enhanced using flat field correction, which is done simply by subtracting the

background image from the yarn image or by dividing the intensities of every single pixel by the corresponding background intensity and weighing by a certain factor. Figure 5-6b shows the yarn image after flat field correction where the improvement in the background can clearly be seen.

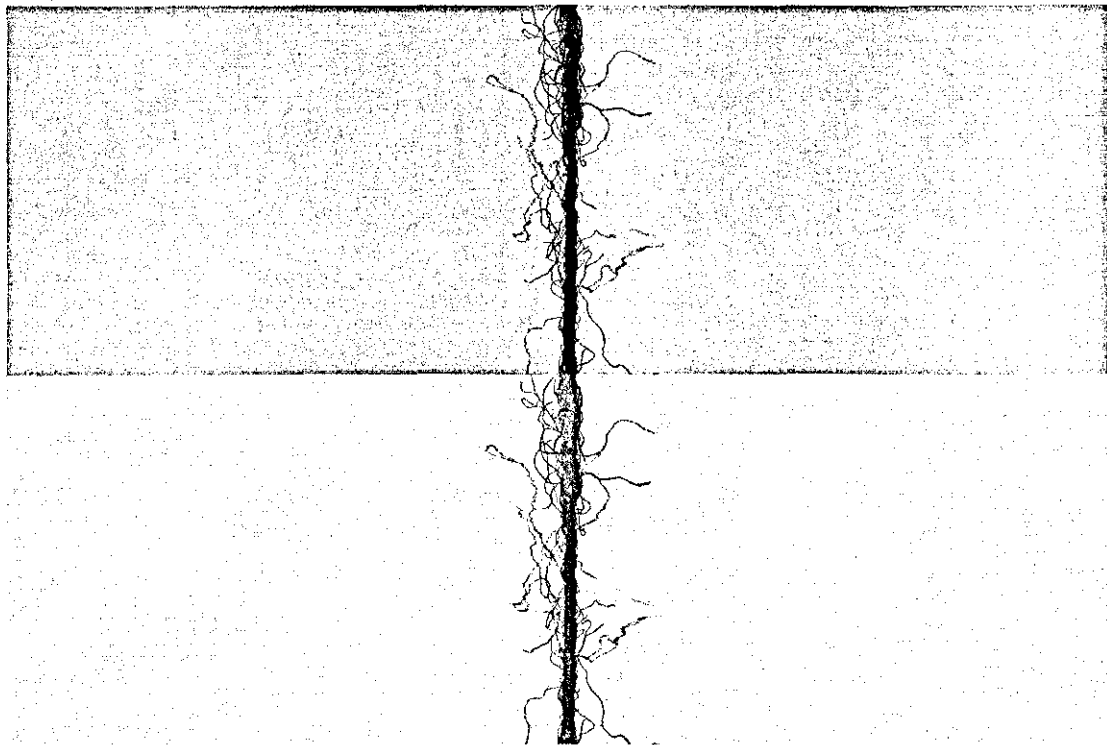


Figure 5-6 a) Yarn image acquired using the field lens set-up, b) Yarn image after flat field correction

The blurring of fibres due to defocusing has been found to be a significant problem in this arrangement. Figure 5-7 shows profiles of a 45μ PP fibre at 0 and 6mm from the exact focus plane. The blurring will of course be more severe for thinner fibres. One of the main factors contributing to the out of field degradation is that the effective size of the light source is magnified through the field lens (see section 3.6).

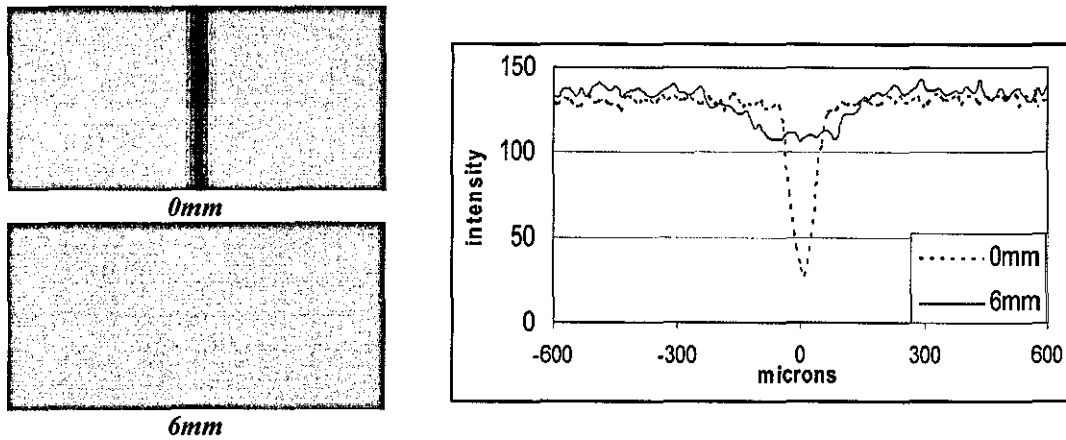


Figure 5-7 Profiles of a 45μ PP fibre at exact focus plane and at 6mm defocusing under field lens illumination

In order to increase the width of the illuminated region on the CCD plane another method is using a diffuser as depicted in Figure 5-8. Figure 5-9 shows a yarn image acquired using a diffuser 50mm both from the yarn and a tungsten filament bulb in opposite sides. It can be seen that the background is quite uniform and wide; however the image quality is quite low with low contrast and poor depth of field.

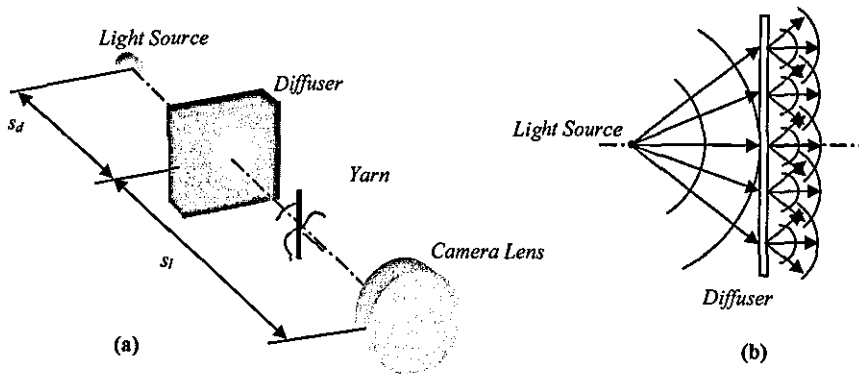


Figure 5-8 a) Arrangement where a diffuser is used to increase the effective size of the light source. b) Scattering of light rays after passing through the diffuser.

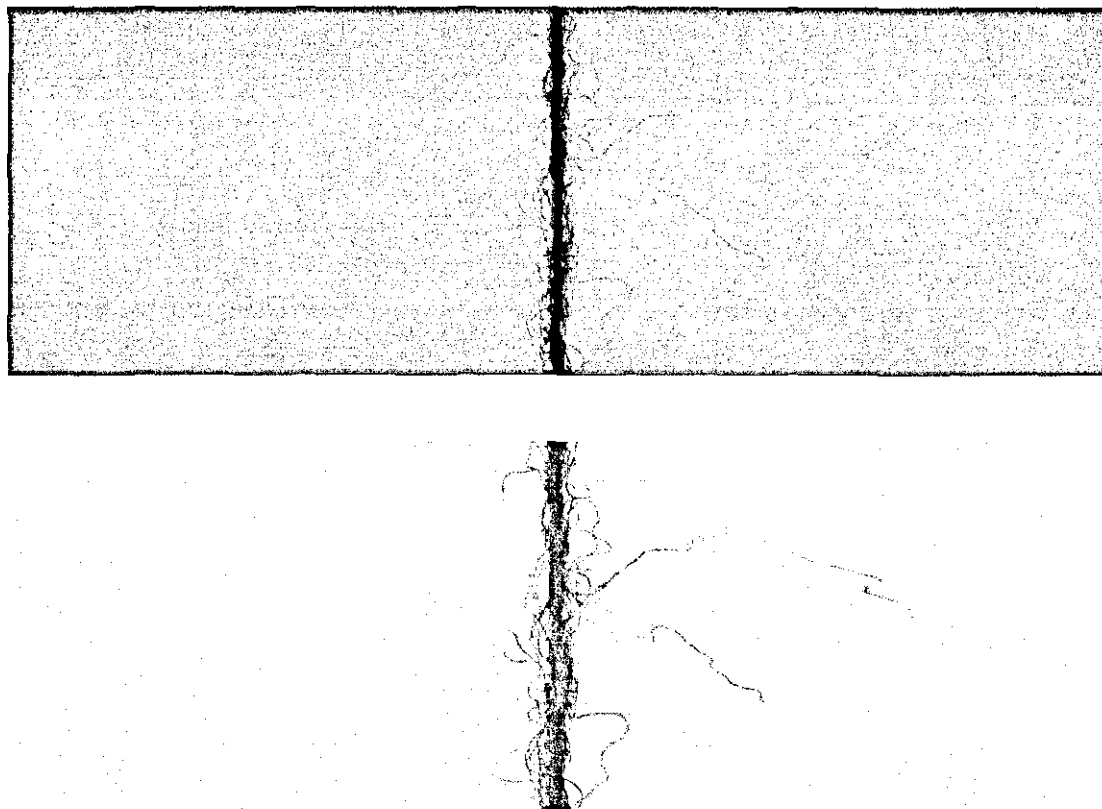


Figure 5-9 a) Image of yarn illuminated using a diffuser, b) (a) after flat field correction

5.2.2 Imaging of Two Orthogonal Views

Since the shape of the yarn core is not always circular, measurement of the yarn diameter and the diametric irregularity from a single view might be erroneous. Jackson et.al.[1995] used an optical arrangement for imaging the two orthogonal views of a yarn using a single camera and a mirror placed 45 degrees to the optical axis. A similar arrangement as shown in Figure 5-10 has also been implemented during this research. An important problem with this arrangement is that if the camera is focused to one side of the yarn, then the other side will be out of focus by a distance of δ as shown in the figure. To equalise the optical path lengths for both sides, the camera is focused to $OPL + \delta/2$. However, in this case the images of both sides will have a misfocus error corresponding to a distance of $\delta/2$. In order to minimize the misfocus error, δ is kept as low as possible at around 1.4mm, assuming

that the core diameter is always below this value. This distance allowed separation of two orthogonal views in the images for the entire range of yarns used for the experiments. Furthermore, the light source is placed around 700mm away from the mirror to minimize the edge blurring due to misfocus. Figure 5-11 shows an Ne10 100% cotton yarn image acquired using this set-up.

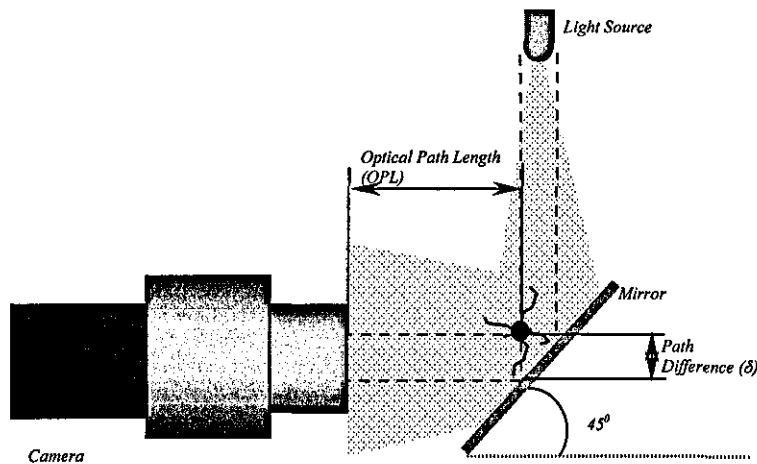


Figure 5-10 Arrangement for imaging of two orthogonal views

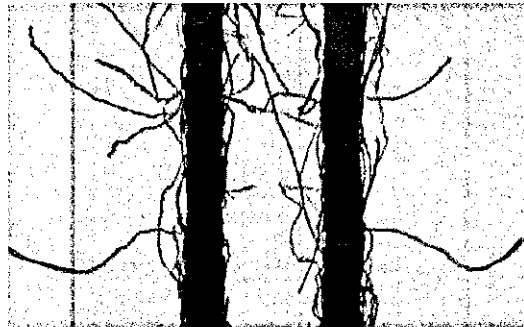


Figure 5-11 Image of a yarn taken using the set-up in Figure 5-10

Millman [2000] suggested focusing the camera to one of the sides and inserting a medium such as glass that has a higher refractive index from the air and by setting the dimensions of the medium so that the optical path length for the second view would be the same as that of the first view. Although he did not implement this arrangement it is an interesting solution to the optical path difference problem. However, with such an arrangement, further degradations in the image might be

expected arising especially from imperfections in the glass medium. We have shown that with the arrangement implemented in this research which has a 0.7mm defocusing for both sides and the light source placed 700mm from the mirror, the error in diameter measurement was negligible.

Figure 5-12 shows the profiles of a 400 μ m wide core at 0mm and 0.7mm defocusing simulated using the parameters of the implemented arrangement ($r_0=700$ mm, $w_L=5$ mm, $\lambda=550$ nm). After applying a threshold to the images, the diameter appears to rise up to only 412 μ m at 0.7mm defocusing. Considering that the pixel pitch of the camera is 14 μ , this difference is negligible at 1:1 magnification. This has also been verified experimentally in Chapter 6, where the diameters of various samples were found to be almost the same when imaged from a single view and two orthogonal views. Nevertheless, 1.4mm separation between two orthogonal views is only suitable if the elliptical diameter is of interest only. In order to measure the hairiness of two orthogonal sides, this distance should be at least 20mm to avoid interference of hairs from separate views. In this case the widening of core due to defocusing would be an important problem.

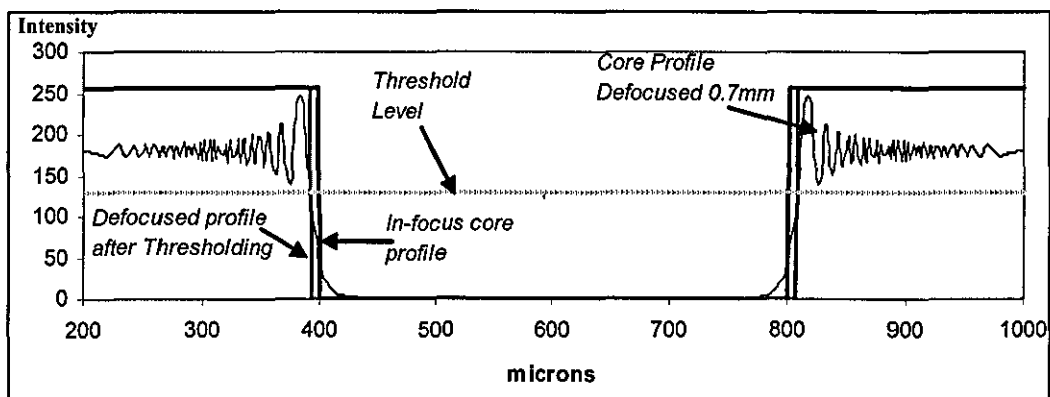


Figure 5-12 Simulated profile of a 0.4mm thick yarn core at 0.7mm defocusing for a 550nm light source with 5mm wide Gaussian profile placed 700mm away compared with the in-focus profile.

5.2.3 Dark Field Illumination

Dark field illumination is a well known technique to illuminate the yarns especially for measuring hairiness. The method is used for hairiness measurement in Uster Tester 4 which uses infrared laser light. Barella implemented dark field illumination in his ITQT tester using a pair of tubular incandescent lamps. Millman [2000] used a fluorescent ring light for dark field illumination. Bamforth [2002], for his lace scalloping system, built an LED ring light arrangement. He found this illumination to be superior to back-lit and front-lit illuminations in that it was easier to determine the boundaries of the lace edge without being affected by the loose fibres, since the denser edges appeared black while the loose fibres were bright. For yarn illumination, a similar arrangement was designed during this project by placing 46 LED lights around a circle of 55mm of diameter. The main difference is that the LED lights are rotated 45 degrees towards the optical axis in order to increase the intensity of light falling onto yarn as shown in Figure 5-13. Furthermore, a field aperture placed between the yarn and the camera is found necessary, which provided a significant improvement on the image background as shown in Figure 5-14. The size of the aperture is set to 3cm, which is slightly more than the field of view (2.8cm).

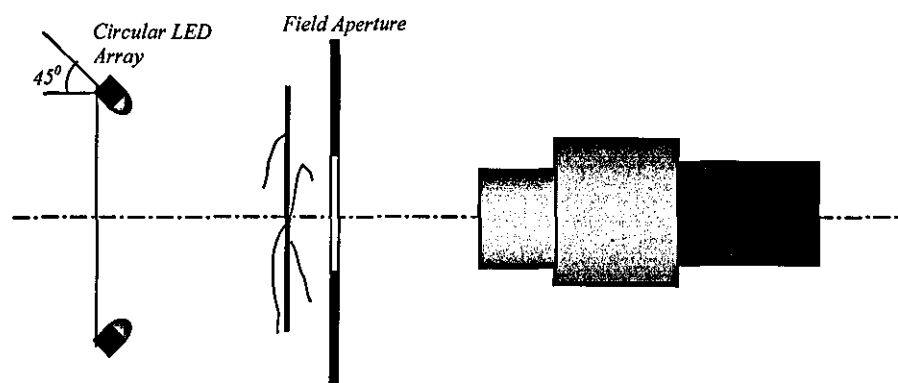


Figure 5-13 Dark Field Illumination Arrangement

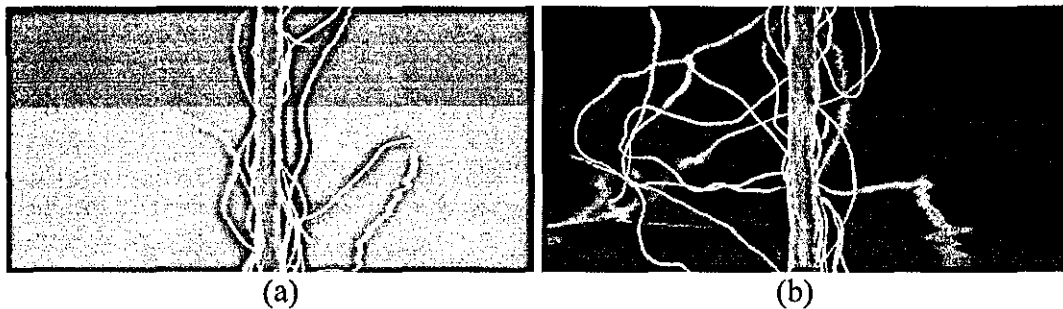


Figure 5-14 Yarn images under dark field illumination: a) without and b) with field aperture. (F5,6; m=1)

One of the problems with the dark field illumination is that different fibres exhibit different brightness levels in the image. This is due to different light absorption levels of fibres with different thickness, material and especially colour. Uster reported that the scattering of light from fibres is not significantly affected by fibre thickness. This might be true for the range of cotton fibres; however it would be erroneous to expect the same amount of scattering from, for example, different synthetic fibres ranging from $5\mu\text{m}$ to $80\mu\text{m}$. The colour on the other hand strongly affects the light absorption especially when using a light source within the visible spectrum. Figure 5-15a-b show images of two 40/60 wool acrylic Nm 30 yarn samples one dyed with black and the other with red colour, where the difference in brightness can clearly be seen. As a result of this, after processing the images, the red fibres appear thicker than the black ones as can be seen in Figure 5-15c-d. One solution to this can be using infrared light as in Uster Tester, nevertheless some dye stuffs are reported to absorb infrared light as well (Barella, [1996]). On the other hand, when using infrared light, the depth of field will decrease due to the increased wavelength. Probably the best solution to the problem is that adopted by Barella in his ITQT tester which adjusts the intensity of the light source automatically according to the maximum intensity in the video signal.

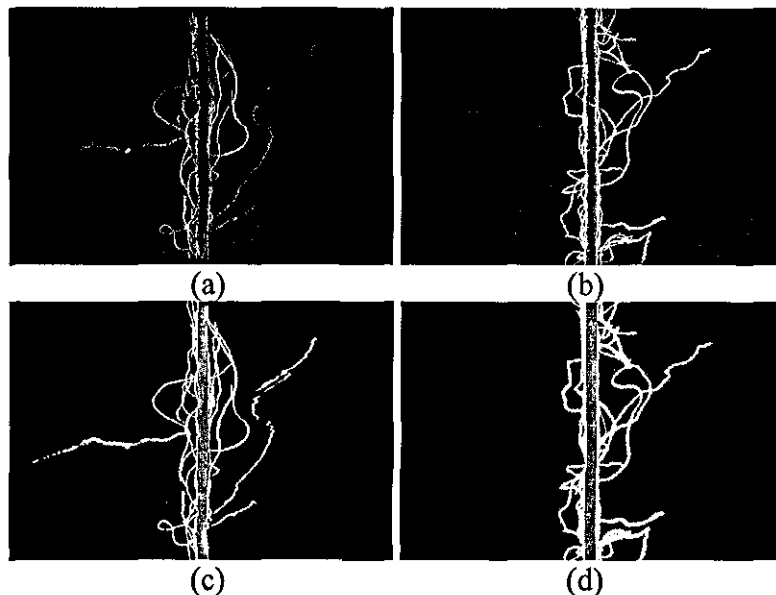


Figure 5-15 Dark field images of two 40/60 wool acrylic Nm 30 yarn samples with a) black and b) red colour (F11; $m=1$). (c) and (d) show (a) and (b) respectively after image processing (see section 5.4.3).

Required exposure time for one line scan when using dark field illumination is around $5\mu\text{s}$ for an aperture set at F5.6. For a larger aperture the required time will of course be less, however still far above 50ns exposure time that is required to achieve maximum line rate. Nevertheless, dark field illumination is investigated in detail during this research in order to examine the differences in nature of hairiness and irregularity measurements compared with back-lit illumination. In future work, the exposure time can be reduced if necessary using a more powerful light source such as a laser.

5.3 Illumination methods for high magnification

High magnification is essentially used for twist measurement and also if more accurate determination of core diameter is required especially for fine yarns. Magnification can be increased by moving the lens further from the CCD plane using extension tubes. Line scan cameras are not found suitable for yarn surface inspection due to the rotation of yarn while being transferred, which is caused by propagation of

twist when some tension is applied to the yarn. For this reason, area scan cameras are used for imaging the yarn surface.

During the first year of this research much work was done on coherent illumination which mainly concentrated on high magnification imaging. For image acquisition, a Sony XC55 progressive scan camera was employed. Figure 5-16 shows the back-lit illumination set-up, which uses a 633nm 1.5mW He-Ne laser. The high intensity of the laser beam is reduced using a green Kodak wratten gelatine filter and an ND 4 filter placed in front of the camera lens. A 5X beam expander is employed that provided around 7mm wide laser beam. Figure 5-17 shows a yarn image acquired using this set-up. Very uniform background and good contrast characteristics of the image make this sort of illumination very suitable for a more precise determination of the core diameter.

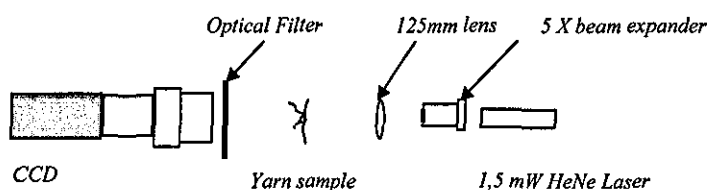


Figure 5-16 Coherent back-lit illumination

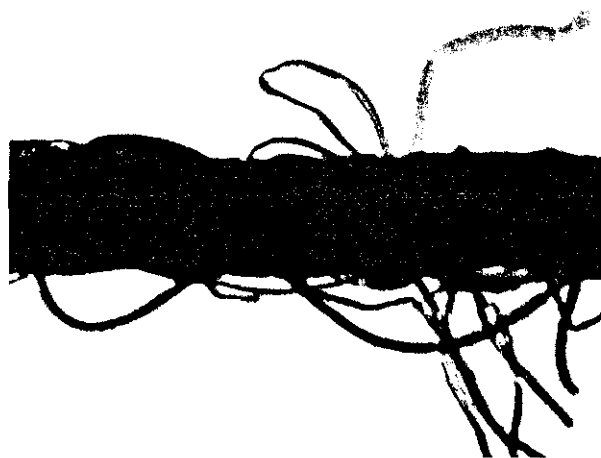


Figure 5-17 A high magnification 70/30 polyester/cotton image using set-up in Figure 5-16

A hybrid of coherent back-lit and incoherent front-lit illuminations depicted in Figure 5-18 is also tested in order to measure yarn twist. The incoherent light source is a 150W filament lamp, where the light beam is directed onto the yarn surface using a fibre optic cable. Figure 5-19 shows a yarn image acquired using this set-up, where the twist details can also be seen in addition to good contrast and uniform background characteristics.

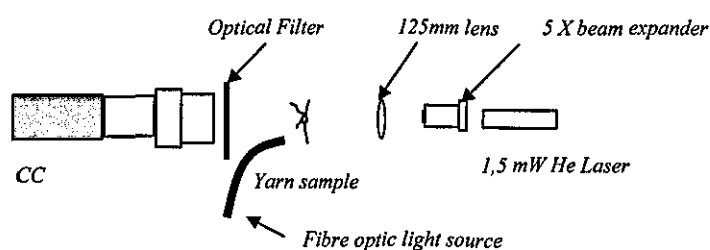


Figure 5-18 A hybrid illumination set-up using coherent back-lit and incoherent front-lit illuminations.

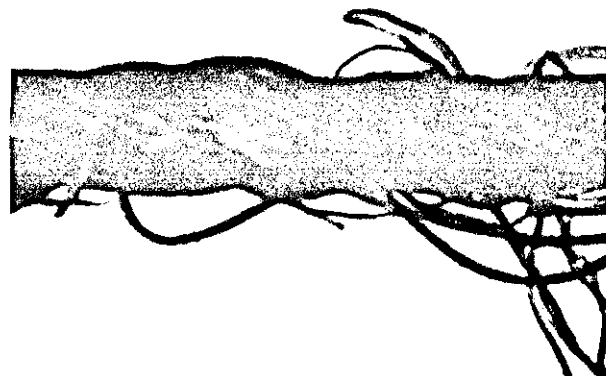


Figure 5-19 Yarn image acquired using set-up in Figure 5-18

For yarn surface imaging, the key point is to find an illumination which provides a good contrast between surface fibres and the borders between them, i.e. the borders have to appear dark while the fibres bright. Figure 5-20 illustrates a co-axial front-lit illumination set-up, where light rays from the diffuser reflect off the beam splitter directly on to the yarn at 90° . It can be seen from Figure 5-21 that co-axial illumination can provide a uniform core image but it lacks contrast within the

surface, since the light rays are also evenly reflected from the rims. Figure 5-22 shows the same yarn section under dark field illumination where the surface details can more clearly be seen.

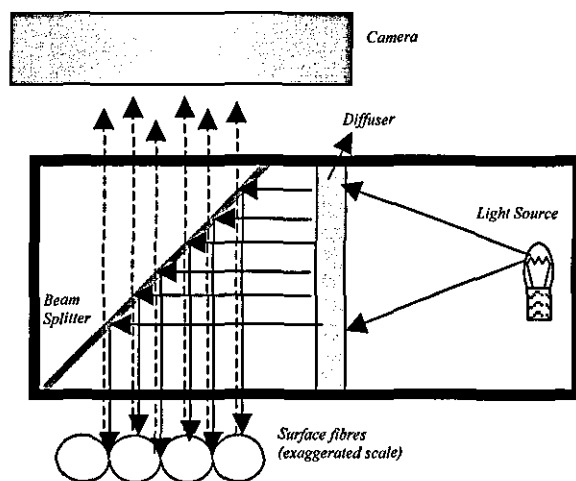


Figure 5-20 Co-axial illumination

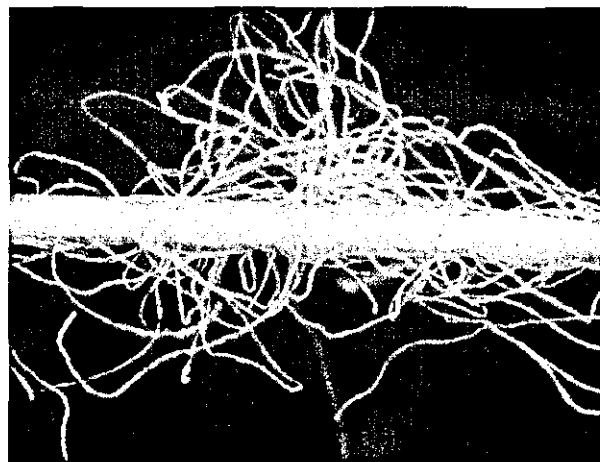


Figure 5-21 Image of a yarn illuminated with co-axial illumination

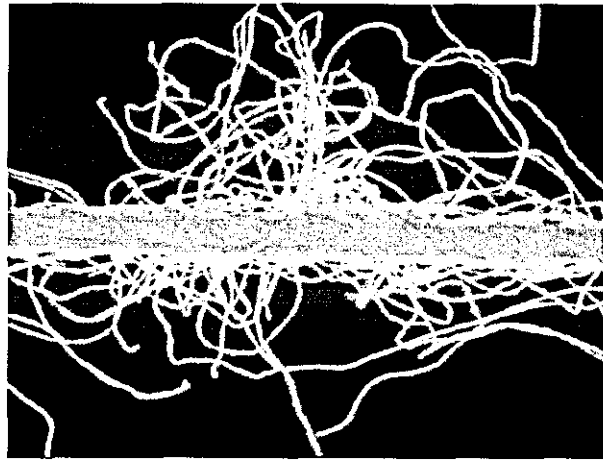


Figure 5-22 Yarn section in Figure 5-21 under dark field illumination.

A ring light is also tested in order to provide different reflection angles to the fibre surfaces and rims as depicted in Figure 5-23, where the yarn is also back-lit using an incoherent light source and a diffuser. There is a certain improvement on the surface contrast as shown in Figure 5-24. When there is no back lighting, there is a gradual decrease in the intensity at the edges making it difficult to locate the core boundaries. However, even when there is back lighting, overall contrast of the image is poor compared to coherent back-lit and incoherent front lit hybrid arrangement shown in Figure 5-18.

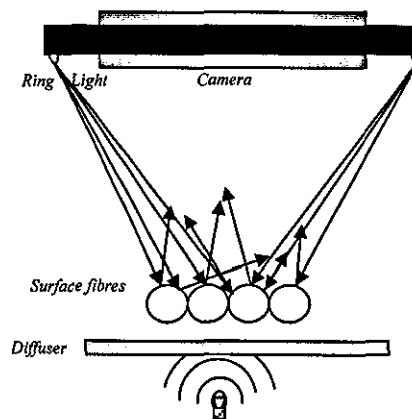


Figure 5-23 Incoherent back-lit and front-lit illumination hybrid where a ring light is used for front-lit illumination

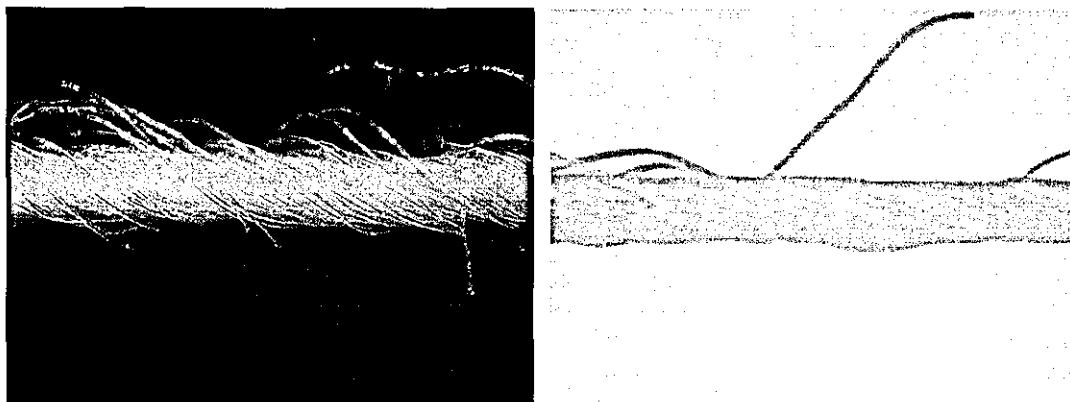


Figure 5-24 Yarn images acquired using ring light for front lit illumination without (Left) and with (right) additional back-lit illumination

5.4 Yarn Image Segmentation

The initial problem of yarn image processing is to find the boundaries between background, core and the hairs. Most of the techniques in the literature scan the yarn perpendicular to the core axis and take the longest connected segment as the core. When using high vertical resolutions, this assumption can sometimes cause hairs lying along the scan line to be identified as the core. Furthermore, there is generally no significant change in the intensity of the CCD signal between highly dense surface fibres and the core. This increases the core diameters if a simple threshold is applied. These problems are addressed in this section and some solutions are developed.

5.4.1 Image Enhancement and Preprocessing Methods for Back-Lit Yarn Images

The histogram (grey level distribution) of a yarn image often has a bimodal shape as shown in Figure 5-25. The first peak in the histogram belongs to the core pixels along with the in focus hairs which appear dark in a back-lit image. The second and larger peak arises from background pixels, which gets narrower for increasing uniformity of the background, allowing a clearer distinction from the first peak.

There are also some pixels falling between these two peaks that come from two different sources, which are i) out of focus hairs and ii) isolated background pixels in between dense fibres occurring especially in close vicinity of the core.

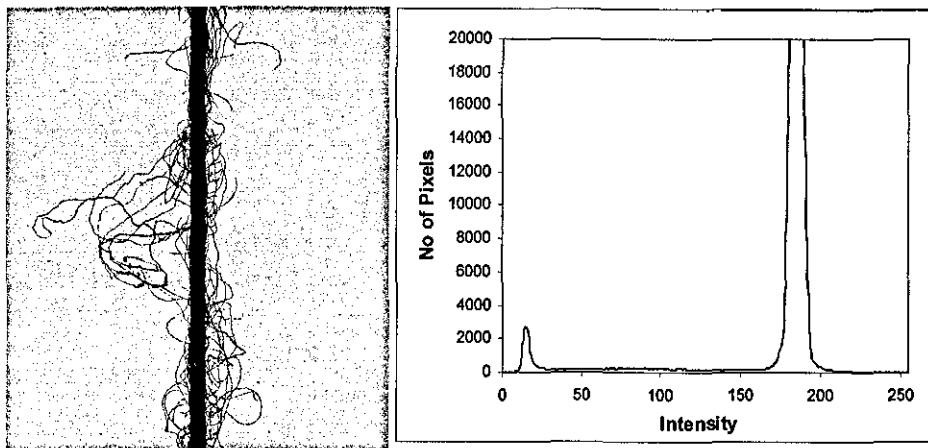


Figure 5-25 A back-lit yarn image and its histogram

Figure 5-26 shows a horizontal image profile where these two types of pixels can be seen. Upon a single thresholding, it is likely that either the shadowed background pixels are considered as part of the yarn or out of focus hairs are underestimated depending on the threshold level. Three algorithms are developed to overcome this problem, which are described below.

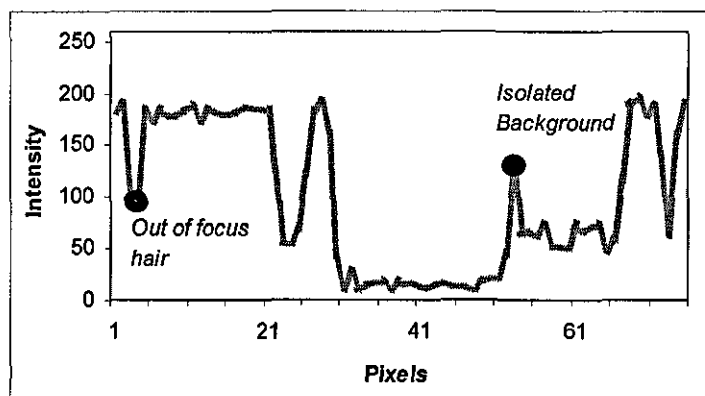


Figure 5-26 A horizontal profile showing an isolated background pixel and an out of focus hair.

5.4.1.1 Contrast Enhancement Using Convolution Filters

This technique involves applying a Gaussian filter followed by a Laplacian filter with a kernel sum of unity. Note that the second operation in this sequence is equivalent to applying a Laplacian filter and then adding the result to the original image. The Gaussian filter aims to eliminate small variations arising from noise especially within the core and background regions, since the Laplacian filter is quite sensitive to noise. Figure 5-27 shows typical 3x3 Gaussian and Laplacian filter kernels.

1	2	1	x 1/16	0	-1	0
2	4	2		-1	5	-1
1	2	1		0	-1	0
Gaussian Filter				Laplacian Filter		

Figure 5-27 Contrast enhancement filters

It has to be noted that, rather than applying a Laplacian and Gaussian filters separately, a common way in the literature is to find the convolution of Gaussian function with the Laplacian and derive a single convolution filter from the resulting function. This filter is known as the Laplacian of Gaussian (LoG) filter. However, for a filter size of 3x3 it is found more appropriate to perform the convolutions in two steps rather than using a single combined filter since this filter size is too small to describe the LoG function. Figure 5-29b shows the effect of applying these two filters to the yarn image.

It was later found that a filter with a size of 5x5 with the kernel shown in Figure 5-28 would be more suitable to handle isolated pixels and defocused fibres. The reason for this is that when a 3x3 filter is applied on an isolated pixel the contrast is increased according to the intensity difference between an isolated pixel and the edge of a fibre. On the other hand, a 5x5 kernel is more likely to calculate the intensity difference between the isolated pixel and the centre of the fibre, which results in a better improvement in the contrast. The same principle applies to a defocused fibre in

the image: a 5x5 kernel will find a bigger difference between the centre of the fibre and surrounding background pixels since an average fibre appears 3-pixel wide in the images. A C code is written to apply this filter that only performs 4 operations at each convolution omitting the cells with zeros, hence no increase in processing time compared to 3x3 kernel. Figure 5-29c shows the effect of this filter on the original profile, where it can be seen that the contrast between defocused fibres and isolated pixels is increased more than that after applying the 3x3 Laplacian filter.

0	0	-1	0	0
0	0	0	0	0
-1	0	5	0	-1
0	0	0	0	0
0	0	-1	0	0

Figure 5-28 Improved Laplacian filter applied to yarn images after Gaussian Filtering

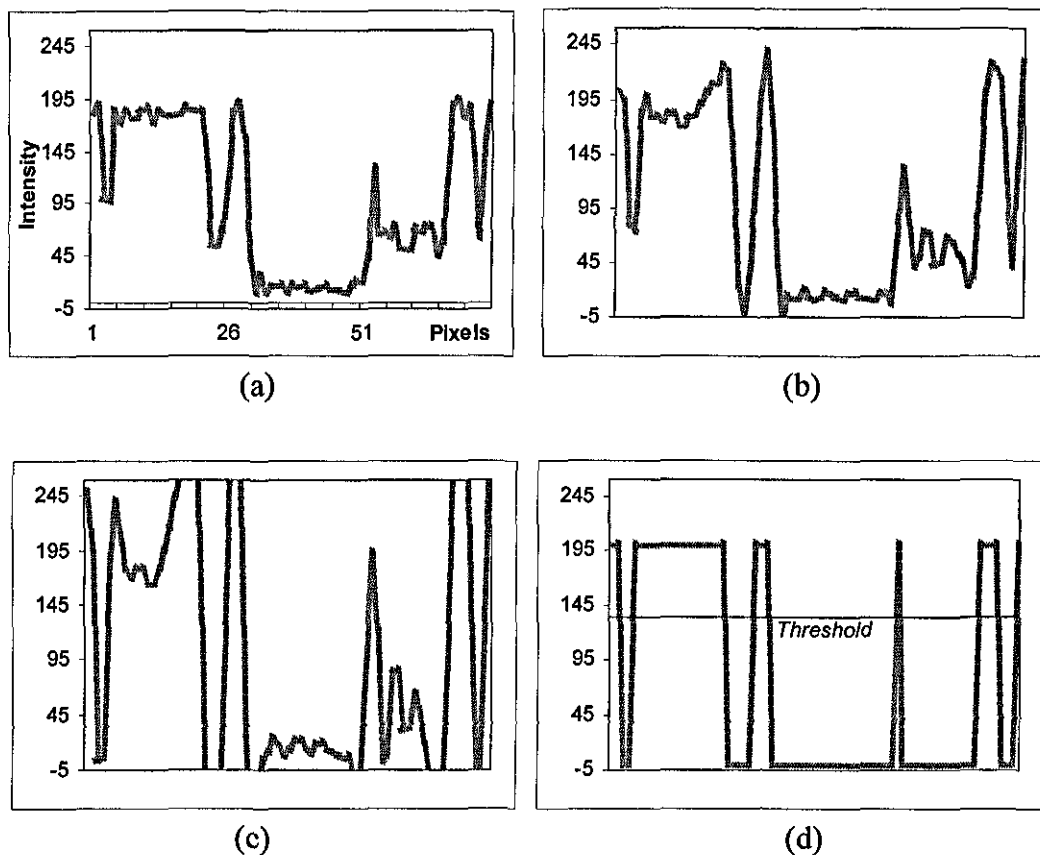


Figure 5-29 a) Original image profile, b) (a) after applying 3x3 Gaussian and 3x3 Laplacian filters, c) (a) after applying 3x3 Gaussian and 5x5 differential filter, d) Threshold applied to (c)

Following contrast enhancement, a single threshold value can confidently be applied to the filtered image. The threshold is taken as two thirds from the minimum to the maximum intensity of the original image as shown in Figure 5-29d. This level of threshold is determined empirically through observation of many images. Figure 5-30 shows the image after filtering and thresholding. This method is found to be quite successful in terms of lack of noise in the processed images and especially its excellent ability to identify isolated pixels enabling separation of close fibres. Another advantage is that the misfocus rings caused by diffraction are also eliminated upon thresholding. The main disadvantage however is the speed. Nevertheless, this technique provided an excellent pre-processing especially for the skeletonising operation described in Section 5.4.5.2.

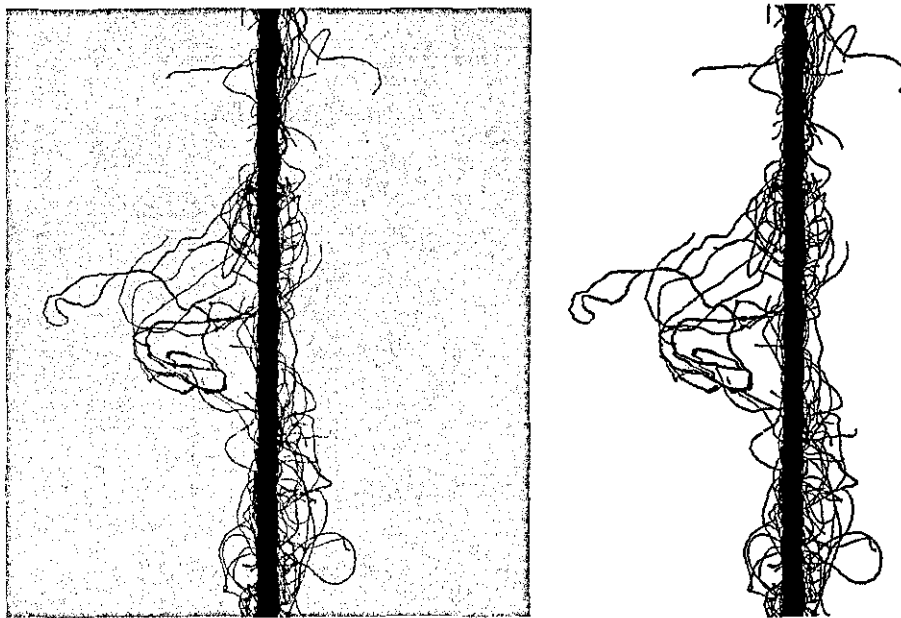


Figure 5-30 a) Original Image b) After contrast enhancement and thresholding

5.4.1.2 Adaptive Two Level Thresholding

This method is based on finding two threshold values from the histogram of the image (see Figure 5-31); the first one close to the background peak to separate all

yarn regions including out of focus hairs from the background, and the second one from between two peaks for a more accurate determination of the core boundaries.

In order to find these threshold values, an algorithm is developed which first calculates the histogram and then tracks it upwards through y axis starting from the minimum y value and for each y value, tracks it leftwards parallel to the x axis starting from the pixel intensity having the maximum number of pixels. This tracking continues until a tracking line parallel to the x axis intersects exactly 3 points on the graph provided that the distance between first two points is more than 20 units. This condition check is found necessary to avoid 3 intersection points to be found because of the small fluctuations at the bottom of the histogram. Figure 5-31 shows these three intersection points on the histogram. The first threshold value is found from the x coordinate of the first intersection point by subtracting an empirical constant of 10. The average of first threshold value and the x coordinate of the second point intersecting the histogram is selected as the second threshold value. In order to improve the speed of the algorithm, the histogram is calculated sampling one of every four pixels in the image. Figure 5-32 shows the images thresholded at these two different levels.

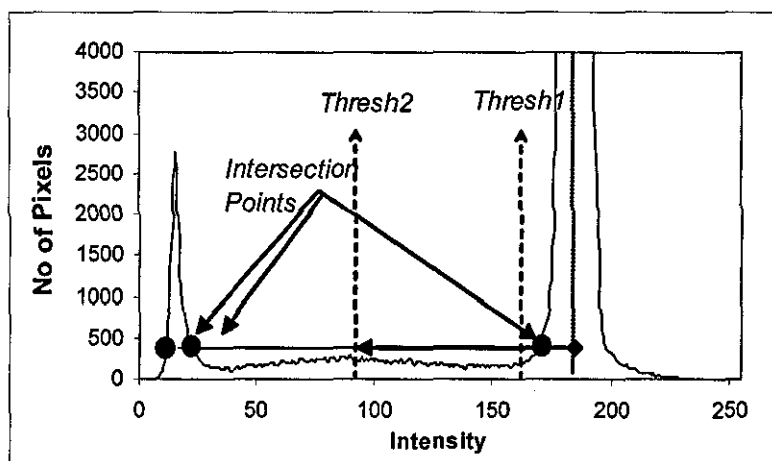


Figure 5-31 Determination of threshold values

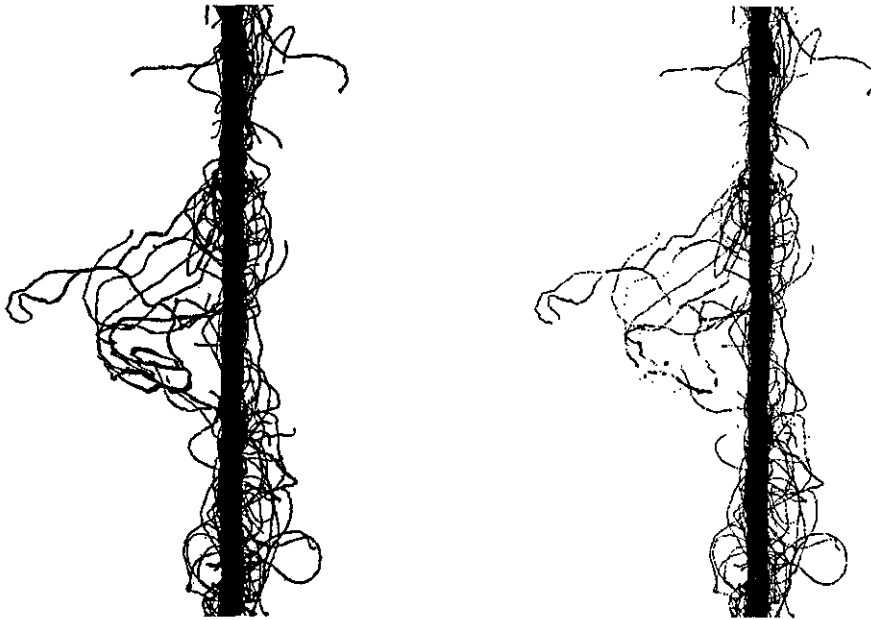


Figure 5-32 Yarn image after applying a) first threshold b) second threshold

Two methods are developed in order to separate the core and hairs based on this two level thresholding method which are described in Section 5.4.2. These techniques use the second thresholded image to locate the core boundaries and the first image to find the hairs.

The main advantage of the technique is its adaptive nature, which enables testing the yarns under any illumination condition (provided that the background is uniform enough) without a need to change the parameters. The measurements are not affected even if the brightness of the light source changes during a test. The isolated pixels at the core boundaries are also clearly defined in the second thresholded image. This technique is used as the major pre-processing algorithm in the developed system. One of the other main advantages is the speed, which is around 20images/second for 1400x1358 images including the post processing stage to separate the core from hairs and perform other analysis. This is 8 times faster than the previous algorithm. The algorithm is watched manually while processing 50000 images taken from 20 different yarn samples and no failure has been observed. One drawback of the algorithm compared to the previous contrast enhancement technique is that it can

only identify isolated pixels between the core and the surface fibres and not those between close hairs.

5.4.1.3 Maxima-Minima Differentiation Method

This algorithm was developed for processing coherent back-lit images suffering from non-uniform background without a need for flat field correction in order to increase the processing speeds. It is designed to work on individual line scans not requiring the whole 2D picture. The algorithm is based on tracking each horizontal profile in the image to find the valleys that correspond to hairs or the core. Here, the term 'valley' refers to the intensity drops in the profile due to the hairs or the core. The algorithm searches the maximum and minimum points in the profile and differentiates the intensities of successive maxima and minima. A maximum-minimum transition having an absolute differential value above a constant threshold value is considered as the left edge of a valley that corresponds to a hair or the core. Similarly, a minimum-maximum transition satisfying the same condition is considered as a right edge. The threshold level is determined empirically and a value of 20 is found suitable.

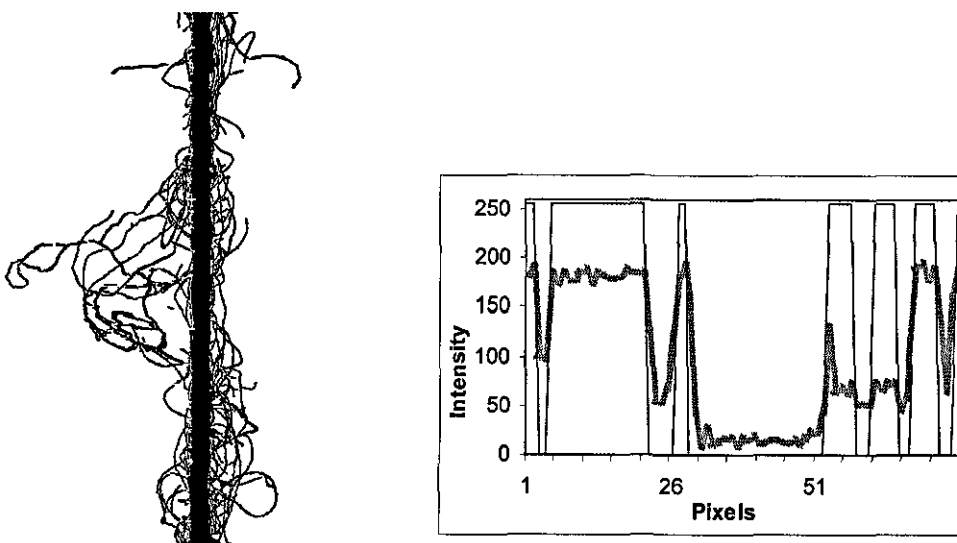


Figure 5-33 Yarn image processed using maxima-minima differentiation.

A considerable amount of time was spent on this algorithm to establish it on a set of rules that account for many different situations observed in the images and some of them are worth mentioning here. Ideally, a maximum-minimum transition has to be followed by a minimum-maximum transition in a profile. However on some occasions, some hairs create edges with more than one step which creates a max-min transition followed by another one or vice versa. To handle this, successive max-min transitions are combined if the minimum of the first is close to the maximum of the next and the distance between them is less than 5 pixels, otherwise they are separated. The same rule applies for successive min-max transitions. Out of focus hairs especially those lying along the scan line created the biggest problem in this algorithm, which sometimes created a valid max-min transition but then gradually increased up to the background intensity with small transitions on the way due to noise. The distance check in the first rule is essentially added to avoid connection of an out of focus hair with a normal hair along with all the background intensities in between. However, as a result of this, an in-focus hair intercepting a defocused hair could cause the whole defocused hair to be omitted as can be seen in Figure 5-34. Diffraction rings also created important problems especially when the background illumination is low, creating high max-min and min-max transitions sometimes causing a background region to be identified as a hair.

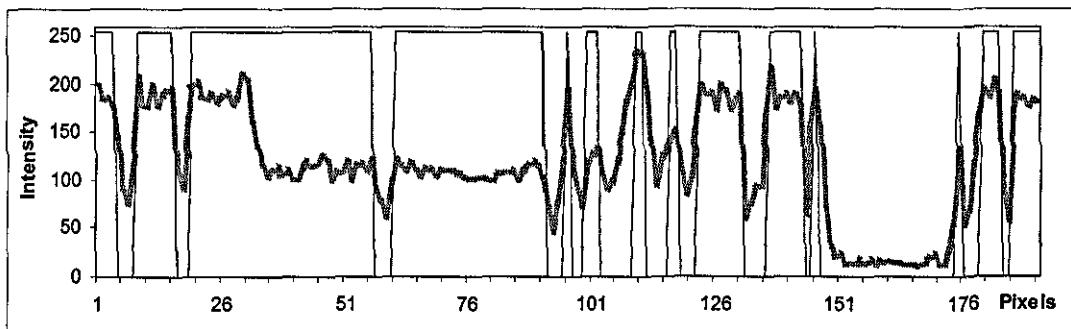


Figure 5-34 A defocused hair lying along the scan line intersected with an in-focus hair in the middle. The algorithm only detects the intersecting hair and omits the whole defocused hair

The technique worked fairly well especially when the effects of diffraction rings were not significant, i.e. when the background intensity is high or when a broad

incoherent light source is employed. However, even in this case, there was sometimes an underestimation of hairs lying along the profile. The processing time varied between 120ms and 170ms depending on the amount of condition checks required. The identification of isolated background pixels was very satisfactory. The main advantage of the technique is its ability to process images with non-uniform background intensity such as that acquired using field lens illumination. Figure 5-35 shows such an image after processing with this technique without any pre-processing. Nevertheless, flat field correction provides an important improvement to the algorithm.

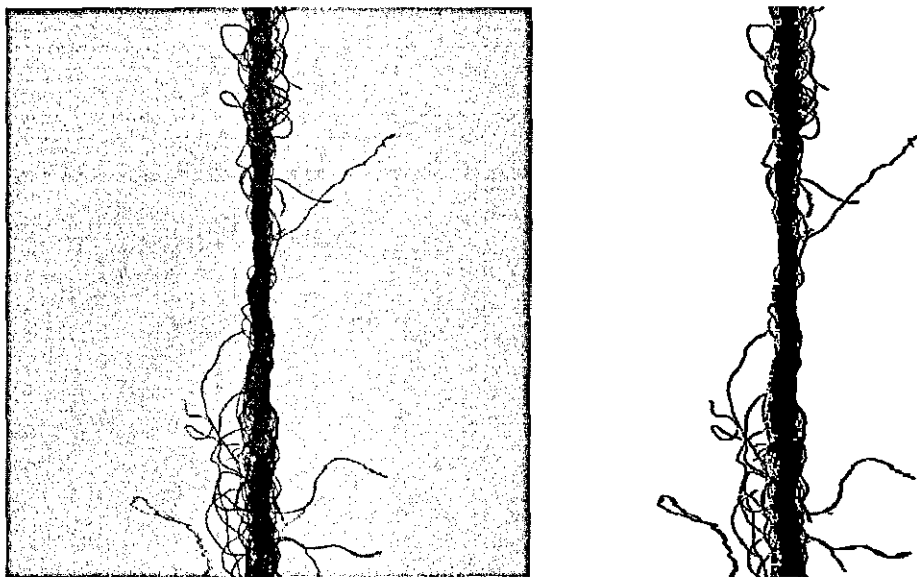


Figure 5-35 (a) A yarn image with non-uniform background intensity, (b) (a) after processing with maxima-minima differentiation algorithm

This algorithm is also very sensitive to salt and pepper type noise (random white and black pixels). During the second year of the research a problem occurred with the camera adding vast amount of impulse noise to the images. A 3-pixel wide one dimensional median filter was applied to overcome this but this seriously increased the processing time and did not provide any improvement in cases where two noise pixels were next to each other. A larger filter size could be applied to prevent this;

however, this would significantly alter the image. Although the problem with the camera was resolved later, the algorithm was abandoned in the mean time.

5.4.1.4 Other Adaptive Thresholding Techniques

There are many papers in the literature studying and developing adaptive thresholding techniques which mostly concentrate on document imaging. Sezgin & Sankur [2004] conducted a comprehensive survey comparing 40 common methods in the literature. They categorize different methods into six groups according to the information they are exploiting which are:

1. Histogram shape-based methods, where, for example, the peaks, valleys and curvatures of the smoothed histogram are analyzed
2. Clustering-based methods, where the gray-level samples are clustered in two parts as background and foreground object, or alternately are modeled as a mixture of two Gaussians.
3. Entropy-based methods result in algorithms that use the entropy of the foreground and background regions, the cross-entropy between the original and binarised image, etc.
4. Object attribute-based methods search a measure of similarity between the gray-level and the binarised images, such as fuzzy shape similarity, edge coincidence, etc.
5. The spatial methods use higher-order probability distribution and/or correlation between pixels
6. Local methods adapt the threshold value on each pixel to the local image characteristics.

This section explores eight common adaptive thresholding techniques in the literature. In Section 5.4.1.4.1 the definitions of the terms are given. The techniques are categorized into two main groups according to that if they are calculating a single threshold value for the whole image (Global) or varying threshold values are calculated for every pixel in the image (Local). Global techniques include those developed by Otsu [1979], Kittler & Illingworth [1986], Kapur et al. [1985] and Abutaleb [1989] and local methods by Niblack [1986], Sauvola & Pietaksinen [2000], Bernsen [1986] and Yanowitz & Bruckstein [1989].

Both techniques are implemented in C language and tested on two yarn images one with a non-uniform and the other with a uniform background. The results are compared in a qualitative manner since a ground truth was not available as in document images (Leedham et.al. [1993]). The results were evaluated based on the following four criteria:

- 1) **Noise in the background:** This is particularly important since the background pixels identified as hairs will cause a higher hairiness value to be measured.
- 2) **Ability to detect out of focus hairs:** The defocused hairs have intensities lower than the background and lower than the in-focus hairs. Global thresholding methods may sometimes identify these pixels as part of the background and a thresholding technique should be capable of identifying these hairs accurately.
- 3) **Hair or core integrity :** Some algorithms might tend to create holes or discontinuities in hairs or the yarn core.
- 4) **Isolated pixels:** These are the background pixels between close fibres often having lower intensity than the actual background. Correct identification of these pixels is especially essential if a thinning algorithm is applied to the thresholded image.
- 5) **Processing time :** Time required to calculate and apply the threshold to a single image.

The results are also compared with the histogram based adaptive two level thresholding and max-min differentiation techniques described in sections 5.4.1.2 and 5.4.1.3 respectively.

5.4.1.4.1 Definitions

The histogram of an image with gray level values ranging from g_{\min} to g_{\max} is denoted by $h(g)$ ($g_{\min} \leq g \leq g_{\max}$). Typically, for an 8 bit unsigned image $g_{\min} = 0$ and $g_{\max} = 255$. For a given gray level i ($g_{\min} \leq i \leq g_{\max}$) $h(i)$ gives the number of pixels in the image having the gray value of 'i'. The normalized histogram or the probability mass function (PMF) $p(g)$ is obtained by dividing $h(g)$ to the total number of pixels in the image, i.e. $p(g) = h(g)/(N \times M)$ for an $N \times M$ image. The cumulative probability function $P(g)$ for a given gray level 'g', is defined as:

$$P(g) = \sum_{i=g_{\min}}^g p(i) \quad (5.1)$$

If a threshold at T is applied to the image, all pixels with gray levels of less than and equal to T will be categorized as the foreground and those with gray levels of higher than T will be categorized as the background. In this case the normalized fractions of pixels that will be classified as the foreground or the background will be:

$$q_f(T) = \sum_{i=g_{\min}}^T p(i), \quad q_b(T) = \sum_{i=T+1}^{g_{\max}} p(i), \quad (q_f(T) + q_b(T) = 1) \quad (5.2)$$

The mean (m) and the variance (σ^2) of the foreground and background as functions of the thresholding level T are denoted as:

$$\begin{aligned}
 m_f(T) &= \sum_{i=g_{\min}}^T ip(i) & \sigma_f^2(T) &= \sum_{i=g_{\min}}^T [i - m_f(T)]^2 p(i) \\
 m_b(T) &= \sum_{i=T+1}^{g_{\max}} ip(i) & \sigma_b^2(T) &= \sum_{i=T+1}^{g_{\max}} [i - m_b(T)]^2 p(i)
 \end{aligned}
 \tag{5.3}$$

The Shannon entropy, parametrically dependant on T is formulated as follows for the foreground and the background (Sezgin & Sankur, 2004):

$$\begin{aligned}
 H_f(T) &= - \sum_{i=g_{\min}}^T p_f(i) \log p_f(i), \\
 H_b(T) &= - \sum_{i=T+1}^{g_{\max}} p_b(i) \log p_b(i)
 \end{aligned}
 \tag{5.4}$$

5.4.1.4.2 Global Thresholding Methods

5.4.1.4.2.1 Otsu's [1979] Method

This is one of the most referenced global thresholding methods in the literature. Otsu's method is a nonparametric and unsupervised method of automatic thresholding selection for image segmentation. It utilizes only the zeroth and the first order cumulative moments of the gray level histogram. It does not depend on modeling the probability density functions; however, it assumes a bimodal distribution of gray-level values. The basic principle is to minimize the weighted sum of the within-class variances (or to maximize the between class variance) of the foreground and the background pixels to find an optimum threshold. This can be expressed as follows:

$$T_{opt} = \arg \max \left\{ \frac{[m_f(T) - m.P(T)]^2}{P(T)[1 - P(T)]} \right\}
 \tag{5.5}$$

where, the expression in the brackets gives the between class variance of the foreground and the background pixels. Figure 5-36 shows the PMF of a yarn image with non-uniform background intensity and determination of the optimum threshold using Otsu's method.

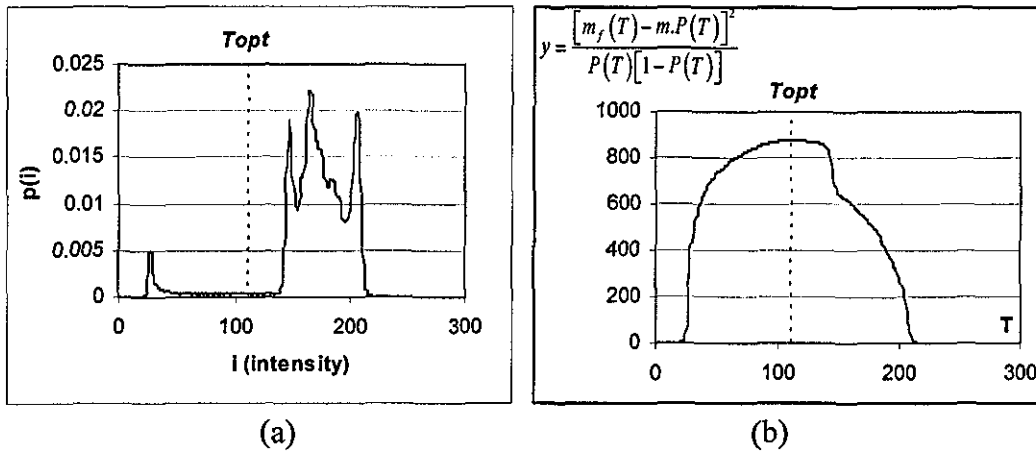


Figure 5-36 a) The probability mass function of a yarn image, b) Between class variances for varying threshold values and selection of the optimum threshold.

5.4.1.4.2.2 Kittler and Illingworth's [1986] Method

In this method the foreground and background class conditional probability density functions are assumed to be Gaussian and do not necessarily have equal variances. The error expression can be interpreted also as a fitting error expression to be minimized such that:

$$T_{opt} = \arg \min \{ P(T) \log \sigma_f(T) + [1 - P(T)] \log \sigma_b(T) - P(T) \log P(T) - [1 - P(T)] \log [1 - P(T)] \} \quad (5.6)$$

Where σ_f and σ_b are the foreground and background variances. Figure 5-37 shows the selection of optimum threshold using Kittler and Illingworth's method.

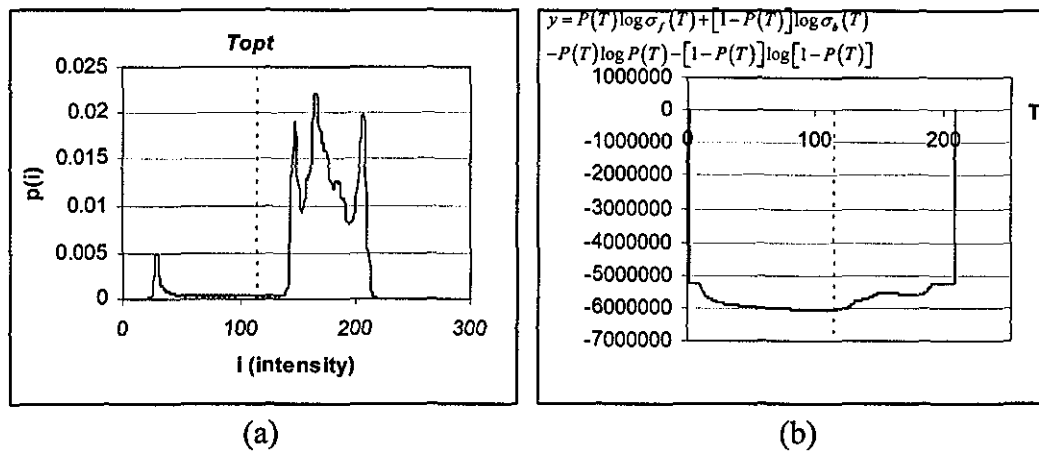


Figure 5-37 The probability mass function (a) and the Gaussian fitting errors for varying thresholds and selection of the optimum threshold (b)

5.4.1.4.2.3 Kapur et al.'s [1985] Entropy Thresholding

In this method, the foreground and background classes are considered as two different sources. When the sum of the two class entropies is a maximum the image is said to be optimally thresholded. The optimum threshold level is expressed as follows:

$$T_{opt} = \arg \max [H_f(T) + H_b(T)] \text{ where,} \tag{5.7}$$

$$H_f(T) = - \sum_{i=s_{min}}^T \frac{p(i)}{P(T)} \log \frac{p(i)}{P(T)},$$

$$H_b(T) = - \sum_{i=T+1}^{s_{min}} \frac{p(i)}{P(T)} \log \frac{p(i)}{P(T)}$$

Figure 5-38 shows determination of the optimum threshold level using this method.

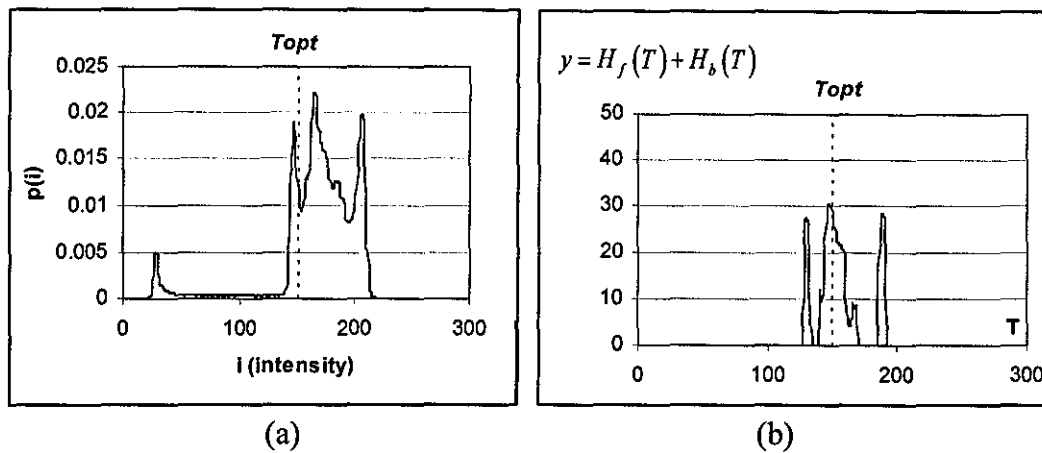


Figure 5-38 The probability mass function (a), and the sum of foreground and background entropies for varying thresholds and selection of the optimum threshold (b)

5.4.1.4.2.4 Abutaleb's [1989] Spatial Thresholding Method (Two-Dimensional Entropy)

Abutaleb introduces the spatial information in the entropy-based thresholding by considering the joint entropy of two related random variables, namely, the image gray value, g , at a pixel and the average gray value, \bar{g} , of a neighborhood centered at that pixel. Using the two-dimensional histogram, $p(g, \bar{g})$, for any threshold pair, (T, \bar{T}) , the foreground and background entropies are defined as follows:

$$\begin{aligned}
 H_f &= - \sum_{i=g_{\min}}^T \sum_{j=\bar{g}_{\min}}^{\bar{T}} \frac{p(i, j)}{P(T, \bar{T})} \log \frac{p(i, j)}{P(T, \bar{T})} \\
 H_b &= - \sum_{i=T+1}^{g_{\max}} \sum_{j=\bar{T}+1}^{\bar{g}_{\max}} \frac{p(i, j)}{1 - P(T, \bar{T})} \log \frac{p(i, j)}{1 - P(T, \bar{T})}
 \end{aligned}
 \tag{5.8}$$

Under the assumption that the off-diagonal terms, that is the two quadrants $[(g_{\min}, T), (\bar{T}, g_{\max})]$ and $[(T, g_{\max}), (g_{\min}, \bar{T})]$, are negligible and contain elements only due to image edges and noise, the optimal pair (T_{opt}, \bar{T}_{opt}) are found as follows:

$$(T_{opt}, \overline{T}_{opt}) = \arg \min \left\{ \log P(T, \overline{T}) [1 - P(T, \overline{T})] + \frac{H_f}{P(T, \overline{T})} + \frac{H_b}{[1 - P(T, \overline{T})]} \right\} \quad (5.9)$$

Figure 5-39 shows the 2D histogram of a yarn image and determination of the optimum threshold pair using Abutaleb's method.

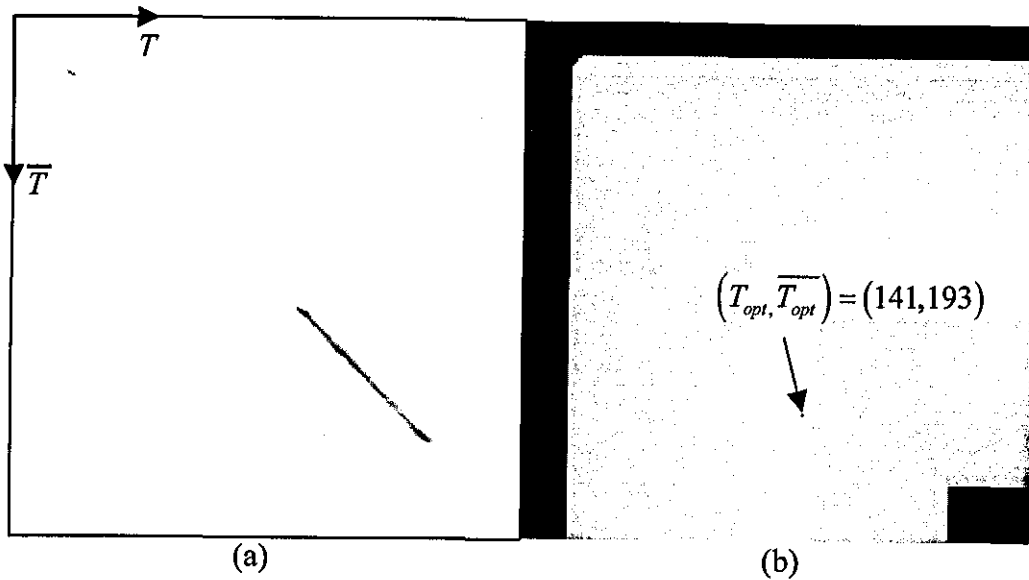


Figure 5-39 a) 2D Histogram normalized to 8bits (and inverted for visibility), b) Argument of equation (5.9) for varying (T, \overline{T}) (normalized to 8 bits) and selection of optimum threshold pair.

5.4.1.4.3 Local Adaptive Thresholding Techniques

5.4.1.4.3.1 Niblack's [1986] Method

The idea of this method is to vary the threshold over the image, based on the local mean and local standard deviation. The threshold at pixel (i, j) is calculated as

$$T(i, j) = m(i, j) + k \cdot \sigma(i, j) \quad (5.10)$$

Where $m(i, j)$ and $\sigma(i, j)$ are the sample mean and standard deviation values, respectively, in a local neighborhood of (i, j) . The size of the neighborhood should be small enough to preserve local details, but at the same time large enough to suppress noise. 5×5 neighborhood is found to be a good choice for yarn images. The value of k is used to adjust how much of the object boundary is taken as a part of the object.

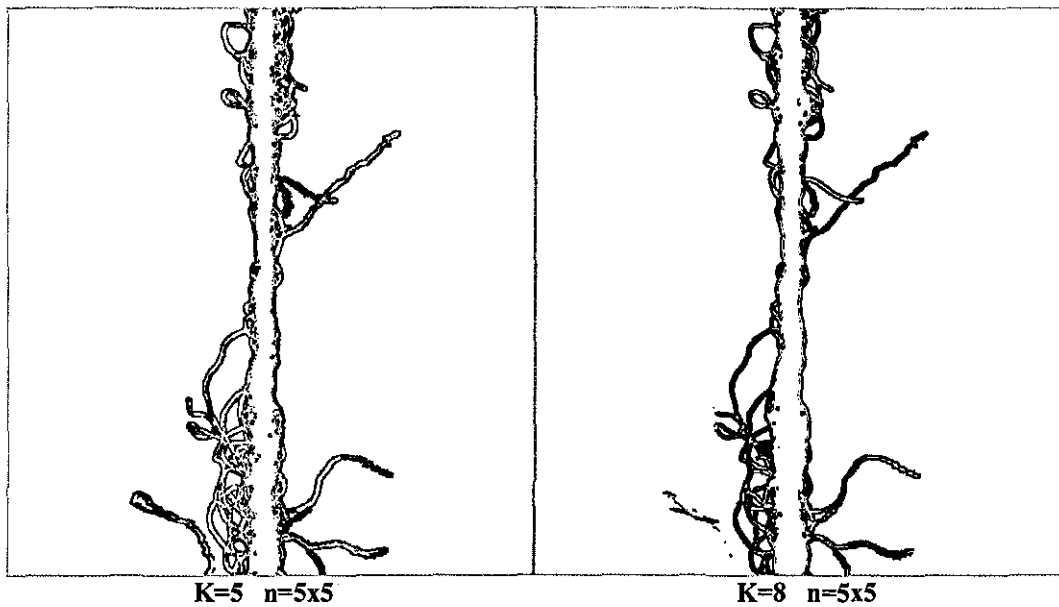


Figure 5-40 Niblack's thresholding method results for 5×5 neighborhood and given k 's.

5.4.1.4.3.2 Sauvola and Pietaksinen's [2000] Method

This method is an improved version of Niblack's method, especially for badly illuminated images and to overcome the problems arising from the background texture when using Niblack's method. The threshold at pixel (i, j) is calculated as

$$T(i, j) = m(i, j) \left\{ 1 - k \cdot \left[1 - \frac{\sigma(i, j)}{R} \right] \right\} \quad (5.11)$$

Where, R is the dynamic range of std.dev., which is 128 for a typical 8 bit image and k is suggested as 0.5. Figure 5-41 shows the results of this method on a yarn image. It can be seen that as the frame size gets bigger the out of focus hairs are more likely

to be detected by the threshold and the core edges tend to get thicker. On the other hand, as k is increased the edges are thinned while when it is decreased speckles occur in the thresholded image.

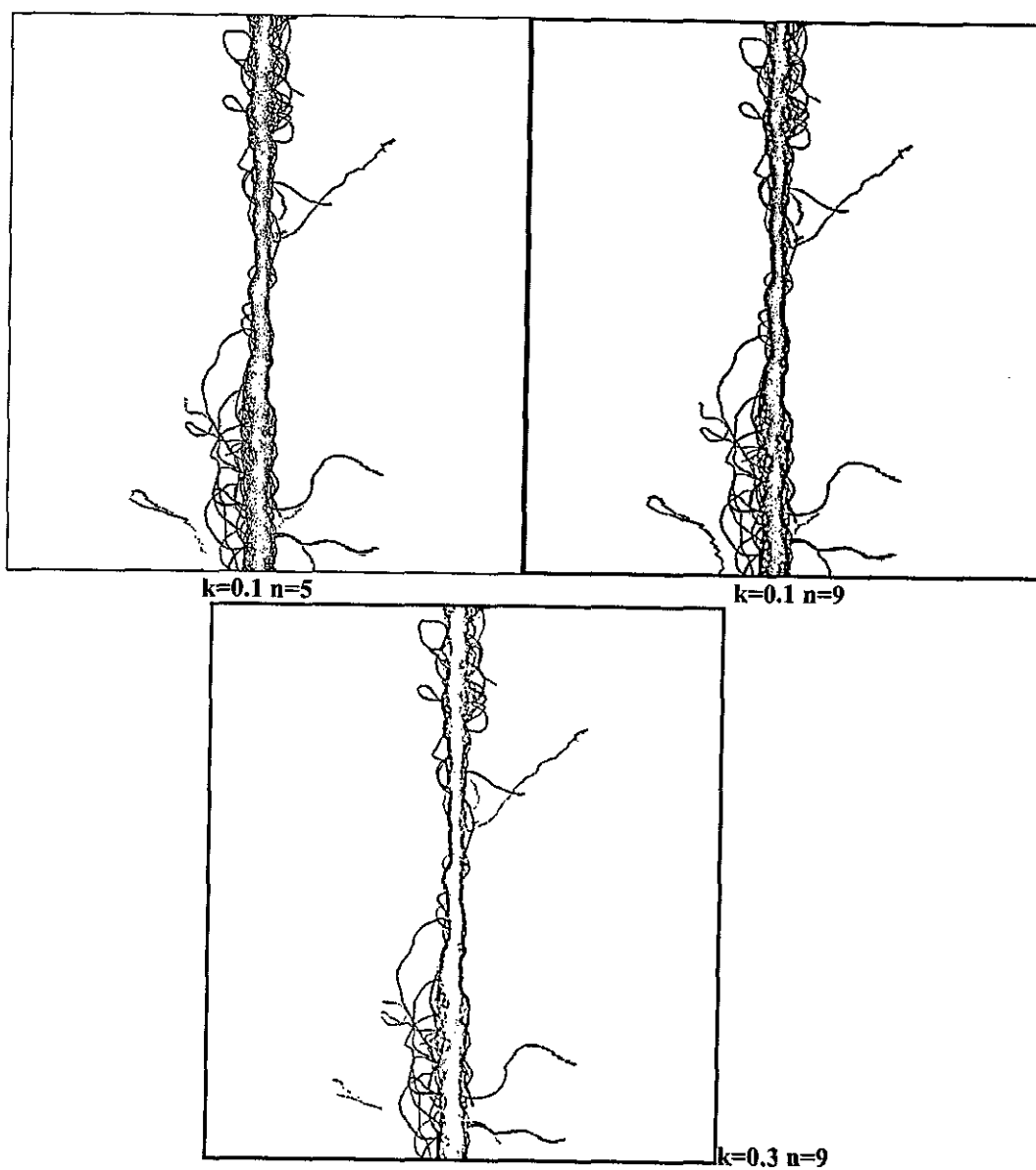


Figure 5-41 Results of Sauvola and Pietaksinen's method for varying k and frame sizes (n)

5.4.1.4.3.3 Bernsen's [1986] Method

In this method, for each pixel (i, j) , the threshold $T(i, j) = (Z_{low} + Z_{high}) / 2$ is used, where Z_{low} and Z_{high} are the lowest and highest gray level pixel values in a square measure $n \times n$ neighborhood centered at (i, j) . However, if the contrast measure $C(i, j) = (Z_{low} - Z_{high})/255 < L$, then the neighborhood consists only of one class, foreground or background. Figure 5-42 shows thresholded yarn images using this method for varying L values and frame sizes. It can be seen that as L is decreased the effect of noise on the background is amplified, however when it is increased only the hairs with high contrast, i.e. the in focus hairs are detected. On the other hand, as the frame size gets larger the edges get thicker.

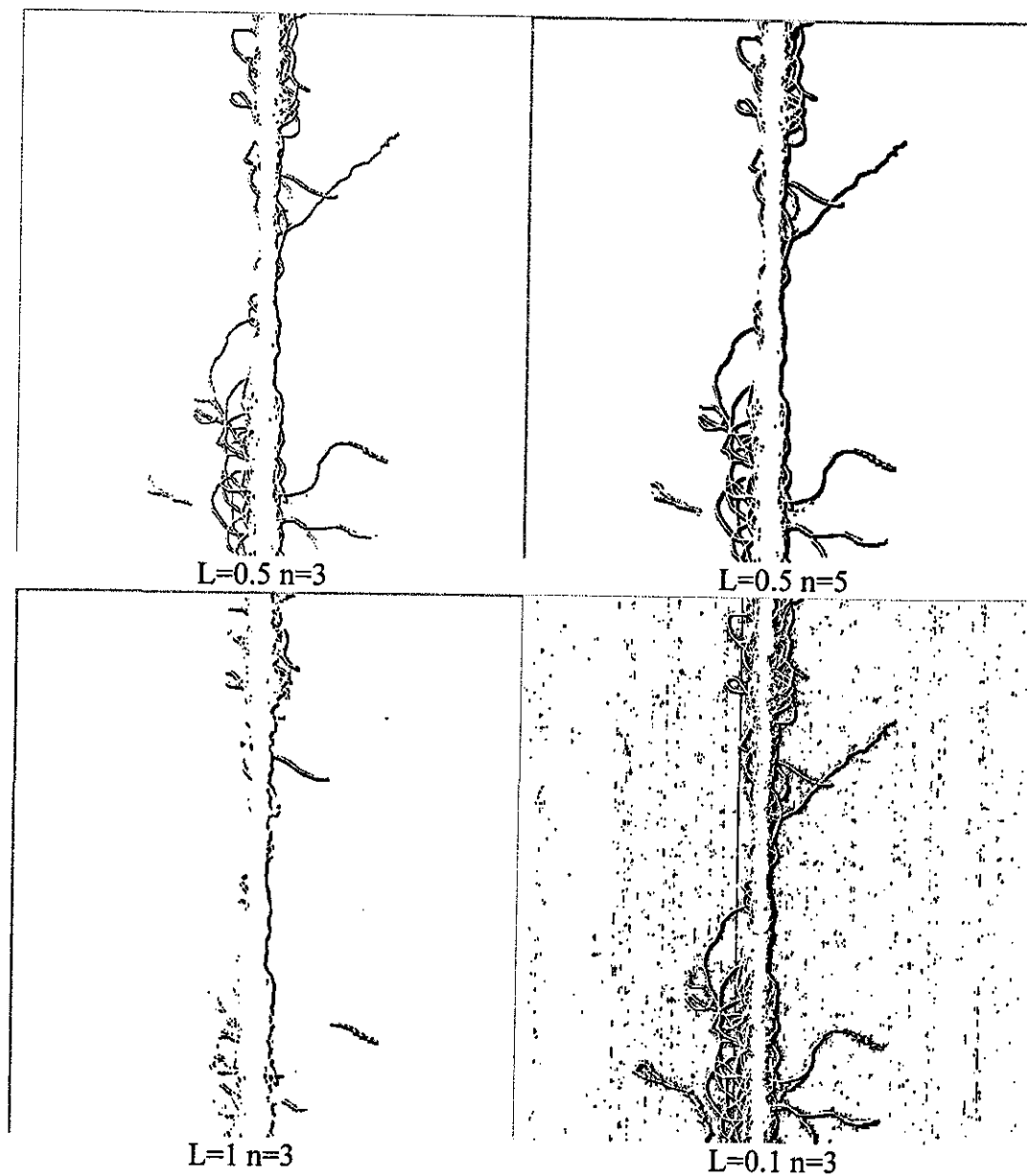


Figure 5-42 Bernsen's method applied to a yarn image for varying L and frame size values.

5.4.1.4.3.4 Yanowitz and Bruckstein's [1989] Method

Yanowitz and Bruckstein [1989] suggested using the grey-level values at high gradient regions as known data to interpolate the threshold surface of image document texture features. The key steps of this method are:

1. Smooth the image by average filtering.

2. Derive the gradient magnitude (By applying a Sobel filter).
3. Apply a thinning algorithm to find the object boundary points.
4. Sample the grey-level in the smoothed image at the boundary points. These are the support points for interpolation in step 5.
5. Find the threshold surface $T(x, y)$ that is equal to the image values at the support points and satisfies the Laplace equation using Southwell's [1946] successive over relaxation method
6. Using the obtained $T(x,y)$, segment the image.

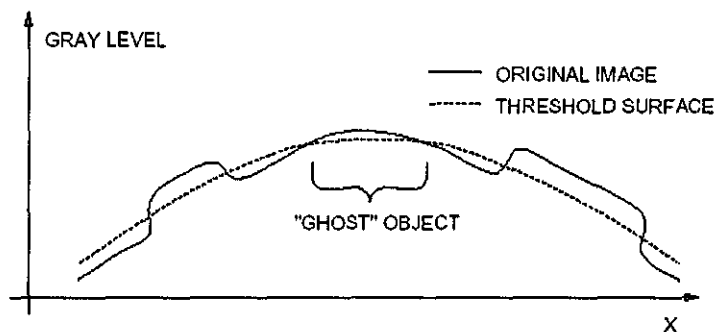


Figure 5-43 Cross section through an image, illustrating how "ghost" objects might occur (Trier & Taxt [1995])

A postprocessing step is used in Yanowitz and Bruckstein's method to remove "ghost" objects (Figure 5-43). The average gradient value at the edge of each printed object is calculated. Objects having an average gradient below a threshold T_p are labeled as misclassified, and are removed. The main steps of the algorithm are given below (Trier & Taxt [1995]):

1. Smooth the original image by a (3x3) mean filter to remove noise.

2. Calculate the gradient magnitude image G of the smoothed image, using, e.g., Sobel's edge operator

4. For all 4-connected foreground components, calculate the average gradient of the edge pixels. Edge pixels are foreground pixels that are 4-connected to the background. Remove foreground components having an average edge gradient below the threshold T_p .

Figure 5-44 shows the main steps of the algorithm applied on a yarn image. It can be seen that the algorithm initially identifies significant number of background pixels as foreground. After the ghost removing process, these pixels are converted to background, however some core regions also disappear, too. The value of T_p is set to 5 by trial and error. For lower values of T_p , background noise could not completely be removed, while as T_p is increased more core regions tended to be identified as the background. Trier and Taxt [1995] used the mean of the gradient image as the optimum T_p value.

It is clear that this method requires *numerous manual inputs*. Especially the gradient magnitude threshold and thinning algorithms will influence the positions of the boundary point, and consequently affect the interpolation process. Chan et.al. [1998] proposed a new method that is similar to Yanowitz & Bruckstein's method that locates the object boundaries by solving a Poisson equation which requires a single parameter α .

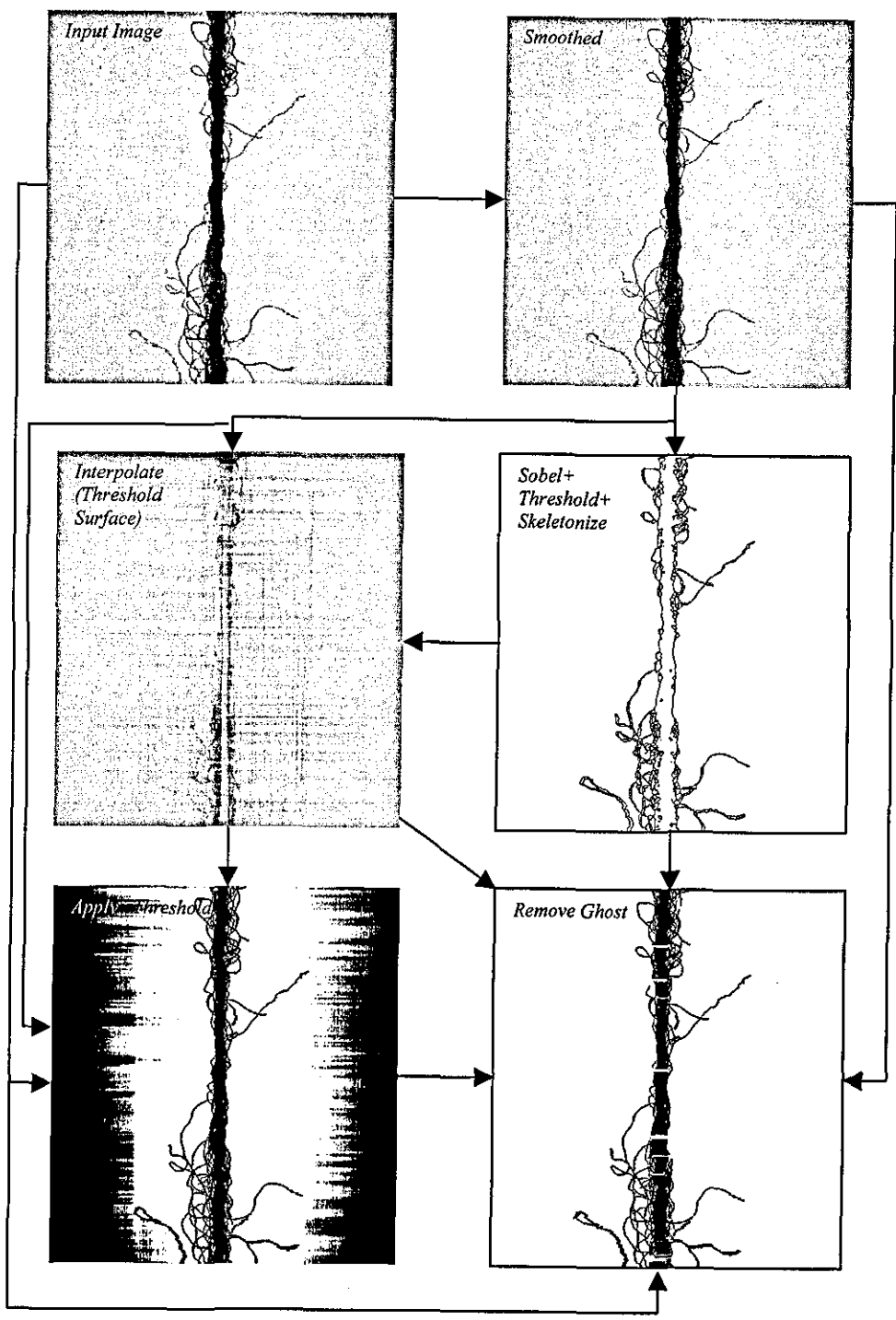


Figure 5-44 Main steps of Yanowitz and Bruckstein's method

5.4.1.4.4 Comparison of thresholding methods

Two different yarn images the first one with a non-uniform (Figure 5-45a) and the other with a uniform background (Figure 5-46a) are used in the evaluation of different thresholding methods. The thresholded images are shown in Figure 5-45b-k and Figure 5-46b-k.

5.4.1.4.4.1 Noise in the background

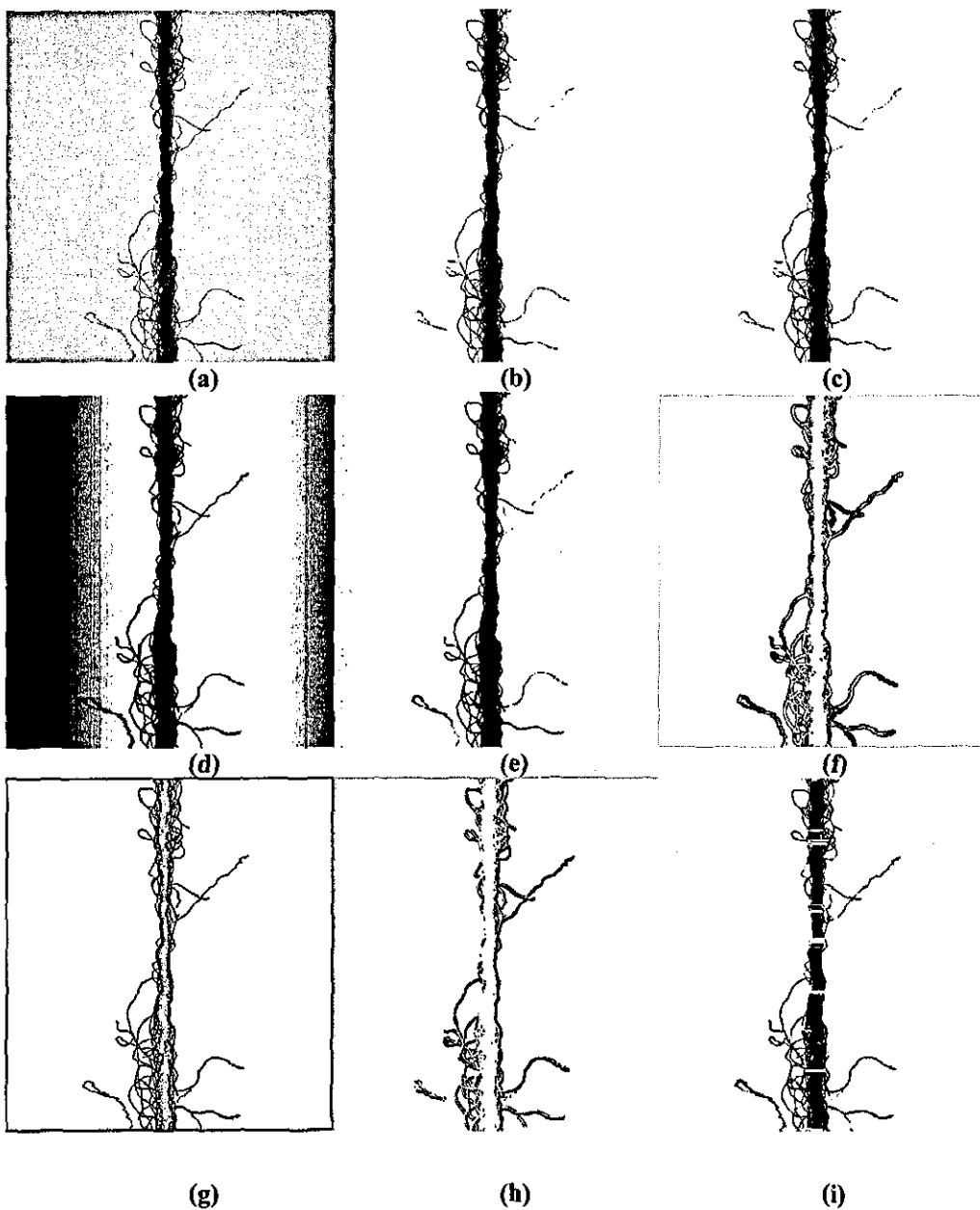
Kapur's entropy thresholding gave unacceptable results in terms of background noise. The main reason for this is due to the big difference in numbers of background and foreground pixels, which results in a threshold being found within the background region of the histogram. Niblack's, Sauvola & Pietaksinen's and Bernsen's methods both identify the core region as the background. This might be helpful if only the hairiness is of interest; however the core region in Sauvola & Pietaksinen's method is quite noisy and it is hard to separate the core from the surrounding hairs.

5.4.1.4.4.2 Ability to detect out of focus hairs

Global thresholding methods mostly fail in detecting defocused hairs when the background is not uniform (Figure 5-45b, c, e, j). Nevertheless, with uniform background Kittler & Illingworth's, Abutaleb's and 2-Level adaptive thresholding techniques gave good threshold values enabling the detection of defocused fibres. Among the local adaptive methods, Sauvola & Pietaksinen's, Yanowitz & Bruckstein's and min-max differentiation methods gave the best results in detecting defocused hairs. Sauvola & Pietaksinen's method was especially successful that the defocused fibres were not thicker than the in-focus fibres as in the other methods.

5.4.1.4.4.3 Hair or core integrity

Yanowitz & Bruckstein's method tends to erode some core regions following the ghost removal step which is unacceptable. The min-max differentiation method also deletes some small parts from the edges of the fibres, nevertheless this is within acceptable limits. As mentioned before, global thresholding methods fail to maintain the integrity of defocused hairs when the background is not uniform.



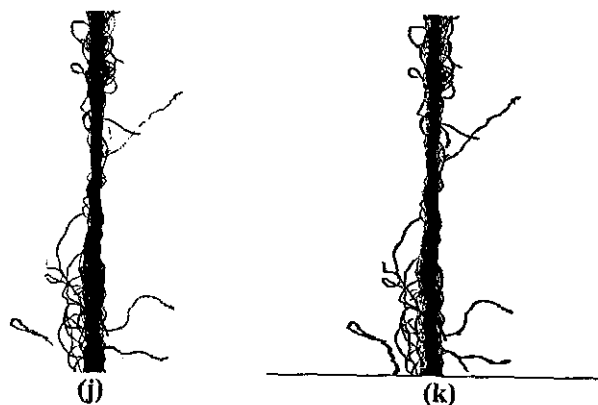
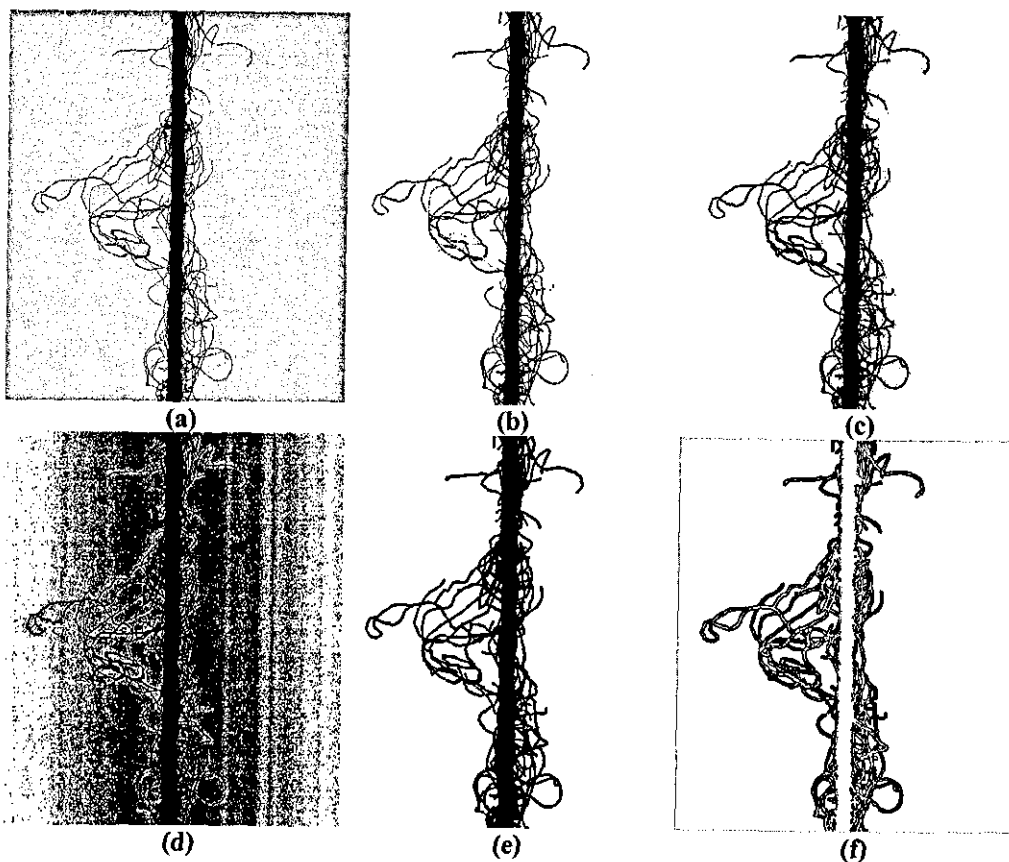


Figure 5-45 a) Original yarn image with non-uniform background, (b-k) (a) binarised using the methods of: b) Otsu, c) Kittler & Illingworth, d) Kapur et al., e) Abutaleb, f) Niblack ($k=5$, $n=5 \times 5$), g) Sauvola & Pietaksinen ($k=0.1$, $n=9 \times 9$, $R=128$), h) Bernsen ($L=0.5$, $n=5 \times 5$), i) Yanowitz & Bruckstein ($\beta=1.5$, iterations=3, $T_p=5$, Edge detection threshold=12), j) Two level adaptive Thresholding, k) Horizontal Tracking (Slope threshold=20)



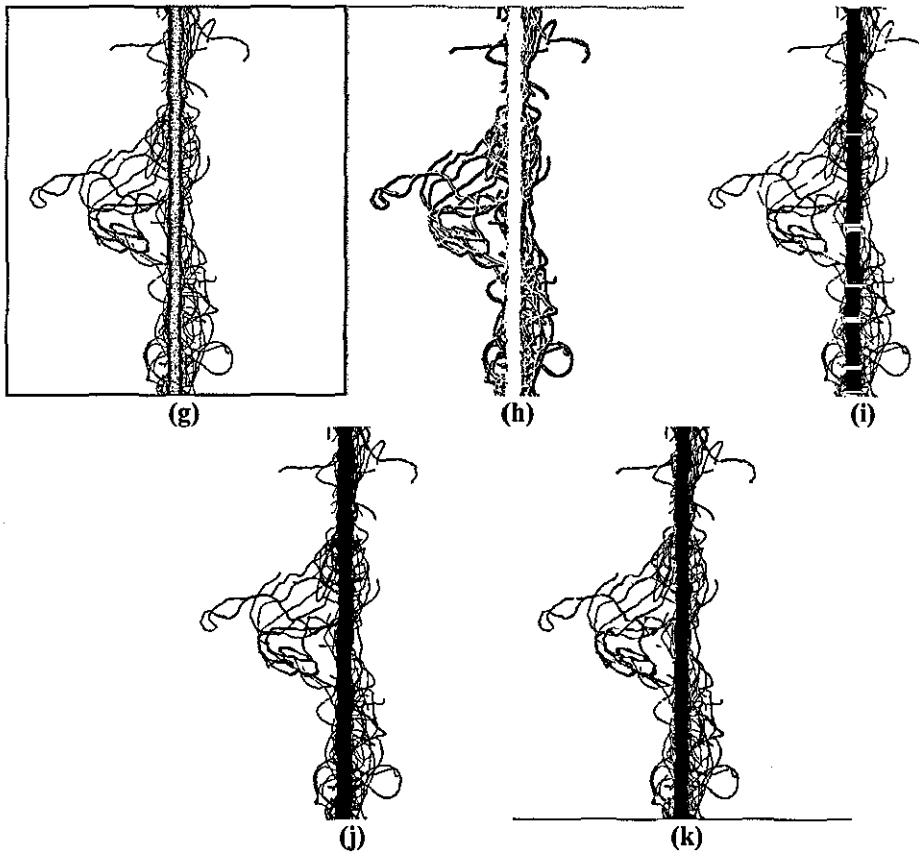
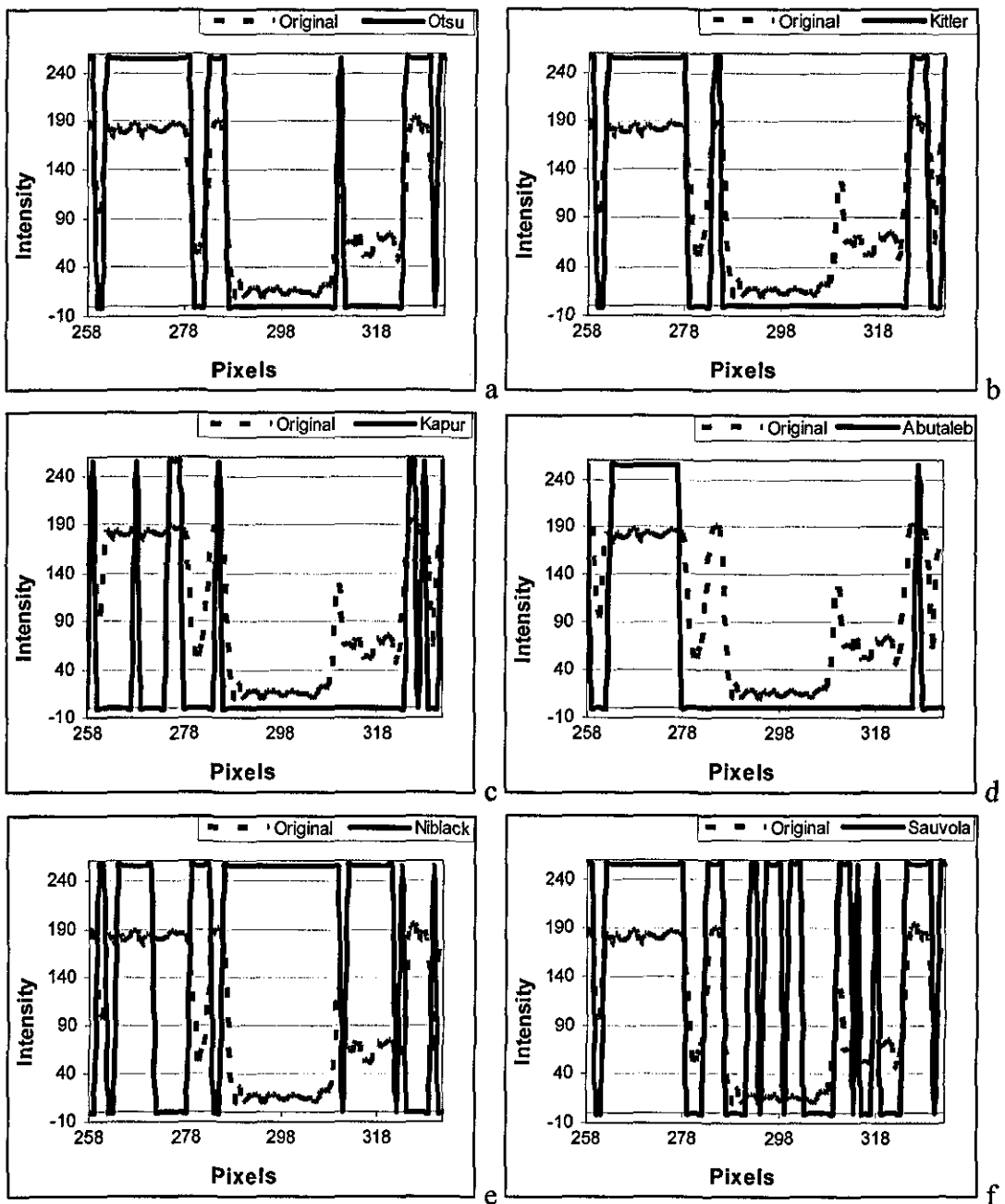


Figure 5-46 a) Original yarn image with uniform background, (b-k) (a) binarised using the methods of: b) Otsu, c) Kittler & Illingworth, d) Kapur et al., e) Abutaleb, f) Niblack ($k=5$, $n=5 \times 5$), g) Sauvola & Pietaksinen ($k=0.1$, $n=9 \times 9$, $R=128$), h) Bernsen ($L=0.5$, $n=5 \times 5$), i) Yanowitz & Bruckstein ($\beta=1.5$, iterations=3, $T_p=5$, Edge detection threshold=12), j) Two level adaptive Thresholding, k) Horizontal Tracking (Slope threshold=20)

5.4.1.4.4.4 Isolated pixels

Among the global thresholding methods, Otsu's method (Figure 5-47a) was the best in identifying the isolated background pixels, which is because the threshold value found by this method is closer to the foreground peak than it is in any other method. This of course results in misclassification of defocused fibres. The 2-Level adaptive thresholding method (Figure 5-47i) was the most successful in identifying the isolated pixels around the core. Niblack's, Sauvola & Pietaksinen's and Bernsen's (Figure 5-47e-g) methods were also successful in detecting the isolated background pixels, nevertheless Sauvola & Pietaksinen's method (Figure 5-47f) was best among the three. These are the background pixels between close fibres often having lower

intensity than the actual background. Correct identification of these pixels is especially essential if a thinning algorithm is applied to the thresholded image. Min-max differentiation method (Figure 5-47j) could identify most isolated pixels, however some defocused fibre profiles were also accounted for the background. Yanowitz & Bruckstein's method (Figure 5-47h) appeared to perform best in detecting isolated pixels.



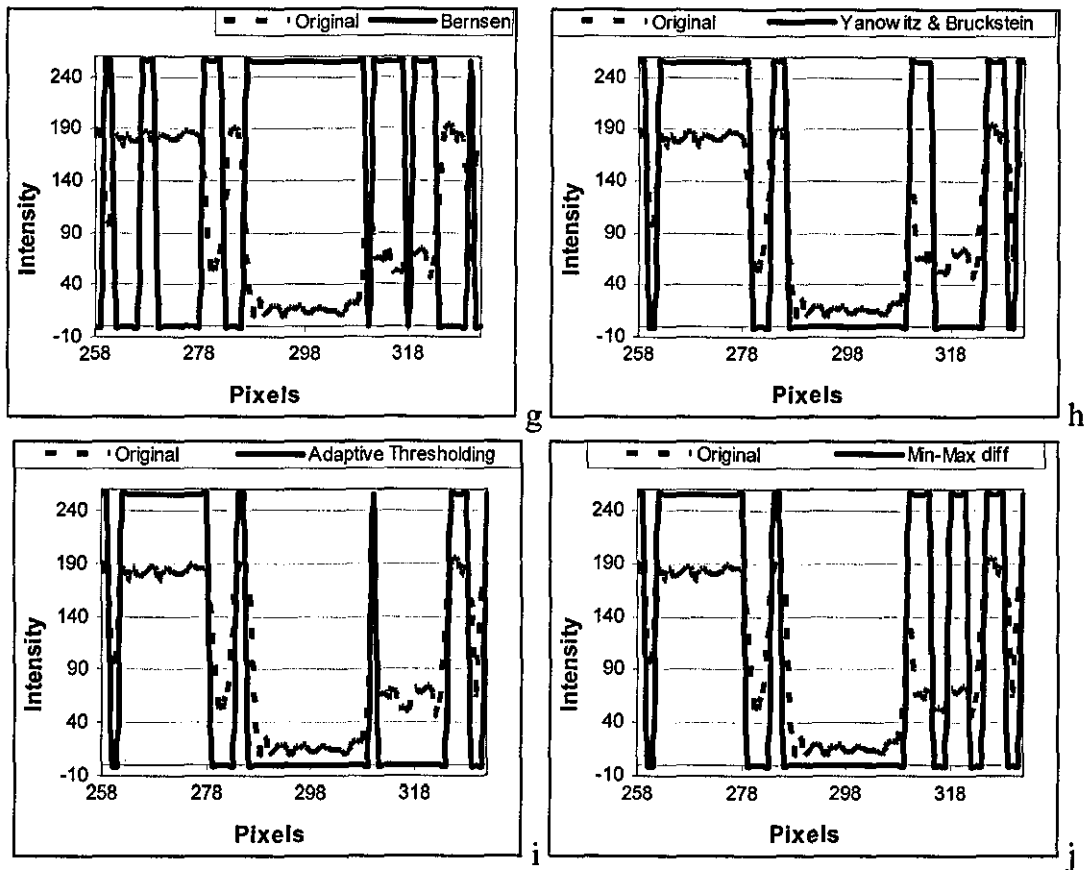


Figure 5-47 The comparison of the original image profiles with the thresholded profiles obtained using different techniques.

5.4.1.4.4.5 Processing time

Table 5-1 shows the processing times required for each thresholding method to process a single yarn image. It can be seen that Yanowitz & Bruckstein's method which requires time consuming thinning and iteration algorithms and Sauvola & Pietaksinen's method that requires a 9x9 convolution are far the slowest among the others. Adaptive 2-Level thresholding that requires a 1-D histogram tracking was the fastest with 2ms processing time.

Table 5-1 The processing times when using different methods.

Method	Processing Time (ms)	Method	Processing Time (ms)
Otsu	12	Sauvola & Pietaksinen	782
Kitler & Illingworth	12	Bernsen	212
Kapur	19	Yanowitz & Bruckstein	848
Abutaleb	93	Adaptive 2-Level Thresholding	2
Niblack	233	Min-Max diff	9

5.4.2 Core-Hair separation Methods for Back-Lit Images

Two different algorithms are implemented during this project designed to work on both high and low aspect ratio images. The first task common to both methods is to locate the core axis. The algorithm developed for this purpose initially integrates each column for the first 25 rows of the binary yarn image. Along the columns in vicinity of the core axis, the integration will result in 0, so the longest interval of zero sums will give the minimum width of the core and the centre of the interval gives the core axis as shown in Figure 5-48. Since the hairs perpendicular to the core will have diameters less than 25 pixels, the integrations in those regions will always be above zero. On the other hand, even if a hair lies parallel to the core and creates an interval with a sum of zero, this interval will be shorter than the one corresponding to the core; hence the correct position of the core axis can always be located.

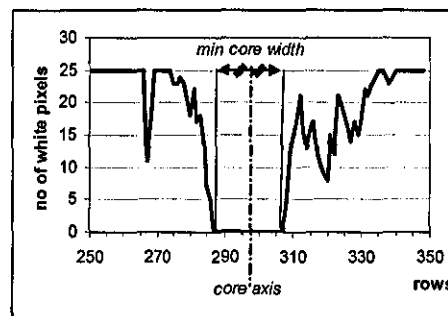


Figure 5-48 Integrated columns for the first 25 rows of second thresholded image and location of the core.

5.4.2.1 Morphological filtering

In order to find the boundaries of the core, one of the first techniques developed during this research was based on morphological filtering. The idea is simply applying a morphological close operation to the second thresholded image. Closing is a two step operation often used to fill in holes and small gaps on binary images. The first step is dilation, which is performed by laying a structuring element on the image and sliding it across the image in a manner similar to convolution. If at a certain position of the structuring element, the origin coincides with a non-zero pixel in the image then an OR operation is performed on all pixels within the structuring element, otherwise the image is not altered. Dilation is followed by erosion which deletes a non-zero pixel on the image coinciding with the centre of the structuring element if not all the nonzero pixels in the structuring element coincide with non-zero pixels on the image. A more detailed discussion on morphological filtering can be found in Umbaugh [1998, pp 92-97]. Morphological operations are based mathematically on set theory. In this sense, dilation can be defined as an operation that combines two sets using vector addition of set elements. This can be formulised as follows:

$$A \oplus B = \{c \in Z^2 \mid c = a + b \text{ for some } a \in A, b \in B\} \quad (5.12)$$

Where A and B are subsets in 2-D space representing the image undergoing analysis and the structuring element respectively and \oplus denotes dilation. Similarly, erosion combines two sets using the vector subtraction of set elements and can be formulised as follows:

$$\begin{aligned} A \ominus B &= \{x \in Z^2 \mid \text{for every } b \in B, \text{ exist an } a \in A \text{ s.t. } x = a - b\} \\ &= \{x \in Z^2 \mid x + b \in A \text{ for every } b \in B\} \end{aligned} \quad (5.13)$$

Where $A \ominus B$ denotes the erosion of A by B.

After dilation, the hairs disappear while the core shrinks on each side and when erosion is performed with the same structuring element, the shrunk parts of the core expand back, while completely disappeared hairs cannot be recovered. Note that the background pixels are white while the yarn pixels are black in the images and thus the background pixels correspond to the object in the image processing terms. For this reason, the dilation operation is actually expanding the background which consequently erodes the yarn pixels. The process is depicted in Figure 5-49.

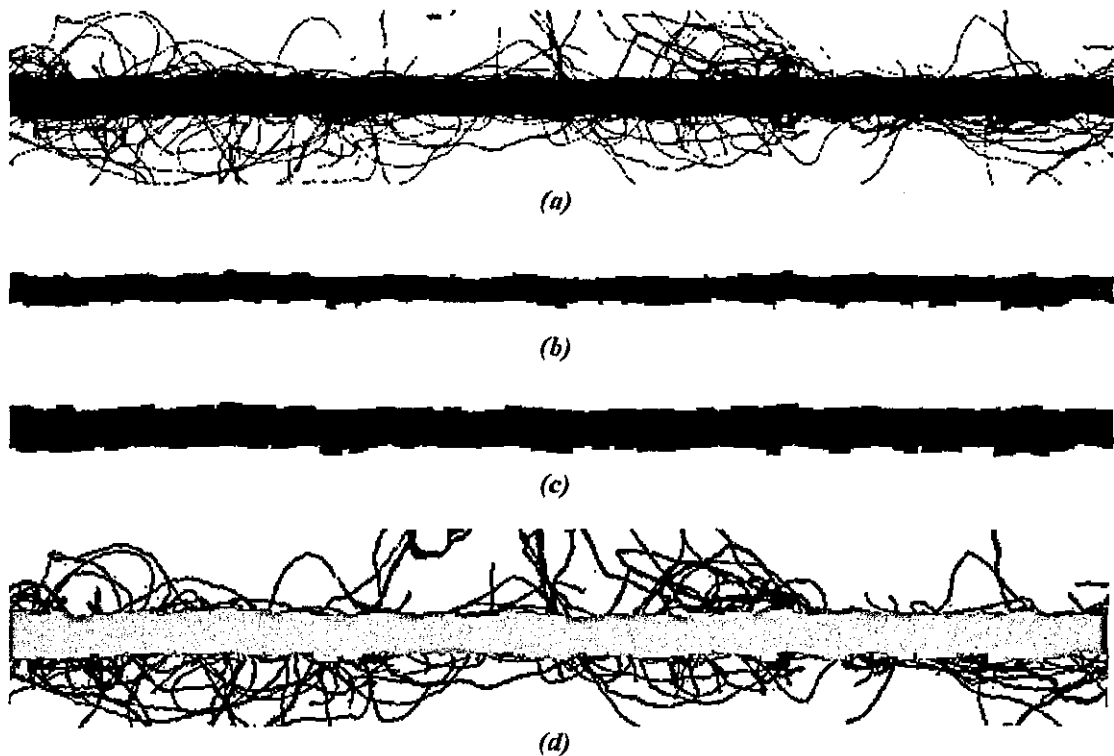


Figure 5-49 Closing operation. a) Second thresholded image b) (a) after dilation with a 9x9 rectangular structuring element, c) (b) after erosion, d) (c) overlaid on the first thresholded image showing hairs and the core.

Two characteristics of structuring element are the shape and the size. The shape is selected rectangular for simplicity. The size on the other hand is very critical since if the structuring element is small, some hairs might be left in the image and if it is large there is a possibility that core may be deleted during the dilation step. To ensure that the core is not deleted, the size is calculated automatically during the algorithm for locating the core axis by finding two thirds of the minimum core width

as shown in Figure 5-48. This size is also sufficient to delete the fibres since the fibres will be thinner than two thirds of the core width.

5.4.2.2 Horizontal tracking method

This method involves tracking every line in the image in both directions from the core axis perpendicular to it until the first threshold value is reached. Figure 5-50b shows the extracted core through this process. It can be seen that this method overestimates the diameter at many regions because of the fibres protruding from the core. To overcome this problem, a filtering process is applied, which limits the change in diameter if a sudden increase or decrease is observed between successive lines. The parameters for this filtering are determined manually through observation of many images and it is found that at 1:1 magnification and 1:1 aspect ratio, displacements of edge boundaries by more than 3 pixels between successive scans were often due to the surface fibres. In such cases, it is found appropriate to limit the increase to $1/7$ pixels to ensure that a protruding fibre did not affect the core boundary. Furthermore, if the change was because of a thin or thick place this allowed a gradual change to catch this trend. The maximum displacement can be changed for different magnification and aspect ratio settings. The core boundaries are corrected at two passes first top to bottom and then bottom to top. Figure 5-50c shows the core profile after this correction process.

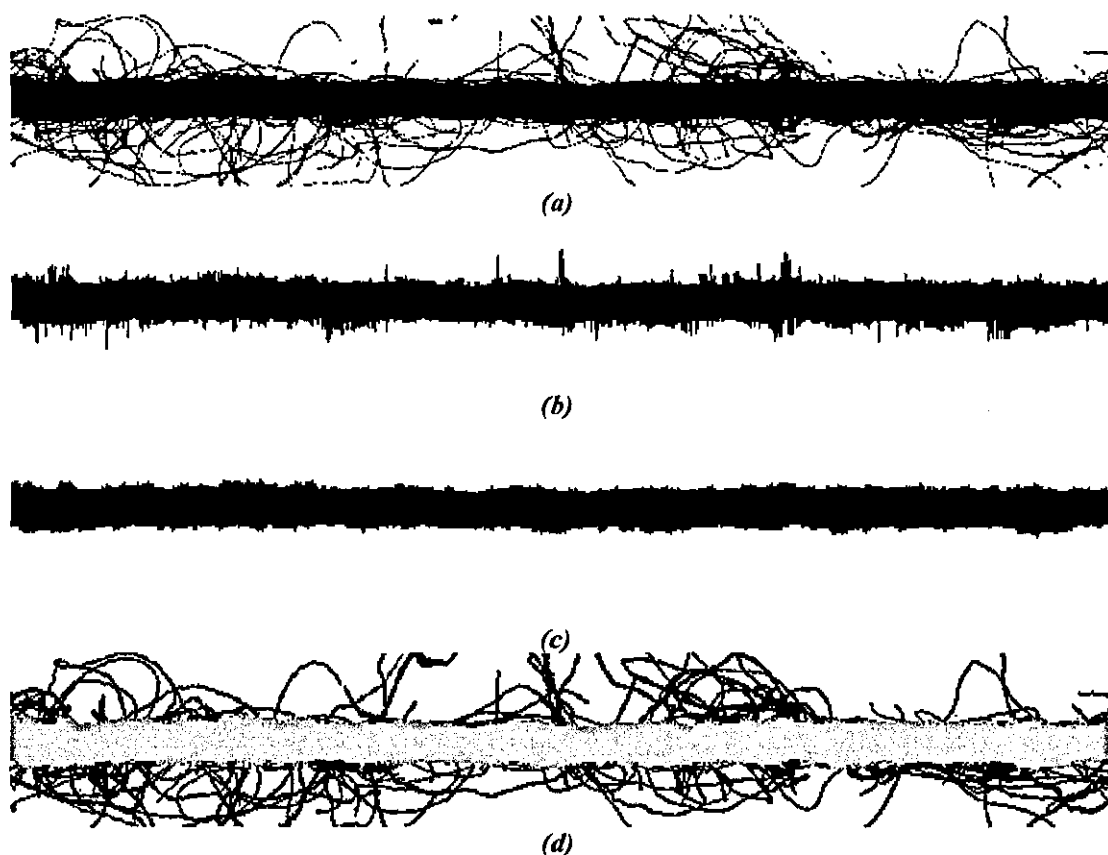


Figure 5-50 Edge tracking method. a) Second thresholded image, b) Core extracted by tracking c) (b) after correction, d) (c) overlaid on the first thresholded image showing hairs and the core.

Because of this filtering process, the change in diameter is limited to around $280\ \mu\text{m}$ within 1mm of yarn section. This however causes an underestimation of faults like neps and such regions in the yarn contribute to hairiness rather than the diameter. Figure 5-51 shows a neps and the processed image. It can be seen that the algorithm only allows a certain increase in the diameter creating triangular regions on both sides of the core.

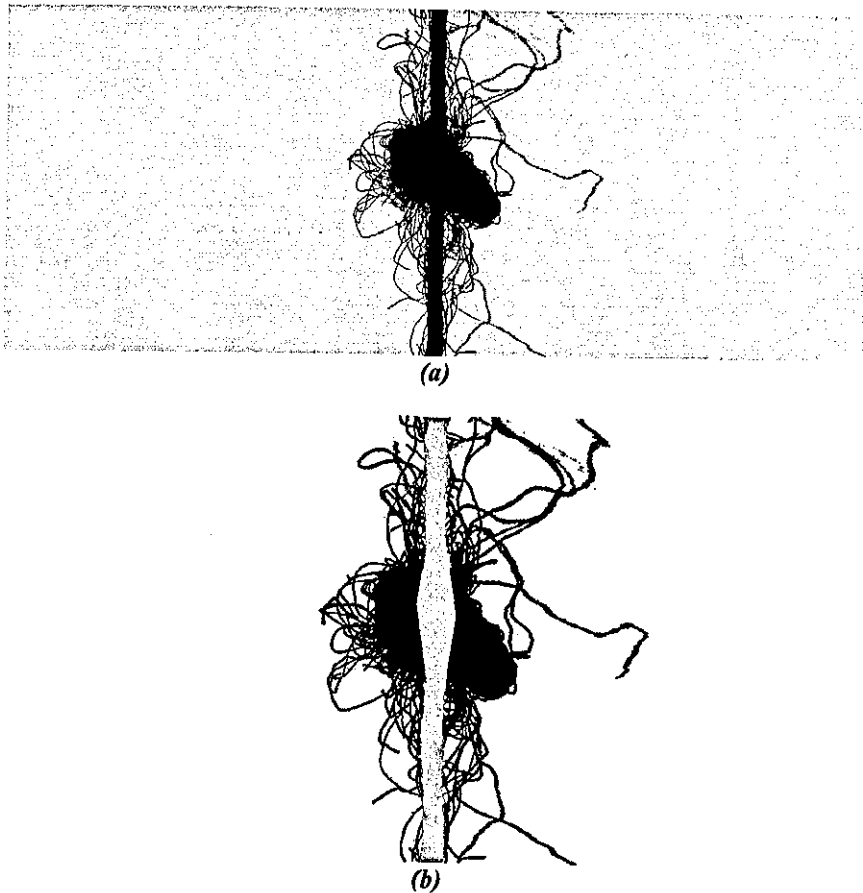


Figure 5-51 Effect of filtering on neps

To overcome the problem, the regions on the yarn core that are affected by the filtering process are identified and successive filtered rows that correspond to more than 1mm yarn length are reprocessed with no filtering and identified as a yarn fault. The fault length and the average diameter within the faulty region are then calculated. Figure 5-52a shows the filtered regions in a yarn image. In Figure 5-52b, a fault is shown as identified by the algorithm. This technique provides a very accurate measure of the fault lengths compared to sampling techniques since a fault can start at any point in the yarn and can be at any length. If the diameter was to be measured say using 2mm sampling length, a fault with 1mm length falling into a 2mm section would be identified as being twice the length and half the magnitude. If the faulty section falls in the middle of two successive 2mm sections, this effect would be more. Such a problem would not occur in the developed method.

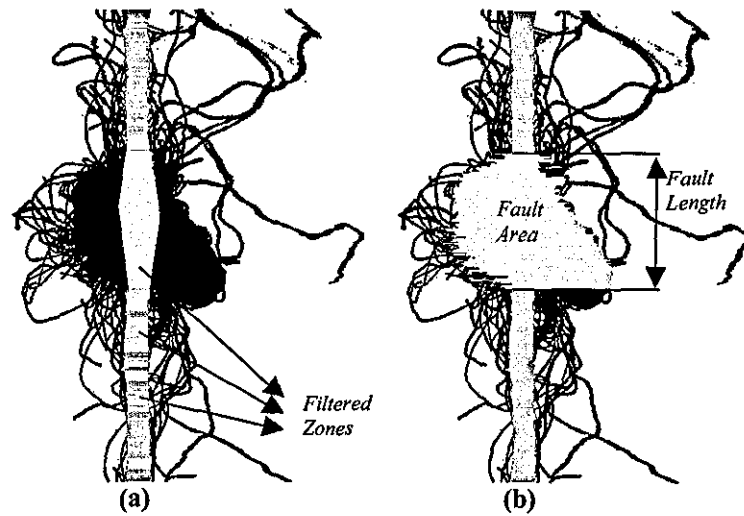


Figure 5-52 Identification of faults

5.4.3 Processing of Dark Field Yarn Images

Yarn images under dark field illumination do not exhibit a bimodal histogram since there are three major partitions in the image arising from the background, hairs and the core. Therefore, pre-processing algorithms developed for back-lit images cannot be applied for dark-field yarn images. It is quite straightforward to separate the background from yarn pixels by applying a single threshold. This threshold value is determined empirically by observing dark background images obtained with no yarn present and set to 25, which was found above the maximum background intensity. Figure 5-53 shows a dark-field image after applying this threshold.



Figure 5-53 (a) A dark field yarn image (b) (a) after applying a threshold @25

It can be seen from Figure 5-53 that upon thresholding, some core regions also disappear, since some core pixels have intensities very close to the average background intensity. Therefore, the core boundaries cannot be found from the thresholded image.

For determination of core boundaries, the first approach was to track every single row starting from the core axis until a rise in the intensity is reached, considering the fact that the edges of the core appear bright in a dark field image. However, it was realised that the extraction of diameter for every single row would be very difficult because of hairs on the core surface sometimes appearing bright and resulting in a small diameter to be found. Furthermore, in some cases where no hairs are present around the core, a significant increase in intensity could not be observed at the core edges. For these reasons, it was found necessary to find an average diameter from successive rows rather than for every single row.

The basic principle of the developed method is to integrate a number of rows corresponding to 1mm yarn section along every column and then to find the core edges from the obtained profile. At 1:1 scanning aspect ratio, 1 mm corresponds to approximately 70 rows. Figure 5-54 shows a typical profile obtained by integrating 70 rows along each column in a dark field image. It can be seen from this profile that there are two major peaks arising from the surface hairs on the left and right sides of the core. The processing algorithm automatically locates these two peaks and the left and right edges of the core are taken as the columns corresponding to these maximum points. Figure 5-55 shows a dark field image after hair-core background separation process.

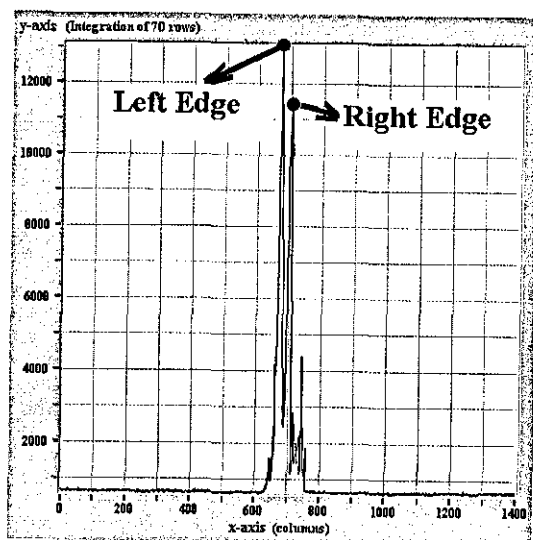


Figure 5-54 Integration of 70 rows for each column on a dark field image showing the selection of core edges

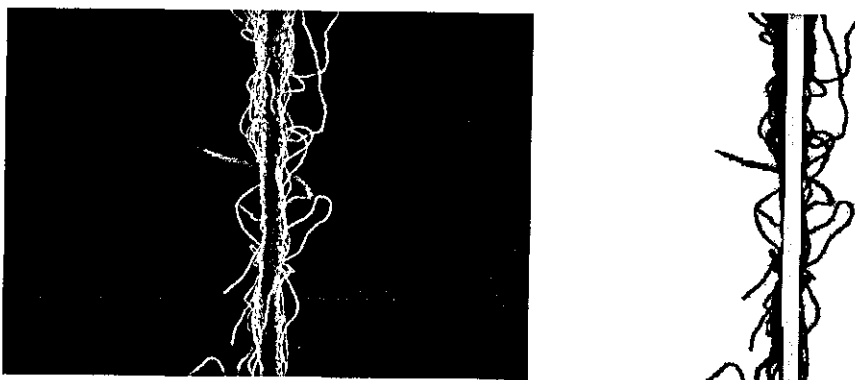


Figure 5-55 (a) Dark field yarn image (b) (a) after hair-core-background separation

The average processing time of the algorithm was around 70ms for 1400x1400 images. Through manual observation on many images, the technique is found completely successful in terms of locating the core boundaries as defined above. The main disadvantage of the method is that for diametric variation calculation, the minimum sampling length is limited to 1mm.

5.4.4 Processing of Two-Orthogonal Images

The processing of the images taken using the set-up in 5.2.2 is almost the same as that used for processing back-lit images. Two thresholds are found using the adaptive thresholding algorithm in 5.4.1.2 and the core axis is extracted using the column integration method in 5.4.2. The only difference is that two axis are extracted in this case as shown Figure 5-56. The core boundaries are then found for both orthogonal views using the horizontal tracking method described in 5.4.2.2. Finally, for each row an elliptical diameter is found from the left and right diameters d_l and d_r by taking the square root of their product. Figure 5-57 shows a two orthogonal image before and after processing. The grey parts in the processed image are the extracted core regions for two orthogonal views, while the black part in the centre is generated using the elliptical diameters for each row. It can be seen that the elliptical diameter is more uniform from single side views.

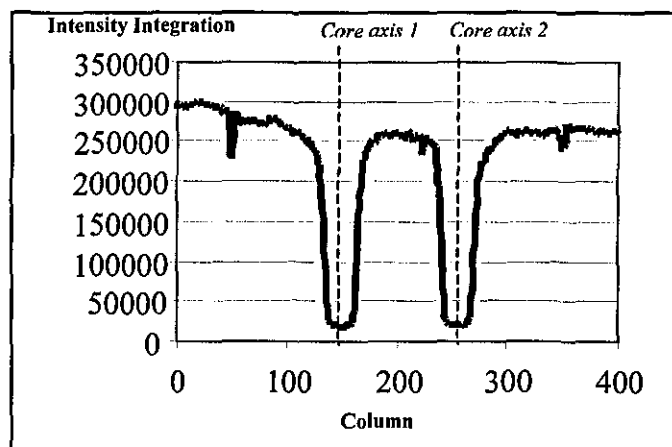


Figure 5-56 Integrated columns of a two orthogonal yarn image

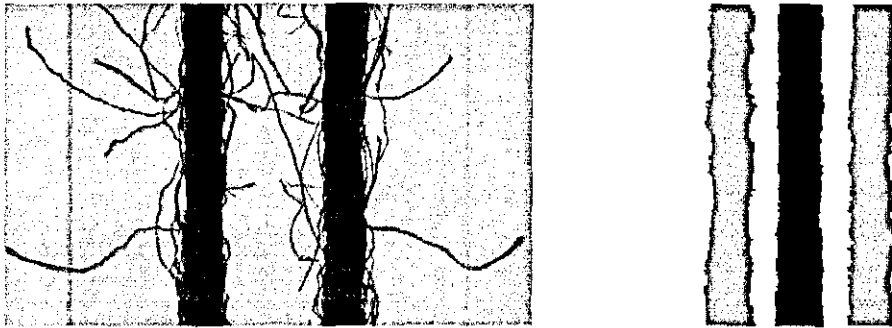


Figure 5-57 A two orthogonal yarn image before and after processing

5.4.5 Methods to Estimate the Hair Length

Once the pixels corresponding to hairs and the core are identified in a yarn image, the next task is to calculate the “amount” of hairs as well as the core diameter. It would be ideal to be able to extract the 3D chain code of every single hair, which would give the best estimate of the distribution of lengths as well as the distribution of, for example, wild and protruding fibres and loops. During this research, a fibre tracking algorithm was developed that tracks individual hairs to extract XY projections and predicts the Z displacements (defocusing) from the intensities. Unfortunately, due to the complex distribution of hairs, the algorithm could not accurately work on all yarn images. Nevertheless, the 2D tracking algorithm is briefly mentioned below. Later work concentrated on calculating the projection length assuming that it is statistically proportional with the total hair length. For this purpose, the simplest approach is to find the number of pixels that corresponds to the hairs. To account for defocusing, a couple of methods are also investigated such as skeletonising and grey level integration.

5.4.5.1 Fibre Tracking Algorithm

The basic principle of this algorithm is to track the fibres through successive scan lines. Once extracting a hair from a line scan using the method in 5.4.2.2, the boundary coordinates of this hair are stored in an array. In every successive scan, a

given valley (indicating a hair) is checked whether it is in the close vicinity of a valley in the previous scan line; if so it is assigned to the array holding that hair. If a given valley is not in the close vicinity of another valley in the previous scan then this indicates a new hair appearing in the scan. If a hair discontinues or adjoins the core in a particular scan line, then this scan is considered to be the end of that hair.

The orientation of hairs could be in any direction; they often cross each other and are generally not straight, as schematically illustrated in Figure 5-59a. The extended rule based algorithm handles the cross-section positions, bending of hairs, joint fibres and hairs running parallel to the scan line. If one or more hairs adjoin a particular valley in a given scan as in Figure 5-58a, that valley is marked as a cross-section and the joining coordinates of the fibres are stored in the memory. Up to 8 fibres can be stored in one cross section. If a cross section branches, the fibres inside are distributed to these branches according to the thickness of the branches and the entrance positions of the fibres to the cross-section. For example if there are two fibres in a cross section and the cross section divides into two branches then the fibre entering the cross section at the upper position is matched with the exit branch at the lower position. If there are for example more than two fibres in a cross section which then divides into a number of branches less than the number of fibres in it, the fibres are distributed to the branches according to their entrance positions and the thickness of exit branches. If a wide fibre separates into two branches at a certain scan, then it is assumed to have a 'C' shape as in Figure 5-58b and when the branches end as assumed they are connected into one fibre. If a narrow fibre separates into two branches, then it is handled as if two joined fibres are separating as in Figure 5-58c. If the width of a fibre suddenly increases then it is handled assuming that it is intersecting a perpendicular fibre as in Figure 5-58d. Figure 5-59b shows the output of the algorithm applied on an artificial image with all these different cases. Individually identified hairs are marked with different grey levels.

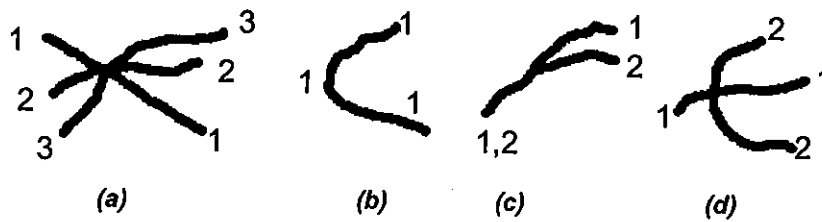


Figure 5-58 Different situations handled in the fibre tracking algorithm

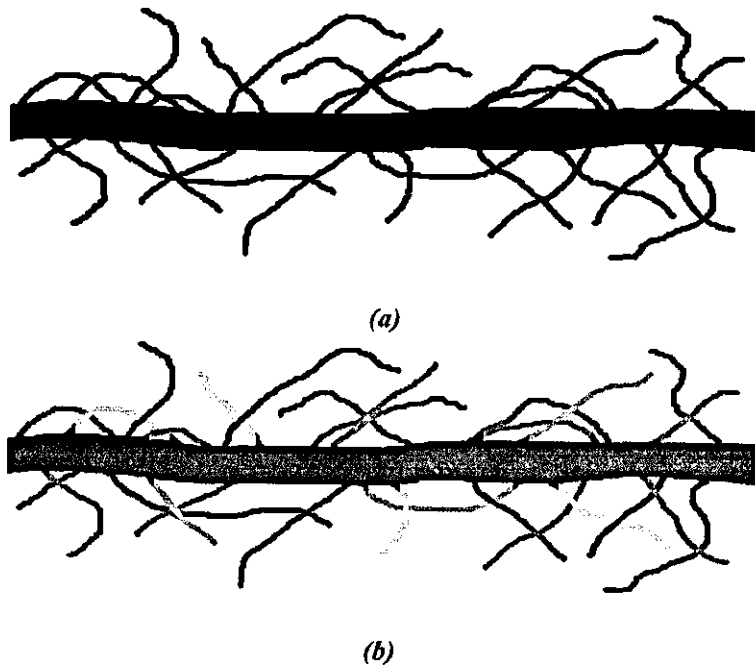


Figure 5-59 a) Various hair distribution possibilities. b) (a) after processing, different fibres are marked with different grey tones.

On actual yarn images, the algorithm could only work well on tracking hairs apart from the core, however in the region close to the core, it has been found very difficult to track individual hairs accurately due to the complex structure in most images. In such cases even a manual tracking was often found impossible. Although the considerable amount of time spent to improve the technique, extraction of the chain codes of every single hair on a yarn image has not been found feasible.

5.4.5.2 Skeltonising and “Bit Quads” Methods

Since the hairs in a yarn image may occupy different areas depending on the fibre thickness and especially due to defocusing, determination of the amount of hairs, or the total projection length from the number of pixels would be erroneous to some level. Skeletonisation is a well known image processing technique for reducing foreground regions in a binary image to a skeletal remnant that largely preserves the extent and connectivity of the original region while throwing away most of the original foreground pixels. Figure 5-60 shows a yarn image binarised using contrast enhancement and thresholding process described in 5.4.1.1 before and after skeletonising. Skeletonising is performed using a standard Wit 7.1 operator. It can be seen that upon skeletonisation, all hairs are reduced down to a width of one pixel regardless from the actual width in the binary image.

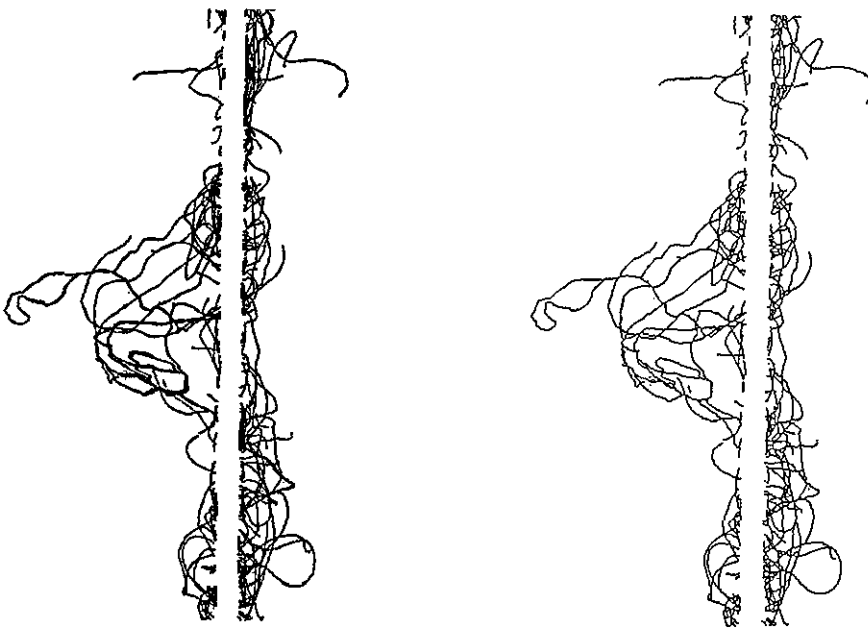


Figure 5-60 Binary yarn image before (a) and after (a) skeletonising

However, accurate calculation of hair lengths from the skeletonised image is not an easy task. It is well recognized in the image processing literature that length estimation from digitised contours is problematic since many possible contours all

having different lengths, correspond to a specific discrete realisation. The problem can better be understood from Figure 5-61 where a circle with 1-pixel thickness and 100-pixel diameter is shown. It can be seen that various possible contours are represented as either horizontal, vertical or 45 degree diagonal pixel pairs. In order to estimate the perimeter, if the number of pixels corresponding to the circle is calculated in the image, it gives 279, while the actual perimeter is 314.

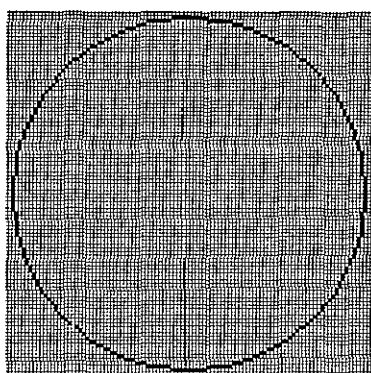


Figure 5-61 Digital representation of a circle with 1 pixel thickness and 100 pixel diameter

There are two common approaches to estimate the perimeter and areas of objects represented by square pixels. The first one is based on extracting the chain codes of objects in the binary image and then estimating curves that fits to the discrete chain representation. A discussion on these methods can be found in Yang et.al. [1994]. The other method first proposed by Gray [1971] (cited in Yang et.al. [1994]) uses some predefined patterns named "Bit Quads" and each small region in the image is matched with these patterns. The Bit Quads are given as follows;

Q_0	<table style="border-collapse: collapse;"> <tr><td style="padding: 2px 5px;">0</td><td style="padding: 2px 5px;">0</td></tr> <tr><td style="padding: 2px 5px;">0</td><td style="padding: 2px 5px;">0</td></tr> </table>	0	0	0	0																
0	0																				
0	0																				
Q_1	<table style="border-collapse: collapse;"> <tr><td style="padding: 2px 5px;">1</td><td style="padding: 2px 5px;">0</td></tr> <tr><td style="padding: 2px 5px;">0</td><td style="padding: 2px 5px;">0</td></tr> </table>	1	0	0	0	<table style="border-collapse: collapse;"> <tr><td style="padding: 2px 5px;">0</td><td style="padding: 2px 5px;">1</td></tr> <tr><td style="padding: 2px 5px;">0</td><td style="padding: 2px 5px;">0</td></tr> </table>	0	1	0	0	<table style="border-collapse: collapse;"> <tr><td style="padding: 2px 5px;">0</td><td style="padding: 2px 5px;">0</td></tr> <tr><td style="padding: 2px 5px;">0</td><td style="padding: 2px 5px;">1</td></tr> </table>	0	0	0	1	<table style="border-collapse: collapse;"> <tr><td style="padding: 2px 5px;">0</td><td style="padding: 2px 5px;">0</td></tr> <tr><td style="padding: 2px 5px;">1</td><td style="padding: 2px 5px;">0</td></tr> </table>	0	0	1	0	
1	0																				
0	0																				
0	1																				
0	0																				
0	0																				
0	1																				
0	0																				
1	0																				
Q_2	<table style="border-collapse: collapse;"> <tr><td style="padding: 2px 5px;">1</td><td style="padding: 2px 5px;">1</td></tr> <tr><td style="padding: 2px 5px;">0</td><td style="padding: 2px 5px;">0</td></tr> </table>	1	1	0	0	<table style="border-collapse: collapse;"> <tr><td style="padding: 2px 5px;">0</td><td style="padding: 2px 5px;">1</td></tr> <tr><td style="padding: 2px 5px;">0</td><td style="padding: 2px 5px;">1</td></tr> </table>	0	1	0	1	<table style="border-collapse: collapse;"> <tr><td style="padding: 2px 5px;">0</td><td style="padding: 2px 5px;">0</td></tr> <tr><td style="padding: 2px 5px;">1</td><td style="padding: 2px 5px;">1</td></tr> </table>	0	0	1	1	<table style="border-collapse: collapse;"> <tr><td style="padding: 2px 5px;">1</td><td style="padding: 2px 5px;">0</td></tr> <tr><td style="padding: 2px 5px;">1</td><td style="padding: 2px 5px;">0</td></tr> </table>	1	0	1	0	
1	1																				
0	0																				
0	1																				
0	1																				
0	0																				
1	1																				
1	0																				
1	0																				
Q_3	<table style="border-collapse: collapse;"> <tr><td style="padding: 2px 5px;">1</td><td style="padding: 2px 5px;">1</td></tr> <tr><td style="padding: 2px 5px;">0</td><td style="padding: 2px 5px;">1</td></tr> </table>	1	1	0	1	<table style="border-collapse: collapse;"> <tr><td style="padding: 2px 5px;">0</td><td style="padding: 2px 5px;">1</td></tr> <tr><td style="padding: 2px 5px;">1</td><td style="padding: 2px 5px;">1</td></tr> </table>	0	1	1	1	<table style="border-collapse: collapse;"> <tr><td style="padding: 2px 5px;">1</td><td style="padding: 2px 5px;">0</td></tr> <tr><td style="padding: 2px 5px;">1</td><td style="padding: 2px 5px;">1</td></tr> </table>	1	0	1	1	<table style="border-collapse: collapse;"> <tr><td style="padding: 2px 5px;">1</td><td style="padding: 2px 5px;">1</td></tr> <tr><td style="padding: 2px 5px;">1</td><td style="padding: 2px 5px;">0</td></tr> </table>	1	1	1	0	
1	1																				
0	1																				
0	1																				
1	1																				
1	0																				
1	1																				
1	1																				
1	0																				
Q_4	<table style="border-collapse: collapse;"> <tr><td style="padding: 2px 5px;">1</td><td style="padding: 2px 5px;">1</td></tr> <tr><td style="padding: 2px 5px;">1</td><td style="padding: 2px 5px;">1</td></tr> </table>	1	1	1	1																
1	1																				
1	1																				
Q_D	<table style="border-collapse: collapse;"> <tr><td style="padding: 2px 5px;">1</td><td style="padding: 2px 5px;">0</td></tr> <tr><td style="padding: 2px 5px;">0</td><td style="padding: 2px 5px;">1</td></tr> </table>	1	0	0	1	<table style="border-collapse: collapse;"> <tr><td style="padding: 2px 5px;">0</td><td style="padding: 2px 5px;">1</td></tr> <tr><td style="padding: 2px 5px;">1</td><td style="padding: 2px 5px;">0</td></tr> </table>	0	1	1	0											
1	0																				
0	1																				
0	1																				
1	0																				

Figure 5-62 Bit Quads

Using Bit Quads, the total area (A) and the perimeter (P) of the objects in an image is calculated using the following formula;

$$A = \frac{1}{4} [n\{Q_1\} + 2n\{Q_2\} + 3n\{Q_3\} + 4n\{Q_4\} + 2n\{Q_D\}] \quad (5.14)$$

$$P = n\{Q_1\} + n\{Q_2\} + n\{Q_3\} + 2n\{Q_D\}$$

Where $n\{Q\}$ is the number of matches between the image pixels and pattern Q. Pratt [1991] (cited in Yang et.al. [1994]) introduced following method based on Bit Quads for area and perimeter estimation which he found to be more accurate than the previous formula;

$$A = \frac{1}{4} \left[n\{Q_1\} + \frac{1}{2}n\{Q_2\} + \frac{7}{8}n\{Q_3\} + n\{Q_4\} + \frac{3}{4}n\{Q_D\} \right] \quad (5.15)$$

$$P = n\{Q_2\} + \frac{1}{\sqrt{2}} [n\{Q_1\} + n\{Q_3\} + 2n\{Q_D\}]$$

The major advantage of Bit Quads technique is that it does not require any tracking algorithm to extract the chain code. Due to its practicality, this technique is implemented in a custom function and used in conjunction with skeletonising method for a better estimation of hair lengths from the skeletonised yarn image. When applied to the circle image in Figure 5-61, the perimeter is found as 335 pixels, which is closer to the actual perimeter than the perimeter value obtained using the number of pixels. It is clear that as the object departs from circularity, that is, the contour becomes more linear, the Bit Quads method will give a more accurate length estimation compared to counting the number of pixels.

5.4.6 Comparison of Image Processing Methods for Back-Lit Yarn Images

In order to examine the effects of different processing methods on measurements 1700 images from 17 different yarn samples are processed using various techniques.

Figure 5-63 shows the number of pixels corresponding to the yarn, i.e. core pixels plus hair pixels, after background separation using three different methods. It can be seen that min-max differentiation technique exhibits very close results with adaptive thresholding, whereas filtering plus thresholding method exhibits smaller values. The main reason for this is that contrast enhancement operation shrinks the width of the objects, being especially significant on hairs.

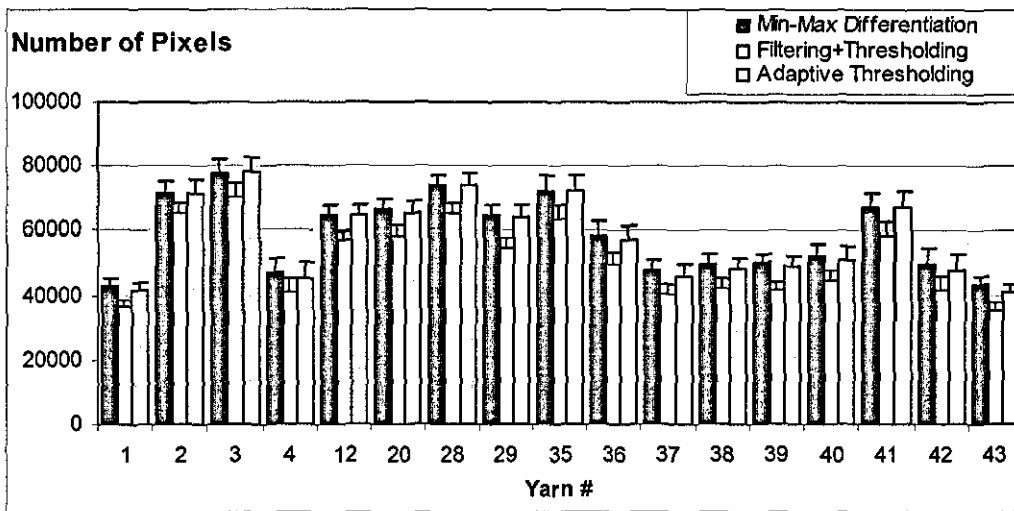


Figure 5-63 Number of pixels corresponding to yarn (hair+core pixels) found using different segmentation methods (Error bars correspond to +[Standard Deviation])

Figure 5-64 shows the average number of core pixels from different core-hair separation techniques. Morphological filtering and core edge filtering followed by horizontal tracking appear to have the same effect on hair-core boundaries. The min-max differentiation method, where no sort of further filtering is applied to initially found boundaries, exhibits slightly higher values as to be expected.

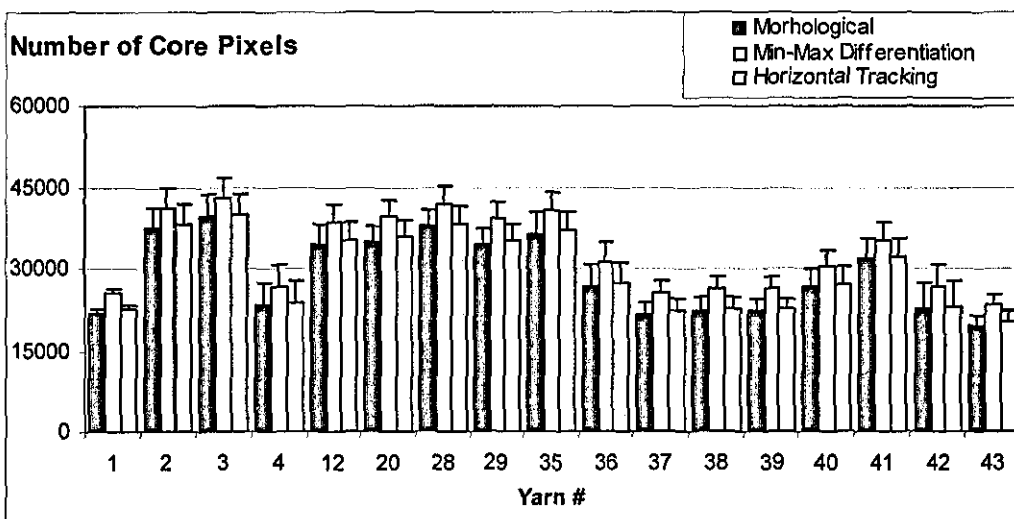


Figure 5-64 Comparison of number of core pixels measured using 3 different processing techniques (Error bars correspond to +[Standard Deviation])

Figure 5-65 shows the relation between the hair lengths (hair length in cm per unit yarn length in cm) found from the skeletons and total number of hair pixels calculated from adaptive thresholding method. It is interesting to note that although the 17 different yarn samples tested might have different fibre thicknesses and the effect of defocusing would be at different levels for different yarns due to varying average hair lengths, the average lengths from the skeleton images exhibit a very good linear relation with total number of hair pixels. This suggests that the average projected hair lengths can be estimated from number of pixels with the same accuracy as the skeletonising method. However, there is a little offset where the skeleton length has some value where the number of hair pixels is zero. The reason for this is probably due to thin core edges, which make important contributions in the skeletonised image, whereas they have very little effect on total number of hair pixels.

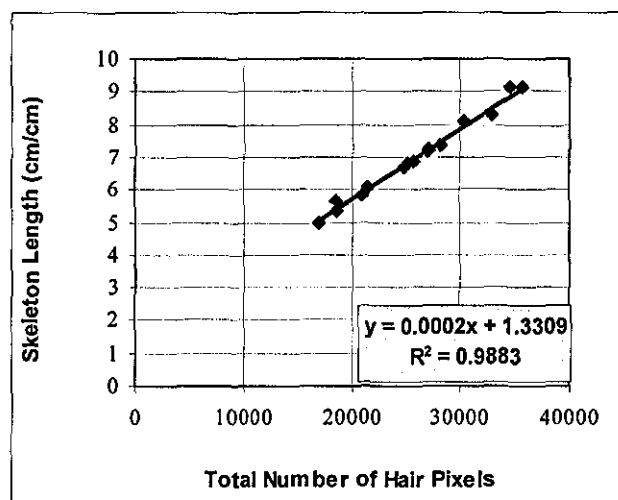


Figure 5-65 Comparison of the average hair length calculated from skeletonising technique with number of pixels without skeletonising

Figure 5-66 shows the effect of "Bit Quads" technique on calculated skeleton lengths. It can be seen that with "Bit Quads" technique, the skeleton length is always higher. It is also interesting that there is a perfect linear relation between the results obtained with and without applying "Bit Quads" method. It could be expected that

for yarns having more curly hairs, "Bit Quads" technique would make a bigger difference than for the yarns with more straight hairs.

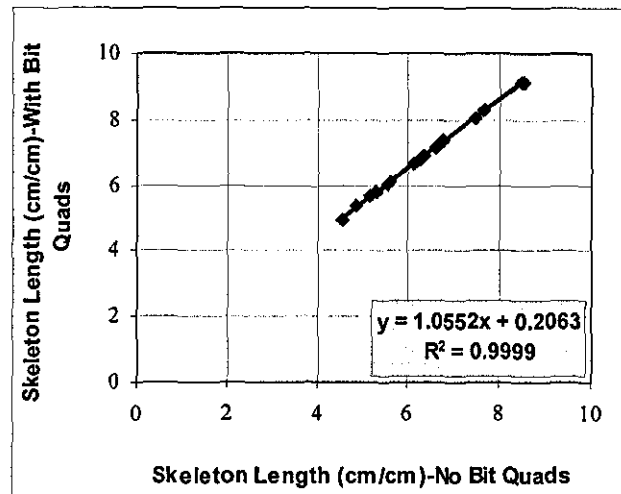


Figure 5-66 Comparison of average hair lengths (cm of hair per cm of yarn length) calculated with and without using "Bit Quads" method after skeletonising

Table 5-2 shows the average processing times on an 800 MHz Pentium3 computer for 1400x1358 yarn images that corresponds to a 2cm yarn length and 20mm of field of view. It can be seen that adaptive thresholding for yarn background separation and horizontal tracking for core-hair separation give the fastest processing speed at around 16images/second. The required processing speed to meet the maximum line rate of the camera is around 14.4 images/second (40MHz Data Rate / 2048pixels / 1358 lines). The speeds can of course be increased using a faster computer processor, which are available as fast as 3.2 GHz nowadays. However, even on such a computer, the filtering+thresholding method cannot meet the required speed. The speed can be increased using hardware convolution filters, which are unfortunately quite expensive. The skeletonising method is the most time consuming method which requires a further 1046ms after filtering and thresholding. Considering its speed advantage and that all techniques give highly correlated results, the adaptive thresholding and horizontal tracking method is found to be the most suitable technique and used for the analysis throughout Chapters 5 and 6.

Table 5-2 Comparison of average processing times of four different IP methods for 1400x1358 images

Processing Method	Processing Time (ms/image)
Adaptive Thresholding + Morphological Filtering	280
Min-Max Differentiation	152
Filtering + Thresholding	386
Adaptive Thresholding + Horizontal Tracking	62

5.5 Digital Modification of Scanning Aspect Ratio and Definition of Aspect Ratio Classes

The scanning aspect ratio is given as the ratio of the height of one CCD pixel to the width of the object that one pixel corresponds to as mentioned in section 3.3. Since the height of one CCD pixel of the camera used in LYSS is 14 μm , an aspect ratio of 1:1 at 1:1 magnification requires acquisition of a scan line as the yarn moves 14 μm . However, the yarn transport and camera acquisition system of LYSS allows a line scan every 14.7 μm . This scanning ratio corresponds to a resolution of 68 lines per mm and taken as the reference aspect ratio class 1:1 from this point forward.

Since the camera has a limited data rate there is a limit to how fast the yarn can be transferred at 1:1 scanning aspect ratio. This limit is around 0.3m/s for the camera used in this research. In order to investigate the minimum allowable aspect ratios for both hairiness and irregularity measurements, lower aspect ratios are simulated from high aspect ratio images. The basic principle is to take the average of n successive lines in the original image and generate an image with 1: n aspect ratio from these average values. The resultant image will of course have a height of H/n and a resolution of N/n , where H and N are the height and the resolution of the original image respectively. It is found more appropriate to select n so that N/n would be an integer to enable a better comparison of hairiness and diameter variation values between different aspect ratio classes.

Three different aspect ratio classes are defined as 1:1, 1:4.9 and 1:11.9 corresponding to 68, 14 and 6 lines per mm resolutions respectively. Figure 5-67 shows an original AR 1:1 image and AR 1:4.9 and AR 1:11.9 images derived from the original image.

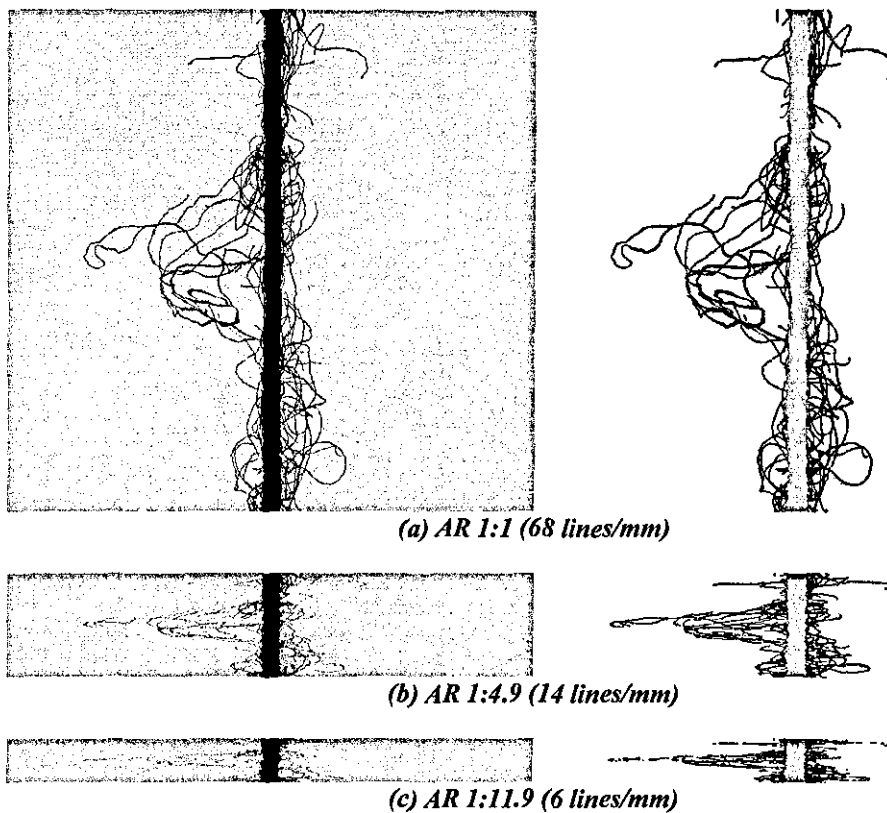


Figure 5-67 Original image acquired from the camera at 1:1 aspect ratio (a) and the images converted into AR 1:4.9 (b) and AR 1:11.9 (c). The images on the right are after applying the two level thresholding and horizontal tracking algorithms to the images on the left.

5.6 Conclusions

Three different illumination arrangements are tested for back-lit illumination. Placing the light source simply behind the yarn with no additional optical elements is found superior in terms of contrast and depth of field. However, the effective field of view was limited with the aperture size in this method and a minimum aperture size of F/2.6 is found necessary to achieve the maximum field of view allowed by the CCD array. The lens used for the experiments provided 21mm field of view with its maximum available aperture size of F/3.5. Tungsten filament bulbs are found

superior compared to LED light sources considering the minimum exposure times achievable, which depends on the intensity of the light source. A field lens in order to improve the field of view is employed but at the expense of degradation in image background quality and loss in depth of field, hence not found suitable. A diffuser is also tested to increase the field of view but the image quality was below desirable limits.

A mirror placed at 45° to the camera axis behind the yarn is employed to acquire the images of a yarn from two orthogonal views. The optical path difference problem between two orthogonal views is addressed, but found negligible for a centre to centre distance of 1.4mm.

A ring light furnished with a number of LED light sources each directed towards the yarn core at a certain angle is used for dark field illumination. A field aperture is employed to improve the image background quality. This illumination is found to be very successful in terms of highlighting the boundaries between the core and surface hairs; however, it was strongly affected by the fibre colour. An infrared light source can be used in the future to overcome the problem.

For yarn surface inspection using high magnifications, a back-lit and front-lit illumination hybrid is found to be the more suitable compared to front-lit illumination alone. It is seen that a coherent light source used for back-lit illumination provided a better contrast compared to incoherent light sources, which would enable a more accurate determination of diameter. For front-lit illumination, projecting the light from an angle rather than perpendicular to the yarn surface enables a better definition of yarn surface. However, front-lit illumination parameters such as the wavelength of the light source and the suitable projection angle should be studied further.

Various image processing algorithms are developed for back-lit yarn images. Contrast enhancement using convolution filters is found to be very useful in terms of

identifying the isolated background pixels between hairs. However, convolution filters meant a significant increase in processing time. Maxima-minima differentiation algorithm provided a fast and adaptive nature but was seriously affected by impulse noise and diffraction fringes. Adaptive two level thresholding algorithm is found to be very suitable in terms of speed and reliability.

Eight popular adaptive thresholding methods are also evaluated. The experiments on two yarn images one with non-uniform and the other with a uniform background revealed that global single thresholding algorithms tended to fail identifying either in the background or the defocused fibres depending on the threshold level. Kapur's entropy thresholding is not found suitable due to the fact that the fraction of foreground pixels is low compared to the background pixels, which favors the optimum threshold value towards the background region in the histogram. The locally adaptive thresholding algorithms were more promising for identification of defocused fibres. However, those based on the statistical information within local neighborhoods (Niblack's, Sauvola & Pietaksinen's and Bernsen's methods) mostly deleted the interiors of foreground objects. This could be useful for determination of hairiness; however determination of core diameter from these images does not appear to be an easy task especially for Bernsen's technique which gives noise within the core region. The locally adaptive thresholding algorithms that rely on edge information (Yanowitz & Bruckstein, Min-Max differentiation) performed quite well in identifying the isolated pixels as well as the defocused fibers. Adaptive two level thresholding technique was also very successful in this sense at regions around the core. However, Yanowitz & Bruckstein's method deleted some core regions during the ghost removal process, which was unacceptable.

For core-hair separation, two methods one based on morphological filtering and the other on core edge tracking are described. A filtering process is introduced for the latter algorithm to avoid the surface hairs from creating an artificial increase in diameter. Both methods exhibited close results when the number of extracted hair pixels are compared, hence the second algorithm is preferred due to its speed.

In order to estimate the total hairiness an algorithm is studied that aims to track and extract the chain codes of every single hair, however due to the complexity of the hairs at the vicinity of the core, the technique is not found feasible. A method called "Bit Quads" to calculate the total hair length from the skeletonised yarn images is described. A perfect correlation is observed between the total number of hair pixels and the hair lengths obtained using the "Bit Quads" method, which suggested that the number of hair pixels could be used as a measure of total hair length regardless from the fibre width, at least for the range of samples tested.

Three different aspect ratio classes are defined and derivation of lower aspect ratio images from a 1:1 aspect ratio image is demonstrated. The effects of using lower aspect ratios on hairiness and irregularity measurements are discussed based on this method in Chapters 6 and 7.

CHAPTER 6 - Evaluation of Hairiness

6.1 Introduction

This chapter explains various methods implemented in LYSS to describe yarn hairiness. The first section to follow describes a new method developed to simulate photo electric sensors such as the one in Zweigle G565 Hairiness Tester. The effects of sensor resolution, signal threshold level and selection of zero reference position from the core are investigated. The simulations are also correlated with the measurements from Zweigle G565.

In Section 6.4, various indices are described to define total hairiness based on integration of grey levels, number of hair pixels and skeleton length of hairs. These indices are compared with the Uster Tester's H index. The indices obtained from dark field and back-lit images are also compared. A new method that gives the distribution of hairs around the core is described in Section 6.5.

In Section 6.6, the effects of using different scanning aspect ratios on hairiness measurements are investigated.

6.2 Yarn Samples

43 ring spun yarn samples listed in Table 6-1 are obtained from Istanbul Technical University Textile Engineering Department and NCSU School of Textiles. Various tests have been carried out on different sets of samples. Within the next 3 Chapters, these yarns will be referred to using the sample numbers given on the left column of Table 6-1.

Table 6-1 The characteristics of yarn samples used in the experiments

Sample #	Type	Blend	Count	Twist-T/inch	Twist-T/m
1	Ring	65/35 Cotton/Polyester	Ne 30/1	21.59	850
2	Ring	100% Cotton	Ne 10/1	12.33	485
3	Ring	100% Cotton	Ne 10/1	10.43	410
4	Ring	65/35 Cotton/Polyester	Ne 30/1	19.8	779
5	Ring	65/35 Cotton/Polyester	Ne 30/1	18.12	713
6	Ring	65/35 Polyester/Cotton	Ne 20/1	14.7	578
7	Ring	65/35 Polyester/Cotton	Ne 20/1	16.1	633
8	Ring	100% Cotton	Ne 20/1	17.49	688
9	Ring	100% Polyester	Ne 20/1	16.1	633
10	Ring	100% Polyester	Ne 10/1	10.43	410
11	Ring	65/35 Polyester/Cotton	Ne 20/1	17.43	686
12	Ring	65/35 Polyester/Cotton	Ne 10/1	11.38	448
13	Ring	100% Polyester	Ne 10/1	12.33	485
14	Ring	65/35 Polyester/Cotton	Ne 10/1	10.43	410
15	Ring	100% Cotton	Ne 30/1	18.2	716
16	Ring	65/35 Polyester/Cotton	Ne 30/1	19.1	751
17	Ring	100% Polyester	Ne 20/1	14.7	578
18	Ring	100% Cotton	Ne 20/1	14.7	578
19	Ring	65/35 Cotton/Polyester	Ne 10/1	10.43	410
20	Ring	65/35 Cotton/Polyester	Ne 10/1	12.33	485
21	Ring	65/35 Polyester/Cotton	Ne 20/1	17.49	688
22	Ring	100% Polyester	Ne 10/1	11.38	448
23	Ring	65/35 Cotton/Polyester	Ne 10/1	11.38	448
24	Ring	100% Polyester	Ne 20/1	17.49	688
25	Ring	65/35 Cotton/Polyester	Ne 20/1	16.1	633
26	Ring	65/35 Cotton/Polyester	Ne 20/1	14.7	578
27	Ring	100% Cotton	Ne 20/1	16.1	633
28	Ring	100% Cotton	Ne 10/1	11.38	448
29	Ring	65/35 Polyester/Cotton	Ne 10/1	12.3	484
30	Ring	65/35 Polyester/Cotton	Ne 30/1	18.2	716
31	Ring	60/40 Acrylic/Wool	Nm 30/1	12.2	480
32	Ring	60/40 Acrylic/Wool	Nm 30/1	9.65	380
33	Ring	70/30 Acrylic/Wool	Nm 32/1	13.08	515
34	Ring	100% Cotton	Ne 60/1	29.21	1150
35	Ring	100% Cotton	Ne 10/1	11.05	435
36	Ring	100% Cotton	Ne 20/1	15.24	600
37	Ring	100% Cotton	Ne 30/1	19.56	770
38	Ring	100% Cotton	Ne 30/1	22.36	880.4
39	Ring	100% Cotton	Ne 30/1	21.96	864.4
40	Ring	100% Cotton	Ne 18/1	-	-
41	Ring	100% Cotton	Ne 12/1	-	-
42	Ring	100% Cotton	Ne 30/1	-	-
43	Ring	100% Cotton	Ne 28/1	-	-

6.3 Simulation of Photoelectric Sensors for Counting Hairs using Image Processing

A common method used to measure the hairiness is based on photoelectric sensors placed at certain distances from the yarn core edge and counting number of signals generated by the hair shadows projected onto the sensors through some magnification elements [Lappage & Onions, 1964] or more generally through a slit [Slack, 1970; Ghosh, 1988] as shown in Figure 6-1. If the intensity of light drops below a certain percentage of the intensity of light when no interruption is present, then the sensor generates a signal indicating a hair intersection. The resolution of a sensor can be defined as the minimum detectable signal fluctuation. In the system depicted in Figure 6-1, the resolution is determined by the width and the height of the slit, that is if there are two hairs separated by a distance less than the width of the slit parallel to the yarn axis or less than the height of the slit perpendicular to the yarn, it will not be possible to separate them by this system. This restriction is recognised in the literature, being important particularly for rotor spun yarns having surface fibres wrapped around the core [Barella et.al., 1992].

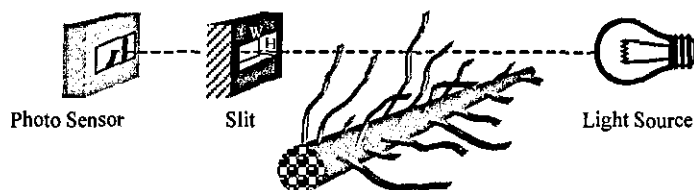


Figure 6-1 Principle of hair counting method using a photo electric sensor.

Another important restriction when using photo electric sensors arises from the variations of the yarn core diameter, and therefore, the zero length position of the hairs. If the sensor distance were set too close to the yarn core, then variations of the core diameter would cause a fixed sensor distance to result in misleading hair count. This, of course, applies to all hair length distances. However, since the number of hairs increase exponentially approaching to the core, the problem is more amplified at short hair distances.

An image processing technique to simulate the hair counts measurement from conventional photo sensors is developed during this research. The technique also allowed investigation of the effects of many parameters on the measurements highlighting possible drawbacks of photo electric sensors.

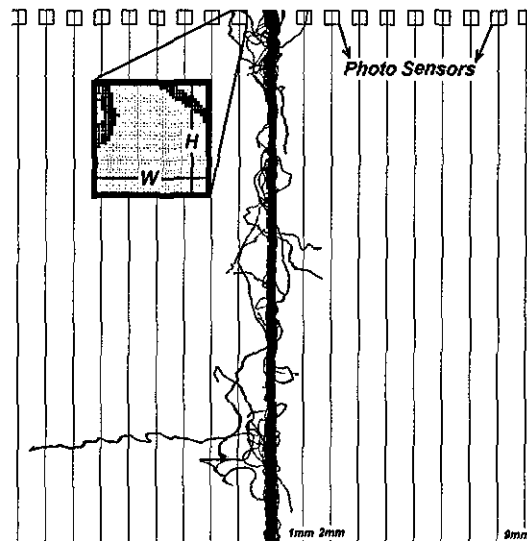


Figure 6-2 The sub-windows for simulating the photosensors

After separating the yarn from background pixels and determining the core boundaries, the photoelectric sensors are simulated as rectangular elements of certain dimensions as depicted in Figure 6-2. If the light is first passing through a slit as in Figure 6-1, the dimensions W and H of the subwindows correspond to the slit dimensions. On a typical image, a 1×1 mm rectangle corresponds to 70×70 pixels. The processing program allows definition of any number of photo-sensors at any distances from the core. The sum of the pixel intensities within the rectangle is considered to be proportional to the intensity of light falling on the photo sensor. The sums of intensities are calculated for each row in order to obtain a light-distance profile parallel to the yarn axis. Figure 6-3 shows typical profiles for sensors 1, 2 and 3mm from the core. It can be seen that the profile from 1mm is generally more complex while in other profiles individual hairs are more clearly separated. After applying a threshold to these signals, each 0-1 transition is counted as a hair.

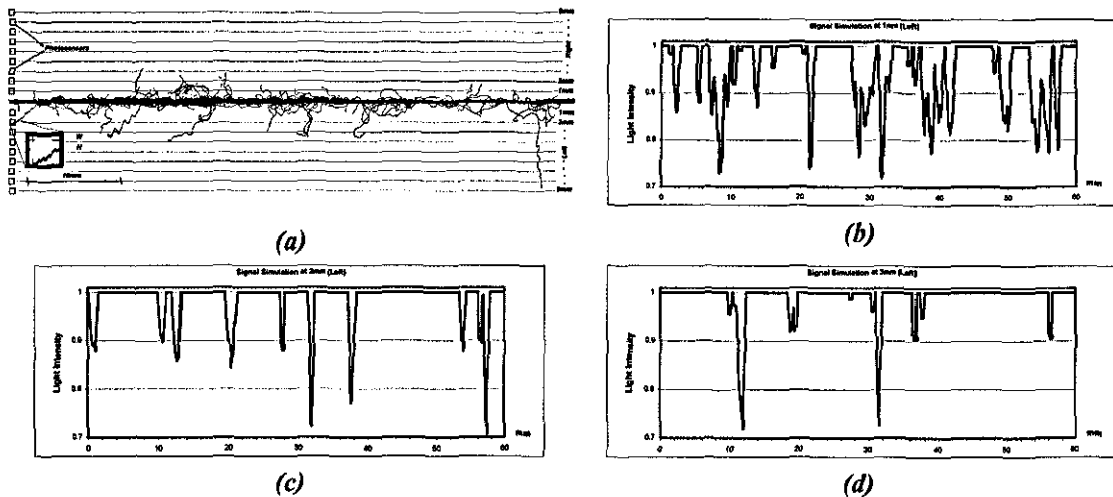


Figure 6-3 (a) Image of a yarn corresponding to 60mm (b-d) Light intensity profiles for photo sensors 1, 2 and 3mm apart from the core

Yarn samples 20-39 are first tested on a Zweigle G565 and then a set of experiments are carried out using LYSS to investigate the parameters affecting the measurements in photo sensor simulation algorithm. For each sample, 1250 images corresponding to 25m of yarn length are grabbed and stored. This allowed testing different configurations for the same yarn sections. Due to the time required for the computer to store images in real time, the yarn transfer speed was kept slow at 4m/min during image acquisition. The 25m test length is found to be adequate following the experiments which measure the average number of intersections for different test lengths. Figure 6-4 shows the average N1 (The number of hairs at 1mm from the core) measurements of all 20 yarn samples for different test lengths, where it can be seen that all yarns exhibit a steady N1 average after 10m. This test length is also found adequate to determine the average number of hairs at other distances from the core (N2-N9) as well as the S3 values (Total number of hairs at 3mm and further from the core).

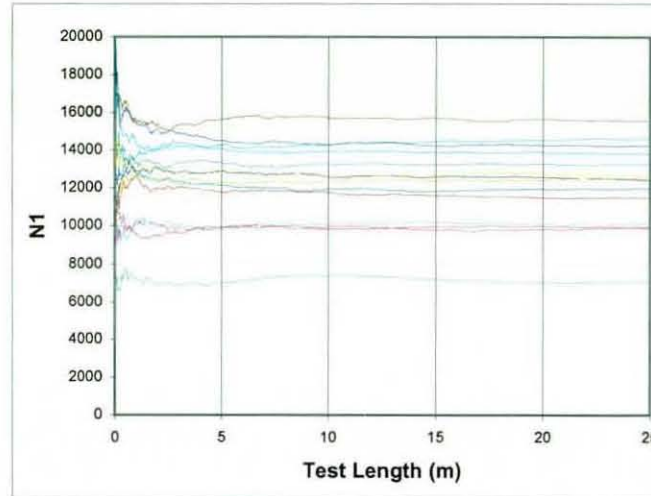


Figure 6-4 Change of average N1 values according to the test length

Initially, the effects of sensor resolution parameters are investigated. Figure 6-5 shows the measurements for 5 yarn samples using 4 different resolution settings in the simulations. It can be seen that the change of sensor resolution does not affect all the yarns in the same way, particularly for N1 values. For instance, the N1 value for sample 20 is largest when using a 1mmx0.5mm sensor compared to the values obtained with other sensor resolutions for the same sample. Sample 33 on the other hand has much less value at this resolution than it has at 0.1mmx0.1mm resolution. Another interesting point to note is that the N1 value is smaller for sample 33 than sample 20 at 0.5mmx0.5mm resolution while it is larger at a higher resolution of 0.1mmx0.1mm. This is due to dense distribution of hairs in sample 33 which can only be observed accurately by using higher sensor resolutions. This shows that the N1 measurements with low sensor resolutions do not give comparable results for different yarns especially those having densely distributed hairs. Since the hairs are spatially more distinctly separated at distances more than 1 mm from the core, the effect of sensor resolution decreases at these distances and the hair counts act more consistently according to the sensor resolution for different samples.

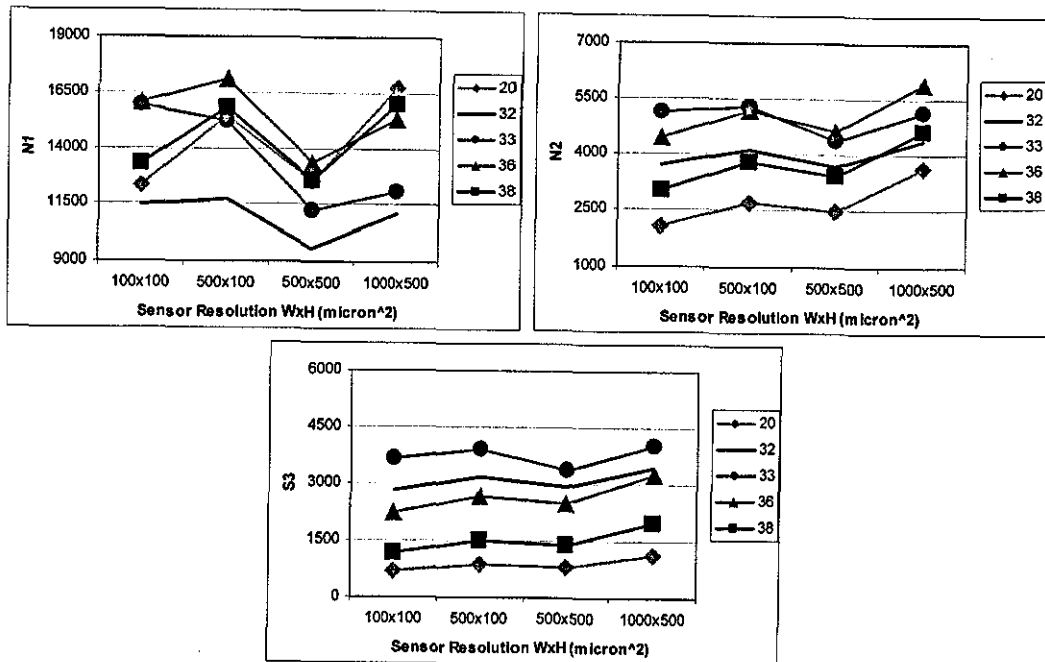


Figure 6-5 Comparison of N1, N2, S3 measurements using different sensor dimensions

When digitizing the simulated photo sensor signal, a threshold level at 99.9% allows any hair pixel entering the photo-sensor zone to change the signal from 1 to 0. This level can confidently be used in image processing since a threshold operation is carried out in the pre-processing stage. However, when using an actual photo-sensor, such a threshold level will not practically be possible due to noise and need for a higher tolerance for light intensity fluctuations. Figure 6-6 shows the effect of using different threshold levels where the sensor resolution is kept constant at 0.5x0.5mm. The number of intersections generally decreases as the threshold level is decreased. However for sample 33, decreasing the threshold level down to a certain level increases the number of hairs at 1mm from the core due to the disappearance of some points in the profile acting as a bridge.

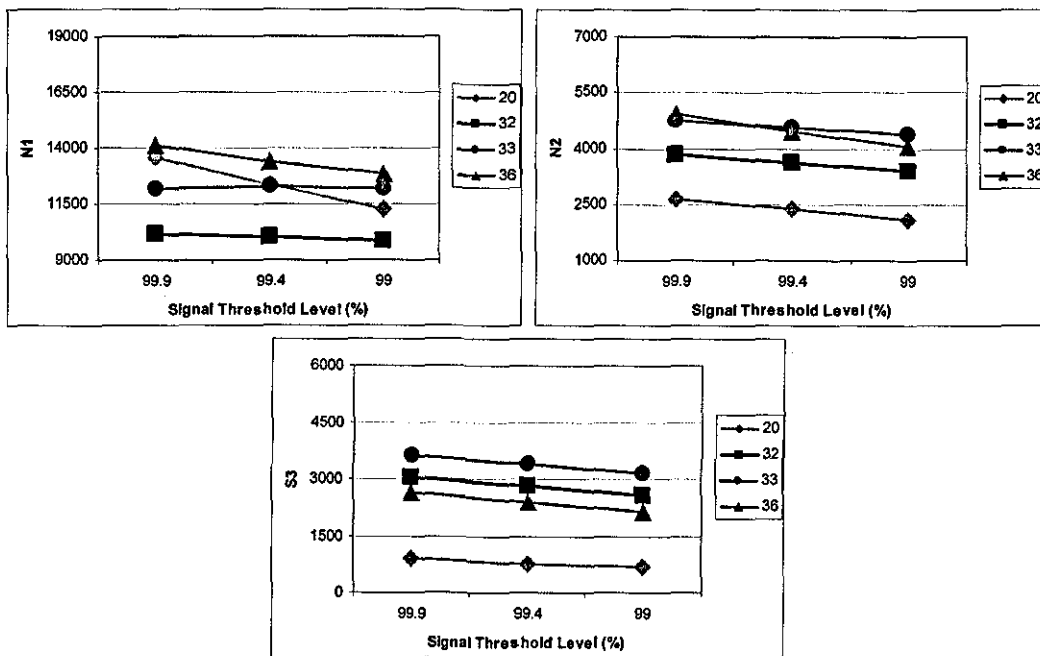


Figure 6-6 Comparison of results using different signal threshold levels

When performing the photo sensor simulation, the processing algorithm finds a reference core edge position automatically for every image that corresponds to 20mm of yarn length (1400 rows). In both Zweigle G565 and Shirley Hairiness Tester the core edge is located once at the beginning of the test by moving the yarn transport rollers at the measuring zone manually until the core does not block past the reference point. The exact method how the core edge is determined and the precision of this alignment could not be found in the literature. It has been shown during this work that the selection of the 0 reference line strongly affects hair count measurements with increasing amplitude closer to the core, thus requires a high precision. Three different configurations are tested to investigate the effect of 0 reference line to overall measurements. The first one takes the closest edge of the core to the core axis among 1400 rows (MIN), while the other one takes the furthest edge position from the core axis (MAX) and the final one calculates the 0 reference line by taking the average of the core positions of 1400 rows (MEAN). Figure 6-7 shows the results of these measurements. In all configurations the sensor resolution is kept constant at 0.5x0.5mm and the threshold level at 99.9%.

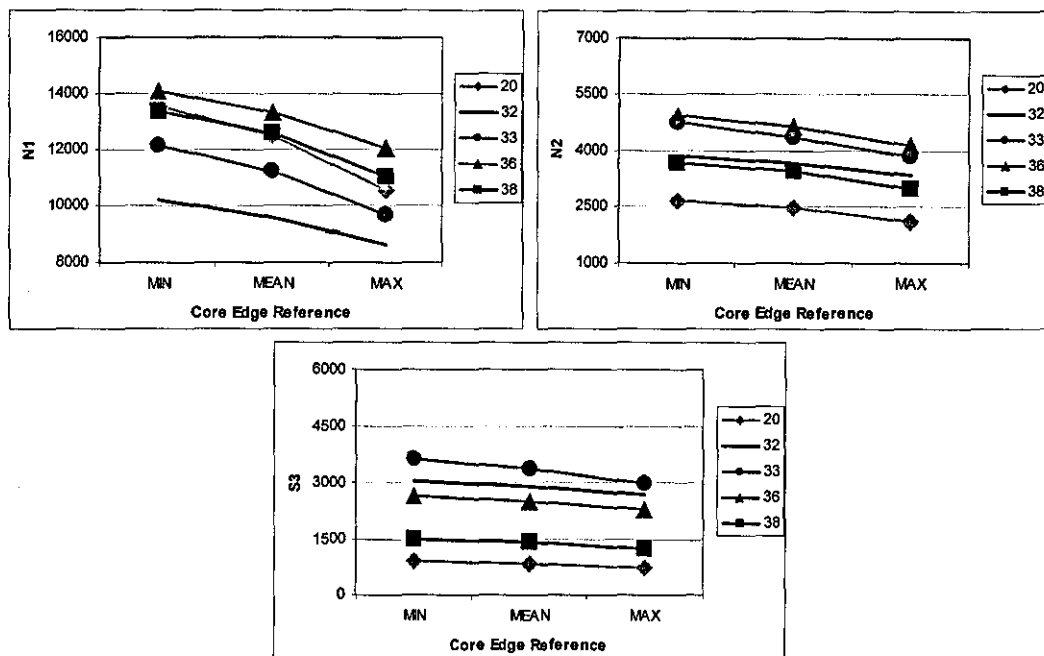


Figure 6-7 Comparison of results using different zero length positions

It can be seen that as the reference position gets closer to the core axis, the number of intersections increase, which is expected considering the fact that the number of hairs decrease exponentially going further from the core. It is interesting to note that the effect of reference point is very significant for N1 hair counts and that the hair counts decrease by around 20% as the reference line is moved from MAX to MIN. This shift of the reference line corresponds to around 100 μm at average for most of the samples. This reveals the level of precision required for locating the core edge.

In order to simulate Zweigle G565 hairiness tester in LYSS, the sensor dimensions are set to 0.5mm x 0.5mm, the signal threshold is set to 99.9% of the maximum intensity and the reference line is selected as the mean distance from the core axis for every image in the simulations. Table 6-2 shows the comparison of the N1, N2 and S3 measurements using these parameters and the Zweigle G565 Hairiness Tester. For the developed system, the numbers of intersections are calculated from the average of intersections found on the right and left sides of the core. It can be seen that the N1 and N2 values from Zweigle and the developed system are often in very good

agreement. However for some samples the latter gave higher hair counts. This may be due to the difference in selection of the 0-reference point in two testers, which is done at a high precision on LYSS and probably not as precise on Zweigle, due to the mechanical adjustment procedure. For S3 measurements on the other hand, the Zweigle exhibits higher values for a number of samples. This can be due to the fact that the S3 values tend to increase according to the test speed as reported by Wang [1996]; the speed used on LYSS is 5m/min while it is 50m/min on Zweigle, higher S3 values might be expected on the latter instrument. Furthermore, Wang & Chang [1999] stated that the differing contact conditions between the yarns and the various yarn guides on different hairiness testers may also affect the hairiness measurements. Nevertheless, the overall correlations between two testers were quite significant with R values of 0.94, 0.92 and 0.88 for N1, N2 and S3 measurements respectively.

Table 6-2 Comparison of hair counts from Zweigle G565 with the simulation results using 0.5x0.5mm sensor resolution

Yarn #	N1		N2		S3	
	G565	Simulation	G565	Simulation	G565	Simulation
20	12028	11155	2469	2293	767	858
21	9120	9199	1616	1608	406	629
22	15824	15763	3506	3074	826	981
23	13552	13233	3290	2668	1176	955
24	9294	9301	1663	1413	377	393
25	10410	11072	2556	2028	830	715
26	11092	9489	2747	1688	907	534
27	13772	11853	3696	2491	1372	892
28	15278	17564	4044	3827	1566	1532
29	12124	12348	2810	2408	862	956
30	8810	7400	1928	1215	595	419
31	6996	5308	2405	1868	1597	2529
32	9196	7218	3648	2628	2472	2653
33	11616	11427	4387	3521	2914	2863
34	7908	5200	1783	1026	720	533
35	14470	14920	4729	4720	2094	3710
36	12834	11712	4649	3840	2241	2860
37	9070	9643	2301	2565	796	1343
38	11390	11618	3423	3117	1302	1058
39	11578	12622	3475	3287	1267	1669
	R=0.939726		R=0.919491		R=0.882095	

Barella & Manich [1993] showed that the hair counts measured on Zweigle G565 exhibit two different trends on a logarithmic scale one between 1 and 3mm and the other above 3mm. For yarn samples with long hairiness tested during this research, this behaviour has also been observed on measurements from this instrument. However, for the same samples, the measurements from LYSS did not exhibit such a discrepancy. This is quite evident from Figure 6-8 where the numbers of hairs are plotted against the distance from the core on a logarithmic scale for four different samples with long hairiness.

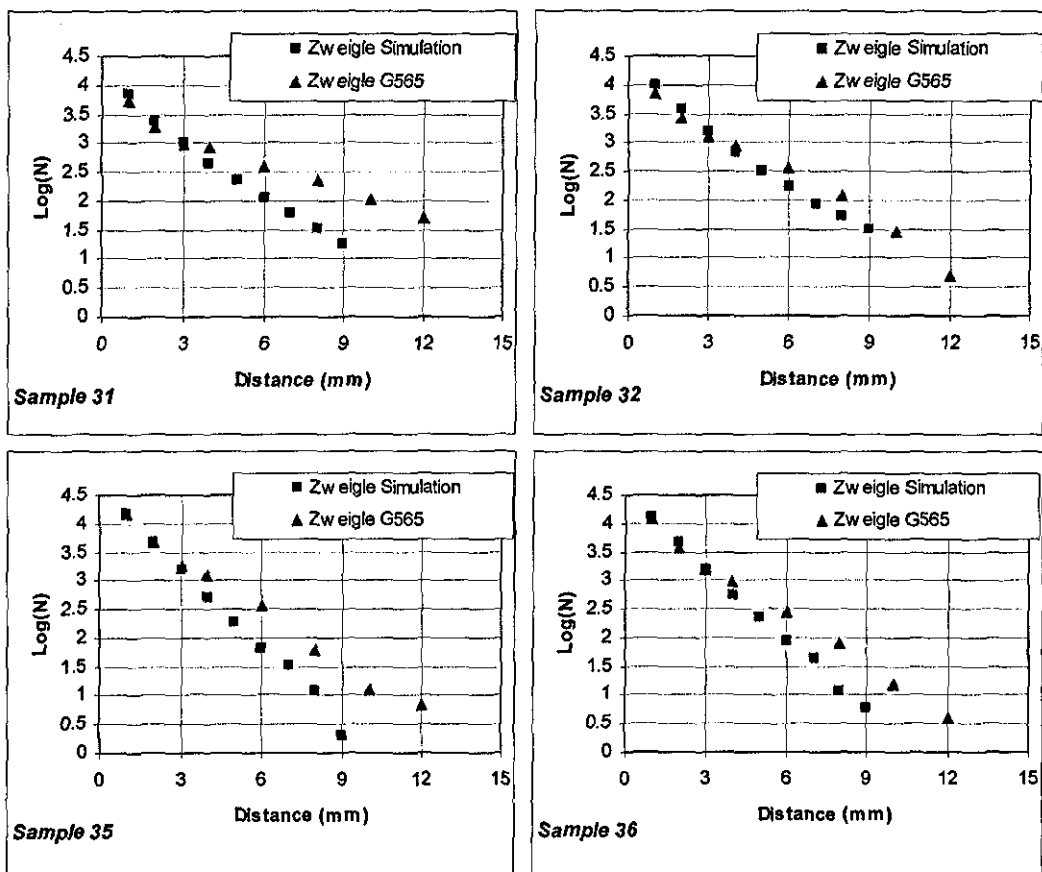


Figure 6-8 Comparison of hair numbers from Zweigle G565 and LYSS simulation for four samples with long hairiness

The slopes of the lines fitted to hair counts less than and equal to 3mm on logarithmic scale found from the simulations exhibited a good linear relation with

those found from the measurements using Zweigle G565 as shown in Figure 6-9. However, the slopes of the trend lines fitted to all hair counts measurements did not agree quite well Zweigle G565 exhibiting around twice the slope as that of the simulations as shown in Figure 6-10. This is due to the discrepancy in trend line below and above 3mm for Zweigle G565 tester.

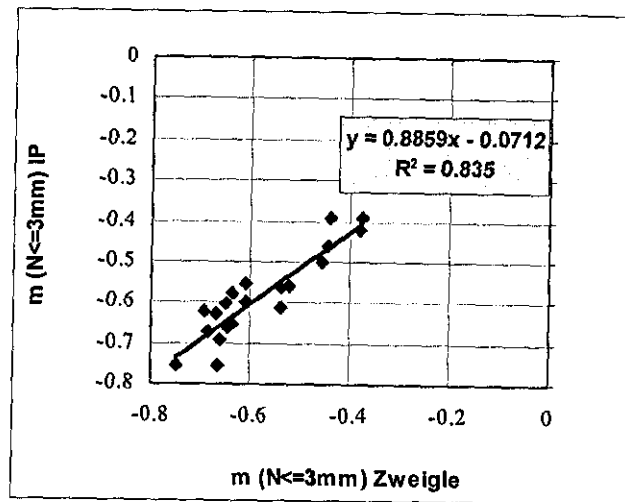


Figure 6-9 Comparison of slopes of hair counts ≤ 3 mm on logarithmic scale

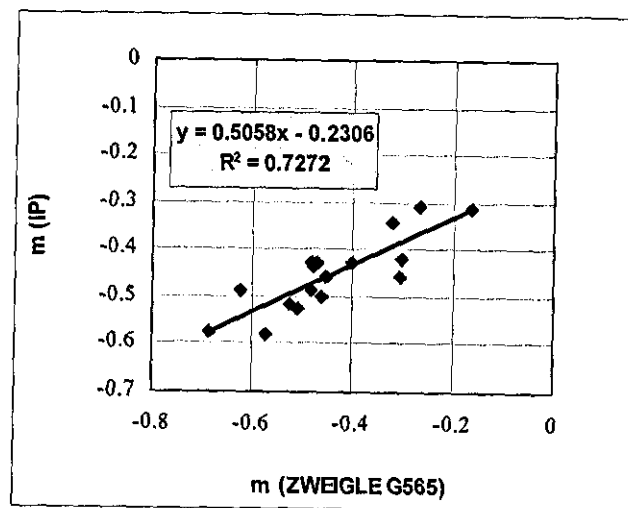


Figure 6-10 Comparison of slopes of hair counts ≥ 1 mm on logarithmic scale

In Figure 6-11, the S3 values from Zweigle G565 are compared with Uster's H index for samples 20, 28, 29 and 31-39. A clear correlation could not be observed between these two common hairiness indices for all types of yarns ($R=0.65$).

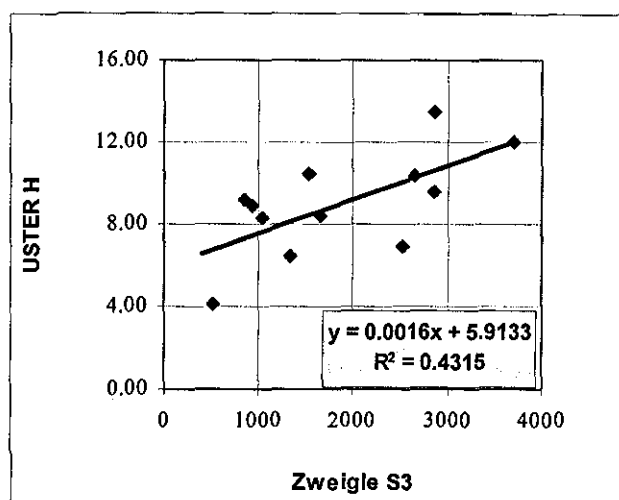


Figure 6-11 Comparison of USTER H with Zweigle S3

6.4 Estimation of Total Hairiness

The hairs observed in an image are the projections of three dimensionally distributed hairs. Three different ways of estimating the projected total hairiness are mentioned in this section and correlated with USTER's Total Hairiness index (H).

6.4.1 THw Index

This index is found from the number of hair pixels, which is quite similar to Barella's V index [Barella and Viaplana, 1970a]. To make the index independent from the horizontal and vertical resolutions, the average number of pixels in one metre length of yarn is multiplied by the area of one pixel in mm^2 .

Figure 6-12 shows the comparison of THw calculated from back-lit images with USTER's H index for yarn samples 1-4, 7, 12, 20, 28, 29, 31-43. A good correlation

has been observed between two indices with a correlation coefficient of 0.93; however there is a small offset where USTER H index has a value where THw is zero. One of the main reasons for this is the difference between the definition of core boundaries in back-lit and dark field images, where there is a more significant contribution of surface fibres to total hairiness in dark-field illuminated images.

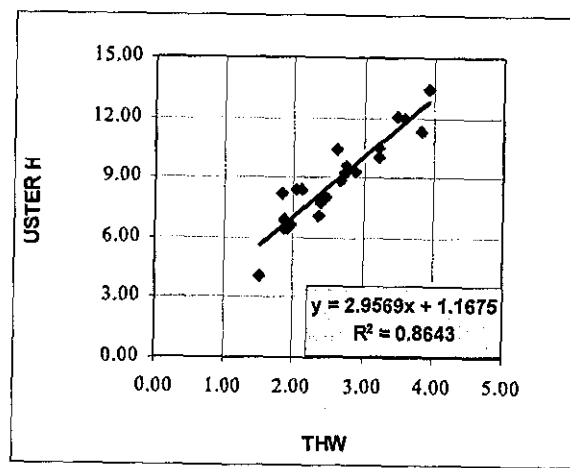


Figure 6-12 Comparison of back-lit THw with USTER H index

The CV% values calculated from THw values for 1cm sampling length exhibited a reasonable agreement with USTER H CV% values as shown in the Figure 6-13. The measurements from two testers are of the same order of value.

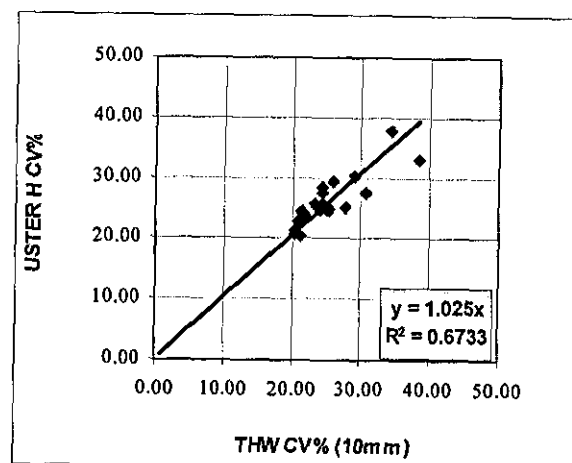


Figure 6-13 Comparison of THw CV% for 1cm sampling length with USTER H CV%

Figure 6-14 shows the comparison of USTER H and THw for grey cotton-cotton/polyester samples only (Samples 31-33, which are dyed wool/acrylic blends and samples 37-39, which are dyed cotton are excluded). It can be seen that there is a better correlation ($R=0.97$) between the two indices for grey yarns. This suggests that different blends and colours have a negative influence on the correlation between two indices. All excluded samples fell above the trend line shown in Figure 6-14, which means that with reference to the relation between USTER H and THw for grey cotton-cotton/polyester yarns, USTER H exhibited higher hairiness for these samples. In Section 5.4.6, it was seen that the number of hair pixels exhibited an almost perfect correlation with skeletal hair lengths for all samples. This means that the THw is not affected by fibre width for the range of samples tested. Furthermore, the colour should not have an effect on THw due to the nature of back-lit illumination. Consequently, it can be argued that the USTER H index is probably affected by colour and/or different spectral characteristics of, for example, wool/acrylic blends.

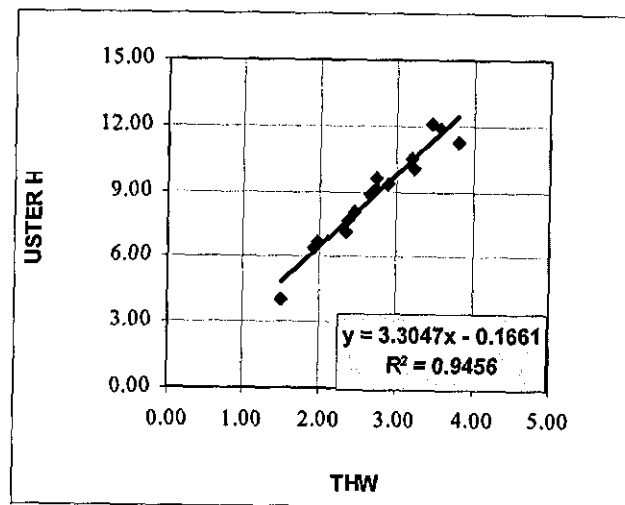


Figure 6-14 Comparison of THw with USTER H for grey yarn samples

The THw indices are also calculated for dark-field yarn images and the results are compared with USTER H for samples 28, 32, 33, 36-43 as shown in Figure 6-15. This set of samples include all the dyed yarn samples except for 31, which has a

black colour and appeared very dark in the images that the hair pixels were often below the fixed threshold value. It is interesting to note that for this set of samples, back-lit THw exhibited a weaker linear relation with USTER H exhibiting an R^2 value of 0.85 and an offset of 2.6. This suggests that THw found from dark field images exhibit better agreement with USTER H index with a smaller offset.

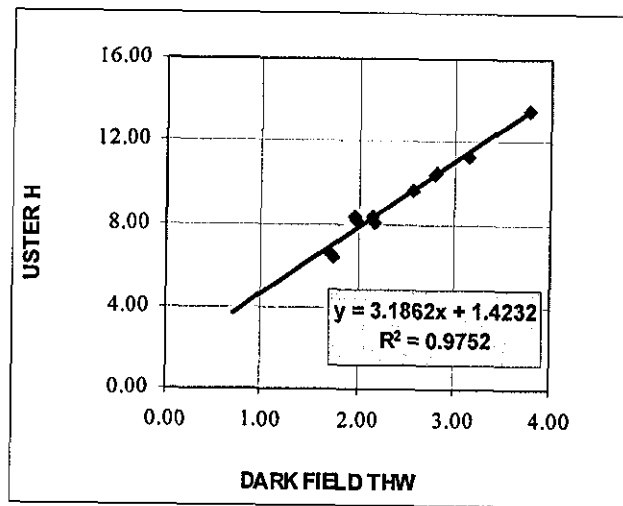


Figure 6-15 Comparison of dark-field THw with USTER H

Figure 6-16 shows the comparison of CV% values for dark-field THw and USTER H. A reasonable correlation is observed, however USTER H CV% values appear higher than dark field THw CV% values. Furthermore, for the same set of samples the back-lit THw CV% has given an R^2 value of 0.74 and the slope of the trend line was 1.07 when compared with USTER H CV% values. The reason why dark field THw is exhibiting smaller CV% values can be that due to the definition of core boundaries at the image processing stage the contributions from the surface fibres to the total hairiness exhibits a small variation, decreasing the variation of total hairiness.

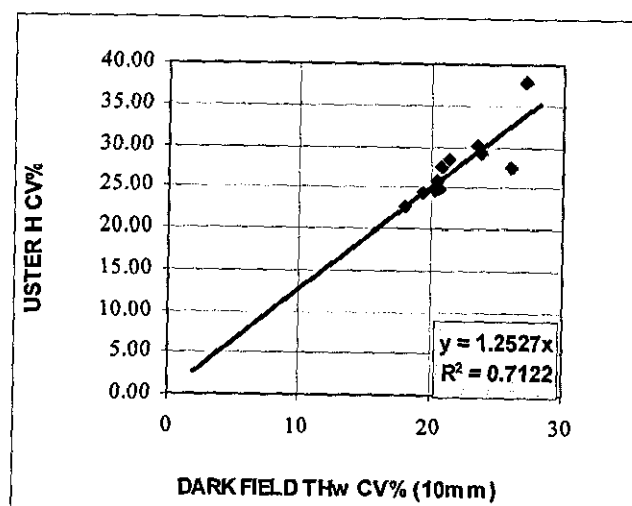


Figure 6-16 Comparison of Dark-Field THw CV% with USTER H CV%

6.4.2 TH_L Index

This index is calculated from the length of hairs found using Bit Quads technique on skeletonised images. It is given in cm of total hair length in 1 cm yarn section. The length in cm is calculated by multiplying the length in pixel units by the width of one pixel in cm. An important point to note about this method is that if the width and height of one pixel are not equal, the horizontal and vertical neighbours should be weighed accordingly when calculating the length using Bit Quads method.

Figure 6-17 shows the comparison of TH_L with USTER H index. The linear relation between two indices is again quite reasonable with a very small offset. The comparison of back-lit THw and USTER H for the same set of images also exhibited an R² value of around 0.89 but with a higher offset of 1.4.

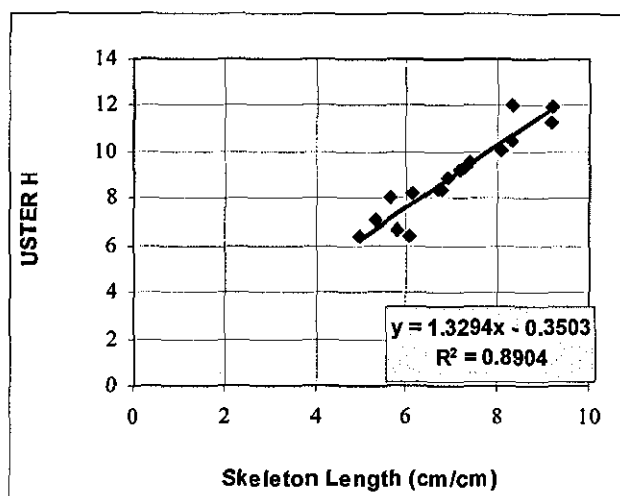


Figure 6-17 Comparison of hair skeleton lengths with USTER H

6.4.3 THg Index

This index is calculated by integrating the inversed intensities of hair pixels in backlit yarn images. This index is quite similar to Millman's *M* index where the hair intensities are subtracted from the average intensity and then integrated. However, when calculating THg index, the intensities are subtracted from a constant value. The main reason for this is that following a set of experiments, the intensities of hair pixels at different defocus distances are found not to be seriously affected by the background intensity; hence subtracting them from the average background intensity would be erroneous. The main purpose of THg is to give an index that is better correlated with the projection lengths, considering the fact that when fibres are defocused and through the digitization process, the number of pixels can significantly increase while the inversed intensities are less affected as theoretically shown in section 3.5.

Figure 6-18 shows the comparison of THg with USTER H for the set of samples as in Figure 6-12. The correlation of THg with USTER H appears to be slightly stronger than that of THw ($R=0.95$). For grey samples, the correlation increases as shown in Figure 6-19 ($R=0.97$). When compared with Figure 6-12, the linear relation of THw

and THg with USTER H for grey yarn samples appear to be almost the same both with very little offset.

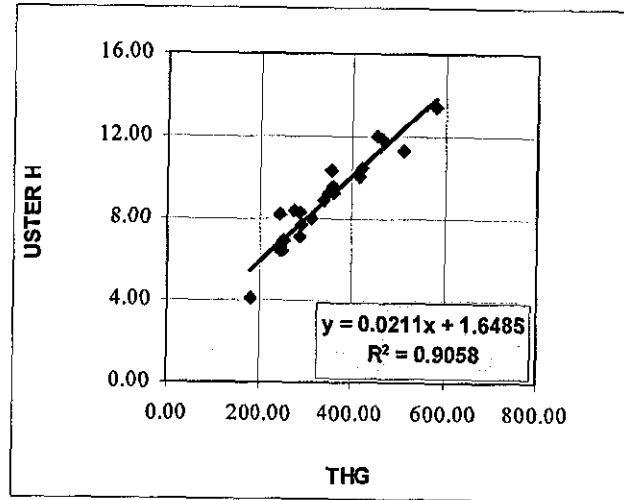


Figure 6-18 Comparison of THg with USTER H

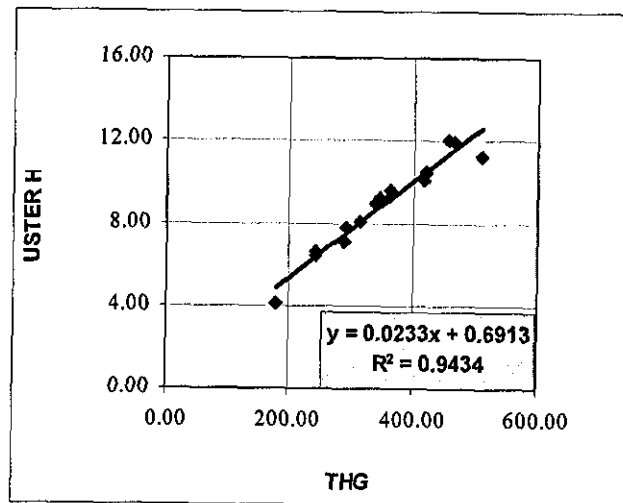


Figure 6-19 Comparison of THg with USTER H for grey yarn samples

The CV% values calculated from THg measurements for 1cm sampling length also exhibited slightly better correlation than THw CV% with USTER H CV% as shown in the Figure 6-20 ($R=0.85$).

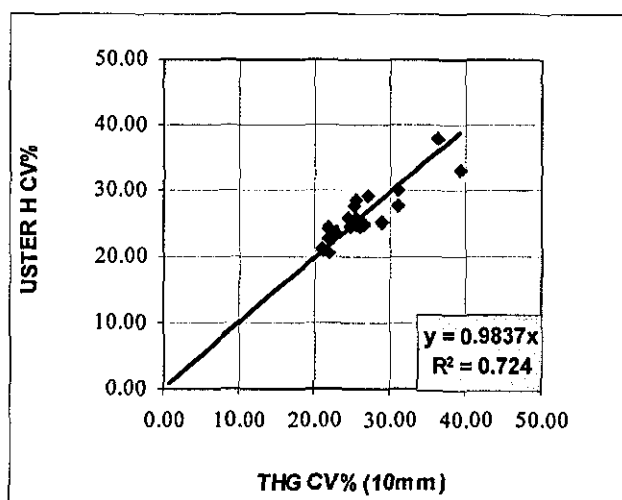


Figure 6-20 Comparison of THG CV% for 1cm sampling length with USTER H CV%

6.5 Hair Density Distribution Profiles

It has been shown in section 6.1 that the hair counts found using conventional photo electric sensors are not quite accurate due to the limitations in resolution of these sensors. On the other hand a single total hairiness index does not provide the information of how the hairs are distributed around the core. For these reasons a new method called hair density distribution profiles (HDDP) is introduced during this research to describe the distribution of hairs around the core. The method is based on calculating the probability that a point is covered by a hair for varying distances from the core. This is found by finding the number of hair pixels at each distance from the core and then dividing it by the total number of pixels processed for that distance. Figure 6-21 shows a typical HDDP that belongs to sample 33.

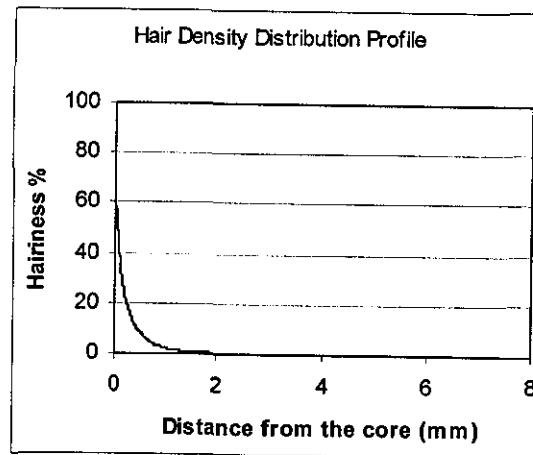


Figure 6-21 Hair density distribution profile of sample 33

It is found that HDDP exhibits two different exponential behaviours, one for distances less than 0.75mm and the other above that as shown in Figure 6-22. Furthermore, it has been observed that the exponential nature of the distribution above 0.75mm was quite similar to the Zweigle's exponential distribution of hair counts as shown in the same figure. It was later found that the exponential nature of HDDP between 0.75 and 3.25mm correlated very well with the hair counts distribution for distances less than and equal to 3mm ($R=0.98$). Figure 6-23 shows the slope values found from the lines best fit to the logarithmic HDDP with the slopes corresponding to the logarithm of hair counts for these distance ranges. However, the linear relation was rather weak for the slopes of HDDPs for the range between 0 and 0.75mm (with an R^2 value of 0.50). This suggests that the short hair hairiness (<1mm) is not correlated well with long hair hairiness (>1mm).

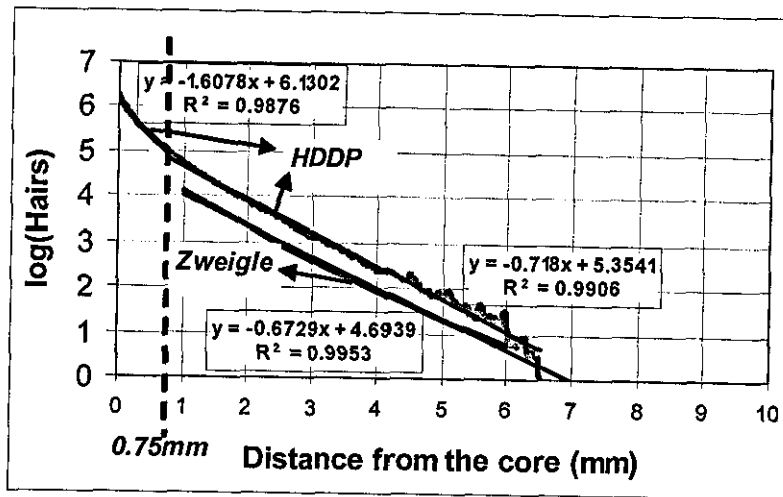


Figure 6-22 HDDP compared with Zweigle hair counts on a logarithmic scale

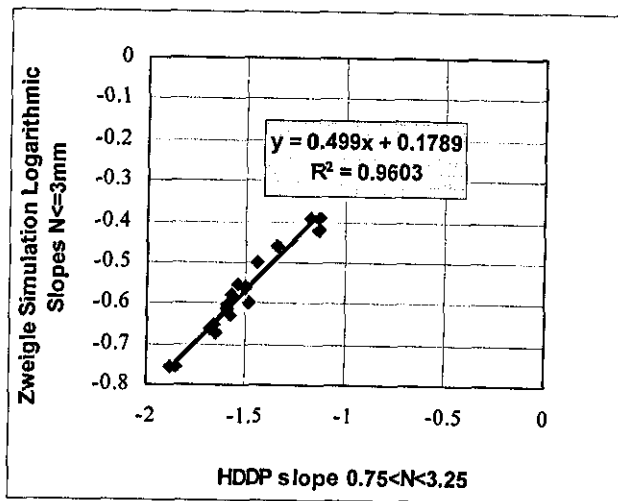


Figure 6-23 Comparison of logarithmic slopes of HDDP for distances between 0.75m and 3.25mm with the logarithmic slope of hair counts for distances <=3mm

The main advantage of HDDP is that it provides information on both short and long hair hairiness characteristics of yarns. The THw total hairiness index described in 6.4.1 can also be obtained from the area under the HDDP. In Chapter 8, a method is described to utilize HDDP in yarn and fabric simulations to add the effect of hairiness.

6.6 Effect of Scanning Aspect Ratio on Hairiness Measurements

The measurements mentioned so far are all obtained from images scanned at 1:1 vertical aspect ratio. By applying the method in section 5.5 it has been possible to examine the effects of using lower aspect ratios on measurements and to investigate the smallest aspect ratios that can confidently be used for various measurements. The aspect ratios compared with 1:1 aspect ratio are 1:4.9 and 1:11.3 as described in Section 5.5.

Figure 6-24 show the comparison of aspect ratios for THw and THg measurements. It can be seen that AR1:4.9 exhibits an almost perfect agreement with AR1:1, while at AR1:11.3 the correlation is not as good. It is interesting to note that the THw values obtained at AR1:4.9 were higher than those obtained at 1:1, the reason for this is probably the hairs lying perpendicular to the core axis which have a diameter of 2-3 pixels at AR1:1, while having a diameter of 1 pixel at AR1:4.9 despite the 4.9 times reduction in the scale. This effect is less significant for THg values, as to be expected, since the grey level of such hairs are averaged when converting the image to smaller aspect ratios, which makes the same contribution to THg as of AR1:1.

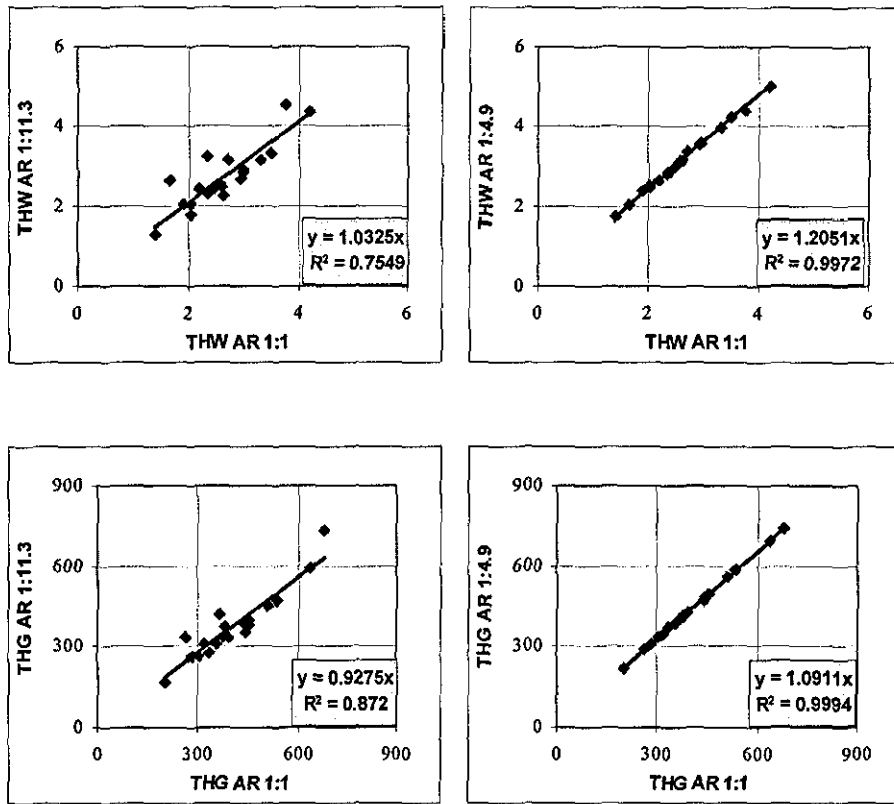


Figure 6-24 Comparison of THw and THg measurements for smaller aspect ratios

It is found that the hairiness variation could also be confidently calculated for aspect ratios down to 1:4.9 as shown in Figure 6-25.

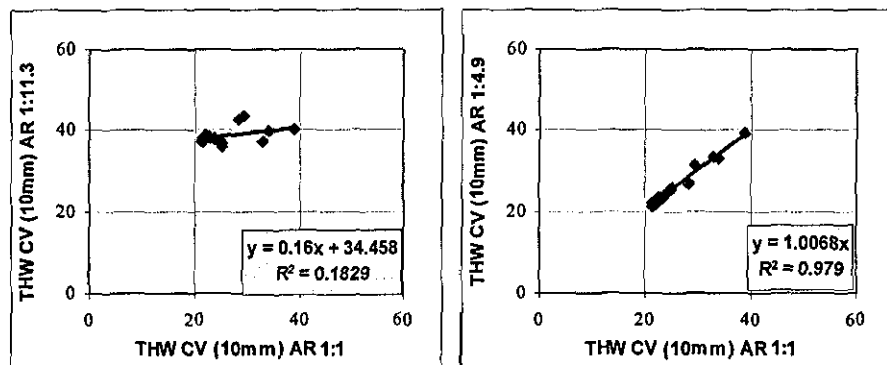


Figure 6-25 Comparison of THw CV% measurements for smaller aspect ratios

There was again almost a perfect agreement between AR1:1 and AR1:4.9 for N1, N2 and S3 values as shown in Figure 6-26. However, the measurements significantly dropped for AR1:11.3.

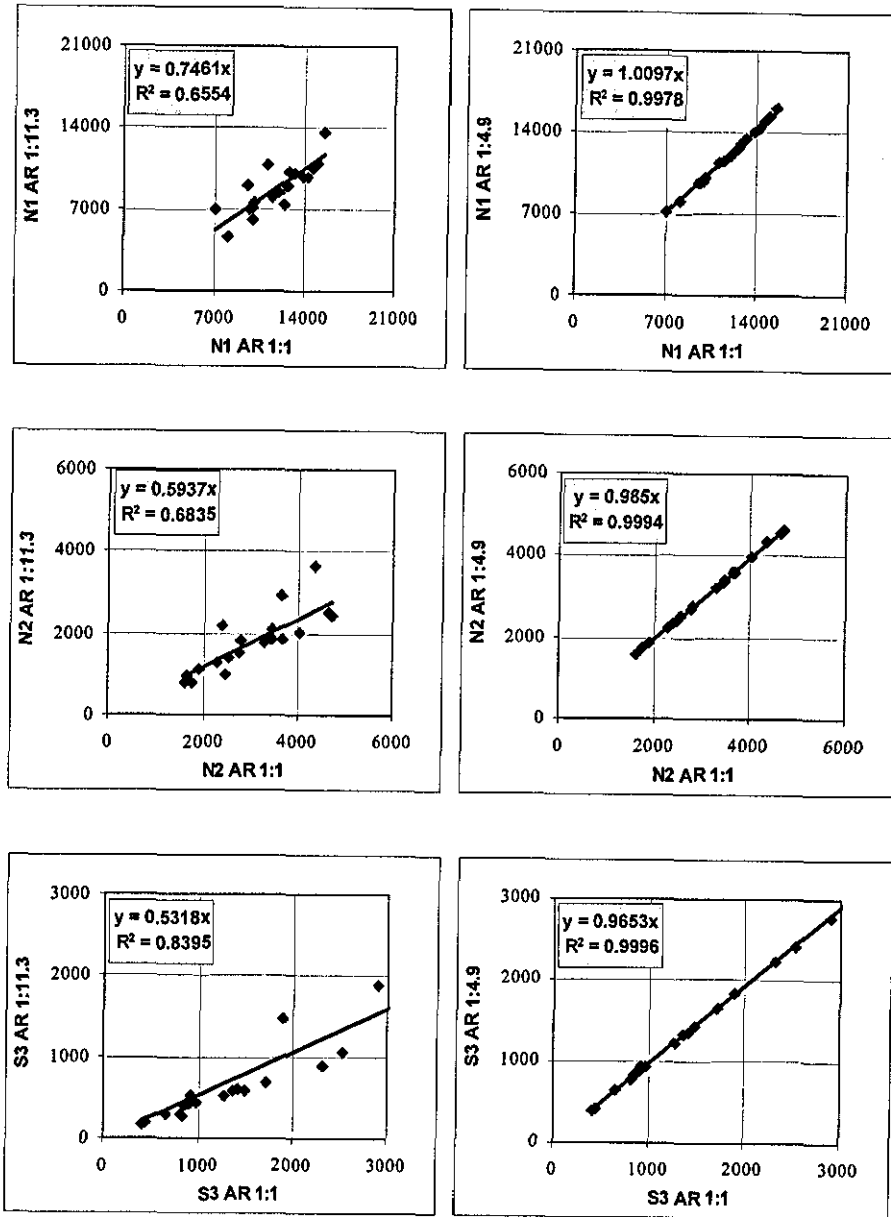


Figure 6-26 Comparison of N1, N2 and S3 values for lower aspect ratios

6.7 Conclusions

An image analysis technique is demonstrated to simulate photo electric sensors used for counting the number of hairs at fixed distances from the core. Effects of parameters such as the dimensions of the sensor, signal threshold level and the zero reference point on the measurements are investigated. It is found that a sensor resolution of 0.5mm x 0.5mm would not be adequate to distinguish between N1 hair count values of different yarns. The need for a very high precision in determining the zero reference point is also addressed. It is observed that with appropriate sensor parameters, the computer vision technique can be very successful in simulating the N1, N2 and N3 measurements from Zweigle G565 Hairiness Tester.

Various indices are given to describe total hairiness. The developed total hairiness indices almost perfectly agreed with Uster Tester's H index for grey cotton-cotton/polyester samples, however, colour or different blends appeared to decrease this correlation. This is believed to be due to the fact that colour and material can affect the measurements on Uster Tester while such yarn characteristics have no effect on back-lit images. The total hairiness indices obtained from dark field images exhibited a better correlation with a very small offset when compared to the Uster Tester's H index than similar indices obtained from back-lit images. The hairiness index found by integrating the grey levels agreed with Uster H Index slightly better than the one found from the number of hair pixels. The CV% values calculated for 1cm sampling length also agreed very well with UT3 CVh% exhibiting measurements with the same order of value. However, the CV% values obtained from dark field images exhibited lower values.

A new method to describe the hairiness named Hair Density Distribution Profile (HDDP) is introduced. It is found that the long hairiness content within the profile agreed very well with the hair counts measurement in terms of the nature of the distribution according to the distance from the core. Short hair hairiness is found not to be correlated with long hair hairiness, which suggested that long hair hairiness, as

measured on Zweigle G565 for example, cannot describe the overall hairiness of a yarn accurately. A major advantage of HDDP is that both short and long hair hairiness can separately be obtained.

Two different low aspect ratio classes are tested against AR 1:1. Aspect ratios lower than 1:4.9 are not found suitable for hairiness measurement, in other terms, the scanning resolution for hairiness evaluation should not be less than 14 scans per mm.

CHAPTER 7 - Yarn Irregularity

7.1 Introduction

This Chapter covers practical results on diameter and diametric irregularity measurements. In Section 7.2, the diameter and irregularity measurements obtained from back-lit, dark field and two orthogonal images are compared with those obtained from commercial testers such as CYROS and UT3.

In Section 7.3, the effects of using lower scanning aspect ratios are investigated. Section 7.4 describes numerous methods implemented in LYSS to evaluate the irregularity. These methods are applied to several yarn samples and results are discussed. A new method to assess irregularity called "variation plots" is also introduced.

7.2 Diameter and Irregularity Measurements

A series of tests were carried out on 20 samples (1,2-4,7,12,28,29,31,32,35-43) using CYROS tester and LYSS. The diameter measurement configurations tested on LYSS include back-lit and dark field illuminations and imaging of two orthogonal views described in Chapter 4.

Figure 7-1 and Figure 7-2 show the diameter and CV% values respectively from CYROS and LYSS back-lit illumination. The CV% values are calculated for 1mm sampling length on LYSS as in CYROS. Almost a perfect agreement with a correlation coefficient of 0.99 is found between diameter measurements from two testers. The variation values from two testers were also of the same order of value exhibiting a significant correlation with an R value of 0.92.

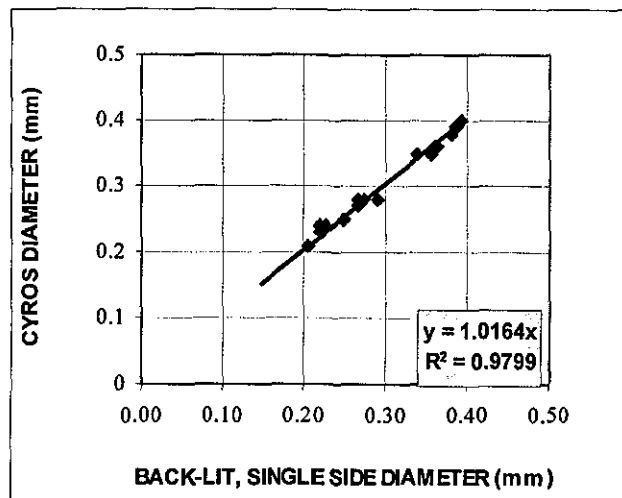


Figure 7-1 Comparison of diameter measurements from CYROS and LYSS

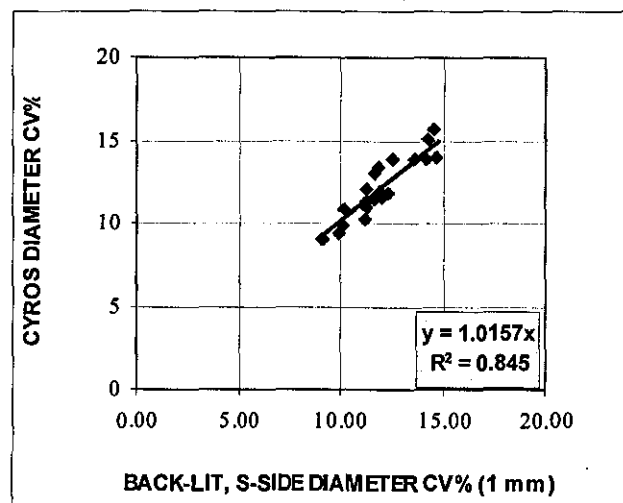


Figure 7-2 Comparison of diameter CV% values from CYROS and LYSS

The filtering process described in Section 5.4.2.2 applied to the core data probably favours the correlation between LYSS and CYROS. Millman's [1999] diameter measurements where he defined the core diameter as the longest interval of connected core pixels, exhibited around 20% higher values when compared to Zweigle G580. The CV% values on the other hand did not correlate well with Zweigle G580.

Following a conversation with Dr. Jasper about their CCD scanning system attached to a Lawson Hemphill CTT to measure the diameter and diameter variation of yarns (Suh et.al. [2000]) it was understood that the CV% values they obtained were significantly higher than CYROS tester. To verify this 4 yarn samples (31, 32, 35 and 36) are tested on their system and compared with the measurements from CYROS and LYSS back-lit method. The results are shown in Figure 7-3. It can be seen that the diameter measurements from Jasper's system are slightly lower than both CYROS and LYSS, while LYSS appears to exhibit a better agreement with CYROS. The reason for that Jasper's system is exhibiting lower diameter measurements is probably due to the image capturing system or the processing algorithm that they implemented. The CV% values obtained from Jasper's system on the other hand are significantly higher than the other two testers, which again agree reasonably well with each other. The main reason for higher CV% values obtained on Jasper's system is probably due to very low scanning aspect ratio used (1 scan/mm) since these scans might take place at regions with protruding fibres. It can be argued that the image processing algorithms implemented in LYSS are more accurate in terms of simulating commercial optical sensors such as the one in CYROS. This is due to the fact that surface hairs especially those lying perpendicular to the core axis do not affect the measurements on LYSS owing to the filtering process described in Chapter 4.

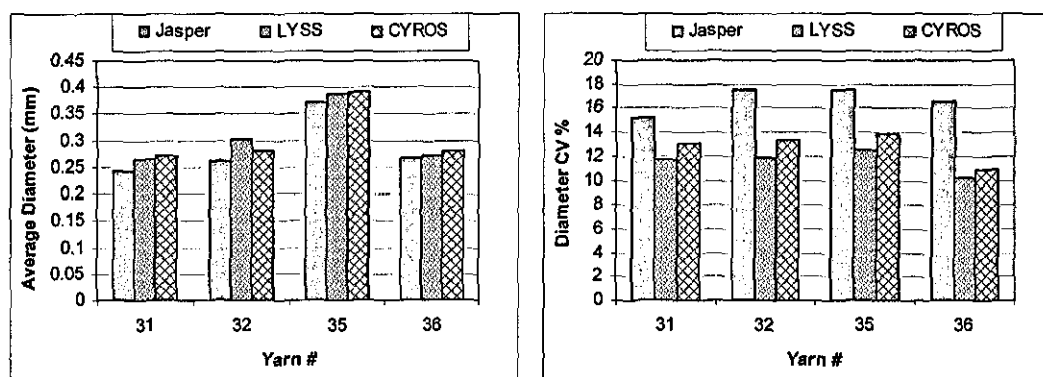


Figure 7-3 Comparison of diameter and diameter CV% values from Lawson Hemphill CTT, LYSS and CYROS

Figure 7-4 correlates the squares of diameters with direct yarn counts for fourteen 100% cotton samples (2, 3, 28, 29, 34-43). The yarn counts are measured on a UT3. A very strong correlation has been observed between two quantities ($R=0.99$); however this relation can only stand if the densities of the samples are of the same value. For this reason only 100% cotton samples are considered here, however, it has to be noted that the same fibre material does not guarantee the same density since it is strongly affected by yarn twist.

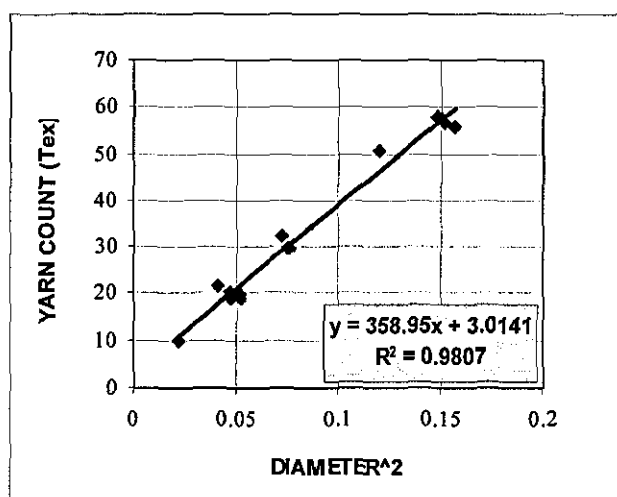


Figure 7-4 Comparison of yarn counts (Tex) with squares of diameters for 100% cotton samples

Figure 7-5 and Figure 7-6 show the comparison of diameter and diameter variation values obtained using dark field illumination with the measurements from CYROS. Although there is a very good correlation for diameter measurements ($R=0.99$) there is an offset favouring the CYROS diameter values. The reason for this is the difference in definition of the core boundaries in back lit and dark field illuminations, where the surface fibres covering the core account for the core in back-lit illumination while being identified as hairs in dark field illumination. This point was also discussed in Section 6.4 referring to the total hairiness measurements where a smaller offset was found for dark field illumination compared to back lit illumination when comparing the total hairiness index of LYSS with USTER's H index.

The diameter CV% values obtained from dark field images also exhibited a reasonable correlation with CYROS diameter CV% values ($R=0.80$). However, CYROS gave significantly higher values for all of the samples. This again is probably due to definition of core boundaries in dark-field images, where there is a constant contribution to diameter from surface fibres which is likely to decrease overall variation.

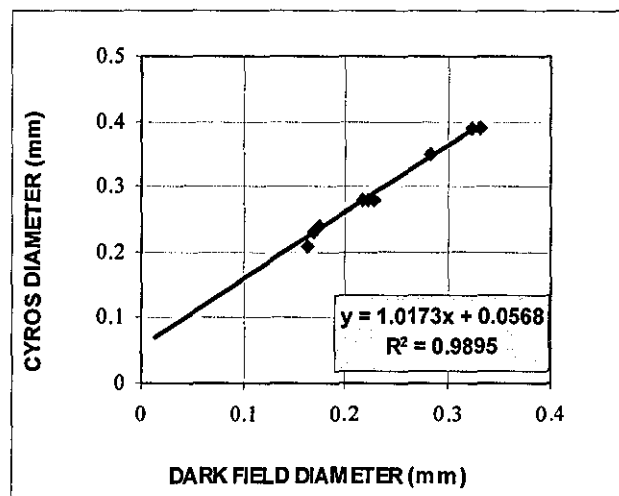


Figure 7-5 Comparison of diameter measurements from CYROS and dark field images

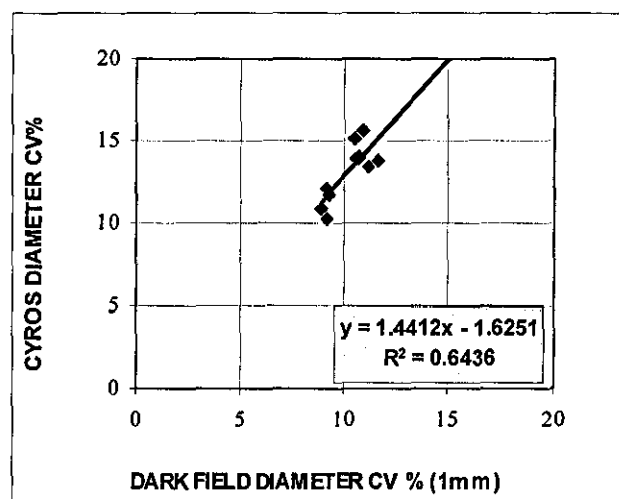


Figure 7-6 Comparison of diameter CV% values from CYROS and dark field images

Figure 7-7 compares the mass variation values from UT3 with diameter variations from LYSS both having a 8mm sampling length for twelve 100% cotton samples (2, 3, 28, 35-43). There appears to be a reasonable correlation between two sets of data ($R=0.88$), mass variations being around 1.4 times larger. However a comparison between mass and diameter variations is a difficult one since they represent different quantities as indicated by Wegener & Hedwig (1969).

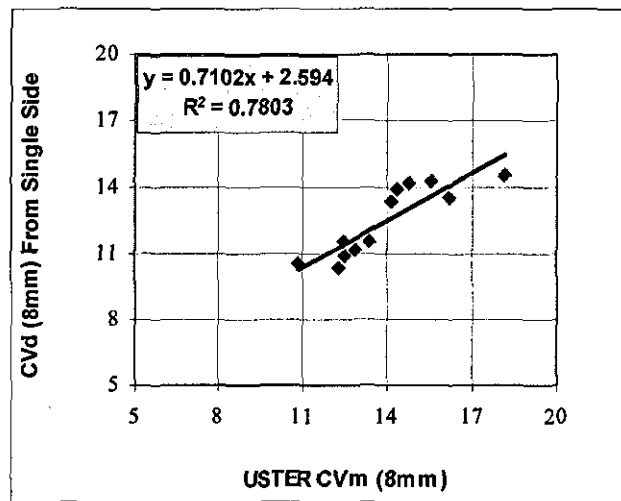


Figure 7-7 Comparison of UT3 mass CV% with diameter CV% from LYSS for 8mm sampling length for 12 100% cotton samples

It has been found that the elliptical diameter variation values obtained from two orthogonal views of the yarn exhibited a stronger correlation with the mass variation when compared to the diameter variation obtained from a single view. Figure 7-8 shows the comparison between the elliptical diameter CV% and UT3 mass CV% for the same 12 cotton samples of Figure 7-7, where a significant improvement in the correlation can be seen with a correlation coefficient of 0.94 and almost no offset in the linear regression.

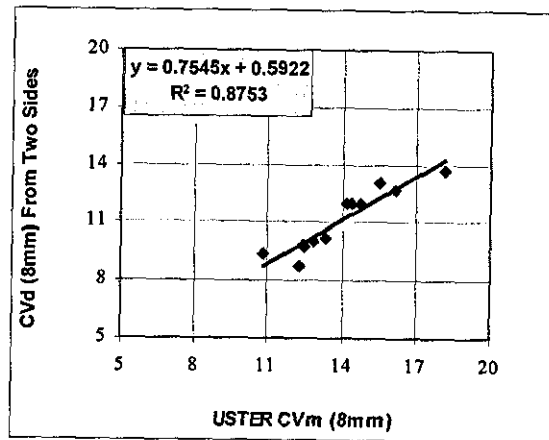


Figure 7-8 Comparison of UT3 mass CV% with elliptical diameter CV% from LYSS for 8mm sampling length for 12 100% cotton samples

Since the surface fibres that have very little contribution to the mass but important contribution to diameter in back-lit illumination, are highlighted in dark-field illumination, a better correlation was expected between dark field diameter variations and UT mass variations. However, the CV% values obtained from dark field images of ten 100% cotton samples (28, 35-43) exhibited zero correlation with UT3 mass variation values as shown in Figure 7-9. Nevertheless, it can be seen in this Figure that the XY plots of the measurements appear to cluster in a narrow region which suggests a certain level of consistency.

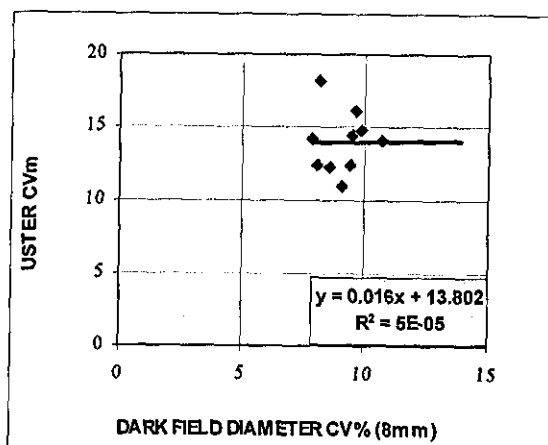


Figure 7-9 Comparison of UT3 mass CV% with dark field diameter CV% from LYSS for 8mm sampling length for 12 100% cotton samples

Suh et.al (1999) derived a statistical relation between mass and diameter variations assuming that the diameter is circular and the density is constant throughout the yarn. They found that theoretically, the mass variation measured for 8mm sampling length (as in UT) should be twice as the diameter variation measured for 2mm sampling length (as in Zweigle G580). However, it was found that the UT3 mass variation was only 1.13 times of the diameter variation measured on LYSS for 2mm sampling length as shown in Figure 7-10. However, these results are in very good agreement with the practical results of Tsai and Chu [1996b].

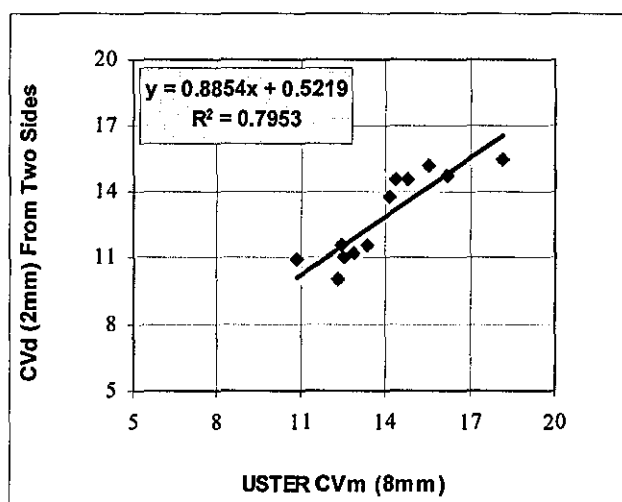


Figure 7-10 Comparison of UT3 mass CV% with elliptical diameter CV% from LYSS for 2mm sampling length for twelve 100% cotton samples

The comparison of the CYROS diameter variations and Uster mass variations for 12 cotton samples is shown in Figure 7-11. It can be seen that there is a very reasonable correlation between two testers ($R=0.90$); however the mass CV% values are only 1.08 times of the diameter CV% values at average.

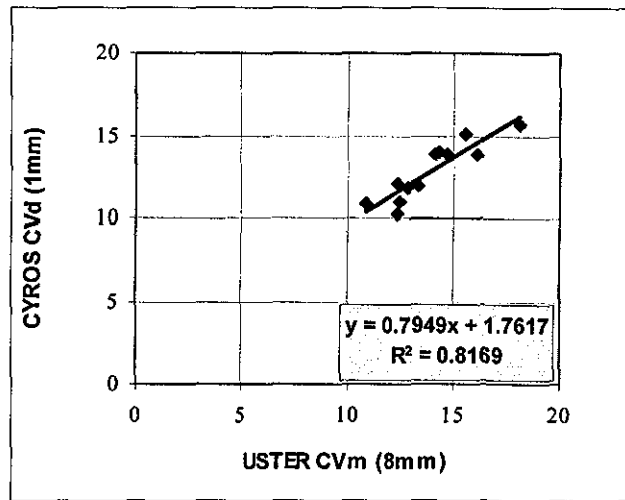


Figure 7-11 Comparison of UT3 mass CV% with CYROS diameter CV% for twelve 100% cotton samples

The average diameters calculated from one and two orthogonal views exhibited almost the same values as shown in Figure 7-12. The CV% values on the other hand, were higher for single views as shown in Figure 7-13.

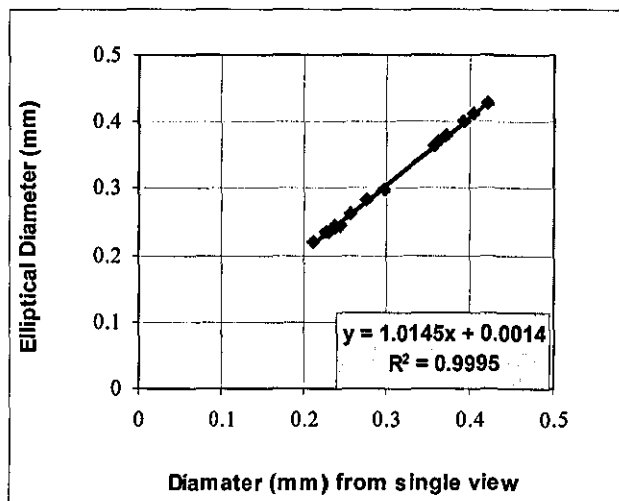


Figure 7-12 Comparison of diameters from single view with elliptical diameter

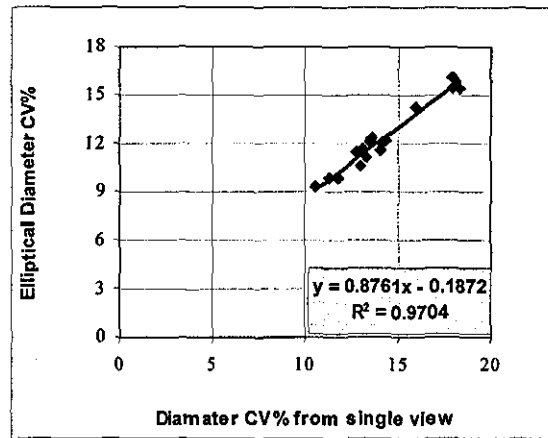


Figure 7-13 Comparison of diameter CV% from one and two views (1mm sampling length)

7.3 Effects of using lower aspect ratios on diameter and irregularity measurements

The diameter and irregularity measurements are obtained for samples 20-39 using three different aspect ratios. Figure 7-14 shows the diameter measurements at 1:4.9 and 1:11.3 aspect ratios compared with the measurements at aspect ratio 1:1. It can be seen that for AR1:4.9 there is no change in diameter and even for AR1:11.3 there is only a 2.26% reduction with perfect correlation with the original data.

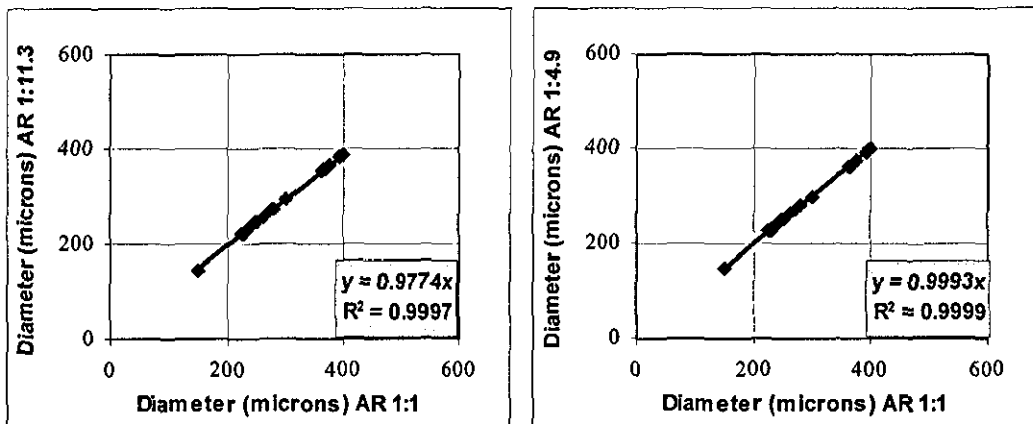


Figure 7-14 Diameter measurements at lower aspect ratios compared with the measurements at AR1:1

Similar results were found for the diameter CV% values as shown in Figure 7-15. The CV% values only negligibly changed even at 1:11.3 aspect ratio. These results suggest that the diameter and irregularity measurements do not necessarily need high resolutions and can be performed at very high speeds even using CCD sensors with low data rates.

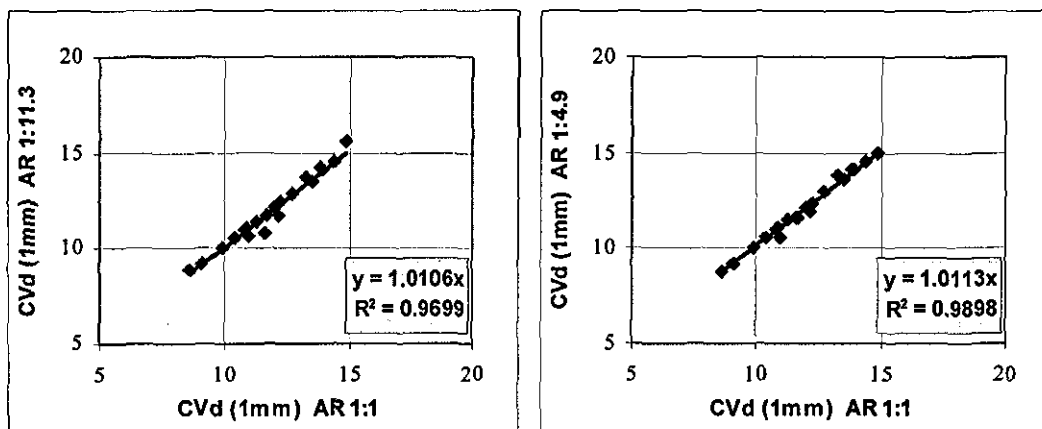


Figure 7-15 Diameter CV% measurements at lower aspect ratios compared with the measurements at AR1:1

7.4 Methods implemented in LYSS to evaluate yarn irregularity

Common methods to evaluate the yarn irregularity were described in Chapter 2. These included coefficient of variation (CV), correlogram, and variance-length curves. All these methods are implemented in LYSS in addition to a new visual method to assess the irregularity named “variation plots”, unique to this work.

7.4.1 Calculation of CV% and Variance-Length Curves

Coefficient of Variation (CV%) is a common measure of irregularity used in textiles. It is given as the ratio between the Standard Deviation (SD) and the average value of the data set. The standard deviation is calculated using the following formula;

$$SD = \sqrt{\frac{n\sum x^2 - (\sum x)^2}{n(n-1)}} \quad (7.1)$$

This formula enables the calculation of a running CV% that does not require the whole data. The CV%-length curves for diameter and total hairiness are calculated and displayed in real time during every test on LYSS. These curves are calculated using the CV% values corresponding to 20 different sampling lengths which are 1, 2, 4, 6, 8, 10, 20, 30, 40, 50, 60, 80, 100, 200, 300, 400, 600, 800, 1000 and 2500mm. These sampling lengths are selected considering the commercial testers and through a set of experiments to enable reading of distinctive characteristics of CV-length curves such as the asymptotic value $B(\infty)$, rapidity of approach to $B(\infty)$ and gradient at the origin as mentioned by Townsend and Cox [1951], where they used 0.5, 1, 5, 10, 50, 150 and 300 cm sampling lengths to draw the variance-length curves.

In LYSS, sampling lengths 1 and 2mm aim to simulate the diameter CV% readings from CYROS and Zweigle G565 respectively. Another common sampling length is 8mm, which is used for measuring the mass variation on Uster Tester. In order to simulate the hairiness variation values of Uster Tester Hairiness Attachment a sampling length of 10mm is used. Longer sampling lengths are determined experimentally to plot the CV%-Length curves in a suitable way. Figure 7-16 shows the CV%-Length curves for 18 different samples. It can be seen that for all samples the curves approach to a limit after 1000mm hence 2500 sampling length is found suitable to describe the asymptotic value $B(\infty)$. Furthermore, the data points to draw the curves appear to be sufficient as the experimental curves are quite similar to the theoretical curves mentioned by Townsend and Cox [1951].

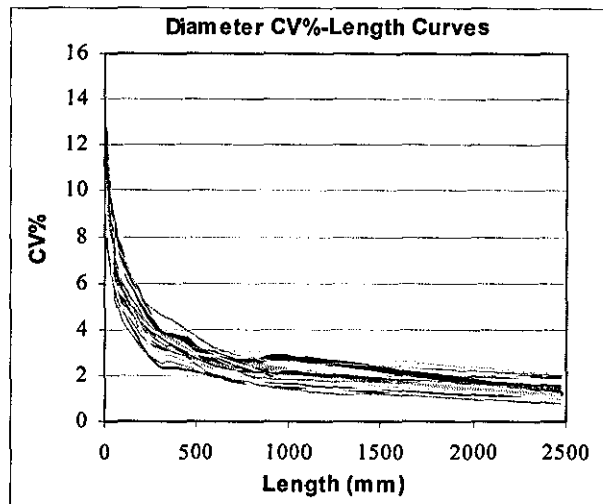


Figure 7-16 CV%-Length curves for 18 yarn samples

Townsend and Cox [1951] described a number of ways to analyse the variance-length curves in order to compare different yarn samples. A couple of comparisons are made here between different samples based on their discussion. Figure 7-17 shows the CV%-Length curves corresponding to the diameter data for samples 4 and 32, which approach to a similar $B(\infty)$ value with different rapidity. According to Townsend and Cox, this suggests that sample 32 has a “long term” variation not present in sample 4.

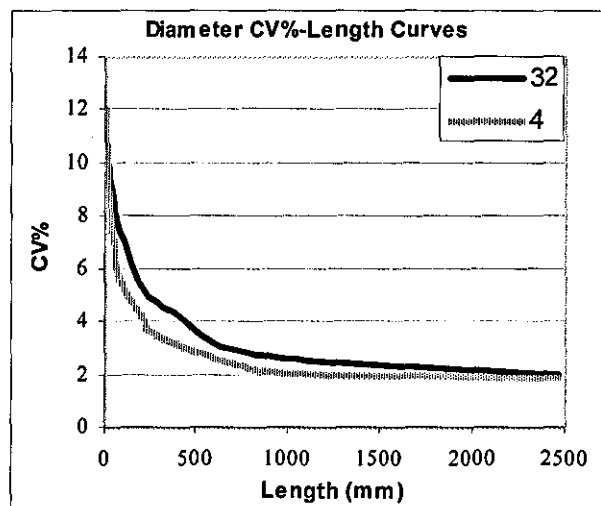


Figure 7-17 Diameter CV%-Length curves for samples 4 and 32

Figure 7-18 shows the CV%-Length curves for samples 29 and 37, which have the same rapidity of approach to a common $B(\infty)$ value. However, the gradients close to the origin between 1 and 50mm are different. According to Townsend and Cox, such yarns do not have identical properties although it is difficult to say which one would be better.

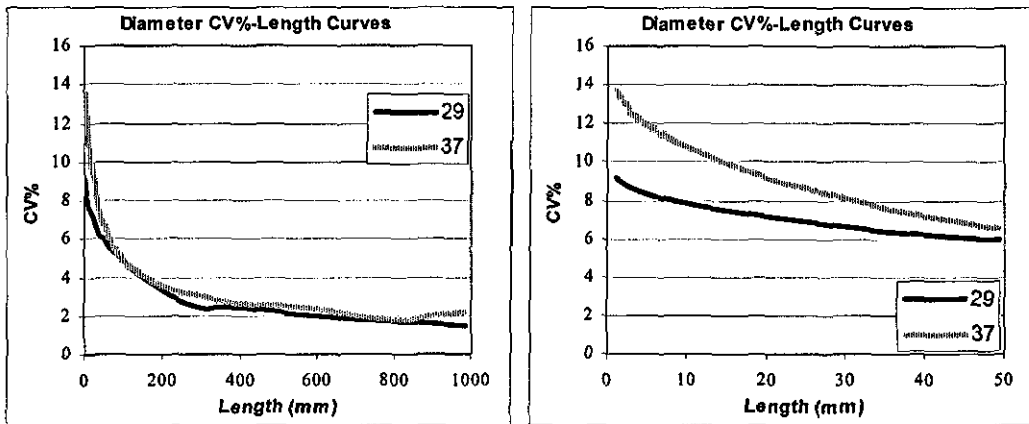


Figure 7-18 Diameter CV%-Length curves for samples 29 and 37

7.4.2 Calculation of Autocorrelation Function (Correlogram)

Autocorrelation refers to the correlation of a time series with its own past and future values. Following equation gives the correlation between observations separated by k units:

$$r_k = \frac{\sum_{i=1}^{N-k} (x_i - \bar{x})(x_{i+k} - \bar{x})}{\sum_{i=1}^{N-k} (x_i - \bar{x})^2} \quad (7.2)$$

Where \bar{x} is the mean value of the data set and N is the number of data. r_k is called the autocorrelation coefficient at lag k . The plot of the autocorrelation function as a function of lag is called the correlogram. A number of publications occurred in the literature addressing the use of correlograms for measuring the yarn irregularity,

which are discussed in section 2.5. Figure 7-19 shows the correlograms calculated from the diameter data of yarn samples 24, 35 and 36 using equation (7.2). Following the discussion by Cox and Townsend [1951], these correlograms suggest that yarns 35 and 36 exhibit a quasi periodic variation of wavelengths 1200 and 500mm respectively, while sample 24 is more uniform in this respect.

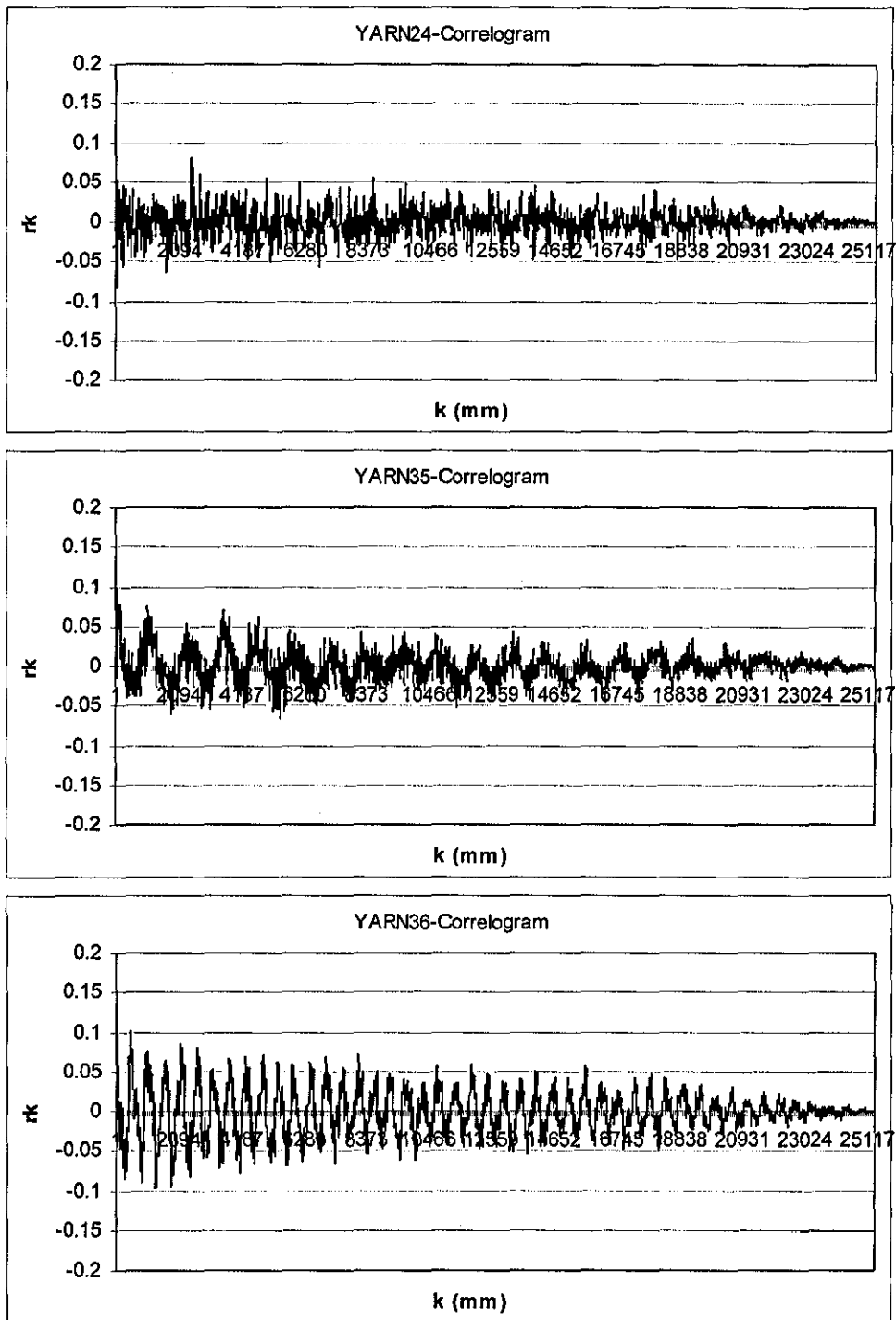


Figure 7-19 Correlogram for yarn samples 24, 35 and 36

7.4.3 Variation Plots

A new method to visualize the irregularity in a yarn is implemented during this work. The technique involves calculating the average diameter of a yarn and then plotting the diameter values in an 8-bit (256 grey levels) 2D image where the intensities of each pixel correspond to the diameter readings from 1mm yarn sections. The diameter values are mapped to values between 0 and 255 in such a way that a grey level of 128 corresponds to the average diameter while 0 and 255 correspond to lower and upper boundaries determined by an offset parameter. This offset is taken as 50% by default which means that all the diameter value greater than and equal to 150% of the mean diameter are assigned the intensity 255 while all values less than or equal to 50% of the mean are plotted with 0 intensity.

Figure 7-20 shows the variation plots of samples 32 and 33 which have CV% values 13.97 and 14.61 respectively. In these variation plots, each row corresponds to a yarn length of 160mm and the total yarn length shown is around 25m (160mm x 160rows). Although two samples have close CV% values, the natures of their irregularity appear to be different; sample 33 exhibits a variation with higher frequency as can be seen from the variation plots. This difference in the frequency of variation is also evident from the correlograms obtained from the diameter data of these two yarn samples as shown in Figure 7-21. However the CV-Length curves appear to reveal no such difference as can be seen in Figure 7-22.

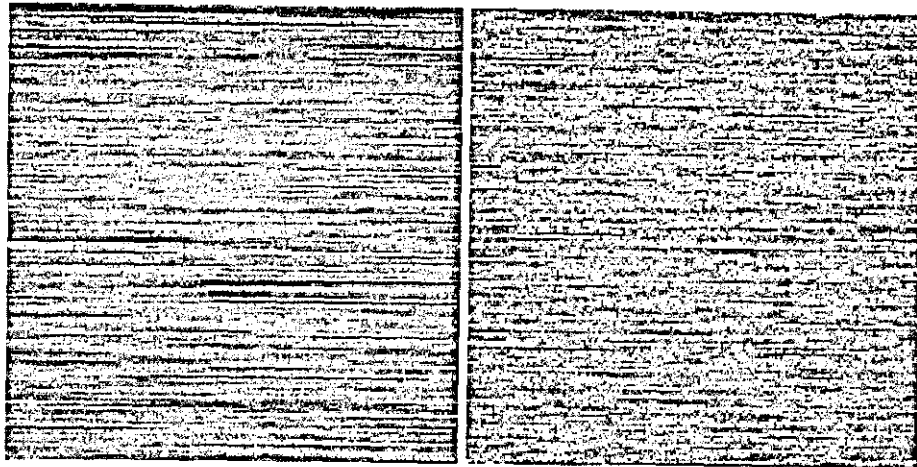


Figure 7-20 Variation plots of samples 32 and 33

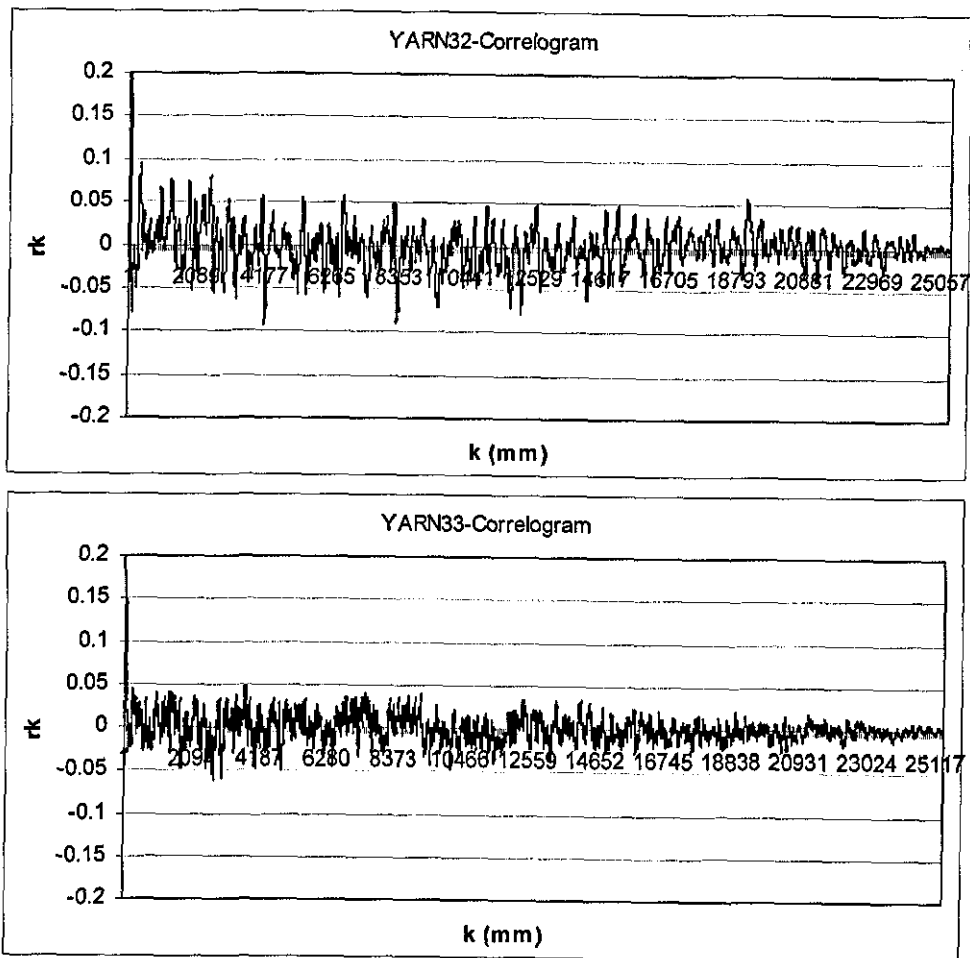


Figure 7-21 Correlograms of samples 32 and 33

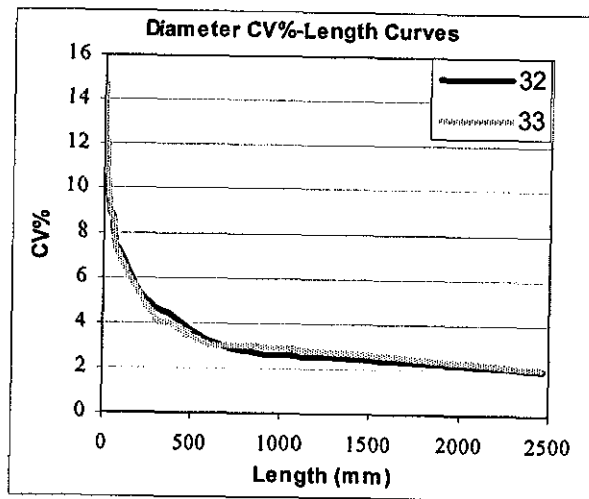


Figure 7-22 CV-Length curves of samples 32 and 33

Thin and thick places especially those with long durations can also easily be observed from the variation plots as can be seen from Figure 7-23 showing the variation plot of sample 22, which has a CV% value of 11.63.

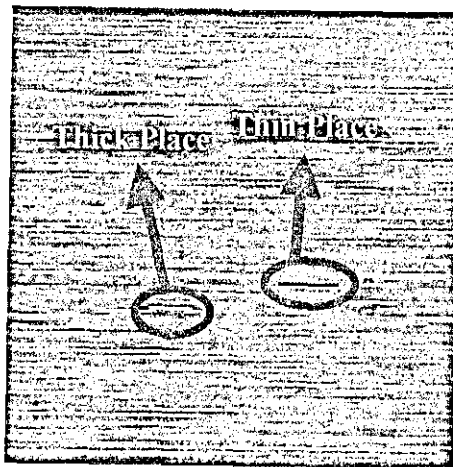


Figure 7-23 Variation plot of sample 22 showing long duration thin and thick places

The number of thin and thick places can easily be calculated from variation plots using simple image processing techniques. For instance, if a threshold, say at 254, is applied to the variation plot then the number of white pixels divided by total number of pixels in the image will give the percentage of places thicker than around 150% of

the average diameter. Figure 7-24 shows the variation plots of samples 32 and 33 thresholded at 254 (and inverted for visibility). The black pixels here correspond to regions having diameters higher than 150% of the average diameter. By counting these pixels, sample 32 turns out to have around 1.27 of such thick places per metre while sample 33 has 2.57.

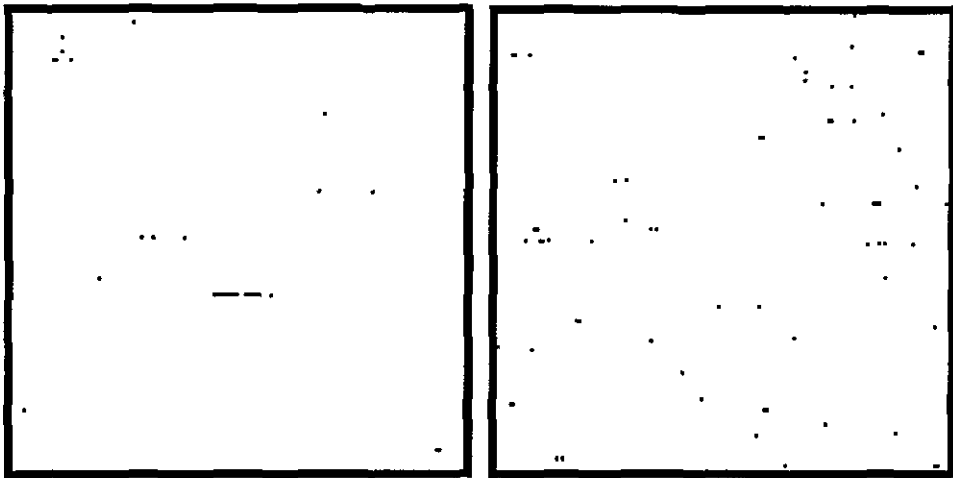


Figure 7-24 Variance plots given in Figure 7-20 thresholded at 254.

Another convenience of the variation plots is that they can be stored in compressed image formats such as JPEG or GIF in order to reduce the amount of space required storing vast amounts of data with very little loss in overall information.

7.5 Conclusions

The diameter and irregularity of the sample yarns measured using back-lit images are found to be in very good agreement with CYROS tester. These results suggested that the processing algorithms implemented in this research were quite successful in terms of simulating a commercial tester. The dark field diameters exhibited lower diameters, which however correlated very well with CYROS. The irregularity values from dark field images on the other hand, were not in good agreement with back-lit irregularity values.

The squares of yarn diameters exhibited a very good correlation with direct yarn counts for 100% cotton samples. For the same set of samples CVd% values obtained for 8mm sampling length agreed reasonably well with UT3 CVm% values. The average elliptical diameters were found to be almost the same as the diameters from one view. However, the former exhibited lower CV% values which correlated better with CVm% values. The theoretical relation between CVd% for 2mm sampling length and CVm% for 8mm sampling length could not be verified and the latter is found to be only 1.13 times the former at average although the theory suggests this ratio to be 2.

The aspect ratios as low as 1:11.3 are found quite reliable in terms of measuring diameter and diametric irregularity. The results suggested that aspect ratios even lower than this can provide almost the same accuracy as 1:1 aspect ratio.

Statistical evaluation techniques such as variance-length curves and autocorrelation function are implemented and demonstrated on various yarn samples. A new method to visualize the irregularity of a yarn called "variation plots" is introduced. It is shown that different samples having the same CV% values but are different in nature of variation, i.e. short term or long term, can be differentiated successfully by means of variation plots. Calculation of the number of thin and thick places from variation plots using simple image processing techniques is also demonstrated.

CHAPTER 8 - Twist Measurement

8.1 Introduction

Twist is an important yarn parameter that affects the characteristics such as strength, handle, and appearance. The twist variation in a yarn creates irregular patterns on the fabric due to different dye absorption levels since low twisted regions absorb more dye compared to high twisted regions. Twist variation is reported as the major reason for “barre effect” in fabrics (Anbarasan et.al., 2003). Conventionally, it is measured by removing all the twist from a certain length of a yarn and then by re-twisting it until it attenuates the starting length. The total number of rotations for untwisting and re-twisting gives twice the number of twist in that specific length. Although currently being the only accepted way to measure yarn twist, it is apparently a time consuming and destructive method, which can only be performed off-line. Furthermore the twist is measured on 50cm samples with this method, which is obviously not sufficient to see high frequency twist variations and hence not suitable to estimate the associated appearance problems on fabrics. Recently, some computer vision techniques have been introduced to measure yarn twist in a non-destructive fashion, which also enable measurement of high frequency twist variations [Vas et.al., 1994; Cybulska 1999; Millman 1999]. In conjunction with yarn diameter, the twist information might lead to estimation of some “invisible” characters such as linear density and mass variation [Cybulska 1999; Hearle & Merchant, 1963; Sust and Barella, [1964]] of yarns which makes twist measurement an exciting part of vision based yarn testing.

For twist measurement, a Hitachi HV C-10 CCD area scan camera attached to a Meiji Techno microscope is used. The images are transferred to the computer using a Viper Quad analogue frame grabber at a frame size of 640x480. A ring light is employed to illuminate the surface of the yarns from the front as described in Section 3.4. Varying magnifications between 2.5:1 and 4:1 are used depending on the fibre fineness of the yarns being tested.

The first section to follow explains the relation between the orientation of surface fibres and twist outlining the parameters that need to be found from the images in order to calculate twist. The image processing task for measuring the twist involves two stages. In the first stage, the core region of the yarn is extracted from the image to perform two essential tasks; the first one being the determination of diameter and the second definition of the area of interest where the twist angles will be searched. The method developed to extract the core region of the yarn is described in Section 7.4.

Two different methods are developed to determine the surface orientation angles. The first one is based on spatial analysis while the other uses frequency domain analysis. These methods are covered in Sections 7.5 and 7.6 respectively. A hybrid method that combines frequency domain filtering with spatial analysis is also studied and described in Section 7.7.

8.2 The Relation between Twist and Twist Angle

Figure 8-1a shows the ideal geometry of a yarn having a diameter d . Due to twist, a surface fibre makes a helix angle θ with the core axis and completes one full rotation in l units parallel to the core axis, i.e. there is one rotation inserted into yarn every l units. The 3-dimensional structure can be unfolded into a right triangle as in the figure. From this triangle the twist in unit length can be calculated using the following equation;

$$T = \frac{\tan(\theta)}{\pi d} \quad (8.1)$$

Where, if the diameter d is given in meters, T will give the twist in turns/meter. Figure 8-1b shows calculation of twist per unit length on a real yarn image.

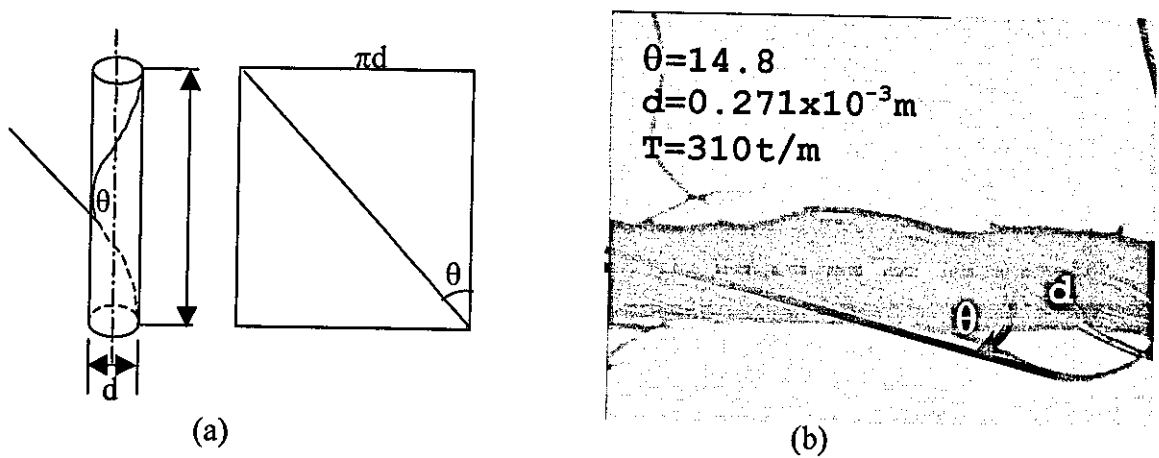


Figure 8-1 a)-An ideal yarn diagram showing the relation between twist angle and twist, b-) Calculation of twist from a yarn image

Another parameter of yarn twist is the twist direction, which can be either “S” or “Z” as depicted in Figure 8-2.



Figure 8-2 Twist direction

8.3 Core Extraction

Figure 8-3 shows a typical image used for twist measurement. The main problem in separating the core from surrounding hairs and the background is that the surface of the yarn is not uniformly bright, which makes a thresholding or a tracking method as previously used in Chapter 4 problematic. For this reason, an algorithm similar to the one used for processing dark field images is developed as described below.

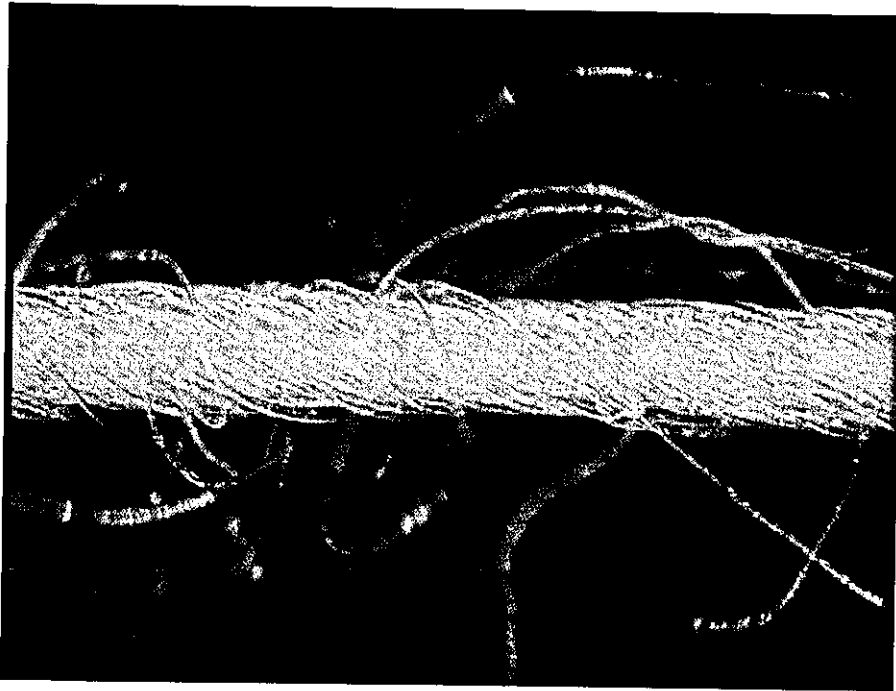


Figure 8-3 A typical yarn image for twist measurement

Initially, 512 pixels wide image portions that correspond to between 1.35 and 2.25mm of yarn section depending on the magnification are extracted from the original image and for each portion, the horizontal projections are calculated. The reason for partitioning the images into 512 pixel-wide segments is for convenience for the frequency domain analysis. Once the horizontal projection is obtained, the boundaries of the core are selected as the region falling above the value defined as one third from the maximum to the average value of the profile as shown in Figure 8-4.

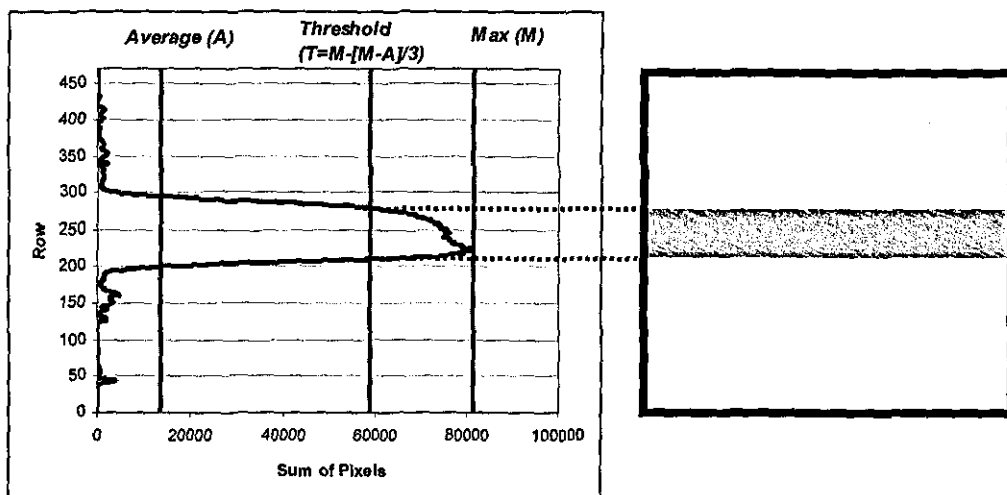


Figure 8-4 Left: The horizontal projection of the image in Figure 8-3 showing the threshold line;
Right: Extracted core region

8.4 Spatial Analysis Method to Extract the Twist Angle

This process involves extraction of the twist angles through the analysis of the core surface. The algorithm starts by applying a 3x3 low pass filter to the extracted core image to decrease the effect of noise while retaining the twist contours. To extract the relatively bright surface fibres, a sobel filter is applied to this image at a slope threshold value of 12 and then by skelotonising, these fibres are reduced to 1 pixel wide contours. To extract the contours resembling a line from this image, first of all, the contours are converted to a polyline structure based on 8-connected neighbourhood of pixels. Following this, line segments are produced from these polylines by checking whether any vertices of the polyline endpoints are more than 4 pixels away from the line connecting its two endpoints; if not, polyline endpoints are considered as line segment endpoints; otherwise, the polyline is split at the vertex farthest from the line and the algorithm is applied recursively to the two resulting polylines. Finally, lines found on the skeleton are merged if the angles are within a 2 degrees tolerance and the endpoints of matching ends are within 5 pixels distance. The lines shorter than 15 pixels are filtered out during this last procedure. All these tasks are performed using built in Wit 7.1 operators.

As a yarn may have either "S" or "Z" twist only, the slopes of the lines representing the twist must be in a certain range. The lines having angles between 10 and 80 which correspond to "S" twist and those having angles between 100 and 170 which correspond to "Z" twist are separated from each other and the dominant line direction is accepted to be the twist direction of the yarn while the lines in the other direction are omitted. Once finding the twist direction, the weighed average of the angles of the lines in that direction is calculated by multiplying the angles with the lengths and then dividing it by the total length of the lines.

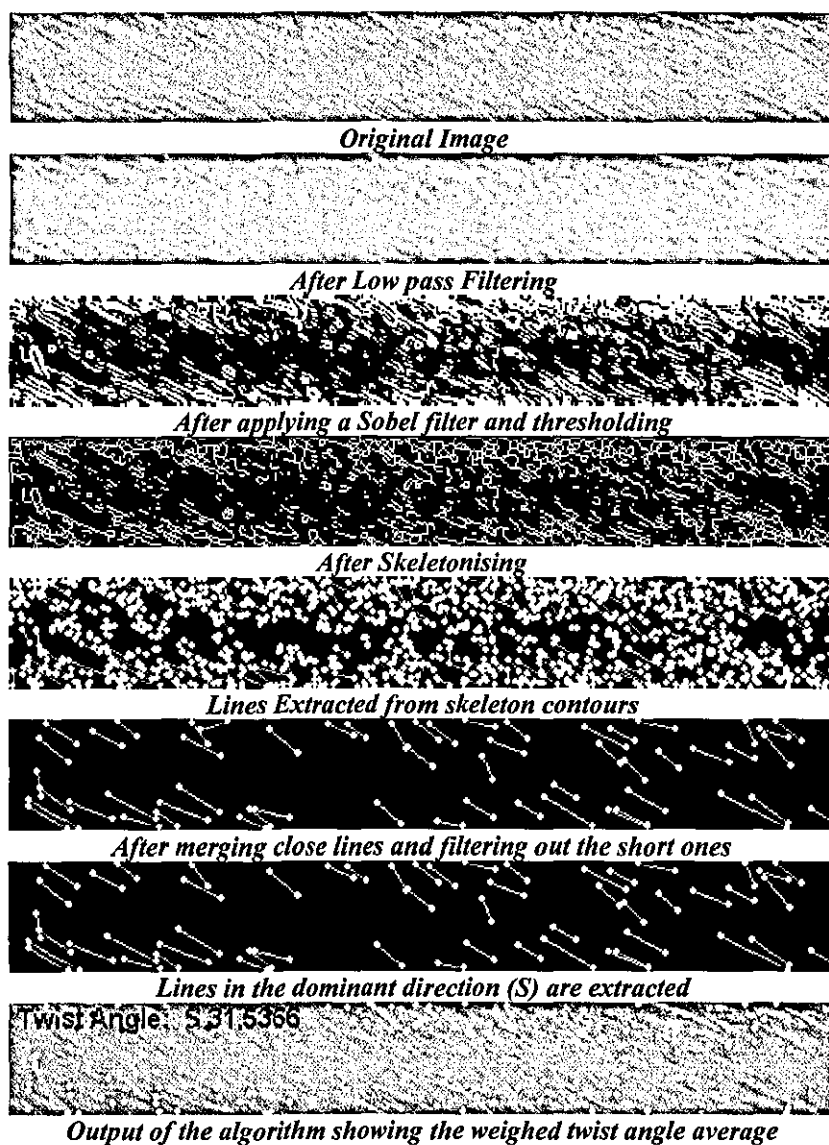


Figure 8-5 Steps of the algorithm to determine the twist angle

8.5 Frequency Domain Analysis

To start the discussion let's first consider a vertical sinusoidal grating plotted on a 256x256 image as shown in Figure 8-6a. In the frequency domain, there will be a single frequency component on the vertical axis corresponding to the frequency of the grating as shown in Figure 8-6b.

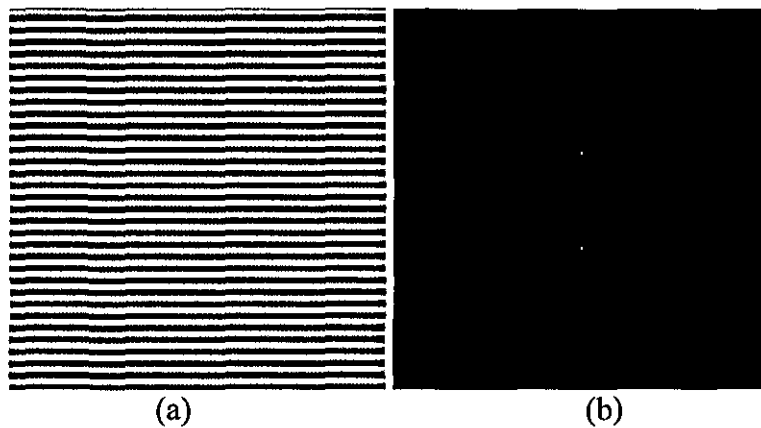


Figure 8-6 a) A vertical sinusoidal grating plotted on a 256x256 image and b) the magnitude component of the FFT of (a)

It is known that there is a direct relation between the orientation in the spatial domain and the orientation in the frequency domain. When the sinusoidal grating is rotated, say by 30 degrees anti-clockwise, as in Figure 8-7a, the spectrum will also be rotated by the same angle as can be seen from Figure 8-7b where the corresponding frequencies appear 30 degrees rotated anti-clockwise from the vertical axis.

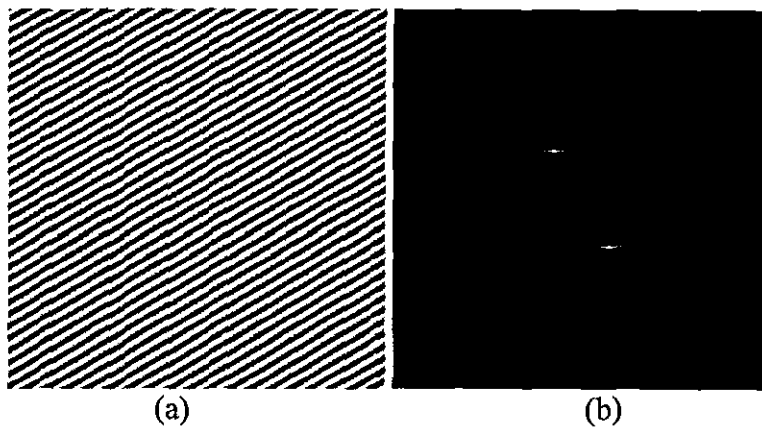


Figure 8-7 a) Sinusoidal grating rotated by 30 degrees, b) the magnitude component of the FFT of (a)

An important convenience of the frequency domain analysis is the ability to separate the components that possess different frequencies in an image. Figure 8-8a shows the sinusoidal grating of Figure 8-7a after adding some significant amount of random high frequency noise, where it is difficult to notice the original grating in the background. However, in the frequency domain, the frequency component of the grating can easily be distinguished as shown in Figure 8-8b. This property is very useful especially when processing images where the problem is to extract some components that are known to have certain frequencies.

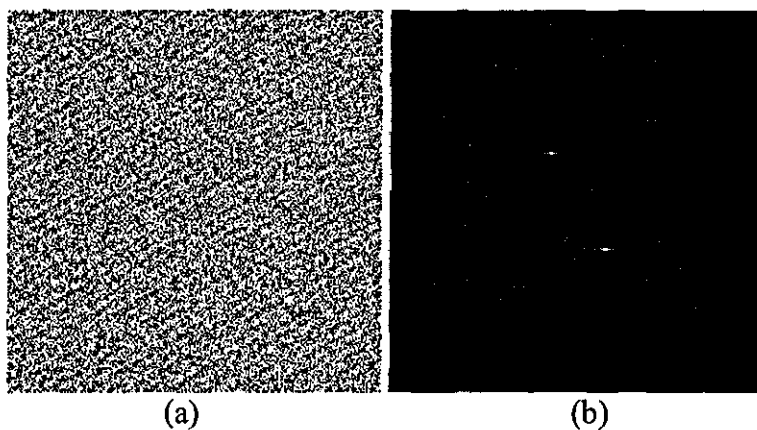


Figure 8-8 a) Figure 8-7a after adding random noise, b) the magnitude component of the FFT of (a)

The frequency domain analysis for twist angle measurement involves the idea that the fibres on the surface have similar spatial characteristics (thickness and brightness) that lead to similar frequency components and since the fibres on the yarn surface are aligned in similar directions, the fibre frequencies might be expected to concentrate in a region that is directly related with the twist angle. Of course the fibres in the spatial domain will not be ideal as the sinusoidal grating pictures discussed above and there will be many different contributions to the frequency domain arising from many different sources.

Figure 8-9 shows the transferred spectrum of an in-focus 14μ fibre (here assumed as a rectangle function) through an $f50/3.5$ lens at 2:1 magnification. It can be seen that almost all of the transferred frequencies are below the first zero crossing (f_0) of the non degraded fibre spectrum (G_g).

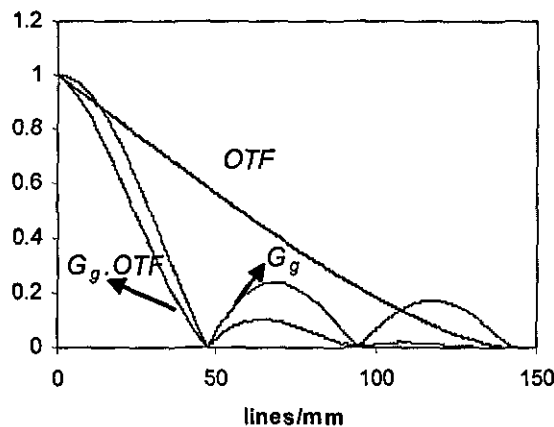


Figure 8-9 Transferred spectrum of a 14μ fibre at 2:1 magnification ($f50/3.5$, $\lambda=670\text{nm}$)

Figure 8-10 shows the ideal focusing plane on the yarn core when imaging the surface fibres. In such a case, if the yarn core diameter is d , the maximum defocusing distance for the surface fibres will be $d/4$. Figure 8-11 shows the transferred spectrum of a 14μ fibre at maximum defocusing assuming the core diameter as 0.4. It can be seen that at this defocus distance, most of the frequencies are still in the region between f_0 and the origin.

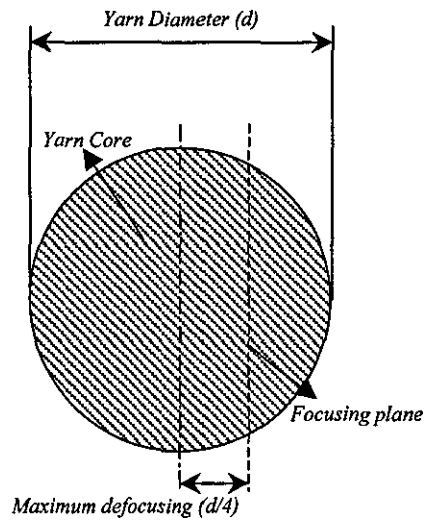


Figure 8-10 Optimum exact focus plane relative to the yarn core for yarn surface imaging

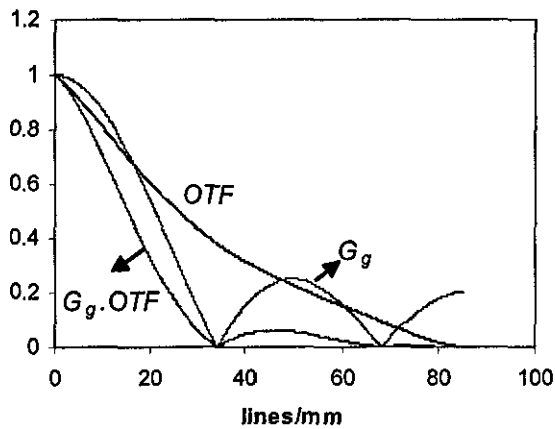


Figure 8-11 Transferred spectrum at 0.1mm defocusing

When imaging the yarn surface there is a high possibility that the surface will be obstructed by hairs protruding from the core. However, these hairs will be significantly defocused compared to the fibres on the surface. In this case, the spectra of these fibres will mainly consist of low frequencies. Figure 8-12 shows the transferred spectrum of a 14μ fibre at 0.4mm defocusing. It can be seen that all of the frequencies are concentrated between the origin and $f_0/2$.

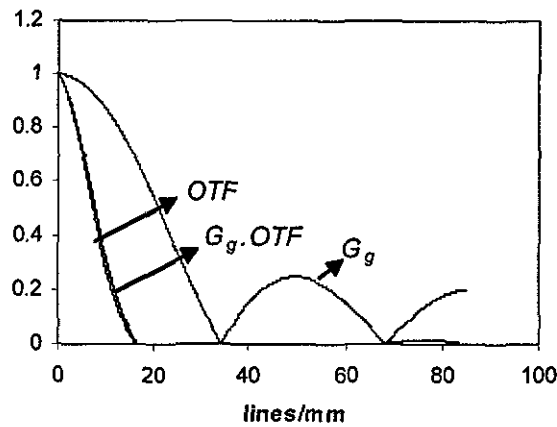


Figure 8-12 Transferred spectrum at 0.4mm defocusing

As a summary, the transferred spectrum of the fibres on the yarn surface are spread over the region from the origin to the first zero crossing (f_0) of the non degraded fibre spectrum (G_g), while on the other hand, for the fibres protruding from the core even at a defocusing of 0.4mm all of the frequencies shrink into a region between the origin and $f_0/2$. From here it can be concluded that the frequencies outside the region between $f_0/2$ and f_0 should not be of interest when analysing the spectrum to extract the surface fibres. So the **region of interest** in the frequency domain is defined as

$$\frac{f_0}{2} < f < f_0 \quad (8.2)$$

Where f denotes the frequency variable.

The algorithm developed for frequency domain analysis of yarn surface images starts by overlaying the 512 pixel wide core portion onto a 512x512 image to enable a square FFT. Figure 8-13 shows the overlaid core image (a) and its FT (Magnitude) on a logarithmic scale (b). Two very interesting frequency components are observed in the fourier domain one corresponding to a sinusoidal aligned 45 degrees in the image with a frequency of 0.5cycles/pixel and the other aligned 71 degrees with a frequency of 0.38 cycles/pixel. It later became clear that these sinusoidal noises were

added to the image due to a problem with the analogue frame grabber used in the experiments.

The frequencies appearing at $v \cong 0$ (vicinity of horizontal axis) mainly arise from the image edges (left and right) and $u \cong 0$ (vertical axis) mainly due to the sharp crossing at the bottom edge of the core in the image. The fibres lying vertically and horizontally would also contribute to the frequencies along u and v axis. Since these frequencies are not of interest they can be eliminated simply by removing the pixels whose coordinates fall in the areas where $|u| \leq 2$ and $|v| \leq 2$.

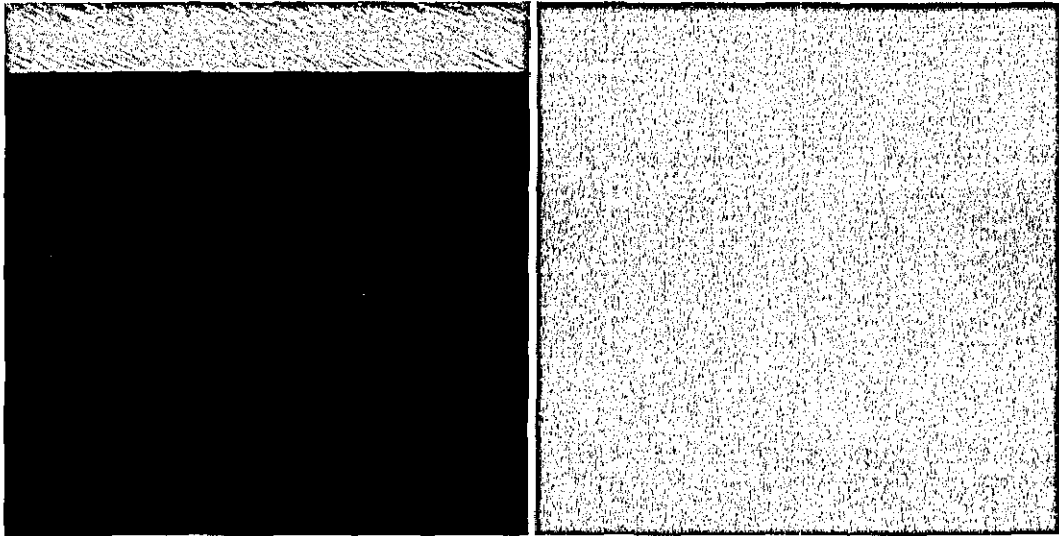


Figure 8-13 a) Image of the yarn core. b) Magnitude of FT on logarithmic scale

If the fibre has a width of n pixels in an $N \times N$ image, from equation (8.2) following band pass filter can be applied in the frequency domain;

$$\frac{N}{2n} < \sqrt{u^2 + v^2} < \frac{N}{n} \quad (8.3)$$

This filtering will get rid of high frequencies from different sources such as the sinusoidal noise caused by the frame grabber without altering the information from

fibres as well as the low frequency components that mainly arise from yarn core and out of focus protruding fibres.

Furthermore, the frequencies can also be filtered according to the twist direction of the yarn. Figure 8-14 shows the positions of frequencies corresponding to surface fibres making a twist angle θ in either S or Z direction. If the twist direction of a yarn sample is known then the frequencies that would arise from the opposite twist direction can be omitted (e.g. Zones 2 & 4 can be filtered out if the yarn has S twist). This filtering helps to eliminate the surface hairs lying in opposite directions to the twist angle.

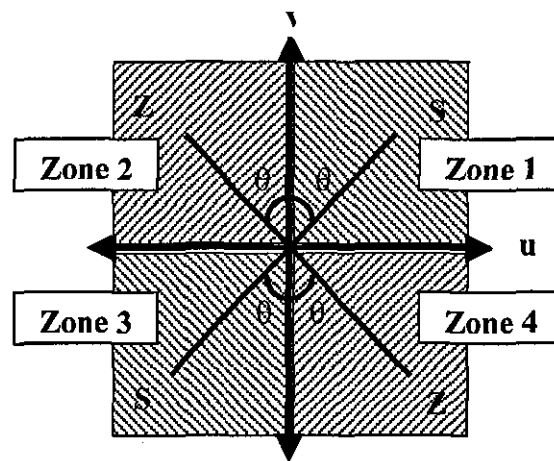


Figure 8-14 Frequency components of S and Z twists.

Figure 8-15 shows the magnitude component of the spectrum after applying the aforementioned filters.

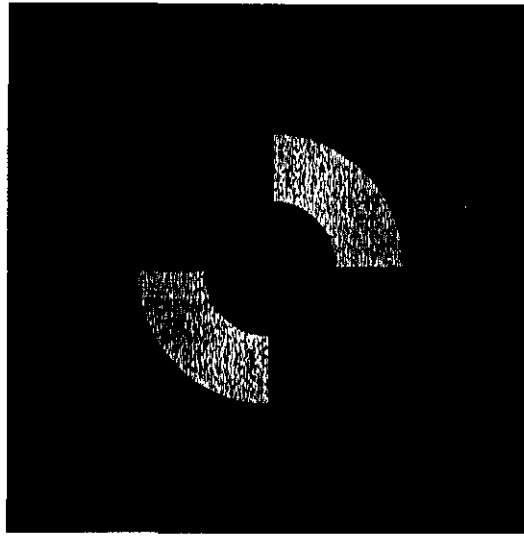


Figure 8-15 Filtered FT (Magnitude); frequencies falling in range $65 < \sqrt{u^2 + v^2} < 130$ within zones 1 and 3 are extracted from the original spectrum.

The final step of the algorithm is to find the dominant direction in the frequency domain. The first approach for this is to calculate the mean magnitude along each angular direction incremented by 1 from 0 to 90 degrees within the zone corresponding to the twist direction (e.g. Zone 1 for S twist). Figure shows the mean magnitudes along each direction from 0 to 90 degrees. The maximum mean magnitude appears along 67 degrees, which indicates an S twist of 23 degrees.

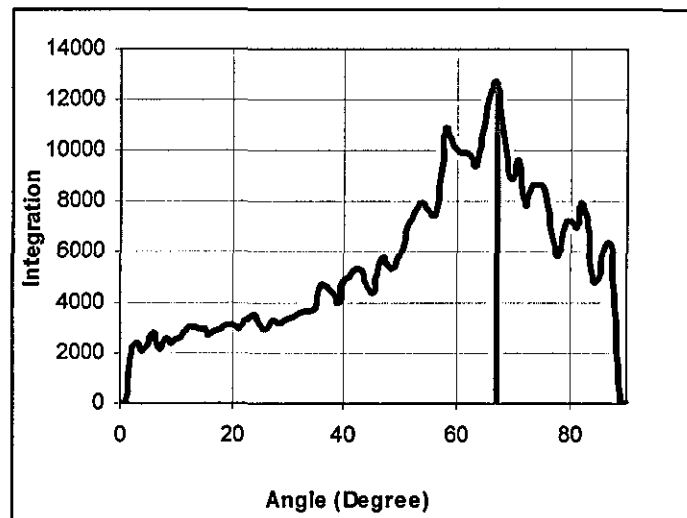


Figure 8-16 Mean magnitudes along varying angles

Another approach to determine the twist angle is simply to find the angle that the v axis makes with the line between the pixels having the maximum magnitude in the spectrum as depicted in Figure 8. The calculated twist angle this time is 22.38 degrees.

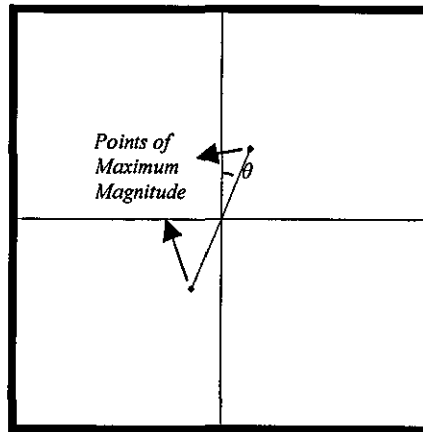


Figure 8-17 Determination of twist angle from the frequency having maximum magnitude

One can expect the twist angles calculated using these two different methods to be in good agreement with each other. However, for most of the images especially those having a complicated surface structure, they did not agree well and in such cases both measurements often gave inaccurate results. For this reason, the twist angle is found from the average of the twist angles calculated from these two different methods if they are within 2 degrees proximity; otherwise both measurements are discarded.

8.6 A Hybrid Method: Frequency Domain Filtering and Spatial Analysis

After working on spatial and frequency domain analysis techniques, it became clear that a hybrid method that incorporates frequency domain filtering followed by spatial analysis would be an interesting method for yarn surface inspection.

Figure 8-18 shows the inverse transform of the filtered spectrum. When a threshold at 0 is applied to the inverse transform, the improvement in the image can be seen compared to the original image as shown in Figure 8-19.

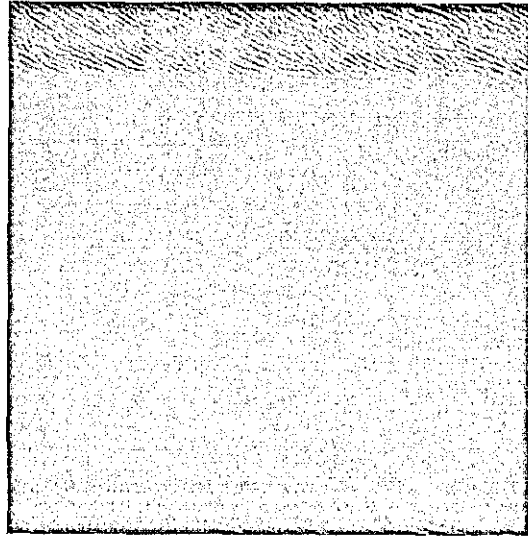


Figure 8-18 Inverse transform of the filtered spectrum.

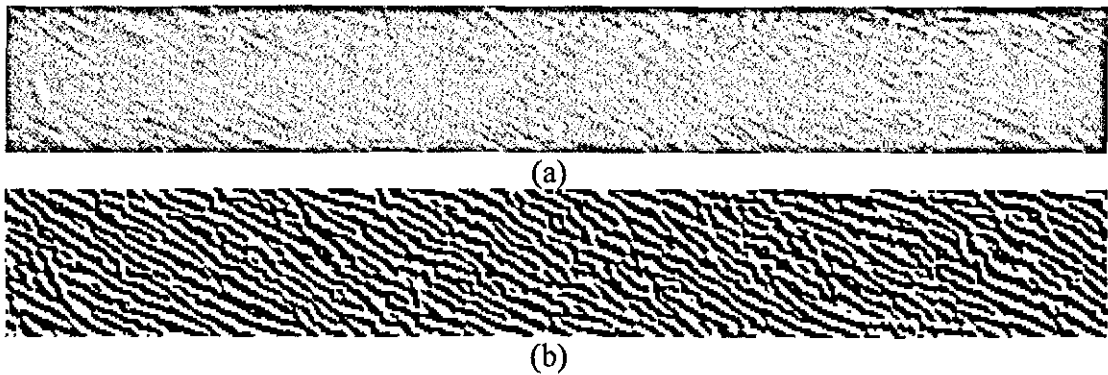


Figure 8-19 a) Original core image b) Inverse of filtered FT after thresholding at 0

From this point the spatial analysis algorithm mentioned in section 8.4 can be applied to the image in Figure 8-19b. However, in this case both the low pass and the sobel edge detection filters are not required and the algorithm can directly start from the skeletonising step. Figure 8-20 shows the output of this algorithm. It can be seen that the contours extracted in this case are more significant.

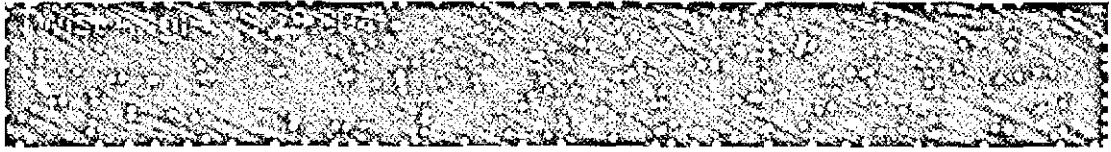


Figure 8-20 Output of the hybrid processing algorithm

This technique worked very well even on yarn images with poor surface detail. Figure 8-21a shows such an image processed using both the spatial analysis algorithm and the hybrid method. It can be seen that the spatial analysis algorithm fails to detect the details with little contrast leading to inaccurate measurements. On the other hand, when the frequency domain filtering is applied, these details are significantly highlighted. Through a careful observation, it can be seen from Figure 8-21a and Figure 8-21d that the hybrid method is quite successful in determining the surface fibre contours.

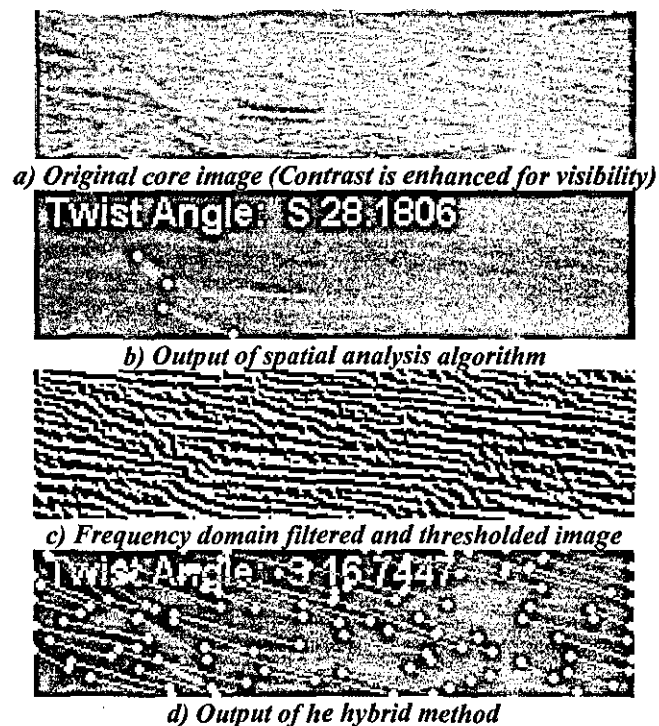


Figure 8-21 Hybrid method applied on a yarn image with poor surface detail

The biggest disadvantage of the hybrid algorithm is the time required to process images; since the method requires two FFT operations one in forward and the other

in reverse directions. To speed up the algorithm, 64x64 windows are used rather than 512x512 as shown in Figure 8-22a. This decreases the number of computations required for FFTs for each image from $2.2 \cdot 2^{18} \cdot \log_2(2^{18})$ to $2.2 \cdot 2^{12} \cdot \log_2(2^{12}) \cdot 8$ corresponding to a 12 times reduction. Of course, a 64x64 frame size would not be suitable for frequency domain analysis due to increasing error arising from digitisation.

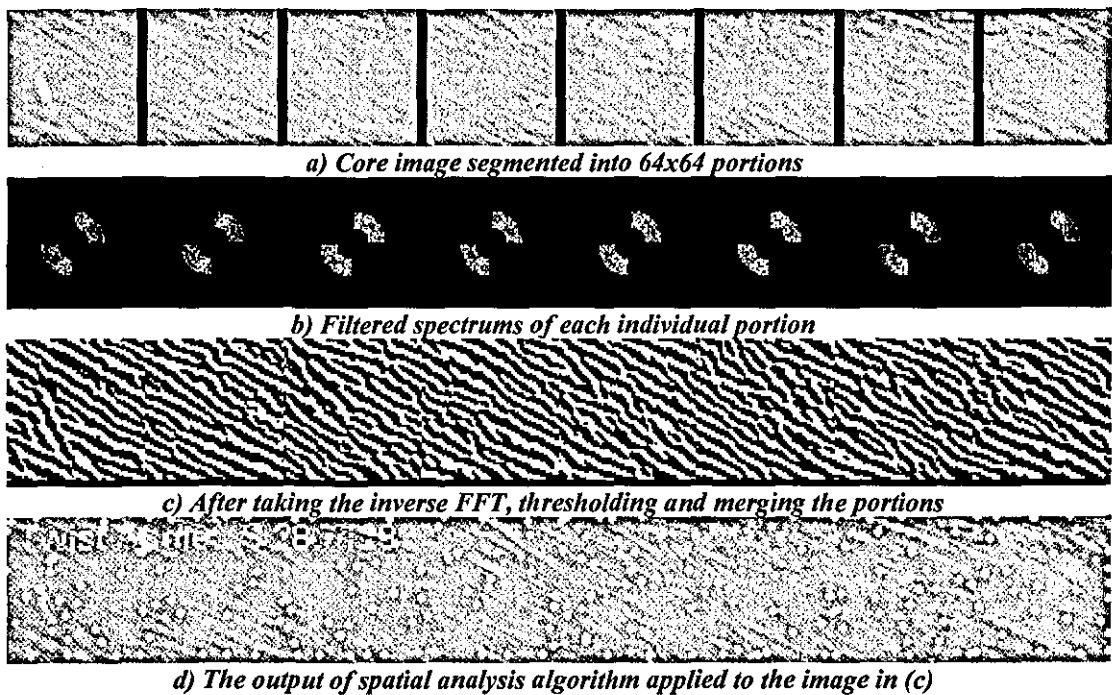


Figure 8-22 Application of the hybrid method using 64x64 image portions.

8.7 Results and Discussion

28 different yarn samples are tested to investigate the accuracy of the algorithms. The yarn samples are first wound onto 60x60mm frames as shown in Figure 8-23, where 7 yarns are wound onto 14 slots of the frame allowing observation of 120mm section for each yarn sample. Around 60 images are taken from each sample and these images are then analysed using all three methods previously described.

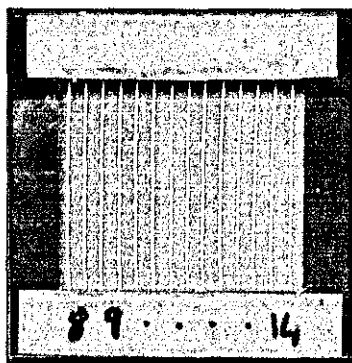


Figure 8-23 Seven yarn samples winded on the sample frame for twist measurement

Figure 8-24 shows the twist measurements using three different methods compared with the actual twist values obtained from the manufacturing labels of the yarn packages. The frequency domain analysis method appears to exhibit very close agreement with the actual values for most of the samples. The spatial analysis method on the other hand exhibits generally significantly higher values, while the hybrid method gives values falling between the values from the frequency domain and spatial domain analysis, but still considerably above the actual values. The correlations with the actual values are low for all methods with R values of 0.65, 0.67 and 0.71 respectively.

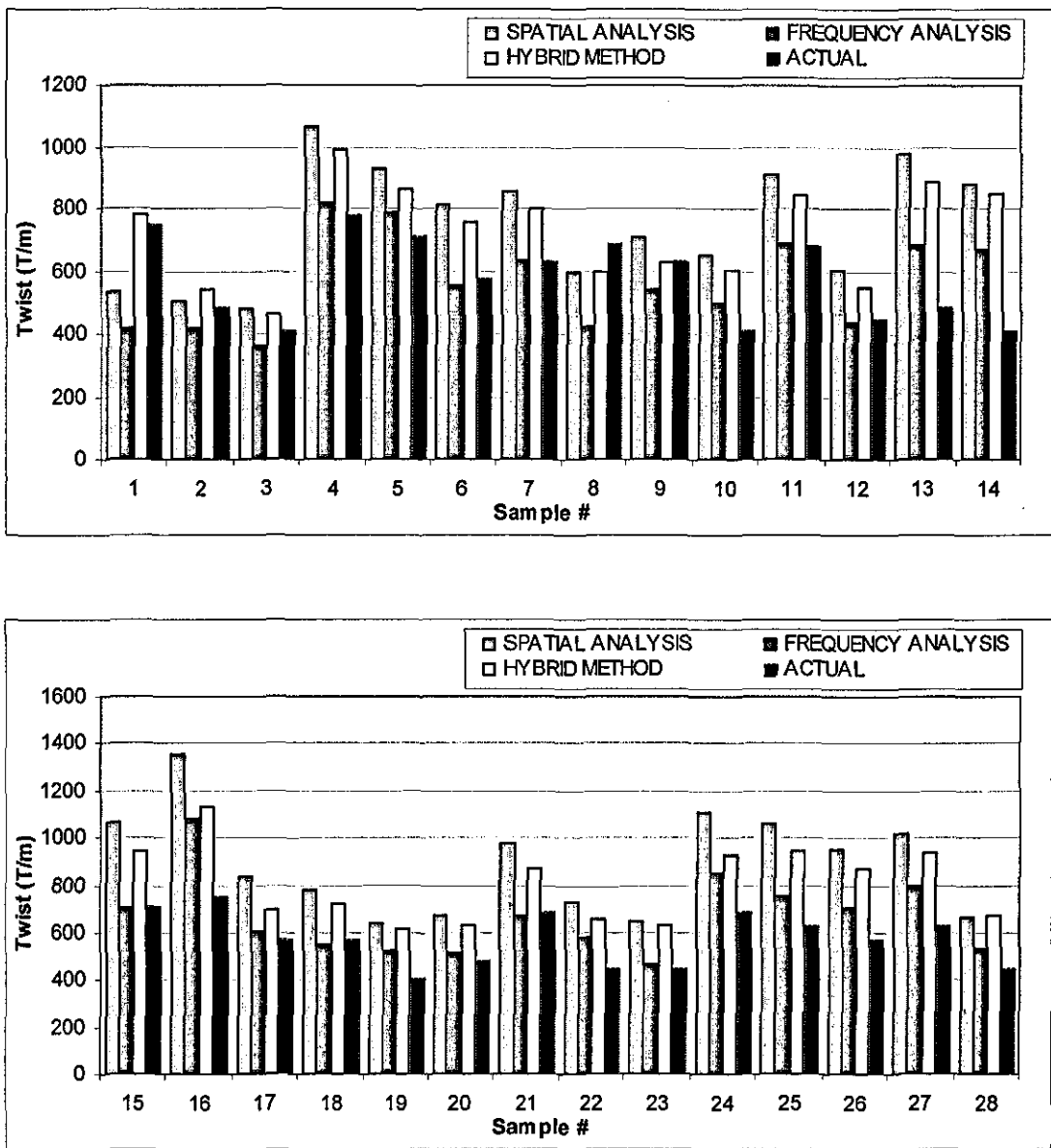


Figure 8-24 Comparison of actual twist values with measurements from different algorithms

An important difference between the frequency domain and spatial domain analysis is that, in the frequency domain, the twist angle value is obtained from the most significant direction while for the spatial analysis method, a weighed average is calculated, which is more likely to be influenced by the surface hairs. These two methods could be expected to exhibit closer results if the same principle was applied to both techniques. Another important difference is the condition check that applies

to the frequency domain analysis omitting images that do not exhibit consistent twist angles from maximum magnitude and the angular integration techniques. As a result of this condition check, the percentage of valid images varied between 25% and 50% for the frequency domain analysis, while on the other hand, all images were taken into account for spatial analysis.

The diameter measurements from front lit high magnification images are compared with those from back lit low magnification images as shown in Figure 8-25, where a poor linear relation can be observed between two sets of measurements. Since the diameters from back lit images have proven quite accurate in Chapter 6, it can be concluded that the diameter measurements from front lit images cannot be attributed high confidence levels.

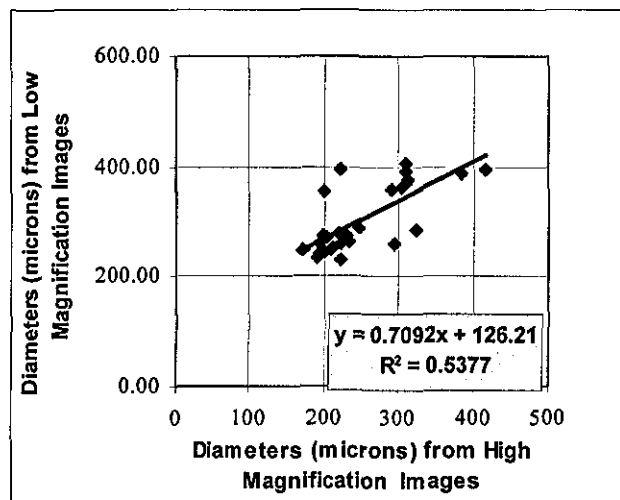


Figure 8-25 Comparison of diameter measurements from back-lit low magnification and front-lit high magnification images

The twist per metre values are calculated using the mean diameters from back lit images and mean twist angles from three different techniques and compared with the actual values as shown in Figure 8-26. It can be seen that, the hybrid method exhibits a very good agreement with the actual twist values, which gave a correlation coefficient of 0.97. The spatial analysis and frequency analysis methods also exhibited reasonable correlations with the actual values with coefficients of 0.93 and

0.89 respectively. These results strongly suggest that for more accurate estimation of twist, the core extraction algorithm should be revised in order for a better agreement with the back-lit diameters. The best way to do this would probably be the use of a front-lit and back-lit hybrid yarn illumination, since the diameter is better defined in back-lit images.

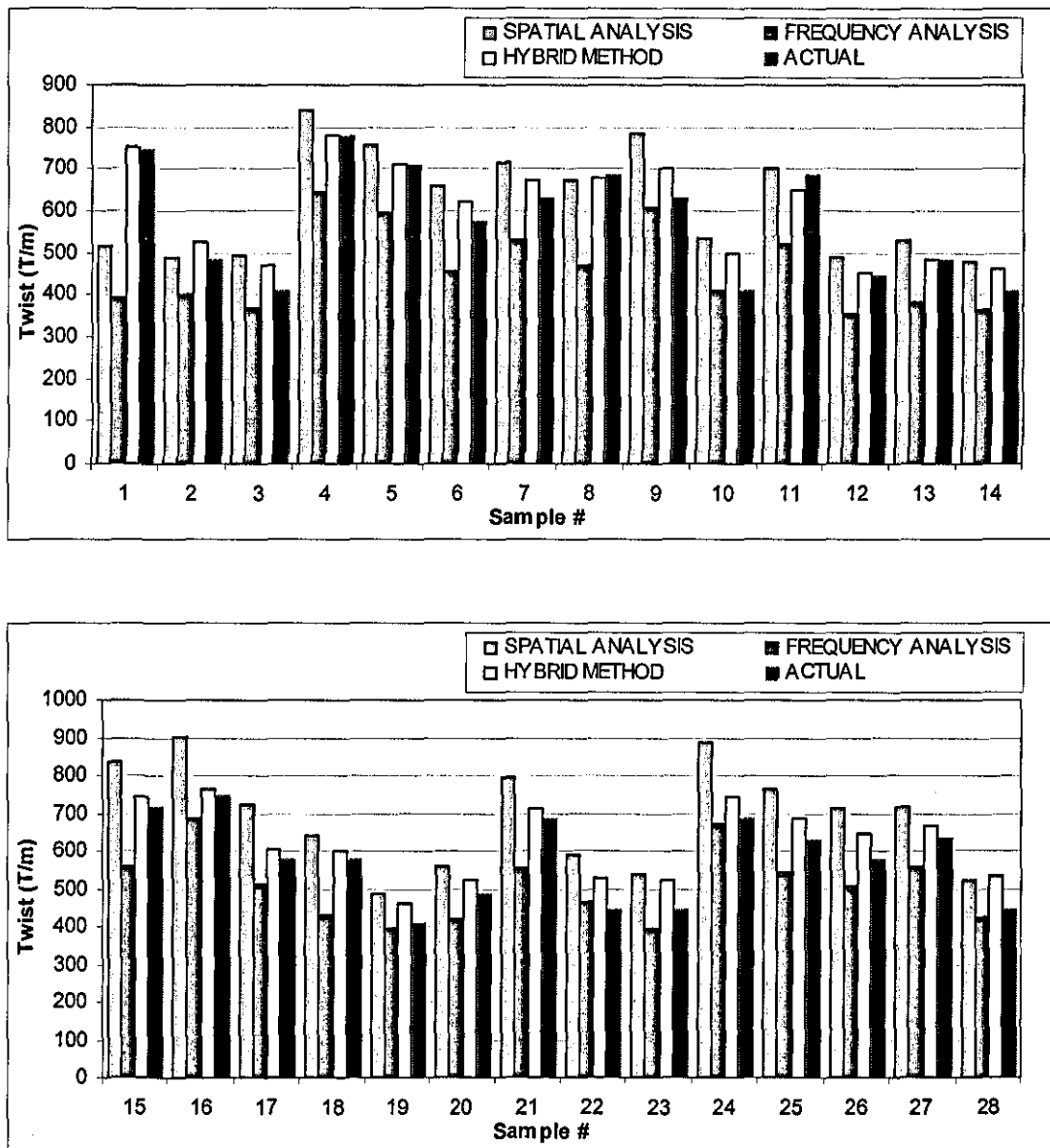


Figure 8-26 Comparison of actual twist values with measurements calculated using the mean twist angles from different algorithms and the mean diameters from back-lit images

A comparison between three different algorithms in terms of the time to process 512x512 images is given in Table 8-1. These values are obtained on a Pentium3-800MHZ computer. It is apparent that because of the time required to carry out the Fast Fourier Transformation on 512x512 images, the frequency analysis technique, requiring a total processing time of 750ms for each image, is 4-5 times slower than the other two techniques. The time required to process a 1m long yarn section using frequency domain analysis will be around 6.25 minutes at average magnification, whereas it will be 1.25 and 1.5minutes for spatial analysis and the hybrid method respectively. These times might be reduced to one sixth by employing a more advanced CPU currently available in the market.

Table 8-1 Comparison of processing times for three different algorithms

<i>Processing Method</i>	<i>Spatial Analysis</i>	<i>Frequency Analysis</i>	<i>Hybrid Method</i>
<i>Processing Time (ms)</i>	150	750	180

8.8 Conclusions

To measure the yarn twist, among the three techniques introduced in this chapter the hybrid method involving frequency domain filtering followed by spatial analysis is found superior in terms of accuracy. The spatial analysis method on the other hand was the fastest. It will, however, be necessary in the future to test the technique for longer lengths using an automated yarn transport mechanism.

The diameter measurements from front lit yarn images are not found quite accurate when compared to back lit diameters. The twist values calculated using the diameter measurements from back-lit images and twist angles from the front-lit images are found to be more accurate when compared to the actual values. The conceptual illumination design incorporating coherent back-lit and low angle front lit

illuminations suggested in Chapter 10 would be worth investigation in the future for a more accurate diameter measurement.

Both image processing algorithms described here are only applicable for off-line yarn testing since the processing speeds are far below the yarn production speeds even if a very fast PC were employed. It would be interesting in the future to investigate if the frequency domain analysis method could be implemented purely in optical means using lenses performing optical fourier transformation and real frequency masks for filtering.

CHAPTER 9 - Yarn and Fabric Simulations

9.1 Introduction

Fabric simulation programs are widely used to design fabrics with different pattern and colour combinations. In recent years a trend can be seen on fabric simulation software that use the actual yarn irregularity data to see the possible appearance faults on fabrics that cannot be predicted before the fabric is actually produced. This chapter describes algorithms developed during this research to generate yarn board and plain knitted fabric simulations.

The first section to follow explains the basic principle of converting from vector to bitmaps used in simulations. In Section 9.3, the yarn board simulation algorithm is described. A new method to visualise the effect of hairiness on simulations using THw and HDDP measurements from LYSS is also introduced. Section 9.4 gives the loop geometry implemented in knitting simulation program. The knitting simulations are compared with actual fabrics as well as corresponding CYROS simulations in a visual manner.

An algorithm to calculate the so called variance area curves is also implemented and discussed in Section 9.5. The curves obtained from actual fabric images as well as LYSS and CYROS simulations are compared. The effect of hairiness on variance area curves is also discussed.

9.2 *Simulation of Yarns*

In the simulations, 1 mm wide yarn sections are defined in vector form as rectangles, the height of which corresponds to the average diameter of the section. The position and shape of the sections are determined using the geometry of what is being simulated (eg yarn board or knitted fabric). The vector definitions are then converted into bitmaps based on the quantisation principle, which requires assigning a certain grey level to every pixel depending on the area covered by the yarn in a particular pixel. For an 8-bit unsigned image the quantisation range is between 0-255, i.e. the percentage of the area covered by yarn in a particular pixel is multiplied by 255, rounded to the nearest integer and then assigned to that pixel. To find the intersection areas of a particular pixel and a yarn section, the pixels are first defined as squares the dimensions of which are defined by the resolution of the simulation, and then the areas of overlap between these squares and the yarn sections are calculated geometrically. In Figure 9-1, the quantisation process is depicted, where an infinite resolution (vector) yarn segment is represented with grey levels depending on the areas of overlap between the yarn and the pixels. This is basically the same principle with how the scanners or other image capture devices work. It is clear that as the resolution of the simulation gets higher, the pixels will get smaller allowing a better definition of yarn contours. However, even at low resolutions, the loss of information in terms of the effect of diameter to the simulation is very small owing to the quantisation process. Furthermore, if the simulations were generated as 64 bit double precision images, there would be almost no loss of information in this sense. On the contrary, if the simulation were defined in binary form, which requires assigning "1" to a pixel if it is occupied by yarn more than 50% and "0" otherwise, the resolution of the simulation would gain a big importance.

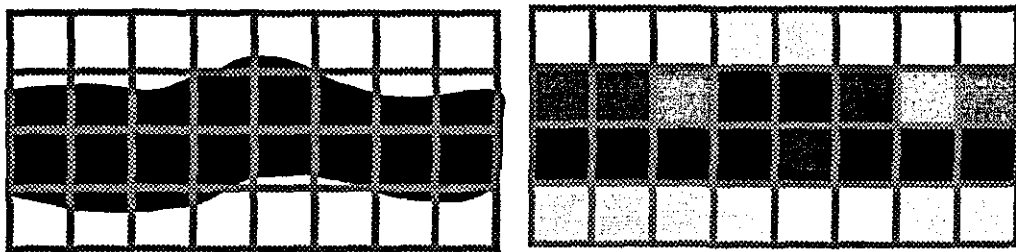


Figure 9-1 Quantisation principle

9.3 Yarn Board Simulation

Using the yarn simulation principle mentioned in the previous section, a yarn board simulation program is developed that estimates the appearance of yarns wound on a rectangular black cardboard. Both the dimensions of the board and the density of the yarns, i.e. the spacing between the yarn cycles can be changed in the program. Figure 9-2a and b show the actual picture of a 2"x2" yarn board with 1mm spacing and the simulated yarn board using the diameter data only from LYSS respectively. It is clear that the hairiness has a very important effect on the appearance and the diameter data alone is not adequate for such a simulation. However, it is possible to examine the diametric irregularity of the yarn from the actual picture by applying a morphological open operation as shown in Figure 9-2c. It can be seen through a careful examination of Figure 9-2b and c that the diametric irregularity can adequately be visualised through the simulation. Nevertheless, the rectangularity of 1mm segments adds a noticeable artificiality to the simulated picture. To avoid this, the sampling length could be selected smaller to minimize the rectangular appearance; however this would enormously increase the sizes of the diameter data files. Another solution could be to simulate the 1mm sections in random shapes generated according to some rules, for example by controlling the change in diameter within a certain range below reasonable limits and keeping the average diameter of the simulated shape equal to the average diameter of the section. However, even if the diameters could be simulated in a very realistic way, the computer generated image would still be away from being realistic because of the effect of hairs on the appearance in real yarns. For

this reason, more emphasis has been put on development of a method to add the effects of hairiness in yarn simulations.

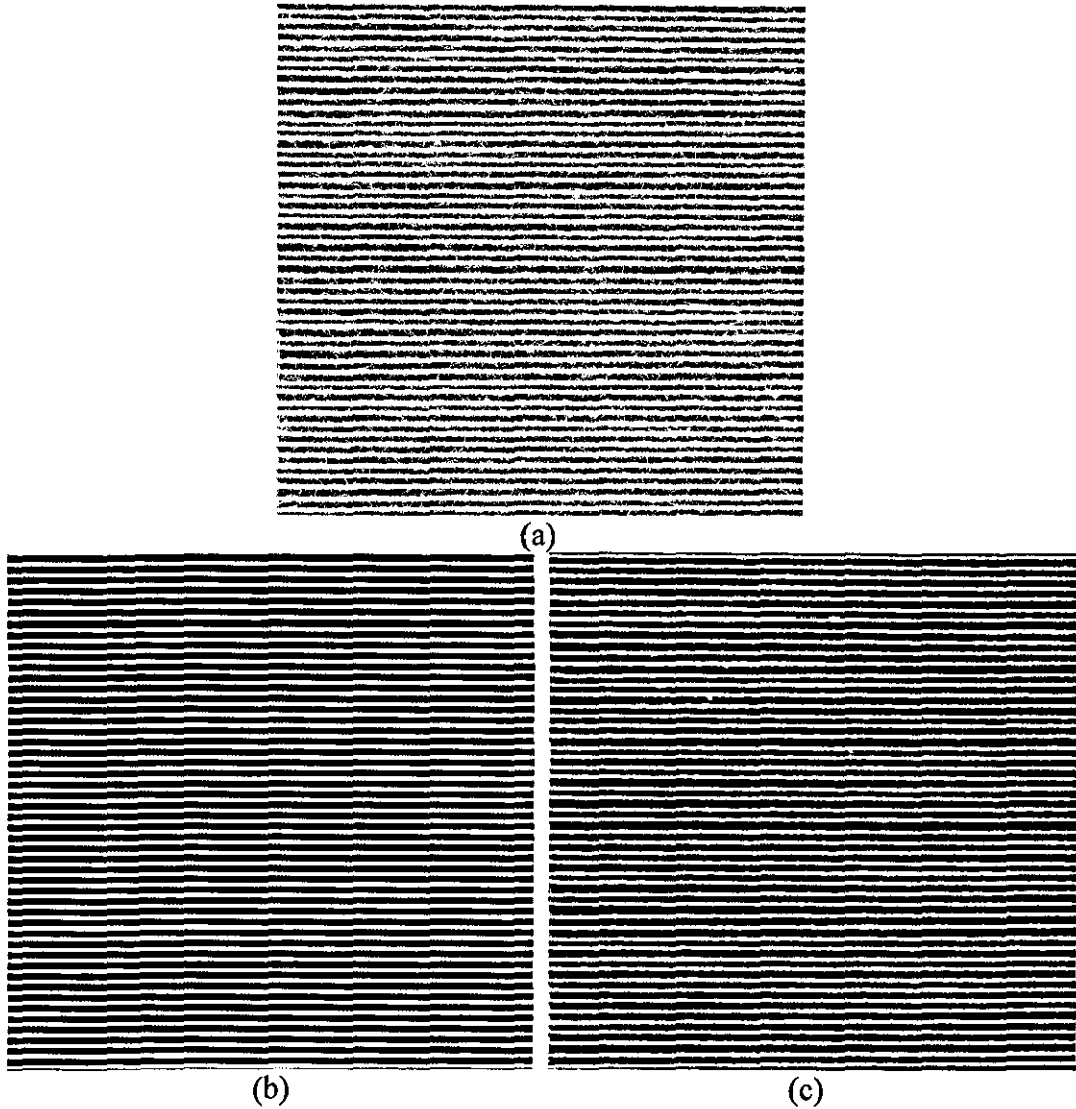


Figure 9-2 a) The actual picture of a yarn bundle; b) The simulated yarn board using the diameter data from LYSS; c) The actual picture of the yarn bundle where the hairs are removed using a 7x7 morphological open operation

The algorithm developed to add the hairiness effect on yarn and fabric simulations uses the total hairiness (THw) values from 1cm yarn segments and the Hair Density Distribution Profile (HDDP), which are both obtained using LYSS. The first task is to map the HDDP according to the resolution of simulation as shown in Figure 9-3

where the HDDP that originally has around 1815 DPI resolution is mapped onto 50 DPI resolution by taking the average of every 36.3 data points in the original profile.

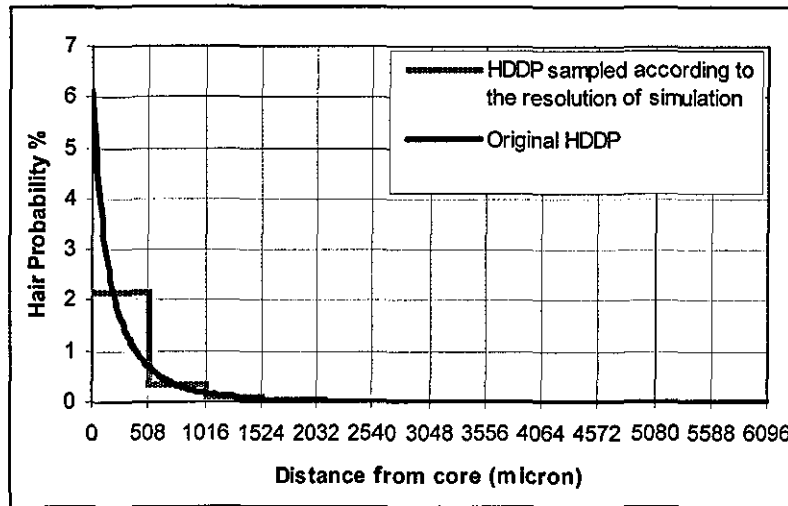


Figure 9-3 The original HDDP mapped for 50DPI resolution

The next task is to distribute the THw values for 1cm yarn segments around the yarn core according to HDDP. An iterative algorithm is developed to perform this that selects points at random distances from the core for randomly selected 1 cm core sections and adds random intensity values to these points, where the intensities correspond to given hair areas. One of the basic rules is that the total intensity assigned for a given 1cm segment cannot exceed the corresponding THw for that section. Another basic rule is that the integration of intensities for all core portions for a certain distance from the core cannot exceed the probability that a hair exists at that distance, which is simply found from the HDDP. A queue type data structure is used in the algorithm that throws away the 1cm yarn segments for which the THw values are reached and continues random selection of yarn segments among the remaining ones. Furthermore, if amount of hairs plotted at a given distance from the core reaches the maximum amount determined by HDDP then again, that distance is no more selected in the random hair distribution process. The algorithm continues until all the THw values are distributed for all yarn segments.

Once the hair-distance distributions are calculated for all yarn segments, the final task is to spread hairs over 1cm length within the simulation. To do this, the number of pixels that corresponds to 1cm in the simulation is first calculated and then for each distance from the core the total hairiness for 1cm is randomly distributed over these pixels with random intensities, where the intensities of the pixels again correspond to varying hair areas.

Figure 9-4 shows the actual picture of a 2"x2" yarn board along with the yarn board simulation generated using both the diameter and hairiness data. It is clear that the simulation is much more realistic in this case than the simulation generated using the diameter data alone.

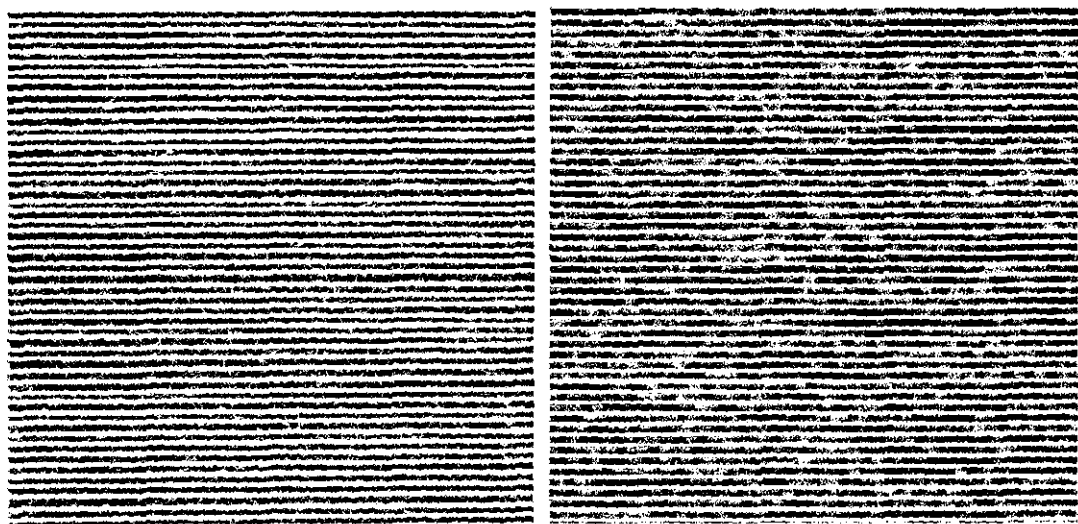


Figure 9-4 Left: The actual picture of the yarn bundle, Right: Corresponding yarn board simulation using hairiness and diameter data.

9.4 Knitting Simulation

In order to simulate single jersey knitted fabrics, a simplified 2D version of the loop geometry studied by Suh [1967] is used. Figure 9-5 shows the top view of jersey loops and the loop construction in this model. Here, P and W are the course and wale spacings.

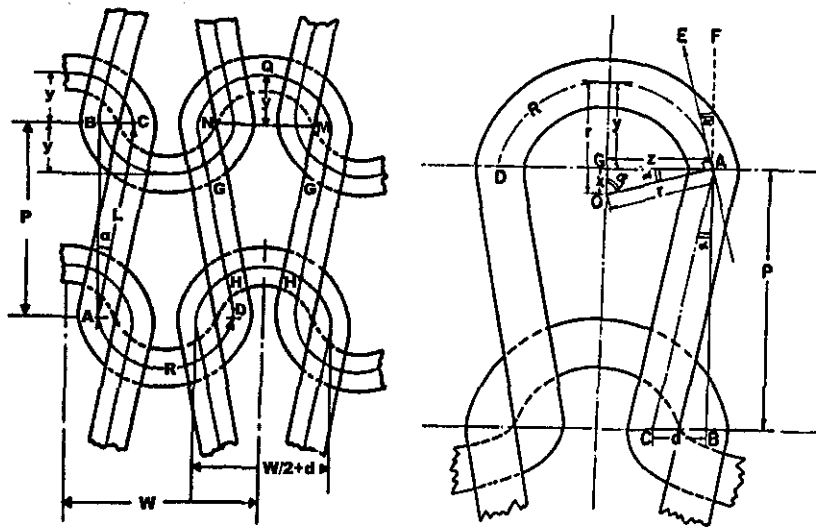


Figure 9-5 Loop geometry. Left: Top view of jersey loops; Right: Construction of sinker and needle loops (Suh [1967], p419)

The arc DA in Figure 9-5 is assumed to be a semicircle centred at O and the curvature length R can be found using the following equation;

$$R = 2.r.\phi \quad (9.1)$$

Where r can be found using,

$$r = \frac{(W + 2.P.\cos(\phi))}{4[\cos^2(\phi) + 2.\sin(\phi)]} \quad (9.2)$$

The length of the loop legs L (AC) is calculated from the following equation,

$$L = P - r.\cos(\phi) \quad (9.3)$$

Finally, the stitch length (S) of a loop is found as follows;

$$S = 2.(L + R) \quad (9.4)$$

It should be noted that the course curvature depicted in Figure 9-6 is not taken into account when calculating the leg length L ; therefore the actual value of L would be longer than that is found from equation(9.3). However, since the simulations are generated using 2D geometry, the legs would appear to have the length calculated from equation (9.3). Nevertheless, the main problem of using 2D geometry is the miscalculation of the stitch length S . For example, if the stitch length is calculated as 6mm while it was say 7mm; the 100th loop for instance, would correspond to the yarn section at 600mm rather than 700mm. As a solution to this problem, the lengths L and R are calculated using 2D geometry; however the stitch length S can be entered manually in the program to enable a more accurate simulation. The most accurate way to calculate the stitch length of a fabric is to unravel certain amount of loops from the knitted fabric and then dividing the total length of the unravelled yarn to the corresponding number of loops.

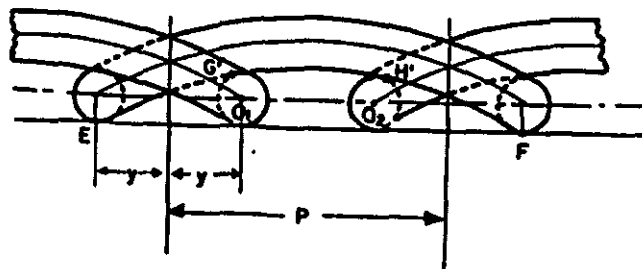


Figure 9-6 Side view of jersey loops (Suh [1967], p419)

The leg angle ϕ is taken as 75° by default, however the program can also calculate it automatically for a given stitch length (S) and course and wale densities by solving equations (9.1)-(9.4) for ϕ .

As in the yarn board simulation, the simulation is first calculated in vector form and then digitised by calculating the areas of overlap between pixels and the yarns and assigning grey level values to the pixels proportional to these areas as depicted in Figure 9-7. The legs are defined as rectangles with a length of L lying at a degree of ϕ to the horizontal axis. The width of the rectangle is calculated from the average

yarn diameter corresponding to that particular segment. The curvatures are defined in a similar fashion as semicircles with a curvature length of R and a thickness corresponding to the average diameter of that section.

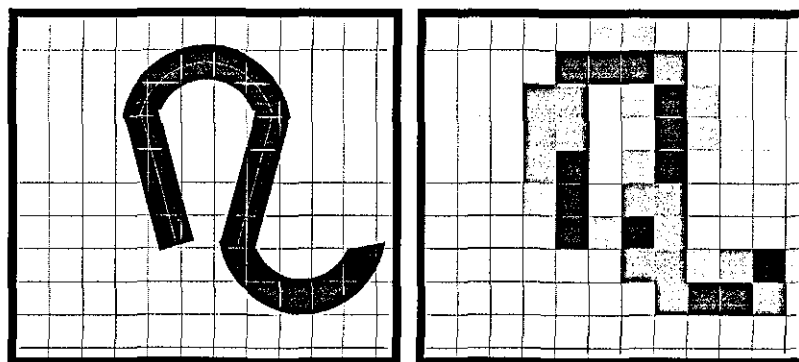


Figure 9-7 Digitisation of geometrically defined loops

The hairiness effect is also implemented for knitting simulations. The hairiness distribution is calculated according to the THw values of 1cm segments and the HDDP using the iterative algorithm described in yarn board simulation section. The main difference from the yarn board simulation is that when plotting the hairs according to their distances from the core, the positions of the pixels are calculated perpendicular to the segment, which can be leg or the curvature of the loop.

Figure 9-8 shows a knitting simulation using the data obtained from LYSS for yarn sample 33. Here, the course and wale densities are taken as 18 and 15 loops per inch respectively and the knitting machine is assumed to have 220 needles. The picture on the left shows the simulation using the diameter data alone and the one on the right using both hairiness and diameter data. The effect of yarn irregularity and the hairiness can clearly be seen on the simulations.

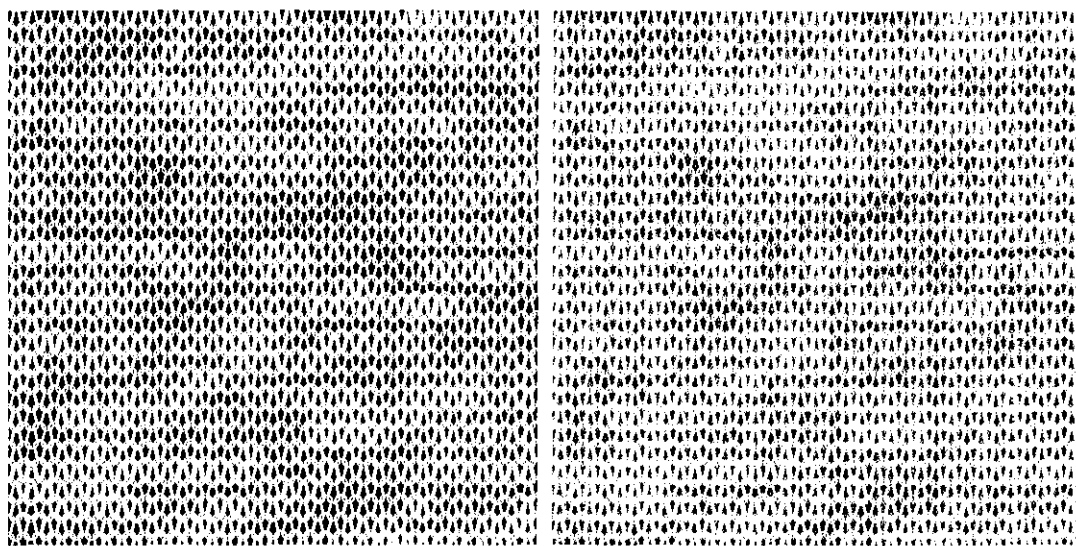


Figure 9-8 Knitting simulation (18 courses/inch, 15 wales/inch, 220 needles). Left: With diameter data; Right: With hairiness and diameter data

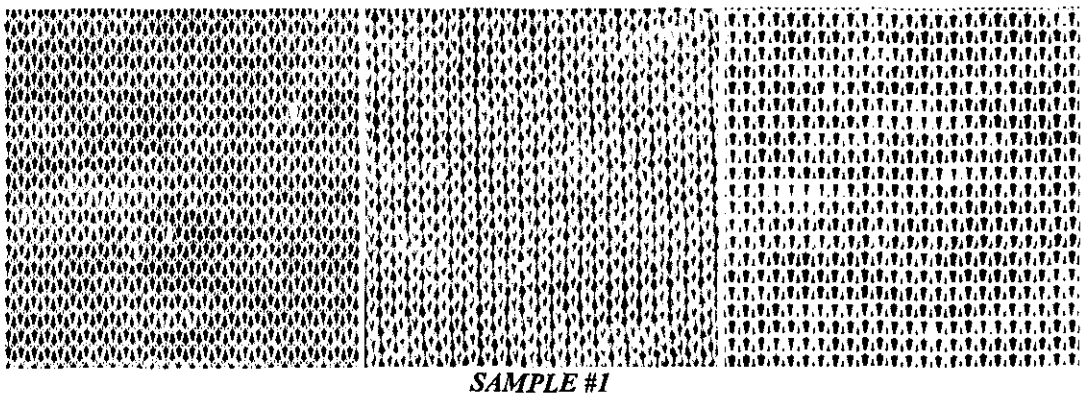
9.4.1 Comparison of fabric simulations from CYROS and LYSS

5 different yarn samples shown in Table 9-1 have been obtained and tested on CYROS and Lawson Hemphill CTT (Jasper's system) at NC State University, College of Textiles. The diameter and CVD% values of the samples shown on the table are obtained from CYROS tester. Single jersey fabric samples are knitted using these yarns on a Lawson Hemphill Fiber Analysis Knitter (FAK) for comparison with simulations. This circular knitting machine has 220 needles with a 29 gauge cylinder. Computer simulations are generated on CYROS system and LYSS. Unfortunately, these yarns could not be brought to Loughborough to be tested on LYSS, so the LYSS simulations shown in this section rely on the diameter data from CTT. For the same reason, the hairiness effect could not be added in the simulations since this also requires the yarns to be tested on LYSS in order to obtain THw and HDDP values.

Table 9-1 Properties of the yarn samples used for knitting simulations

Sample #	NeC	Material	Diameter(μm)	CVd%	Colour
1	18	100% Cotton	280	14.40	Grey
2	30	100% Cotton	240	16.60	Grey
3	20	100% Cotton	280	15.54	Grey
4	20	100% Cotton	250	13.69	Orange
5	36	100% Cotton	200	13.37	Pink

Figure 9-9 shows the images of 1 inch² fabric portions knitted from the yarn samples listed in Table 9-1 along with the simulations from LYSS and CYROS. At the first glance, the CYROS simulation appears more successful in estimating the variation on the fabric. There is an artificial appearance in LYSS simulations arising from the gaps at the vertical connection points of loops. However, the loop geometry appears to be represented better in LYSS simulations. The hairiness also has an important effect on the fabric appearance adding fuzz to the pictures especially for sample 3. This effect is apparently not reflected in both simulations since only the diameter data is used.



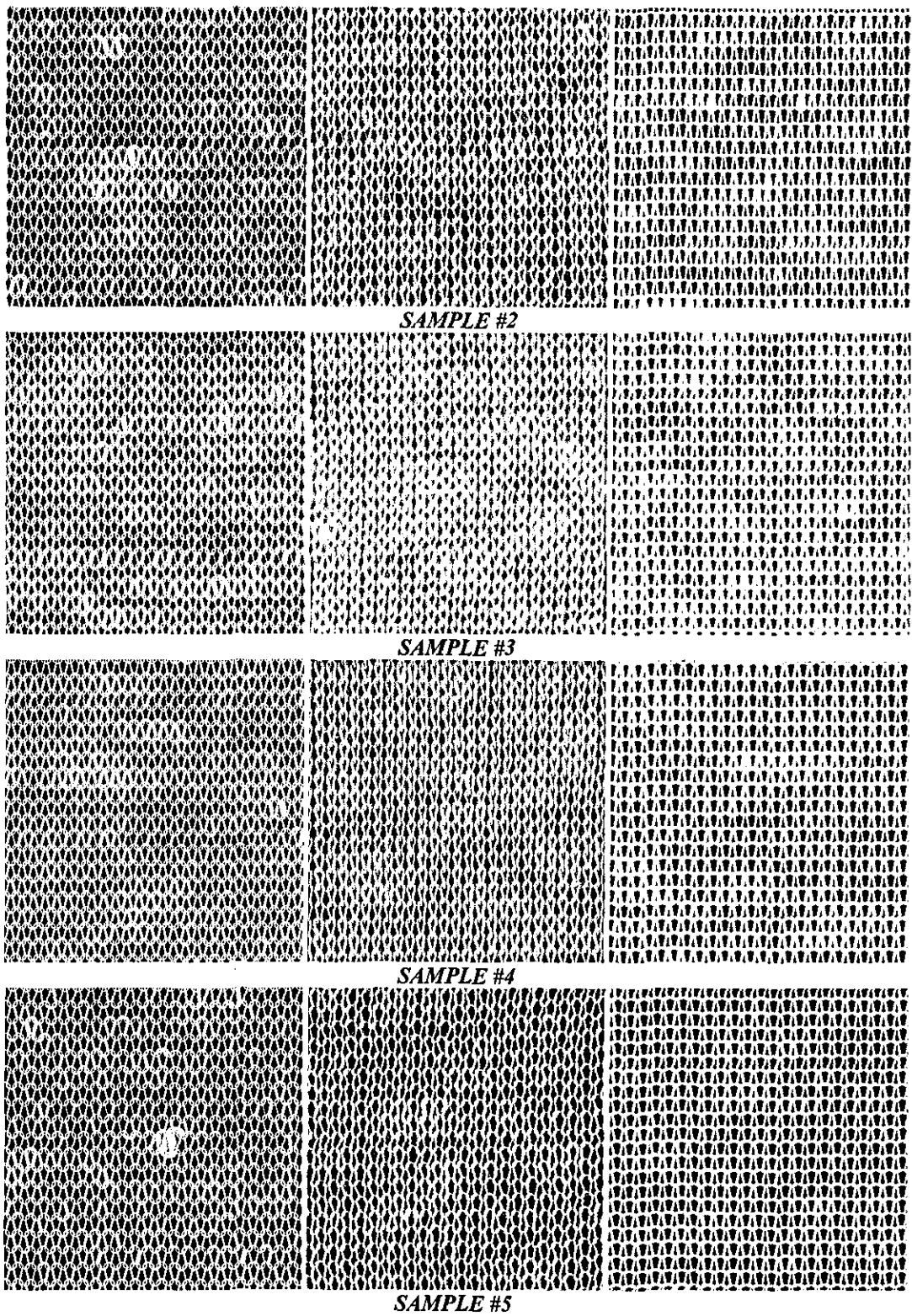


Figure 9-9 First Column: Fabric simulations from LYSS (using yarn data from CTT); Middle column: Actual fabric pictures; Right Column: Simulations from CYROS

CYROS saves the test data in a special binary file format with a 968 byte header that contains the test parameters. A program is written to convert this file into ASCII format to enable LYSS to read it. Using this ASCII file, the fabric simulations can be created on LYSS based on the diameter data from CYROS as shown in Figure 9-10. It can be seen that the short term variations cannot be reflected on this simulation, while the simulation from CYROS program reflects some short term variations with the same set of data. This is due to the reason that CYROS samples the data readings from 1mm yarn sections and does not store the whole data for every successive 1mm sections and when generating the simulations, it uses a stochastic method to predict the short term variations. Considering this fact, it can be expected that the simulations using CTT or LYSS data will be more accurate since these testers store the diameter readings for every successive 1mm sections.

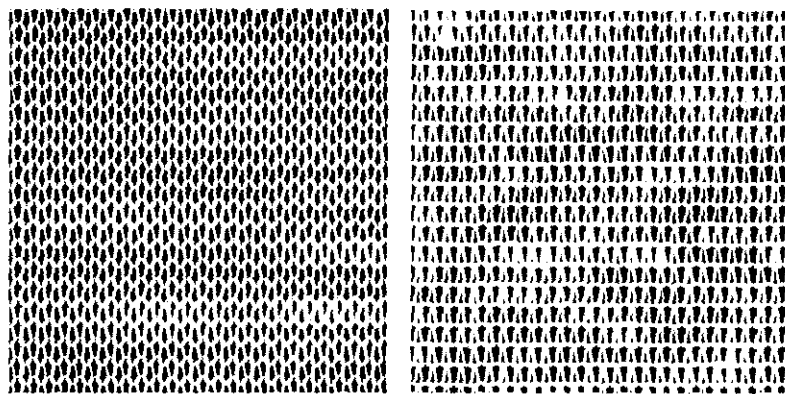
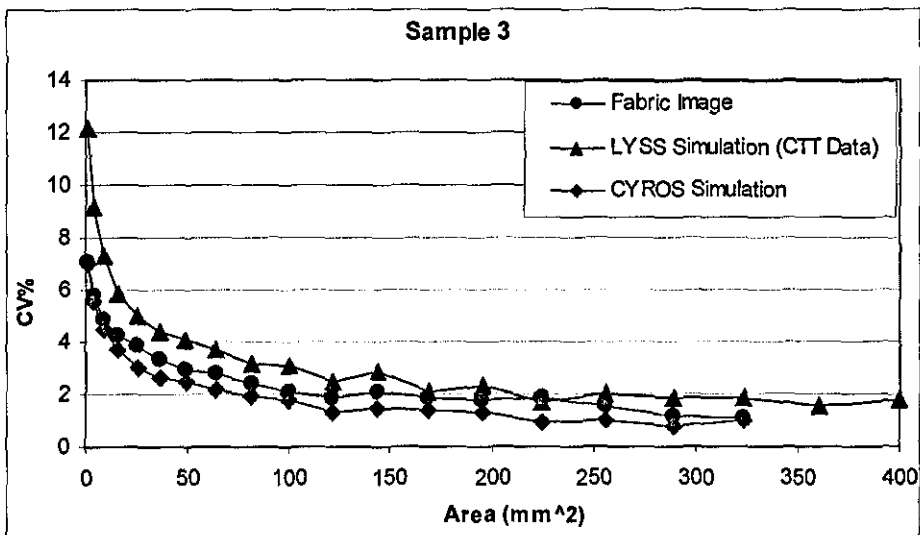
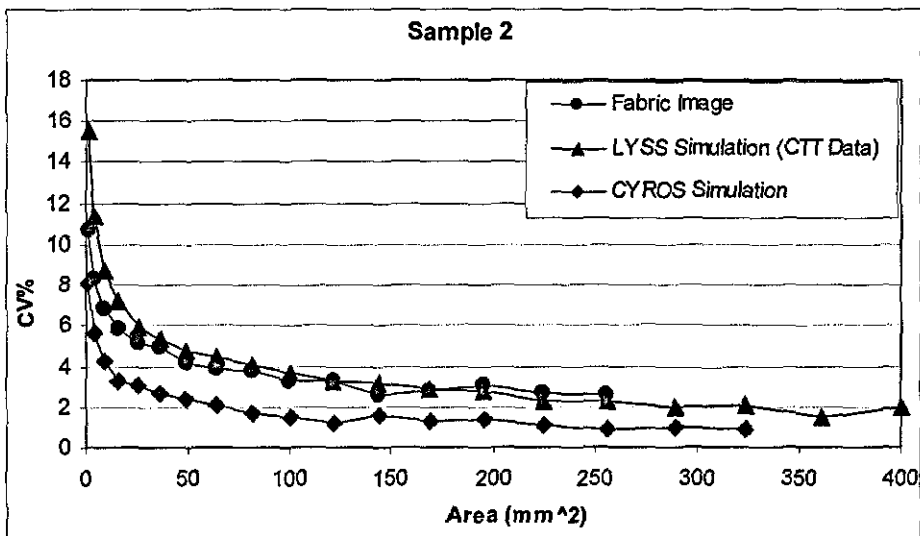
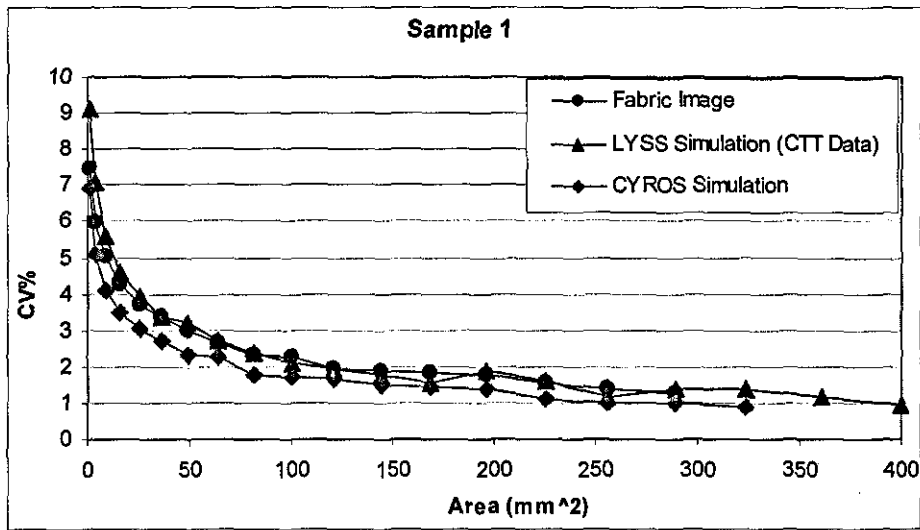


Figure 9-10 Left: Simulation from LYSS using CYROS data (Sample 2); Right CYROS simulation using the same data

9.5 Variance-Area Curves

A program is written that calculates the CV% values between the average intensities found within certain areas in a fabric image. When these CV% values are plotted against the areas, the so called B(A) curves (Variation between areas) can be obtained. The areas considered in the calculations are 1, 4, 9, 16, 25, 36, 49, 64, 81, 100, 121, 144, 169, 196, 225, 289, 324, 361 and 400 mm² all with square shape. The B(A) curves are calculated for 5 yarn samples from the actual fabric images as well

as LYSS and CYROS fabric simulations. No pre-processing is applied to the fabric images before calculating the $B(A)$ curves. The LYSS simulations are generated using CTT data. The $B(A)$ curves obtained from these different images are compared in Figure 9-11. It can be seen that the LYSS simulations using CTT data exhibits a better agreement with the fabric images than the CYROS simulations do, which always exhibits smaller CV% values. For sample 3, the CV% values from the fabric image appear to be lower than the LYSS CV% values. This is probably due to the effect of hairiness on the appearance which reduces the surface intensity variations as will be seen in the next section. For sample 4, the $B(A)$ curve cannot be predicted accurately from the simulations. It appears that the rapidity of approach to $B(\infty)$ is similar for both the LYSS simulation and the actual picture, however, the $B(\infty)$ asymptote value is lower for the simulation. This might be due to some long term variations within the fabric arising from the knitting process and not depending on the yarn irregularity.



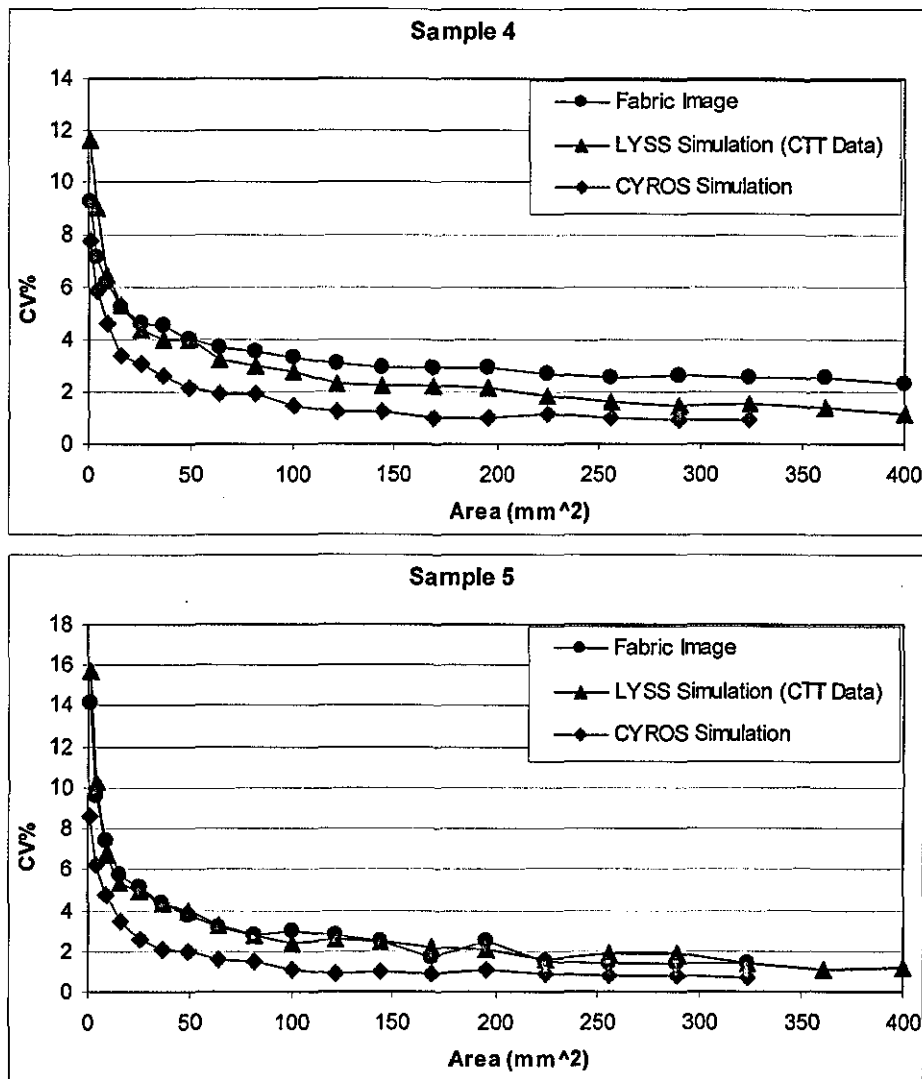


Figure 9-11 Comparison of B(A) curves obtained from actual yarn images, LYSS simulations using CTT and CYROS yarn data and CYROS simulations for 5 yarn samples

9.5.1 Effect of hairiness on B(A) curves

The effect of hairiness on B(A) curves is investigated on simulations generated using the hairiness and diameter data from two different yarn samples tested on LYSS. The diameter and total hairiness values along with the diameter and hairiness variations are listed in Table 9-2. These two samples are chosen deliberately for they have the same average diameter but different hairiness values. For both samples, knitting simulations are created with and without using the hairiness data. Figure 9-12 shows

1 inch² portions from these simulations. For both fabrics, the vertical and horizontal densities are 15 and 18 loops/inch respectively.

Table 9-2 The properties of two samples for investigation of (B(A) curves

Sample #	Diameter (μm)	CVd 1mm	THW-CV	THW
29	360	9.15	20.27	2.67
33	360	14.73	34.44	3.93

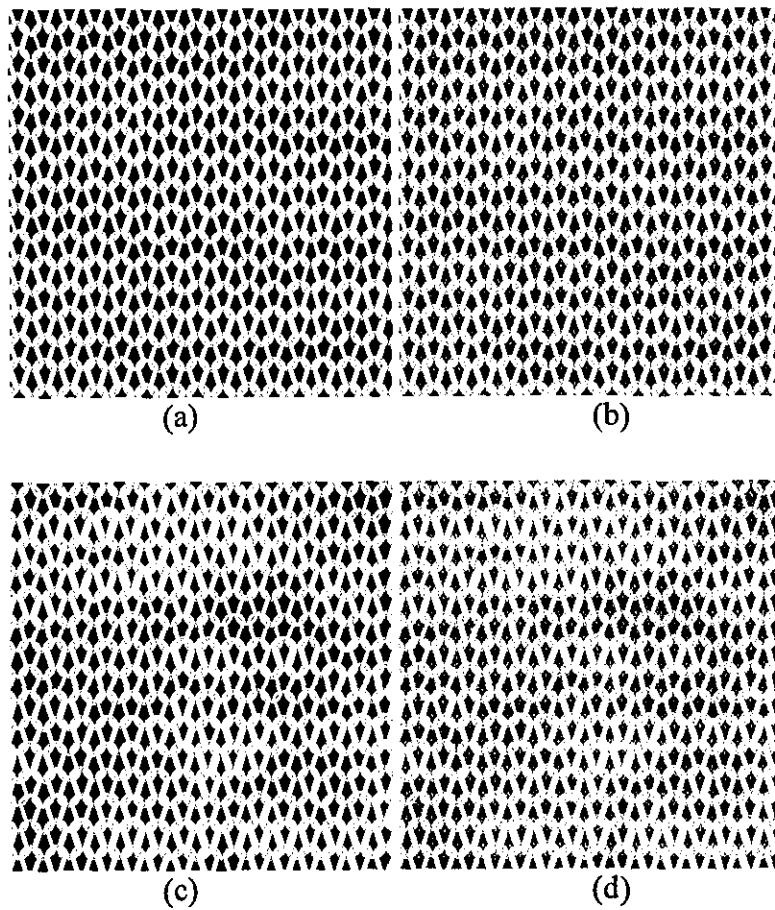


Figure 9-12 The fabric simulations with (a) and without (b) hairiness data for sample 29. (c) and (d) are the simulations for sample 33.

Figure 9-13 shows the B(A) curves obtained from these simulations. It can be seen that for both samples the hairiness effect decreases the overall variation in the fabric simulations. This decrease in the overall variation appears to be proportional to the total hairiness of the yarn; for sample 29 that has a lower THw value, the variations differ only slightly between simulations with and without using the hairiness data, while for sample 33 which has a higher hairiness index, the hairiness has a significant effect on B(A) curves.

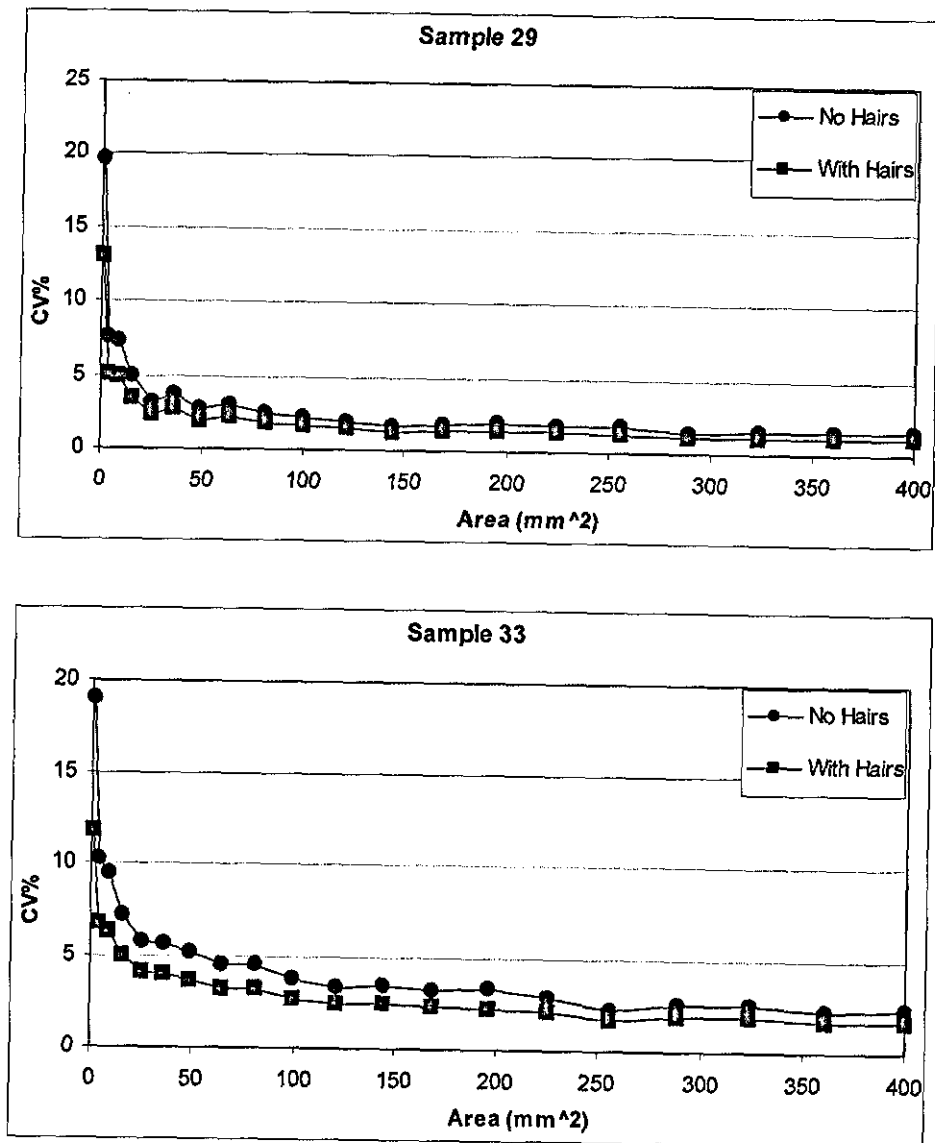


Figure 9-13 Comparison of B(A) curves obtained from simulations with and without hairiness data for two yarn samples.

9.6 Summary and Conclusions

Algorithms to generate 2D yarn board and knitting simulations are introduced. It is shown that the diameter data alone is not adequate to generate realistic simulations due to the effect of hairiness on appearance. An iterative algorithm is demonstrated that uses the hairiness data and Hair Density Distribution Profiles obtained from LYSS. The method is incorporated in both yarn board and knitting simulations.

An algorithm is developed to calculate the variance-area curves from fabric images. The diameter data of five different yarn samples are obtained from a CYROS system and Jasper's yarn scanning system attached to a Lawson Hemphill CTT. Single jersey fabrics are knitted on a Lawson Hemphill FAK and compared with the simulations obtained from CYROS and LYSS. The CYROS simulations appear to be in a better agreement with the actual fabric images in terms of reflecting the variation on the fabric visually. However, the loop geometry is found to be represented better on LYSS simulations. Furthermore, the B(A) curves obtained from the actual fabric images exhibited a better agreement with the curves from the LYSS simulations.

The effect of hairiness on variance-area curves is investigated and the hairiness is found to decrease the variation in fabric appearance.

CHAPTER 10 - Summary of Conclusions

The thesis first explored the factors affecting the yarn image quality. The front-lit and back-lit illuminations are theoretically modelled and investigated in detail. It is seen that under front-lit illumination, the defocus aberration creates a very significant problem widening the observed diameter and decreasing the contrast. Possible improvements on depth of field are discussed regarding the light and lens characteristics, however no method is found to be able to provide the required depth of field to detect the hairs. The back-lit illumination is found to be superior to front-lit illumination in terms of defocus tolerance. The effects of size of the light source and its distance from the yarn are investigated for back-lit illumination. It is seen that moving the light away from the yarn increased the defocusing characteristics, however this improvement was only negligible after around 500mm and significant fringe patterns occurred further from that distance. It is also observed that a chromatic light source could be advantageous over a monochromatic one in terms of the decreasing amplitude of fringes appearing in the images. The size of the light source is found to be very important and it is seen that the contrast of a defocused fibre in the image can rapidly decrease as the size of the light source is increased. The effects of other aberrations such as off-axis displacement in back-lit illumination, spherical aberration and chromatic aberration are found negligible for the imaging system used in this research.

Three different illumination arrangements are tested for back-lit illumination. Placing the light source simply behind the yarn with no additional optical elements is found superior in terms of contrast and depth of field. However, the effective field of view was limited with the aperture size in this method and a minimum aperture size of $F/2.6$ is found necessary to achieve the maximum field of view allowed by the CCD

array. The lens used for the experiments provided 21mm field of view with its maximum available aperture size of F/3.5. Tungsten filament bulbs are found superior compared to LED light sources considering the minimum exposure times achievable, which depends on the intensity of the light source. A field lens in order to improve the field of view is employed but at the expense of degradation in image background quality and loss in depth of field, hence not found suitable. A diffuser is also tested to increase the field of view but the image quality was below desirable limits. A mirror placed at 45° to the camera axis behind the yarn is employed to image the yarn from two orthogonal views. The optical path difference problem between two orthogonal views is addressed, but found negligible for a centre to centre distance of 1.4mm. Dark field illumination is found to be very successful in terms of highlighting the boundaries between the core and surface hairs; however, it was strongly affected by the fibre colour.

For yarn surface inspection, a back-lit and front-lit illumination hybrid is found to be more suitable compared to front-lit illumination alone. It is seen that a coherent light source used for back-lit illumination provided a better contrast compared to incoherent light sources, which would enable a more accurate determination of diameter. For front-lit illumination, projecting the light from an angle rather than perpendicular to the yarn surface enables a better definition of yarn surface. However, front-lit illumination parameters such as the wavelength of the light source and the suitable projection angle should be studied further.

Various image processing algorithms are developed for back-lit yarn images. Contrast enhancement using convolution filters is found to be very useful in terms of identifying the isolated background pixels between hairs. However, convolution filters meant a significant increase in processing time. Two other methods for separation of background in yarn images are described one based on differentiating the successive maxima and minima in every row and the other on an adaptive thresholding method based on the image histogram. The first algorithm provided a fast and adaptive nature but was seriously affected by salt type noise and diffraction

fringes. The second algorithm is found to be very suitable in terms of speed and reliability.

For core-hair separation, two methods one based on morphological filtering and the other on core edge tracking are described. A filtering process is introduced to be used with the latter algorithm to avoid the surface hairs from creating an artificial increase in diameter. Both methods exhibited close results when the number of extracted hair pixels are compared, hence the second algorithm is preferred due to its speed.

In order to estimate the total hairiness an algorithm is studied that aims to track and extract the chain codes of every single hair, however due to the complexity of the hairs at the vicinity of the core, the technique is not found feasible. A method called "Bit Quads" to calculate the total hair length from the skeletonised yarn images is described. A perfect correlation is observed between the total number of hair pixels and the hair lengths obtained using the "Bit Quads" method, which suggested that the number of hair pixels could be used as a measure of total hair length regardless from the fibre width, at least for the range of samples tested.

An image analysis technique is demonstrated to simulate photo electric sensors used for counting the number of hairs at fixed distances from the core. Effects of parameters such as the dimensions of the sensor, signal threshold level and the zero reference point on the measurements are investigated. It is found that a sensor resolution of 0.5mm x 0.5mm would not be adequate to distinguish between N1 hair count values of different yarns. The need for a very high precision in determining the zero reference point is also addressed. It is observed that with appropriate sensor parameters, the computer vision technique can be very successful in simulating Zweigle G565 Hairiness Tester.

Various indices are given to describe total hairiness. The developed total hairiness indices almost perfectly agreed with Uster Tester's H index for grey cotton-cotton/polyester samples, however, colour or different blends appeared to decrease

this correlation. This is believed to be due to the fact that colour and material can affect the measurements on Uster Tester while such yarn characteristics have no effect on back-lit images. The total hairiness indices obtained from dark field images exhibited a better correlation with a very small offset when compared to the Uster Tester's H index than similar indices obtained from back-lit images. The hairiness index found by integrating the grey levels agreed with Uster H Index slightly better than the one found from the number of hair pixels. The CV% values calculated for 1cm sampling length also agreed very well with UT3 CVh% exhibiting measurements with the same order of value. However, the CV% values obtained from dark field images exhibited lower values.

A new method to describe the hairiness named Hair Density Distribution Profile (HDDP) is introduced that provides information on both short and long hair hairiness. It is found that the long hairiness content within the profile agreed very well with the hair counts measurement in terms of the nature of the distribution according to the distance from the core. Short hair hairiness is found not to be correlated with long hair hairiness, which suggested that long hair hairiness, as measured on Zweigle G565 for example, cannot describe the overall hairiness of a yarn accurately.

Two different low aspect ratio classes are tested against AR 1:1. Aspect ratios lower than 1:4.9 are not found suitable for hairiness measurement, in other terms, the scanning resolution for hairiness evaluation should not be less than 14 scans per mm.

The diameter and irregularity measurements using back-lit images are found to be in very good agreement with CYROS tester. The dark field diameters exhibited lower diameters, but still exhibiting an almost perfect correlation with CYROS. However, the irregularity values from dark field images did not agree with back-lit irregularity values.

The squares of yarn diameters exhibited a very good correlation with direct yarn counts for 100% cotton samples. For the same set of samples CVd% values obtained for 8mm sampling length agreed reasonably well with UT3 CVm% values. The average elliptical diameters were found to be almost the same as the diameters from one view. However, the former exhibited lower CV% values which correlated better with CVm% values. The theoretical relation between CVd% for 2mm sampling length and CVm% for 8mm sampling length could not be verified and the latter is found to be only 1.13 times the former at average although the theory suggests this ratio to be 2.

The aspect ratios as low as 1:11.3 are found quite reliable in terms of measuring diameter and diametric irregularity. The results suggested that aspect ratios even lower than this can provide almost the same accuracy as 1:1 aspect ratio.

Statistical evaluation techniques such as variance-length curves and autocorrelation function are implemented and demonstrated on various yarn samples. A new method to visualize the irregularity of a yarn called "variation plots" is introduced. It is shown that different samples having the same CV% values but are different in nature of variation, i.e. short term or long term, can be differentiated successfully by means of variation plots. The number of thin and thick places could also be calculated from variation plots using simple image processing techniques.

To measure the yarn twist, spatial and frequency domain analysis methods are developed. A hybrid method involving frequency domain filtering followed by spatial analysis is found to be very accurate. However, the results suggested that the definition of yarn diameter from high magnification front-lit images was problematic. A hybrid of front-lit and back-lit illuminations is believed to be more promising in this respect.

Algorithms to generate 2D yarn board and knitting simulations are introduced. It is shown that the diameter data alone is not adequate to generate realistic simulations

due to the effect of hairiness on appearance. An iterative algorithm is demonstrated that uses the hairiness data and Hair Density Distribution Profiles obtained from LYSS. The method is incorporated in both yarn board and knitting simulations. The knitting simulations are found quite successful in reflecting the loop geometry. The variance area curves obtained from simulations were also in good agreement with the curves obtained from real fabric images. The effect of hairiness on variance-area curves is investigated and the hairiness is found to decrease the variation in fabric appearance.

CHAPTER 11 - Suggestions for Further Work

It should be of significant interest to researchers to study estimation of yarn density using laser transmission as implemented by Riddle and Davis [2000]. However, a laser source with lower wavelength as opposed to 633nm He-Ne laser they used would probably be more suitable since cotton exhibits high absorption characteristics at that wavelength. If this can be implemented successfully, twist could also be estimated using diameter and density information.

The Hair Density Distribution Profiles developed during this work should also be studied further. A mathematical model can be established in the future that account for defocusing in order to estimate the three dimensional distribution of hairs around the core. This might help to compensate for the information loss in especially front-lit illumination due to defocusing.

The filtering algorithm applied for core-hair separation enabled very good correlations with commercial testers such as CYROS and UT3. However, it should be studied further in the future in order to establish a more sophisticated model that accounts for yarn faults such as neps.

A number of illumination techniques for high magnification imaging are described in Chapter 4 and image processing algorithms to measure the twist from front-lit images are described in Chapter 7. However, the diameter measurements from these images are not found quite accurate when compared to back lit diameters. There is also a need for an enhanced front-lit illumination technique to highlight the surface details in a better manner. It can be expected to improve the surface contrast using a low angle ring light, which is commonly used in some machine vision applications

for detecting surface details and defects such as scratches on surfaces, and raised/embossed characters on products. Figure 11-1 shows a conceptual design which aims a good background-yarn contrast for accurate diameter measurement using coherent back-lit illumination as well as good surface details with the help of low angle ring light system. The ring light should be selected with the minimum wavelength possible in order to improve the depth of field. The back light on the other hand should be selected with a very different wavelength from the ring light so that its intensity can be reduced using a gelatine filter with the same colour as the front light in order not to attenuate the intensity of the reflected light.

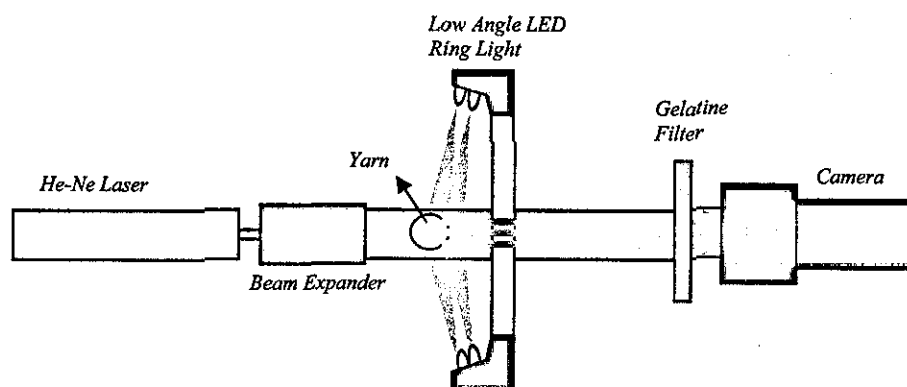


Figure 11-1 Conceptual design for yarn surface imaging

Using the relations between linear density, diameter and twist, the mass variation in yarns can be estimated. Although being maybe the most interesting aspect of yarn twist measurement using computer vision, this subject is left here as a suggestion for future work because of the scope of the project.

Both image processing algorithms described for twist measurement are only applicable for off-line yarn testing since the processing speeds are far below the yarn production speeds even if a very fast PC were employed. It would be interesting in the future to investigate if the frequency domain analysis method could be

implemented purely in optical means using lenses performing optical fourier transformation and real frequency masks for filtering.

Yarn board and knitting simulation algorithms as well as calculation of variance-area curves are demonstrated in Chapter 8. It might be interesting in the future to improve the knitting simulation algorithm to simulate different knitting patterns as well as multi feeder knitting machines. This might lead investigation of the effects of the irregularity variation among the yarn packages knitted in the same fabric. The hair density distribution profiles are applied in the simulations as they are measured on the yarns, however, it will be necessary in the future to take the effects of knitting process and post treatments such as shrinkage on the hair density distribution into account. It is believed that HDDP can effectively be adapted to such calculations.

APPENDIX A – Custom C Functions

This Appendix describes the inputs, outputs and tasks of some of the custom C functions developed during this research. The functions are compiled under “CFunctions” library and can be accessed from Wit igraphs as Wit operators. The functions are listed in alphabetical order.

11.1 *abutalebThreshold.c*

```
operator abutalebThreshold
{
input CorImage "in" (0,20);
output CorImage "out" (60,20);
}
```

This function performs a thresholding operation on an input image using Abutaleb’s [1986] method (see Section 5.4.1.4.2.4)

11.2 *applyHistoMap.c*

```
operator applyHistoMap
{
input CorImage "in" (0,10);
input uint8[] "map" (0,30);
output CorImage "out" (60,20);
}
```

This function takes an input image and applies a gray scale map given in the “map” array. The gray levels corresponding to the index of each element in the “map” array is converted into the value of the element in the output image.

11.3 *array2file*

```
operator array2file
{
input sync "Trigger" (0,20);
output CorImage "visual" (60,0);
output CorImage "out" (60,20);
output double[] "autocor" (60,40);
}
```

```

param file "filename";
param int "range"=20;
param file "outfile";
param int "corelogram" <choice "yes", "no">;
depend "outfile" : "corelogram"=="yes";

}

```

This function reads the hairiness or the diameter data from a given file and generates the variation plots explained in Section 7.4.3. The data is plotted on an unsigned 8 bit image, where the values falling into the range defined as “mean value±range%” are assigned gray levels between 0 and 255. If the “corelogram” option is selected the correlogram is calculated from the input data and written to an output file given as “outfile”.

11.4 backLit.c

```

operator backLit
{
input CorImage "in" (0,20);
output CorImage "out" (60,20);

param int "ImageW"=1500;
param int "ImageH"=300;
param int "pitch"=14;
param double "amplifier"=1;

param double "dlight"=900;
param double "dscreen"=200;
param double "flens"=100;
param double "FNumber"=3.5;

param int "customprofile" <choice "yes", "no">;
param double "lwidth"=4;
depend "lwidth" : "customprofile"=="yes";
param int "Gaussian" <choice "yes", "no">;
depend "Gaussian" : "customprofile"=="yes";

param int "fibrepresent" <choice "yes", "no">;
param double "dfibre"=200;
param double "wfibre"=45;
param double "hfibre"=0;
depend "dfibre" : "fibrepresent"=="yes";
depend "wfibre" : "fibrepresent"=="yes";
depend "hfibre" : "fibrepresent"=="yes";

param int "fieldlens" <choice "yes", "no">;

```

```
param double "dfieldlens"=786;
param double "ffieldlens"=100;
depend "dfieldlens" : "fieldlens"=="yes";
depend "ffieldlens" : "fieldlens"=="yes";
}
```

This function simulates the image of a fiber under back-lit illumination using geometrical approach.

11.5 backThreshold.c

```
operator backThreshold
{
input CorImage "in" (0,20);
output CorImage "out" (60,20);
param int "threshold";
}
```

This function takes an unsigned 8-bit input image and changes the gray levels above the given "threshold" value to 255.

11.6 bernsenThreshold.c

```
operator bernsenThreshold
{
input CorImage "in" (0,20);
output CorImage "out" (60,20);
output CorImage "TSurface" (60,40);
param int "framesize"=15;
param double "L"=1.5;
}
```

This function performs a thresholding operation on an input image using Bernsen's [1986] method (see Section 5.4.1.4.3.3)

11.7 BitQuads.c

```
operator BitQuads
{
input CorImage "in" (0,20);
output double "area" (60,10);
output double "perimeter" (60,30);
}
```

This function calculates the areas and the perimeters in a binary image using the BitQuads technique described in Section 5.4.5.2.

11.8 *cardBoard.c*

```

operator cardBoard
{
input sync "in" (0,20);
output CorImage "out" (60,20);
param CorFile "coredatafile"="coredata.xls";
param int "SamplingLength"=1000;

param int "ImageDPI"=300;
param double "width"=3;
param double "height"=3;
param double "spacingmm"=1;
param int "haireffect" <choice "yes", "no">;

param CorFile "hairdatafile"="hairdata.xls";
param CorFile "hairdistfile"="hairdist.xls";
param int "HairinessSampling"=10000;
param int "DensityRes"=14;

depend "hairdatafile" : "haireffect"=="yes";
depend "hairdistfile" : "haireffect"=="yes";
depend "HairinessSampling" : "haireffect"=="yes";
depend "DensityRes" : "haireffect"=="yes";
}

```

This function generates a cardboard simulation discussed in Section 9.3 at a given resolution using the given core data, hair data and HDDP files. The “width” and the “height” define the size of the output image in inches and the “spacingmm” parameter defines the vertical gap between yarns in mm.

11.9 *cyros2Image.c*

```

operator cyros2Image
{
input Sync "in" (0,20);
output CorImage "out" (60,10);
output String "info" (60,30);
param File "infile";
param int "width"=512;
param int "height"=512;
}

```

This function reads the data from CYROS files, displays the file info stored on the file header and converts the test data to an unsigned 8-bit image.

11.10 *Diffedge.c*

```
operator diffedge
{
input CorImage "in" (0,20);
output CorImage "out" (60,20);

param int "operation" <choice "subtract", "add">;
param int "threshold" <choice "yes", "no">;
param int "T"=0;
depend "T":"threshold"=="yes";
}
```

This function applies the convolution filter to an input image as described in Section 5.4.1.1. If the “threshold” option is selected the pixels with gray levels below “T” are omitted.

11.11 *enhanceVector.c*

```
operator enhanceVector
{
    input uint8[] "in" (0,20);
    output uint8[] "out" (60,20);
    param int "threshold";
}
```

This function differentiates the successive maxima and minima in an input array and if the difference is below a threshold value, assigns the average value to all pixels between a given maximum and minimum.

11.12 *findThresholds.c*

```
operator findThresholds
{
input CorImage "in" (0,20);

output CorImage "Threshold1" (60,10);
output CorImage "Threshold2" (60,20);
output int "center" (60,30);
output int "ssize" (60,40);

param int "histThresh";
}
```

This function finds and applies the two threshold values described in Section 5.4.1.2. The core center coordinate and the structuring element size to be used with the morphological filtering explained in Section 5.4.2.1 are also produced.

11.13 *fresnel.c*

```
operator fresnel
{

input CorImage "in" (0,20);
output CorImage "out" (60,20);

param int "W"=600;
param int "H"=30;

param int "Wave" <choice "plane", "spherical">;
param double "ro"=500;
param double "r"=10;
depend "ro" : "Wave"=="spherical";

param double "lambda"=670;
param int "pointsource" <choice "yes", "no">;
depend "pointsource" : "Wave"=="spherical";

param double "pitch"=1;
param double "width"=45;

param CorFile "F1"="f1.txt";
param CorFile "F2"="f2.txt";

}
```

This function generates the diffraction simulation discussed in Section 4.6.2. The Fresnel integrals are read from external files given as “F1” and “F2”.

11.14 *horizontalTrack2.c*

```
operator horizontalTrack2
{
input CorImage "in" (0,20);

output CorImage "out" (60,10);
output int[] "nofhairspxls" (60,20);
output int[] "nofcorepxls" (60,30);

output int[] "upperintersections" (40,40);
output int[] "lowerintersections" (50,40);
output int[] "upperareas" (40,0);
```

```
output int[] "lowerareas" (50,0);
```

```
param int "pixelspermm";
param int "slopthreshold";
param int "imagethreshold";
param int "minimumgap";
param int "zwlenthickness"=1;
param int "aspect_ratio" = 1;
param int "nof_zones" = 1;
param int "reduction"=2;
}
```

This function processes a back-lit yarn image using the maxima-minima differentiation technique described in Section 5.4.1.3. The number of core and hair pixels as well as the hair counts and hair areas at various distances are calculated.

11.15 *integrateColumns.c*

```
operator integrateColumns
{
input CorImage "in" (0,20);
output CorPoint[] "sums" (60,20);
param uchar "Threshold"=20;
}
```

This function calculates the projection of an image to the X axis. The intensities below the "Threshold" value are omitted.

11.16 *kapurThreshold.c*

```
operator kapurThreshold
{
input CorImage "in" (0,20);
output CorImage "out" (60,10);
output uchar "Topt" (60,30);
}
```

This function performs a thresholding operation on an input image using Kapur et.al.'s [1985] method (see Section 5.4.1.4.2.3)

11.17 *kitlerThreshold.c*

```
operator kitlerThreshold
```

```

{
input CorImage "in" (0,20);
output CorImage "out" (60,20);
output int "Threshold" (60,40);
}

```

This function performs a thresholding operation on an input image using Kittler & Illingworth's [1986] method (see Section 5.4.1.4.2.2)

11.18 *knitSimHairiness.c*

```

operator knitSimHairiness
{
input Sync "in" (0,20);
output CorImage "out" (60,20);

param CorFile "coredatafile"="coredata.xls";
param int "SamplingLength"=1000;

param int "StitchLength"=1358;
param int "VerDensity"=20;
param int "HorDensity"=20;
param int "noofneedles"=220;
param int "CropWales"=20;
param int "CropWefts"=20;
param int "ImageDPI"=450;

param int "plotdiameters" <choice "yes", "no">;
param int "haireffect" <choice "yes", "no">;
param CorFile "hairdatafile"="hairdata.xls";
param CorFile "hairdistfile"="hairdist.xls";
param int "HairinessSampling"=10000;
param int "DensityRes"=14;

depend "hairdatafile" : "haireffect"=="yes";
depend "hairdistfile" : "haireffect"=="yes";
depend "HairinessSampling" : "haireffect"=="yes";
depend "DensityRes" : "haireffect"=="yes";
}

```

This function generates the knitting simulations described in Section 9.4 at a given resolution using the given core data, hairiness data and HDDP files.

11.19 *linescan.c*

```

operator linescan
{
input CorImage "in" (0,20);

```

```

output CorImage "out" (60,20);

param double "inpitch"=1;
param double "p"=14;
param double "xe"=14;
param double "AR"=1;

}

```

This function simulates the effects of digitization and yarn motion.

11.20 *logline.c*

```

operator logline
{
input int "current" (0,0);

input int[] "upperintersections" (0,10);
input int[] "lowerintersections" (0,20);
input int[] "corepixels" (0,30);
input int[] "hairpixels" (0,40);

output string "info" (60,0);
output CorImage "out" (60,20);
output CorImage "graf" (60,30);

param int "noz"=12;
param int "N" = 5000;
param int "ntocol" =1;
param int "sampling"=10;
}

```

This function takes the number of hair intersections from the photoelectric sensor simulation and generates an image showing the number of intersections on a logarithmic scale as a bar-chart.

11.21 *MaskFourier.c*

```

operator MaskFourier
{
input CorImage "in" (0,20);
output CorImage "out" (60,10);
output CorImage "out2" (60,20);
output float[] "angles" (60,30);
output String "Twist" (60,40);

param int "diameter";
param int "diameter2";
param int "thickness";
}

```

}
 This function takes the magnitude, phase, real or imaginery component of the FFT of an image and applies the mask mentioned in Section 8.5. It also integrates the angular sections and gives the integrations for each angle in the “angles” array.

11.22 *mergeImages.c*

```
operator mergeImages
{
input CorImage "in1" (0,10);
input CorImage "in2" (0,20);
input CorImage "in3" (0,30);

output CorImage "out" (60,20);

param uchar "level1"=200;
param uchar "level2"=100;
param uchar "level3"=50;
```

}
 This function takes three images and calculates a weighed average according to the “level” variables. This was used to convert RGB images into grayscale in a custom way.

11.23 *mergeMaxs.c*

```
operator mergeMaxs
{
input uint8[] "in" (0,20);
output uint8[] "out" (60,20);
param int "threshold";
}
```

This function smoothes a vector by assigning an average value to the pixels between two maximum points if the sum of differences between these maxima and the minimum in between them is below a given threshold.

11.24 *niblackThreshold.c*

```
operator niblackThreshold
```

```

{
input CorImage "in" (0,20);
output CorImage "out" (60,20);
output CorImage "TSurface" (60,40);
param int "framesize"=15;
param double "k"=1.3;
}

```

This function performs a thresholding operation on an input image using Niblack's [1986] method (see Section 5.4.1.4.3.1)

11.25 *otsuThreshold.c*

```

operator otsuThreshold
{
input CorImage "in" (0,20);
output CorImage "out" (60,20);
output int "Threshold" (60,40);
}

```

This function performs a thresholding operation on an input image using Otsu's [1979] method (see Section 5.4.1.4.2.1)

11.26 *remove_ghost.c*

```

operator remove_ghost
{
input CorImage "yanowitz" (0,10);
input CorImage "original" (0,20);
input CorImage "filtered" (0,30);
input CorImage "sobel" (0,40);
output CorImage "out" (60,20);
param int "val_step_threshold"=1;
}

```

This function performs the postprocessing step of Yanowitz & Bruckstein [1989], used to remove the misidentified background objects (see Section 5.4.1.4.3.4).

11.27 *sauvolaThreshold.c*

```

operator sauvolaThreshold
{
input CorImage "in" (0,20);
output CorImage "out" (60,20);
output CorImage "TSurface" (60,40);
}

```

```

param int "framesize"=5;
param double "k"=0.5;
param int "R"=128;
}

```

This function performs a thresholding operation on an input image using Sauvola & Pietaksinen's [2000] method (see Section 5.4.1.4.3.2)

11.28 *processYarn.c*

```

operator processYarn
{
input CorImage "in" (0,20);
output CorImage "out" (60,5);
output uchar "T1" (60,15);
output uchar "T2" (60,25);
output String "info" (60,35);
output int "done" (50,40);
param int "singlefile" <choice "yes", "no">;
param int "initialize" <choice "yes", "no">;
param int "ntocol"=1000;
param CorFile "filename"="yarn.xls";
param int "AspectRatio"=1358;
param int "NofZones"=20;
param int "imagereduction"=2;
param int "AutoThreshold" <choice "yes", "no">;
param uchar "Threshold1";
param uchar "Threshold2";
param int "CalcZweigle" <choice "yes", "no">;
param int "sensorW"=500;
param int "sensorH"=500;
param int "BQuads" <choice "yes", "no">;
depend "initialize" : "singlefile"=="no";
depend "ntocol" : "singlefile"=="no";
depend "filename" : "singlefile"=="no";
depend "Threshold1" : "AutoThreshold"=="no";
depend "Threshold2" : "AutoThreshold"=="no";
depend "sensorW" : "CalcZweigle"=="yes";
depend "sensorH" : "CalcZweigle"=="yes";
}

```

This function processes an input unsigned 8-bit back-lit yarn image using the techniques described in Sections 5.4.1.2 and 5.4.2.2. The photo-electric sensor simulation can also be performed optionally. The function can process a single image or multiple images. In the latter case, the data is stored in static variables and the average values are displayed in real time. The test data and the statistics are also stored in a tab delimited text file at the end of each test. These static variables have to be initialized at the beginning of the test. The processed image can be generated at a

reduced size to save time when displaying in real time. The CV% values are calculated for upto 20 different lengths at the same time. The two threshold levels can be calculated automatically from the image histogram or entered manually.

11.29 *processYarnDrkFld.c*

```
operator processYarnDrkFld
{
input CorImage "in" (0,20);
output CorImage "out" (60,5);
output uchar "T1" (60,15);
output uchar "T2" (60,25);
output String "info" (60,35);
output int "done" (50,40);
param int "singlefile" <choice "yes", "no">;
param int "initialize" <choice "yes", "no">;
param int "ntocol"=1000;
param CorFile "filename"="yarn.xls";
param int "AspectRatio"=1358;
param int "NofZones"=20;
param int "imagereduction"=2;
param int "AutoThreshold" <choice "yes", "no">;
param uchar "Threshold1";
param uchar "Threshold2";
param int "CalcZweigle" <choice "yes", "no">;
param int "sensorW"=500;
param int "sensorH"=500;
param int "BQuads" <choice "yes", "no">;
depend "initialize" : "singlefile"=="no";
depend "ntocol" : "singlefile"=="no";
depend "filename" : "singlefile"=="no";
depend "Threshold1" : "AutoThreshold"=="no";
depend "Threshold2" : "AutoThreshold"=="no";
depend "sensorW" : "CalcZweigle"=="yes";
depend "sensorH" : "CalcZweigle"=="yes";
}
```

This function is similar to *processYarn.c* but works on dark field images using the technique described in Section 5.4.3.

11.30 *processYarnTwoOrtho.c*

```
operator processYarnTwoOrtho
{
input CorImage "in" (0,20);
output CorImage "out" (60,5);
output uchar "T1" (60,15);
```

```

output uchar "T2" (60,25);
output String "info" (60,35);
output int "done" (50,40);
param int "singlefile" <choice "yes", "no">;
param int "initialize" <choice "yes", "no">;
param int "ntocol"=1000;
param CorFile "filename"="yarn.xls";
param int "AspectRatio"=10000;
param int "NofZones"=20;
param int "imagereduction"=2;
param int "AutoThreshold" <choice "yes", "no">;
param uchar "Threshold1";
param uchar "Threshold2";
param int "BQuads" <choice "yes", "no">;
depend "initialize" : "singlefile"=="no";
depend "ntocol" : "singlefile"=="no";
depend "filename" : "singlefile"=="no";
depend "Threshold1" : "AutoThreshold"=="no";
depend "Threshold2" : "AutoThreshold"=="no";
}

```

This function is again similar to `processYarn.c` but works on images with two orthogonal views using the technique described in Section 5.4.4. The hairiness is not calculated in this function.

11.31 *reduce2Mins.c*

```

operator reduce2Mins
{
input CorImage "in" (0,20);
output CorImage "out" (60,20);

param int "width"=5;
param int "height"=5;
}

```

This function takes the minimum intensities from portions with a given width and height and assigns to a new image that is the reduced version of the original image by `width*height`. This function was designed to decrease the size of a yarn image without losing the hairs.

11.32 *spoke.c*

```

operator spoke
{
input Sync "in" (0,20);

```

```
output CorImage "out" (60,20);

param int "W"=512;
param int "H"=512;
param double "angle"=7.5;

}
```

This function generates a spoke target image with given width, height and angular spacing for the analysis in Section 4.8.

11.33 *trackFiber.c*

```
operator trackFiber
{
input uint8[] "in" (0,0);
input int[][] "hairsy1" (0,10);
input int[][] "hairsy2" (0,20);
input int[] "hairslastelement" (0,30);
input int "noh" (0,40);

input int[] "hairsfirstx" (20,0);
input int[] "hairslastx" (40,0);
input int "line" (20,40);

input int[] "newnoh" (40,40);

output uint8[] "out" (60,20);

param int "threshold";
param int "aspectratio";
}
```

This function performs the fiber tracking algorithm explained in Section 5.4.5.1.

11.34 *VACurve.c*

```
operator VACurve
{
input CorImage "in" (0,20);
output CorPoint[] "CVs" (60,20);
param CorFile "filename"="fabricVA.xls";

param int "ImageDPI";
}
```

This function calculates the variance-area curve of an input image at given resolution and writes the values to an output file.

11.35 *yanowitzThreshold.c*

```
operator yanowitzThreshold
{
input CorImage "in" (0,10);
input CorImage "filtered" (0,30);
input CorImage "edges" (0,40);
output CorImage "out" (60,20);
output CorImage "TSurface" (60,40);
param int "threshold"=0;
param double "beta"=1.5;
param int "max_iterations"=1000;
}
```

This function performs a thresholding operation on an input image using Yanowitz & Bruckstein's [1989] method (see Section 5.4.1.4.3.4).

References

1. Abutaleb A. S. (1989) Automatic thresholding of gray-level pictures using two-dimensional entropy, Computer Vision, Graphics, and Image Processing, vol 47, pp 22-32.
2. Alagha, M. J., Oxenham, W., & Iype, C. (1994). The use of an image analysis technique for structural parameters of friction spun yarns. J. Text. Inst., 85 (3), 383-388.
3. Aminuddin, N., Riddle, E., (1999). Comparison Between Zellweger Uster II and Micro Sensor Inc.'s On-Line Density Tester, EFS System Research Forum November 4-5, 1999, Raleigh, NC. pp.21
4. Anbarasan, M, Upadhayaya, M.B., and Balasubramaniam, V. (2003) " Fibre and yarn property influences on fabric "Barre" Part-I. Influence of yarn hairiness and twist. Premier-1 Newsletters, October 2003. (Available on line at <http://www.premier-1.com>)
5. Barella, A. (1956). New concepts of yarn hairiness. J. Text. Inst., 47 (2), P120-127.
6. Barella, A. (1957). Yarn hairiness: the influence of twist. J. Text. Inst., 48 (4), P268-280.
7. Barella, A. (1966). The hairiness of yarns: a review of the literature and a survey of the present position. J. Text. Inst., 57 (10), T461-489.
8. Barella, A. (1971). The nature of the hairiness of open-end spun yarns. J. Text. Inst. 62 (12), 702-706.
9. Barella, A. (1993). The hairiness of yarns. Textile Progress, 24 (3). Manchester: The Textile Institute.

10. Barella, A. (1998) Letters to Editor-A New Photoelectric Device for the Measurement of Yarn Diameter and Yarn Evenness. J. Text. Inst., 89 T711-T712
11. Barella, A., Bardi, X., and Castro, L., (1991) Yarn attrition and Hairiness: A yarn Self-Rubbing Test, J. Text. Inst., 82 (1), 78-85.
12. Barella, A., Coll-Totosa, L., Espiell, G. S., & Bardi, X. (1992). Neue Gesichtspunkte bei der Messung und Bewertung der Haarigkeit [New criteria for the measurement and evaluation of hairiness]. Textil Praxis, 47 (12), 1116-1125.
13. Barella, A., & Manich, A. M. (1982). Yarn hairiness measurements, present and future. 27th Hungarian Textile Conference (pp. [1-28]). Budapest: Hungarian Society of Textile Technology and Science.
14. Barella, A., & Manich, A. M. (1993). The hair length distribution of yarns, measured by means of the Zweigle G565 hairiness meter. J. Text. Inst., 84 (3), 326-335.
15. Barella, A., Martin, V., Vigo, J. P., & Manich, A. M. (1980). A new hairiness meter for yarns. J. Text. Inst., 71 (6), 277-283.
16. Barella, A., & Viaplana, A. (1970a). Principles of a new procedure for measuring yarn hairiness. Application to the study of the hairiness of open-end yarns. Text. Res. J., 40 (3), 267-272.
17. Bernsen J. (1986) "Dynamic thresholding of grey-level images, Proc. 8th International Conference on Pattern Recognition (ICPR8), pp 1251-1255, Paris, France, October 1986.
18. Boguslavskii, L. A. (1971). Air operated sensor for measuring yarn irregularity. Tech. of Textile Industry U.S.S.R., 3, 125-129.
19. Born, M., and Wolf, E. (1964) Principles of Optics (2nd Edition) New York, The Macmillan Company

20. Boswell, H. R., & Townend, P. P. (1957). Some factors affecting the hairiness of worsted yarns. J. Text. Inst., 48 (5), T135-142.
21. Burger, T., Kuhn, J., Caps, R., & Fricke, J. (1997). Quantitative determination of the scattering and absorption coefficients from diffuse reflectance and transmittance measurements: Application to pharmaceutical powders. Applied Spectroscopy, 51 (3), 309-317.
22. Calvo, M.L., Manzanares, A., Chevalier, M., and Lakshminarayanan, V. (1998) Edge Image Quality Assessment: A New Formulation for Degraded Edge Imaging. Image and Vision Computing 16, 1003-1017.
23. Chan, F. H. Y., Lam, F. K., and Zhu, H (1998) Adaptive thresholding by variational method, IEEE transactions on Image Processing, Vol. 7, No 3, 468-473
24. Chang-Chiun Huang, and Sun-Chong Liu. (2001). Woven Fabric Analysis by Image Processing. Part II: Computing the Twist Angle, . Text. Res. J., 71 (4), 362-366.
25. Chu, W. C., & Tsai, I. (1996a). A new photoelectric device for the measurement of yarn diameter and yarn evenness. Part I: Improvement of the variance of radiant intensity using the area compensation method. J. Text. Inst., 87, Part 1: Fibre Science and Textile Technology (3), 484-495.
26. Chu, W. C., & Tsai, I. (1996b). A new photoelectric device for the measurement of yarn diameter and yarn evenness. Part II: The measurement of yarn diameter and the effect of shape-error factor (SEF) on the measurement of yarn evenness. J. Text. Inst., 87, Part 1: Fibre Science and Textile Technology (3), 496-508.
27. Church, J. S., O'Neill, J. A., & Woodhead, A. L. (1998). Detection of fibrillated polymeric contaminants in wool and cotton yarns. Applied Spectroscopy, 52 (8), 1039-1046.

28. Cox, D. R., & Townsend, M. W. (1951). The use of correlograms for measuring yarn irregularity. J Text. Inst., 42 (4), P145-51.
29. Cybulska, M. (1999). Assessing yarn structure with image analysis methods. Text. Res. J., 69 (5), 369-373
30. Davis, H., McGregor R., Pastore C., Timble N. (1996). Human Perception and Fabric Streakiness. Text. Res. J., 66 (8), 533-534
31. Davis, W., Riddle, E., (1997). On the Packing Fraction Function and the Properties of Migrating Fiber Helical Curves in Fiber-Yarns, EFS System Research Forum November 6-7, 1997, Raleigh, NC. pp. 209
32. Davis, W., Riddle, E., (1999). Sequential Optical Measurement of Fiber-Yarn Density Employed to Approximate Packing Fraction of Cotton Yarns. EFS System Research Forum November 4-5, 1999, Raleigh, NC. pp.95
33. Demiroz, A., and Dias, T. (2000a). A Study of the Graphical Representation of Plain-Knitted Structures. Part I: Stitch Model for the Graphical Representation of Plain-Knitted Structures. J. Text. Inst., 91, Part 1, 463-480.
34. Demiroz, A., and Dias, T. (2000b). A Study of the Graphical Representation of Plain-Knitted Structures. Part I: Experimental Studies and Computer Generation of Plain-Knitted Structures. J. Text. Inst., 91, Part 1, 481-492.
35. Dorst, L, Smeulders, A. W. M. (1984) Discrete Representation of Straight Lines, IEEE Trans. on Pattern Analysis and Machine Intelligence, Vol. PAMI-6, No. 4, pp. 450-463.
36. Edmonds, I. R., (1969) A diffraction Method for the Estimation of Average Diameter and Standard Deviation of Diameter in a Fibre Sample. J. Text. Inst., 60, 161-164
37. FabricLink , Dictionary of Fabric Terms. (available online at <http://www.fabriclink.com/GLOSSARY.html>)
38. Fibre2Fashion, Textile Glossary. (available online at <http://www.fibre2fashion.com/glossary/glossary.htm>)

39. Foster, G. A. R. (1957). The effect of moisture upon the accuracy of capacity-type regularity testers. J. Text. Inst., 48 (4), T109-127.
40. Francini, F., & Longobardi, G. (1989). Quality control of textile yarn by optical filtering technique. Optics & Lasers in Engineering, 10 (2), 119-126.
41. Friedrich, M., & Zahn, D. R. T. (1998). Emission Spectroscopy: An excellent tool for the infrared characterization of textile fibers. Applied Spectroscopy, 52 (12), 1530-1535.
42. Gaskill, J.D., (1993) Linear Systems, Fourier Transformations and Optics. New York, John Wiley and Sons. ISBN 0-471-29288-5
43. Ghosh, S. N., Das, D. K., Bhattacharya, G. K., Jain, A. K., Sil, N. K., & Mukhopadhyay, B. N. (1988). An electronic instrument for measuring the hairiness of jute yarn. J. Text. Inst., 79(4), 634-640.
44. Glasbey, C. A., Hitchcock, D., Russel A. J. F., & Redden, H. (1994). Towards the automatic measurement of cashmere-fibre diameter by image analysis. J. Text. Inst., 85 (3), 301-307.
45. Goodman, J. W. (1996). Introduction to Fourier optics (2nd ed.). New York: McGraw-Hill.
46. Goswami, B. (1969). The hairiness of cotton yarns, an improvement over the existing microscopic technique. Text. Res. J., 39 (3), 234-242.
47. Gray, S. B., (1971). Local properties of binary images in two dimensions. IEEE Trans. Computers, 20(5), 551-561
48. Greer, C., Fundamentals of Machine Vision Cameras (Part 1).
49. Hattenschweiler, P. (1981). Hairiness: Human Eye and Testing Equipment in Comparison, Melliand Textilberichte, 72, 394-395, 12
50. Hearle, J. W. S., & Merchant, V. B. (1963). Relations between specific volume, count, and twist of spun nylon yarns. Text. Res. J., 33 (6), 417-424.

51. Hecht, E., (2002) Optics (4th Edition). New York. Addison Wesley Longman Inc. ISBN 0-8053-8566-5
52. Huang, Y., and Xu, B., (2002) Image Analysis for Cotton Fibres Part I: Longitudinal Measurements. *Text. Res. J.*, 72 (8), 713-720
53. Ikiz, Y. (2000) Fiber Length Measurement by Image Processing. PhD Thesis Graduate Faculty of North Carolina State University.
54. Iridag, Y. (1994). Iplik Tuylulugu Olcumunde Farkli Yaklasimlar [Different Approaches on Yarn Hairiness Measurement]. MSc Thesis. Istanbul Teknik Universitesi, Fen Bilimleri Enstitusu.
55. Jackson, M., Acar, M., Siong, L. Y., and Whitby, D. (1995) A Vision Based Yarn Scanning System. *Mechatronics*, Vol. 5, No 2/3, pp 133-146.
56. Kapur, Sahoo & Wong A new method for Gray-level picture thresholding using the entropy of the histogram, Computer Vision, Graphics, and Image Processing, vol 29, pp 273-285, 1985.
57. Keller, J., (1961). Geometrical Theory of Diffraction. *Journal of the Optical Society of America*. Vol 53, No 2, p116-129
58. Kirtay, N., (2002) Kalitenin Otomatik İzlenmesinde Veri Yönetim Sistemleri ile Değerlendirme Algoritmaları (Data Management Systems and Evaluation Algorithms for Automated Quality Monitoring) Türkiye V. Pamuk Tekstil ve Konfeksiyon Sempozyumu, 28-29 April 2002, Diyarbakir
59. Kittler, J. & Illingworth, J. (1986) Minimum error thresholding, Pattern Recognition, vol 19, pp 41-47, 1986.
60. Langenhove, L. V. (1997a) Simulating the Mechanical Properties of a Yarn Based on the Properties and Arrangement of Its Fibers Part I: The Finite Element Model. *Text. Res. J.*, 67 (4), 263-268.
61. Langenhove, L. V. (1997b) Simulating the Mechanical Properties of a Yarn Based on the Properties and Arrangement of Its Fibers Part II: Results of Simulations. *Text. Res. J.*, 67 (5), 342-347.

62. Langenhove, L. V. (1997c) Simulating the Mechanical Properties of a Yarn Based on the Properties and Arrangement of Its Fibers Part III: Practical Measurements. Text. Res. J., 67 (6), 406-412.
63. Lappage, J., & Onions, W. J. (1964). An instrument for the study of yarn hairiness. J. Text. Inst., 55 (8), T381-395.
64. Leedham, G, Yan, C, Takru, K, Tan, J. H. N. and Mian, L. (2003) Comparison of Some Thresholding Algorithms for Text/Background Segmentation in Difficult Document Images. Proceedings of the Seventh International Conference on Document Analysis and Recognition (ICDAR 2003)
65. Lord, P. R., (1997). Fundamental Problems with Online Data Streams, EFS System Research Forum November 6-7, 1997, Raleigh, NC. pp. 241
66. Lynch, L. J., and Thomas, N. (1971) Optical Diffraction Profiles of Single Fibres. J. Text. Inst., 41, 568-572
67. Lytle, F. E., (1999a) An Introduction to Diffraction. Part I: The Near Field. Applied Spectroscopy. Vol. 53, No. 7, p212a-228a
68. Lytle, F. E., (1999b) An Introduction to Diffraction. Part II: The Far Field. Applied Spectroscopy. Vol. 53, No. 7, p262a-276a
69. Manich, M., Barella, A., & Vigo, J. P. (1981). A contribution to the study of the hairiness of rotor-spun yarns by means of the digital hairiness meter Part I: The influence of the rotor geometry and other spinning parameters on the hairiness of open-end-spun acrylic-fibre yarns. J. Text. Inst., 51 (3), 121-140.
70. Mangold, G., and Topf, W. (1985). Hairiness and hairiness Index: A New Measuring Method. Melliand Textilberichte, 66, 245-247.
71. Millman, M. (1999). Computer vision for yarn quality inspection. Unpublished doctoral dissertation, Loughborough University, Loughborough.

72. Militky, J., Travnickova, M., & Bajzik, V. (1999). Air permeability and light transmission of weaves. International Journal of Clothing Science and Technology, Vol.11 No 2/3, 116-124.
73. Montalvo, J. G. Jr., Faught, S. E., Ramey, H. H. Jr. and Bucu, S. E. (1993) Studies to measure cotton fibre length, strength, micronaire and colour by vis/NIR reflectance spectroscopy. Part I: Descriptive statistics of fibre properties and reflectance spectra, *J. Near Infrared Spectrosc.* 1, 153-173 (1993),
74. Monteiro, J. L., & Couto, C. A. (1995). High resolution capacitive sensors for high speed yarn evenness analysis. In Proceedings of the International Conference on Recent Advances in Mechatronics, Istanbul, August 14-16 (pp. 824-829). Bogazici: Bogazici University Press.
75. Neckář, B, and Voborová, J. (2003) A New Approach For Determination of Yarn Hairiness.
76. Niblack, W. (1986) An introduction to Digital image processing, pp 115-116, Prentice Hall, 1986.
77. Onions, W. J., & Yates, M. (1954). The photoelectric measurement of the irregularity and the hairiness of worsted yarn. *J. Text. Inst.*, 45 (11), T873-885.
78. Otsu N. (1979) A threshold selection method from gray-level histograms, IEEE transactions on Systems, man and cybernetics, vol T-SMC 9, no 1, pp 62-66, 1979.
79. Pai, S. B., & Munshi, V. G. (1978). A new method for the determination of yarn hairiness by digital fibrograph. *Text. Res. J.* 48 (12), 697-700.
80. Pal, N. R & Pal, S. K. (1993) A review on image segmentation techniques, Pattern Recognition Vol 26, pp 1277-1294.
81. Pavlidis, T. (1982). Algorithms for Graphics and Image Processing. ISBN0-914894-65-X Maryland, Computer Science Press

82. Pillay, K. (1964). A study of the hairiness of cotton yarns. Part I – Effect of fiber and yarn factors. Text. Res. J., 34 (8), 663-674.
83. Pourdeyhimi, B., Ramanathan, R., & Dent, R. (1996a). Measuring fiber orientation in nonwovens. Part I: simulation. Text. Res. J., 66 (11), 713-722.
84. Pourdeyhimi, B., Ramanathan, R., & Dent, R. (1996b). Measuring fiber orientation in nonwovens. Part II: direct tracking. Text. Res. J., 66 (12), 747-753.
85. Pourdeyhimi, B., Dent, R., & Davis, H. (1997a) Measuring fiber orientation in nonwovens. Part III: Fourier transform. Text. Res. J., 67 (2), 143-151.
86. Pourdeyhimi, B., & Dent, R. (1997b). Measuring fiber orientation in nonwovens. Part IV: flow field analysis. Text. Res. J., 67 (3), 181-187.
87. Pourdeyhimi, B., Dent, R., Jerbi, A., Tanaka, S, and Deshpande, A. (1999). Measuring fiber orientation in nonwovens. Part V: Real Webs. Text. Res. J., 69 (3), 185-192.
88. Pourdeyhimi, B., & Kim, H. S. (2002). Measuring fiber orientation in nonwovens: The Hough Transform. Text. Res. J., 72 (9), 803-809.
89. Pratt, W. K., (1991). Digital Image Processing, Wiley-Interscience, 2nd Edition.
90. Riddle, E., Aminuddin, N., (1997). Preliminary Examination of Long Sequences of Yarn Capacitive and Optical Evenness Data, EFS System Research Forum November 6-7, 1997, Raleigh, NC. pp.253
91. Riddle, E. R., Davis, W. R. (2000). Successive Optical Measurements of Cotton Fiber-yarns and Their Analysis to obtain Structural Information Including Density and Density Variations. . EFS System Research Forum November 2-3, 2000, Raleigh, NC.

92. Rodrigues, F. C., Silva, M. S., & Morgado, C. p. (1983). The configuration of a textile yarn in the frequency space: A method of measurement of hairiness. J. Text. Inst., 74 (4), 161-169.
93. Rong, G.H., & Slater, K. (1995). Analysis of yarn unevenness by using a digital-signal-processing technique. J. Text. Inst., 86 (4), 590-599.
94. Rousseau, L. and Maron, O. (1963). Visual Regularity of Yarns. J. Text. Inst., 54 T266-T268
95. Rust, J. P., & Peykamian, S. (1992). Yarn hairiness and the process of winding. Text. Res. J., 62 (11), 685-689.
96. S. Schwab Company, Quality Assurance Manual APX 61 (available on line at <http://notes-web.sschwab.com>)
97. Sankur, B& Sezgin, M. (2004) A Survey Over Image Thresholding Techniques And Quantitative Performance Evaluation, Journal of Electronic Imaging, 13(1), 146-165, January, 2004.
98. Sauvola, J., and Pietaksinen, M., [2000] Adaptive document image binarization. Pattern Recognition, 33, p225-236.
99. Silva, M. S., Rodrigues, F. C., Amoreira, L., & Morgado, C. P. (1981). New laser methods for quality control of textiles. International Textile Symposium, 969-972.
100. Sinclair Consultancy, Glossary of Textile Terms (available online at <http://www.sinclair-consultancy.sagenet.co.uk/glossary.htm>)
101. Slack, J. K. (1970). An instrument for measuring the hairiness of yarns. J. Text. Inst., 61 (9), T428-437.
102. Slater, K. (1986). Yarn evenness. Textile Progress 14 (3-4). Manchester: The Textile Institute.
103. Smith, W. J., (2000) Modern optical Engineering (3rd Edition). New York, McGraw Hill, ISBN 0-07-136360-2

104. Soll, W. (1999). Information gain through optoelectronic measurement of the two-dimensionally determined yarn diameter. Melliand English (6), E125-126.
105. Soll, W (1999). Comparison of the capacitive and optical measuring methods to determine evenness. Zellweger Uster, Switzerland. (available from www.uster.com)
106. Sommerville, P., (2003) Fundamental Principles of Fibre Fineness Measurement. Part 7: Optical diffraction. AWTA Ltd. Newsletter. (Available at www.awta.com.au)
107. Southwell, R. (1946) Relaxation Methods in Theoretical Physics, Clarendon Press, Oxford.
108. Suh, M., (1967) A Study of the Shrinkage of Plain Knitted Cotton Fabric, Based on the Structural Changes of the Loop Geometry Due to Yarn Swelling and Deswelling. Text. Res. J., 37, 417-431
109. Suh, M. W., Kim, J. (1996) Fabric Image Simulation by Wavelet Analysis of Yarn Profiles. 9th EFS System Research Forum, November 7-8, Raleigh, NC.
110. Suh, M. W., Kim, J. (1997a). Statistical modeling of spun yarn characteristics under HVI data environment. Annual report to Cotton Inc., Raleigh, NC.
111. Suh, M. W., Kim, J. (1997b) Creation of Virtual Fabrics by Wavelet Analysis of Spun Yarn Density Signals. 10th EFS System Research Forum, November 6-7, Raleigh, NC.
112. Suh, M. W., Jasper W., Woo, J. L., Kim, H. B. (2000). Methods for Fusing Diameter and Mass Measurements of Spun Yarns. EFS System Research Forum November 2-3, 2000, Raleigh, NC.

113. Suh, M.W., Snyder, B., (1999). Wavelet-Base Yarn Quality Measures for Predicting Fabric Appearance. EFS System Research Forum November 4-5, 1999, Raleigh, NC. pp.107
114. Sust, A., and Barella, A. (1964). Twist, Diameter and Unevenness of Yarns-A New Approach. J. Text. Inst., 55 T1-T6
115. Spindelfabrik Suessen, (2002) "Three Years of Practical Experience with the EliTe Q CompactSet in Short-Staple Spinning" Spinnovation, No.17 – March 2002
116. Taylor, R. A. (1999). Measuring Cotton Fiber Mass Using Near Infrared Light.
117. Tottman, J. A., & Slater, K. (1981). The use of microcomputers in deriving variance-length curves. J. Text. Inst., 72 (3), 103-110.
118. Townsend, M. W. H., & Cox, D. R. (1951). The analysis of yarn irregularity. J. Text. Inst., 42 (3), P107-113.
119. Trier, Ø. D. & Taxt, T. (1995) Evaluation of Binarization Methods for Document Images. IEEE Transactions on Pattern Analysis and Machine Intelligence Volume 17, Issue 3 (March 1995) tabl pp: 312-315.
120. Umbaugh, S. E., (1998) Computer Vision and Image Processing: A Practical Approach using CVIPtools. New Jersey, Prentice Hall, Inc. ISBN 0-13-264599-8
121. Walton, W. (1968). Use of a yarn hairiness meter and results showing the effect of some spinning conditions on yarn hairiness. J. Text. Inst., 59 (8), 365-378.
122. Wang, X. (1997). The effect of testing speed on the hairiness of ring-spun and Sirospun yarns. J. Text. Inst., 88, Part 1: Fibre Science and Textile Technology (2), 99-106.
123. Wang, X., & Chang, L. (1999). An experimental study of the effect of test speed on yarn hairiness. Text. Res. J., 69 (1), 25-29.

124. Wang, X., Huang, W., & Huang, X.B.(1999a). Effect of test speed and twist level on the hairiness of worsted yarns. Text. Res. J., 69 (12), 889-892.
125. Wang, X., Huang, W., & Huang, X.B. (1999b). A study on the formation of yarn hairiness. J. Text. Inst., 90 (4), 555-569.
126. Wulfhorst, B., & Bergmann, J. (1989). Comparison of different optical measuring methods for the determination of the real yarn diameter. Melliand English, 70, E41-E42. Translated from Melliand Textilberichte, 70, 95-97.
127. Victor Perrin's glossary (available online at <http://www.victor-perrin.fr/e/glossary.htm>)
128. Yang, L., Albregtsen, F., Lønnestad, T., and Grøttum, P. (1994) Methods to Estimate Areas and Perimeters of Blob-Like Objects: A Comparison Proc. IAPR Workshop on Machine Vision Applications (available at CiteSeer-<http://citeseer.nj.nec.com/cs>)
129. Yanowitz, S.D. & Bruckstein, A.M. (1989) A New Method for Image Segmentation, Comput. Vision Graphics Image Proc., vol 46, no 1, pp 82-95, April 1989

